# Interplay between gravity and bulk phenomena in mixtures and mass-polydisperse colloidal systems

Von der Universität Bayreuth
zur Erlangung des Grades eines
Doktors der Naturwissenschaften (Dr. rer. nat.)
genehmigte Abhandlung

von

**Tobias Eckert**

aus Prien am Chiemsee

1. Gutachter: Prof. Dr. Daniel de las Heras
2. Gutachter: Prof. Dr. Margarida Telo da Gama

Tag der Einreichung: 14. April 2023
Tag des Kolloquiums: 27. Juli 2023

# Abstract

Colloidal particles are nano- to micron-sized particles subject to thermal motion. Despite of being made of millions of atoms, colloidal particles share with atoms and molecules the ability to form similar states of matter such as fluids, solids, and liquid crystalline phases. However, in contrast to molecular systems, colloidal systems can be strongly affected by the Earth's gravitational field over vertical length scales of just a few millimeters.

Sedimentation equilibrium experiments, in which a colloidal suspension reaches equilibrium in a cuvette of a few centimeters height, are ideal candidates to study bulk behaviour and phase transitions. Sedimentation experiments in colloidal science are relatively simple and allow a direct observation of the thermodynamically stable phases of a given colloidal suspension. However, gravity can have a profound effect on the system which needs to be considered for the correct interpretation of the experimental results.

The effect of gravity in sedimentation is particularly relevant if the colloidal particles have different buoyant masses, as it is the case in colloidal mixtures. There, the gravitational field couples differently to each of the species, generating new and counterintuitive phenomenology. For example, several layers of different bulk phases are often found in experiments. Even the same bulk phase can reenter the stacking sequence.

This Thesis is devoted to understanding the interplay between gravity and bulk phenomena in colloidal sedimentation. The gravitational field is incorporated on top of a bulk description via sedimentation path theory, which approximates each horizontal slab of the sedimented sampled by an equilibrium system with the corresponding colloidal concentrations. Using sedimentation path theory and density functional theory, we reinterpret theoretically the findings of iconic sedimentation experiments by van der Kooij and Lekkerkerker in rod-plate colloidal mixtures. We demonstrate that the interplay between gravity and a relatively simple bulk phase diagram is enough to reproduce the complex stacking sequences found in the experiments, including the relative thicknesses of the layers. We also consider plate-sphere mixtures and show how the values of the macroscopic thicknesses of the individual layers in a stacking sequence can be used to estimate microscopic information of the mixture such as the buoyant masses. The ratio between the buoyant masses of the species and the sample height are two key parameters that control the sedimentation-diffusion-equilibrium of the system.

Beyond binary mixtures, we extend sedimentation path theory to mass-polydisperse colloidal systems. That is, a colloidal system in which all the particles are identical except for their buoyant masses, which follow a given distribution. Using statistical mechanics we map the mass-polydisperse system to an effective monodisperse system. The mapping is exact within the local equilibrium approximation of sedimentation path theory. We apply the theory to mass-polydisperse colloidal systems of spheres and rods, and demonstrate that mass-polydispersity can play an important role in experiments near density matching.

# Kurzfassung

Kolloidale Teilchen sind Nano- bis Mikrometer groß und unterliegen thermischen Bewegung. Obwohl sie aus Millionen von Atomen bestehen, haben kolloidale Teilchen mit Atomen und Molekülen gemeinsam, dass sie ähnliche Aggregatzustände wie Flüssigkeiten, Feststoffe und flüssigkristalline Phasen bilden. Im Gegensatz zu molekularen Systemen können kolloidale Systeme jedoch über vertikale Längenskalen von nur wenigen Millimetern stark durch das Gravitationsfeld der Erde beeinflusst werden.

Sedimentationsgleichgewichtsexperimente, bei denen eine kolloidale Suspension in einer Küvette von wenigen Zentimetern Höhe ein Gleichgewicht erreicht, sind ideale Kandidaten für die Untersuchung von Phasenübergängen. Sedimentationsexperimente in der Kolloidforschung sind relativ einfach und ermöglichen eine direkte Beobachtung der thermodynamisch stabilen Phasen einer bestimmten kolloidalen Suspension. Allerdings kann die Schwerkraft einen tiefgreifenden Einfluss auf das System haben, der für die korrekte Interpretation der Versuchsergebnisse berücksichtigt werden muss.

Die Wirkung der Schwerkraft bei der Sedimentation ist besonders relevant, wenn die kolloidalen Teilchen unterschiedliche Auftriebsmassen haben, wie es bei kolloidalen Mischungen der Fall ist. Hier koppelt das Gravitationsfeld unterschiedlich an die einzelnen Spezies, was zu neuen und kontraintuitiven Phänomenen führt. So werden in Experimenten häufig mehrere Schichten unterschiedlicher Phasen gefunden. Sogar ein und dieselbe Phase kann mehrmal in der Schichtung auftreten.

Diese Dissertation widmet sich dem Verständnis des Zusammenspiels von Schwerkraft und thermodynamischen Phänomenen bei der kolloidalen Sedimentation. Das Gravitationsfeld wird mittels der Sedimentationspfadtheorie integriert, die jede horizontale Schnitt der sedimentierten Probe durch ein Gleichgewichtssystem mit den entsprechenden kolloidalen Konzentrationen approximiert. Mit Hilfe der Sedimentationspfadtheorie und der Dichtefunktionaltheorie interpretieren wir theoretisch die Ergebnisse der ikonischen Sedimentationsexperimente von van der Kooij und Lekkerkerker in kolloidalen Stäbchen-Plättchen-Gemischen neu. Wir zeigen, dass das Zusammenspiel von Schwerkraft und einem relativ einfachen Phasendiagramm ausreicht, um die in den Experimenten gefundenen komplexen Schichtungen zu reproduzieren, einschließlich der relativen Dicke der Schichten. Wir betrachten auch Plättchen-Kugel-Gemische und zeigen, wie die Werte der makroskopischen Dicken der einzelnen Schichten verwendet werden können, um mikroskopische Informationen des Gemischs wie die Auftriebsmassen zu schätzen. Das Verhältnis zwischen den Auftriebsmassen der Teilchenarten und die Probenhöhe sind zwei Schlüsselparameter, die das Sedimentations-Diffusions-Gleichgewicht des Systems steuern.

Über binäre Mischungen hinaus erweitern wir die Sedimentationspfadtheorie auf massenpolydisperse kolloidale Systeme. Das heißt, ein kolloidales System, in dem alle Teilchen identisch sind, mit Ausnahme ihrer Auftriebsmassen, die einer bestimmten Wahrscheinlichkeitsverteilung folgen. Mit Hilfe der statistischen Mechanik bilden wir das massenpolydisperse System auf ein effektives

monodisperses System ab. Die Abbildung ist im Rahmen der lokalen Gleichgewichtsannäherung der Sedimentationspfadtheorie exakt. Wir wenden die Theorie auf massenpolydisperse kolloidale Systeme aus Kugeln und Stäbchen an und zeigen, dass Massenpolydispersität in Experimenten nahe der Dichtegleichheit von Teilchen und Lösungmittel eine wichtige Rolle spielen kann.

# Contents

# 1 Introduction

This Thesis addresses the equilibrium behaviour of colloidal mixtures under gravity. We study the formation of layers of different bulk phases that occur due to the interplay between gravity and bulk phenomena, and investigate the dependence of the sequences of layers on the composition of the mixture and the height of the colloidal sample. Furthermore, we examine the influence of mass-polydispersity on colloidal systems under gravity by extending sedimentation path theory from binary mixtures to mass-polydisperse suspensions.

In this first introductory chapter, we give a brief account of the phenomenology of colloidal mixtures of anisotropic particles and theoretical methods for the description and investigation of colloidal suspensions.

## 1.1 Colloidal particles

Colloids are particles on the scale of nano- to micrometer suspended in a solvent which is usually a fluid such as water or organic solvents. Colloidal particles are large compared to the characteristic atomic length scale and can therefore by treated classically. On the other hand, colloidal particles are small compared to the characteristic length scale of granular particles and are therefore subject to thermodynamic fluctuations due to random collisions with the solvent molecules. This random motion of colloidal particles was first observed by Brown [5] in 1827, and the phenomena was later explained by Einstein [6] and Sutherland [7] in 1905. Due to the separation of length scales between the colloidal particles and the solvent particles, a vast number of solvent particles collide at any given time from all directions with the colloidal particles. The sum of all these collisions gives rise to a quasi-random force on the colloidal particles.

Colloids are omnipresent in our everyday life, for instance in the form of gels, emulsions, such as milk or hand cream, pigmented ink or clay. Due to their size, colloidal particles can be experimentally observed using optical confocal microscopy [8, 9]. Colloids can be used as a classical model for atoms since under certain circumstances they behave like “big atoms” [10] and give direct insight into the self-assembly of materials via computer simulations or experimentally.

Theoretically, colloids can be modeled with a wide range of different interparticle interaction potentials. A notable example is the hard core potential [11].

With hard core interparticle interaction, particles are forbidden to overlap. Otherwise the particles do not interact. Systems of hard particles are athermal since there is no finite interaction energy scale, and are thus purely entropically driven. Hard interaction potentials are well studied model colloidal systems [11] and are useful to separate the effect of mutual exclusion of the particles from that of long range interaction.

### 1.1.1 Anisotropy

Many colloidal particles are anisotropic in either their shape, e.g. rods, or their interaction potential, e.g. patchy colloids. An illustrative selection of scanning electron microscope images of experimental colloidal spheres, spheroids, rods and rod-like particles is presented in Fig. 1.1. Anisotropic colloidal particles show rich bulk phenomenology with several liquid-crystalline phases. In material science, nanoparticles such as metal nanorods, nanowires, nanoplates, nanocubes and nanocages are used to engineer the self-assembly of functional materials [12]. In biology, there are filamentous viruses, which resemble hard rod-like colloidal particle [13]. Another example for shape anisotropic colloidal particles in nature is the aqueous suspensions of clay [14]. The existence of a liquid-crystalline order of the plate-like clay was demonstrated using polarized-light microscopy and small-angle X-ray scattering [15, 16].

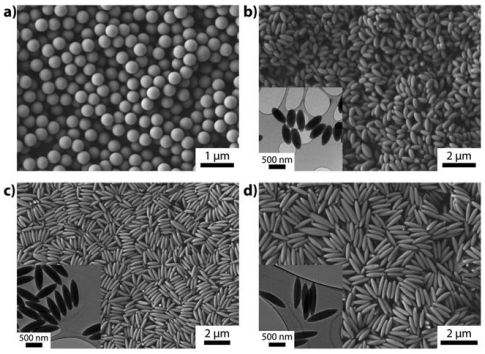


SEM images of amorphous polystyrene spheres (a) and spheroids (b–d) of various aspect ratios. Insets show transmission images (TEM). Adapted from Ref. [17] published under CC-BY license.

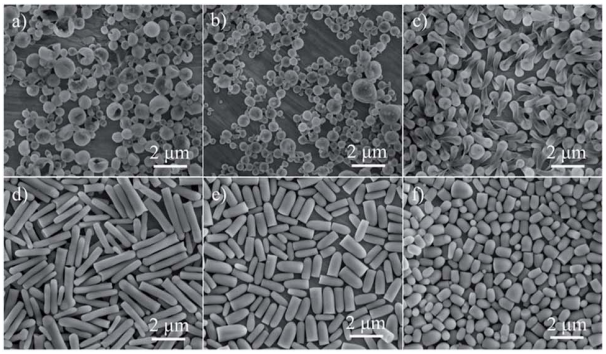


SEM images of anisotropic silica particles with different 1-heptanol/ethanol mixing ratios (v/v): (a) 3:8, (b) 4:7, (c) 5:6, (d) 6:5, (e) 7:4, (f) 8:3. Adapted from Ref. [18] published under CC-BY-NC license.

Figure 1.1: Scanning electron microscope (SEM) images of isotropic and anisotropic experimental colloidal particles.

For technical applications, various types of anisotropic colloidal particles are of special interest. This includes shape anisotropy, such as rods, plates and wires, and anisotropic interparticle interaction potentials, such as electric or magnetic dipoles [19–22].

Most applications of liquid crystals have in common that they exploit the ability of anisotropic particles to form spatially and/or orientationally ordered phases. Hard anisotropic particles are purely entropically driven, thus the transition into ordered phases is due to an increase in the particle concentration (lyotropic liquid crystal). The formation of ordered phases is a balance between orientational and positional entropy. In very dilute systems, the anisotropic particles are free to move and rotate, and particles infrequently interact. The system forms then a homogeneous isotropic (I) phase with every position and orientation of the particles being equally likely, see Fig. 1.2(a). In denser systems, the anisotropic particles are packed more closely together. If the particles were randomly oriented they would interfere with each other and positional freedom and therefore entropy would drastically decrease. The particles would essentially be stuck. To

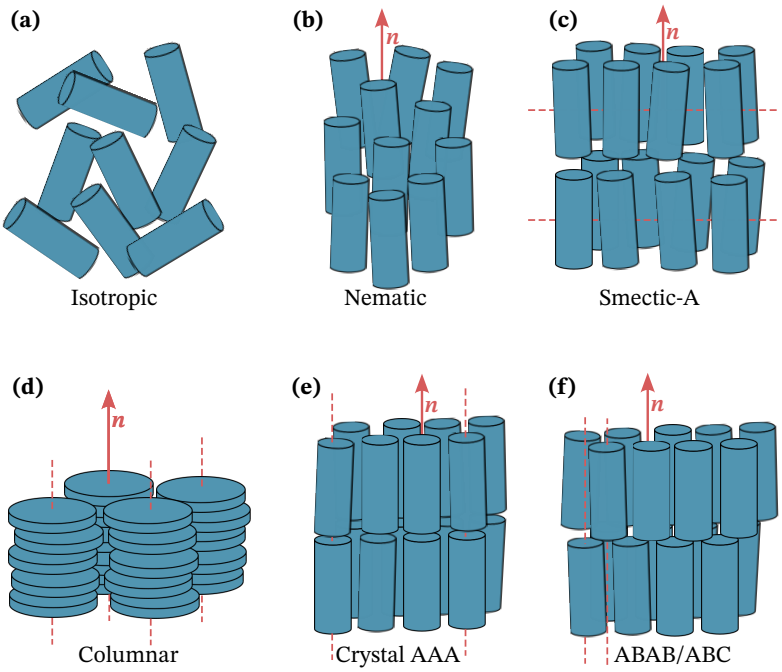


Figure 1.2: Schematics of a selection of the different liquid crystalline phases formed by anisotropic particles: isotropic (I), nematic (N), smectic-A (SmA), columnar (C), crystal AAA, ABAB and ABC. The local director is indicated by the vector $\boldsymbol{n}$. The planes in which the system is ordered are marked by dashed lines.

increase their positional entropy, the particles have to roughly align themselves with each other along a common direction, known as the director, in order to pack more efficiently. This decreases the orientational entropy in favour of an increase in positional entropy. For high enough particle concentration this trade-off is beneficial to the overall entropy of the system and the particles transition into the nematic phase. The nematic (N) phase exhibits orientational order (the particles are roughly aligned) but not positional order (particles are randomly positioned without overlaps), see Fig. 1.2(b). At even higher concentrations anisotropic particles can develop, in addition to orientational order, positional order in one or two spatial directions, depending on their shape. Prolate particles, such as rods tend to transition into a smectic phase with order in one dimension (1D) since particles form layers. If the layers are perpendicular to the director, the phase is called smectic-A (SmA) [see Fig. 1.2(c)]. Other configurations like the Sm-C, in which the direction is not perpendicular to the layers are also possible. Within the 1D layers of a smectic phase there is no positional order. Oblate particles, such as plates or disk tend to form columnar phases, in which particles arrange in columns along the director, see Fig. 1.2(d). At higher concentration the particles can develop crystalline phases, which are ordered in all three spatial dimensions. Several different crystalline phases exist. For example, with the layers of particles aligned (particle on top of particle) like in AAA phase, or with the layers shifted with respect to each other, like in a ABAB or ABC phase, see Fig. 1.2(e-f).

Which of these phases can be observed in a system of colloidal particles depends on their

shape. Thin hard spherocylinders with width-to-length aspect ratio 1:10 for instance exhibit I-N-SmA-AAA-ABC transitions with increasing concentration, whereas for aspect ratio 2:5 the sequence is I-SmA-ABC [23]. Moreover, there exist numerous other liquid crystal phases, such as biaxial nematic, cubatic, cholesteric [24], blue phases [25], several other smectic and crystal phases [26], which we do not cover here, since they do not emerge in the colloidal systems that we study in the following. We refer the read to Ref. [27] for a detailed description of mesophases in liquid crystalline systems.

Although in this Thesis we focus on hard shape-anisotropic colloidal particles, there is a large field of colloids which are anisotropic in their soft interparticle interaction potential such as e.g. patchy colloids [28, 29]. Patchy colloidal particles are anisotropically patterned with attractive interaction sites, modified geometry (such as indentations), or both. Patchy particles can have different types of patches and also different numbers of patches. Due to the patches, the particles can form chains with different junctions and thus show interesting phase behaviour with reentrant phases [30] and formation of networks [31].

### 1.1.2 Polydispersity

Systems of colloidal particles are always polydisperse to a certain degree, specially those formed by natural colloids. Polydispersity means that the colloidal particles in the system have different shape or size, or in general different interparticle interactions. Examples are systems of hard colloidal spheres with varying diameter, and rods or plates with varying length-to-diameter ratios. In colloidal experiments some degree of polydispersity is inevitable [32, 33]. Due to synthesis, the colloidal particles have never identical shape and size [34].

Polydispersity has a strong effect on the phase behaviour of colloidal suspensions. It was shown that the crystal phase of hard spheres ceases to be stable beyond a critical degree of polydispersity of the order of 20% [35]. The crystal nucleation in polydisperse hard sphere colloids is suppressed due to increase of the surface free energy was observed [36]. For a system of hard spherocylinders in the limit of infinite aspect ratio and polydispersity in the length of the particles, it was found that the smectic phase becomes increasingly destabilized up to a degree of polydispersity above which the smectic phase is no longer stable [37]. In polydisperse mixtures of uniaxial rodlike and platelike hard parallelepipeds, polydispersity stabilizes the biaxial phase compared to the corresponding monodisperse mixture [38]. In a monolayer suspension of platelets with a high degree of polydispersity in the diameter, an increase in the isotropic-nematic transition packing fraction as well as the formation of a smectic phase was observed [39]. Thus it is important to understand the effect of polydispersity on colloidal systems in order to interpret colloidal experiments correctly.

In sedimentation-diffusion-equilibrium experiments an additional aspect of polydispersity is revealed. Not only do particles in polydisperse systems have different sizes, but as a consequence they also have different buoyant masses, which affects their behavior under gravity. This makes it more challenging to interpret experiments and to uncouple these two aspects of size polydispersity under gravity. In Ref. [3] we design a model with particles which are only polydisperse in their buoyant masses but not in their size or shape (mass-polydispersity). This circumvent the coupling between size- and mass-polydispersity and tries to isolate the effects of gravity on polydisperse

systems. A mass-polydisperse colloidal suspension can experimentally realized by e.g. core-shell colloids with differently sized cores and shells, but the same overall particle size.

## 1.2 Sedimentation

On Earth the gravitational field is omnipresent in experiments. To minimize the effective influence of gravity, experiments can be done in a reference frame accelerated by gravity. For instance, short time microgravity experiments in free fall towers ($< 9\,\mathrm{s}$), during parabolic flights ($\sim 20\,\mathrm{s}$) or in sounding rockets ($\sim 15\,\mathrm{min}$) [40, 41]. Longer microgravity experiments of up to days can be carried out on the ISS [42]. All other experiments in colloidal science on Earth are inevitably subject to gravity.

Whether or not gravity has a significant influence on sedimentation experiments can be determined by comparing the gravitational length with the length scale of the experiment. The gravitational length is the characteristic length scale by which a particle is lifted due to thermal fluctuations. Comparing the change in potential energy due to lifting one particle a distance $\xi$ in the gravitational field with the thermodynamic energy scale $k_\mathrm{B}T$, leads to the gravitational length

$$\xi = \frac{k_\mathrm{B}T}{mg}. \tag{1.1}$$

Here, $g$ is the gravitational acceleration, $k_\mathrm{B}$ is the Boltzmann's constant, $T$ is absolute temperature and $m$ is the buoyant mass of the colloidal particle. For molecules, $m$ is simply the molecular mass.

In molecular systems the gravitational length is typically of the order of meters to kilometers in Earth's gravitational field and therefore much larger than standard experimental setups. Thus, the effect of gravity is negligible in sedimentation of molecular systems which are dominated by the free diffusion of the molecules rather than by sedimentation under gravity. For colloids, however, the gravitational length is often of the order of micro- to centimeter and it is therefore comparable to the experimental length scales. Thus, gravity cannot be ignored and we observe the settling of colloidal particles towards the bottom of the experiments. For macroscopic objects of sizes larger than millimeters, the gravitational length is below nanoscopic. As we are used to from everyday objects, they do not freely diffuse in air or water, but either settle under gravity or float at an interface. Thermal fluctuations do not play any role for macroscopic objects.

In 1926 Jean Baptiste Perrin received the Nobel Prize in physics for discovering the balance between diffusion of particles in the solvent and settling towards the bottom under gravity [43]. Thus, in equilibrium there is a buoyant mass density gradient with decreasing mass density towards the top of the solution, the so-called sedimentation-diffusion-equilibrium.

This mass density gradient is for instance exploited in differential centrifugation analysis to separate the components of a mixture. As discussed, for molecular mixtures the gravitational length is larger than the vertical height of the experimental test tube and hence no significant separation between molecules of different masses can be achieved. Thus, ultra-centrifuges, which are capable of generating acceleration fields of up to $10^6 g$, must be used. The field was pioneered by Theodor Svedberg, who received the Nobel Prize in chemistry in 1926, the same year as Perrin,

for his use of ultracentrifuges in the research on colloids and proteins [44, 45].

For many colloidal suspensions however, Earth's gravity is sufficient to observe density gradients in cuvettes with heights of centimeters. Colloidal systems can transition from isotropic or disordered phases into ordered phases at higher densities. Thus due to the density gradient, a vertical stacking of layers of different bulk phases, the so-called stacking sequence, can be observed in the vessel (see an example in Fig. 1.3), using for instance crossed polarizers in case of anisotropic colloids. The stacking of several phases under gravity does not imply their coexistence in bulk. There, phases spontaneously separate without any external field. The formation of stacking sequences under gravity arises from a delicate interplay between gravity and bulk behavior. Perrin showed in his pioneering work [43] that in sedimentation experiments, the density profile can provide the full equation of state for monocomponent systems. This was used to study the equation of state in both isotropic [46, 47] and anisotropic [48, 49] colloidal systems.

(a) $IN_r$ (b) $IN_rN_p$ (c) $IN_p$ (d) $IN_rN_pC$ (e) $IN_rSN_pC$ (f) $N_rSN_pC$ (g) $N_pC$

Figure 1.3: Sedimentation experiments on a colloidal mixture of rods and plates (pictures taken between crossed polarizers) by van der Kooij and Lekkerkerker [50]. The liquid crystal phases found in the samples are isotropic ($I$), rod-rich nematic ($N_r$), plate-rich nematic ($N_p$), presumably smectic ($S$) and columnar ($C$). The stacking sequences from top to bottom of the samples as reported in Ref. [34] are given below each sample. Adapted with permission from Ref. [34], Copyright 2000 American Chemical Society.

In mixtures, gravity is especially important since there are two or more, in general different, gravitational lengths. Thus, it is crucial to disentangle the effects of gravity from those due to bulk phenomena in order to understand sedimentation in colloidal mixtures. There is a rich phenomenology of vertical stacked layers of different bulk phases in mixtures. For example, up to six different phases were observed in mixtures of positively charged colloidal plates and nonadsorbing polymers [51]. In mixtures, the same phases can reenter the stacking sequence, e.g. a floating nematic layer between two isotropic layers occurs in platelet-sphere mixtures [52]. The iconic experiments on colloidal mixtures of plates and rods by van der Kooij and Lekkerkerker [34, 50] reported the occurrence of stacking sequences with up to five bulk phases, including isotropic, nematic, smectic and crystalline phases. In binary mixtures of patchy colloids, twenty different stacking sequences were found and the size of the particles was identified as a control parameter to influence the stacking sequence under gravity [53]. The effects of the sample height on the stacking sequence was investigated by Geigenfeind and de las Heras [54] in mixtures of patchy

particles using sedimentation path theory. The height was identified as a vital control parameter in sedimentation-diffusion-equilibrium of colloidal mixtures. In binary mixtures of thick and thin hard rods, the occurrence of an isotropic layer sandwiched between two nematic layers was observed and up to sixteen distinct stacking sequences, including several with five phases, were found [55]. Savenko and Dijkstra investigated hard spherocylinders with a aspect ratio of 5.0 in a semi-infinite system under gravity and compared the stacking behavior with Monte Carlo simulations [48]. Sedimentation in a binary mixture of hard tetramers and hard spheres was proposed as a route to colloidal photonic crystal fabrication of an analogue of the Laves phase [56, 57].

## 1.3 Theoretical treatments of colloidal systems

We provide next the theoretical foundation used in our analysis for sedimentation-diffusion-equilibrium experiments and our formulation of sedimentation path theory for mass-polydisperse systems under gravity.

### 1.3.1 Sedimentation Path Theory

In the following we discuss how to incorporate the effect of gravity into an already existing bulk theory. To achieve this we use a local equilibrium approximation, which assumes that every horizontal slice at the sedimented sample at elevation $z$ can be described by a bulk equilibrium system with the same packing fractions as the slice in the sedimenting system. This approximation is accurate if all correlation length are small compared to the gravitational lengths of every species. This is the case in many colloidal systems where the gravitational length is often of the order of millimeter. Thus, we can couple every slice in sedimentation with the aforementioned bulk theory via a local chemical potential [58]

$$\mu_i(z) = \bar{\mu}_i - m_i g \left( z - \frac{h}{2} \right), \tag{1.2}$$

for each species $i$ with buoyant mass $m_i$. Here $\bar{\mu}_i$ is the chemical potential of species $i$ in the middle of the sample ($z = h/2$), $h$ is the height of the sample ($0 \leq z \leq h$) and $g$ is the gravitational acceleration. The average packing fraction $\bar{\eta}_i$ of species $i$ over the whole sample is controlled by $\bar{\mu}_i$ that can also be understood as the chemical potential of species $i$ in the absence of gravity.

#### Binary mixtures

In binary mixtures, i.e. $i \in \{1, 2\}$, (and also in multicomponent mixtures) we can eliminate the dependency of $\mu_i(z)$ on $z$ in Eq. (1.2). We obtain [58]

$$\mu_2(\mu_1) = s\mu_1 + a, \tag{1.3}$$

which is the equation of a straight line in the plane of $\mu_1$ and $\mu_2$, with a slope given by the buoyant mass ratio $s = m_2/m_1 = \xi_1/\xi_2$ and intercept $a = \bar{\mu}_2 - s\bar{\mu}_1$. Thus, we conclude that we can effectively describe sedimentation-diffusion-equilibrium in colloidal mixtures by straight segments

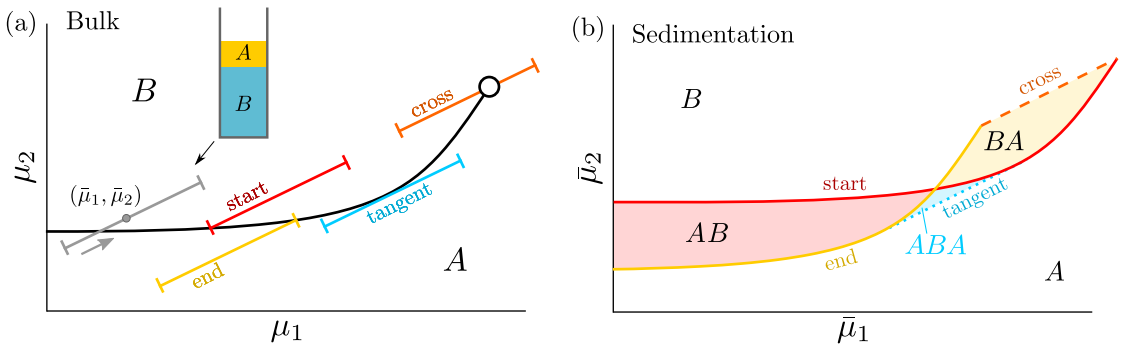


Figure 1.4: (a) Model for a bulk phase diagram in the plane of chemical potentials of the two species, $\mu_1$ and $\mu_2$. The bulk binodal (black-solid line) between phases $A$ and $B$ ends at a critical point (empty circle). The sedimentation paths are represented by segments of straight lines. The gray path that crosses the binodal corresponds to a stacking sequence $AB$ (from top to bottom, indicated by the grey arrow), as schematically depicted. Examples of sedimentation paths that (i) either start (red) or end (yellow) at the binodal, (ii) paths tangent (blue) to the binodal, and (iii) paths crossing (orange) the critical point. This sedimentation paths form the boundaries between different stacking sequences. The stacking sequence can be altered by an infinitesimal displacement of any of such sedimentation paths. (b) Corresponding stacking diagram in the plane of average chemical potentials $\bar{\mu}_1$ and $\bar{\mu}_2$ with colored regions for the different stacking sequences. The boundary lines between sequences are the sedimentation binodals of type I (solid lines) or type II (dotted-blue line), and the terminal lines (dashed-orange line). Adapted from Ref. [1].

of lines, parameterized by the elevations $z$, in the plane of chemical potentials. Accordingly, we call these line segments the sedimentation paths.

If we know the bulk phase diagram in the plane of chemical potentials of a binary mixture, then we also know for each point $(\mu_1, \mu_2)$ the stable bulk phase. Each time the sedimentation path crosses a bulk binodal in the plane of chemical potentials, the sedimented system undergoes a phase transition and the value of the parameter $z$ at which the crossing occurs is the elevation at which the system develops an interface in the sample. The stacking sequence of the system, i.e. the order in which the layers appear from top of the sample to the bottom, can be read off the sedimentation path by noting which phase regions the path crosses in the bulk phase diagram. Sedimentation paths that pass through, e.g. a triple or critical point, or sedimentation paths that do not cross, but touch the bulk binodal are special. Only a slight variation in either the position $a$ or the slope $s$ of the sedimentation path can lead to the path crossing the binodal and therefore changing the stacking sequence.

There are three types of special sedimentation paths which form the three types of sedimentation binodals [54], see Fig. 1.4(a). The first type of special sedimentation paths are those which either start or end at a bulk binodal (red and yellow paths in Fig. 1.4) and constitute the sedimentation binodal of type I. Sedimentation binodals of type II are formed by sedimentation paths tangent to a bulk binodal (blue path in Fig. 1.4). Lastly, sedimentation paths that cross an ending point of a

binodal, e.g. a triple or a critical point (orange path in Fig. 1.4) form the so-called terminal lines.

All these sedimentation binodals constitute the stacking diagram which is analogue to the bulk phase diagram, but for stacking sequences instead of bulk phases. Since stacking sequences consist of the vertically arranged sequences of phases, the stacking diagram can be computed, within the local equilibrium approximation, from the bulk phase diagram. Just like the bulk phase diagram, the stacking diagram can be represented in different planes. One representation for the stacking diagram of a binary mixture is in the plane of average chemical potentials $\bar{\mu}_1$ and $\bar{\mu}_2$. We obtain it by indicating the midpoint $(\bar{\mu}_1, \bar{\mu}_2)$ of each of the special paths of type I and II, and terminal lines, as discussed above, in a diagram. The lines we obtain separate different stacking sequences in the plane of $\bar{\mu}_1$ and $\bar{\mu}_2$ for fixed buoyant masses $m_1$, $m_2$ and total system height $h$. By computing the average packing fractions $\bar{\eta}_1$ and $\bar{\eta}_2$ for each species along these special paths we can transform the stacking diagram into the plane of average packing fractions. The plane of $\bar{\eta}_1$ and $\bar{\eta}_2$ is more relevant for experimentalists, since they can directly prepare solutions with given particle concentrations [59].

### Mass-polydisperse systems

Besides binary mixtures, we also consider systems with a continuous distribution of buoyant masses as described by the parent distribution $f_\mathrm{P}(m)$. That is, the probability of finding a particle with a buoyant mass in the range $m$ to $m + \mathrm{d}m$ in the system is given by $f_\mathrm{P}(m)\,\mathrm{d}m$. Analogous to Eq. (1.2), the local chemical potential at elevation $z$ for particles with buoyant mass $m$ is then given by

$$\mu_m(z) = \mu_m^0 - mgz, \tag{1.4}$$

here $\mu_m^0$ is the chemical potential of the species with buoyant mass $m$ at elevation $z = 0$. The set of constant offsets $\mu_m^0$ in $\mu_m(z)$ is *a priori* unknown and must be determined via an iterative numerical procedure to match the prescribed parent distribution $f_\mathrm{P}(m)$ and average density across all species. The latter is given by

$$\bar{\rho} = \frac{1}{h}\int_0^h \mathrm{d}z \int \mathrm{d}m\, \rho_m(z). \tag{1.5}$$

Here $\rho_m(z)$ is the density profile of particles with buoyant mass $m$ along the vertical axis $z$.

Again, we treat the system using locally the equilibrium approximation, which assumes that each horizontal slice is a bulk equilibrium system. For a single horizontal slice, the ideal contribution to the Helmholtz free energy for a continuous distribution of different particles is exactly known

$$F^\mathrm{id}[\rho_m] = k_\mathrm{B}T \int \mathrm{d}m\, \rho_m \left(\ln\left(\rho_m\right) - 1\right). \tag{1.6}$$

More details on Density Functional Theory (DFT) are given in Section 1.3.2. The expression in Eq. (1.6) includes the entropy of mixing between the particles with different buoyant masses $m$. Furthermore, we exploit that the interparticle interaction is independent of the buoyant mass of the particles. Thus, the excess contribution to the free energy is only a functional of the density across all buoyant masses, $\rho$, and not a functional of the individual density for each buoyant

mass $\rho_m$. Hence, the excess free energy $F^{\text{exc}}$ satisfies the relation

$$F^{\text{exc}}[\{\rho_m\}] = F^{\text{exc}}[\rho], \tag{1.7}$$

where the right hand side is the free energy functional of a one-component system with density $\rho$. This insight enables us to derive, within the local equilibrium approximation, the exact expression of the effective chemical potential of mass-polydisperse suspension in sedimentation [3]

$$\mu_{\text{eff}}(z) = k_{\text{B}}T \ln\left(\int \mathrm{d}m\, e^{\beta(\mu_m^0 - mgz)}\right), \tag{1.8}$$

at elevation $z$ from the individual chemical potentials given according to Eq. (1.4). Here, $\beta = 1/(k_{\text{B}}T)$. The system at a given elevation $z$ behaves like a monodisperse bulk system with chemical potential equal to $\mu_{\text{eff}}(z)$. The density of the system at elevation $z$ across all buoyant masses,

$$\rho(z) = \rho_{\text{EOS}}(\mu_{\text{eff}}(z)), \tag{1.9}$$

is given by the bulk equation of state (EOS) $\rho_{\text{EOS}}(\mu)$ and the effective chemical potential in Eq. (1.8). The density of particles with buoyant mass $m$ at elevation $z$ follows as

$$\rho_m(z) = \rho(z) e^{\beta\left(\mu_m^0 - mgz - \mu_{\text{eff}}(z)\right)}. \tag{1.10}$$

For a detailed derivation see Section II of Ref. [3] as reproduced below in Section 4.3.

Using Eqs. (1.8) to (1.10), we are able to obtain the mass resolved vertical density profiles $\rho_m(z)$ under the influence of a gravitational field from a bulk equation of state $\rho_{\text{EOS}}(\mu)$ in the absence of gravity. The type of particle and their interaction only enters into our theory via the bulk equation of state. Our theory for mass-polydisperse systems can thus be applied to any type of colloidal particles and any method of obtaining an EOS.

To construct the stacking diagram for mass-polydisperse systems we follow a similar route as in the case of binary mixtures laid out above in Section 1.3.1. There are two modifications we need to consider. First, since the reference bulk system is monodisperse, two phases coexist at a single value of the chemical potential instead of along a binodal curve as it is the case in mixtures. Second, the sedimentation path is no longer a segment of a straight line, but in general a curve $\mu_{\text{eff}}(z)$, see Eq. (1.8). The other ideas regarding the construction of the stacking diagram still apply. To construct the stacking diagram in the plane of sample height $h$ and average packing fraction $\bar{\eta}$ for a given parent distribution $f_{\text{P}}(m)$, we fix $h$ and find the corresponding $\bar{\eta}$ such that the sedimentation path $\mu_{\text{eff}}(z)$ either starts ($z = 0$), ends ($z = h$), or is tangential to the bulk binodal (i.e. the chemical potential of coexistence), see Fig. 1.5(a). From that we obtain two or three points $(\bar{\eta}, h)$ in the stacking diagram. (If there is not tangent to $\mu_{\text{eff}}(z)$ within $0 \leq z \leq h$ there are only two distinct points.) We repeat this procedure for every sample height $h$ that we are interested in and every phase transitions that the system exhibits in bulk to fill-in the remaining stacking diagram. These sets of points form the sedimentation binodals, see Fig. 1.5(b). As in the case of binary mixtures, there are again three types of sedimentation binodals. The ones formed by paths that start, end or are tangential to the bulk binodal. Thus, for each phase transition there are up to three sedimentation binodals, which makes the stacking diagram particularly rich for

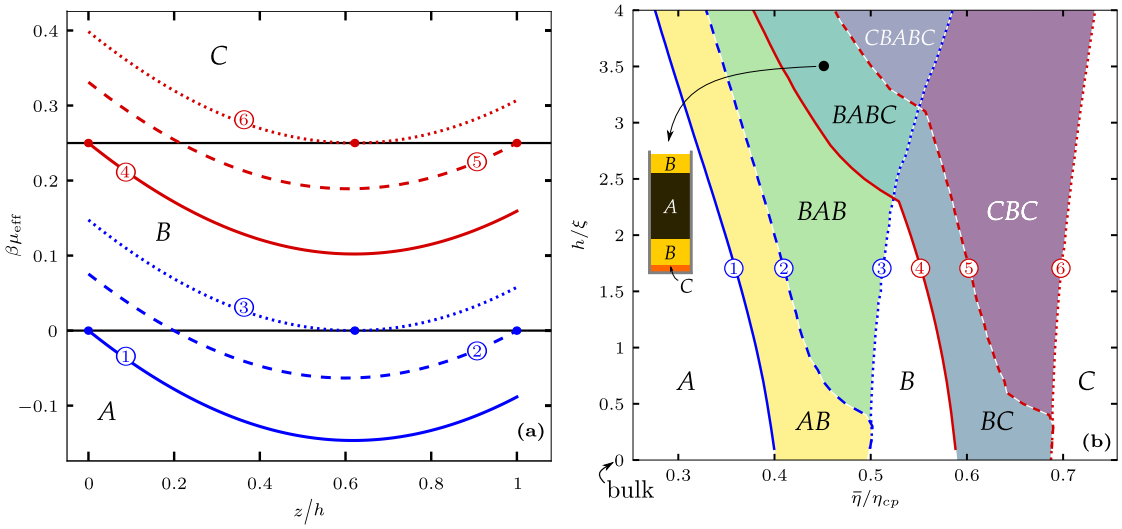


Figure 1.5: Construction of a stacking diagram for an illustrative mass-polydisperse colloidal systems. (a) Scaled sedimentation paths $\beta\mu_{\rm eff}(z)$ as a function of the elevation $z/h$. The coexistence chemical potentials between phases $A$ and $B$, and $B$ and $C$ are marked by solid horizontal lines. The sedimentation paths that end, start, and are tangent to the bulk binodals are indicated with solid-, dashed- and dotted-lines, respectively. (b) Corresponding stacking diagram in the plane of average packing fraction $\bar{\eta}/\eta_{\rm cp}$ and sample height $h/\xi$. The position of the six sedimentation paths in (a) is marked in (b) using the corresponding labels 1 to 6. The sedimentation binodals have the same line style as the sedimentation paths they represent. Adapted from Ref. [3].

systems with multiple phase transitions in bulk.

### 1.3.2 Theoretical description of bulk phenomena

In the previous sections, we showed how to incorporate gravity on top of an existing bulk theory to study sedimentation-diffusion-equilibrium in binary mixtures and mass-polydisperse colloidal systems. What remains to be dealt with is the theoretical description of bulk, i.e. a infinitely large system (in the thermodynamic limit) without any external fields, such as gravity. For many-body systems of interacting particles with a large number of particles this is a non-trivial task. The position and the momentum of each particle constitute to $2DN$ degrees of freedom for a $D$-dimensional system with $N$ isotropic particles. In practice, we are unable to solve the coupled equations of motion of $2DN$ variables. Fortunately, there exist several theoretical approaches to describe bulk systems.

#### Bulk equation of state

Using a known analytic equation of state (EOS) is the simplest approach. The equation of state can be obtained for example by liquid state integral equation theory [60–62], computer

simulations [63–65] and using empirical expressions [66–68].

We chose this route in Ref. [2] and use the Hall EOS [69] for hard spheres. It describes the liquid

$$z_{\text{liquid}} = \frac{1 + \eta + \eta^2 - 0.67825\eta^3 - \eta^4 - 0.5\eta^5 - 1.7\eta^6}{1 - 3\eta + 3\eta^2 - 1.04305\eta^3} \tag{1.11}$$

as well as the crystalline phases

$$z_{\text{crystal}} = \frac{1 + \eta + \eta^2 - 0.67825\eta^3 - \eta^4 - 0.5\eta^5 - 6.028e^{\zeta(7.9-3.9\zeta)}\eta^6}{1 - 3\eta + 3\eta^2 - 1.04305\eta^3} \tag{1.12}$$

of hard spheres. Here, $z = \beta P/\rho$ is the compressibility factor, where $P$ is the osmotic pressure, $\rho$ is the bulk density, $\eta$ is the packing fraction of spheres, and $\zeta = \eta_{\text{cp}} - \eta$ with $\eta_{\text{cp}} = \sqrt{2}\pi/6$ the close packing fraction of hard spheres. Hall's EOS [69] is an empirical EOS with coefficients chosen to fit data from computer simulations. Nevertheless, it is similar to other well known analytic EOS for hard sphere such as those by Carnahan and Starling [70], and by Thiele [71], which are not empirical.

Hall's EOS is formulated in terms of pressure as a function of packing fraction. To convert it to packing fraction as a function of chemical potential, as it is used in Eq. (1.9), see Ref. [72]. The resulting state function is shown in Fig. 1.6.

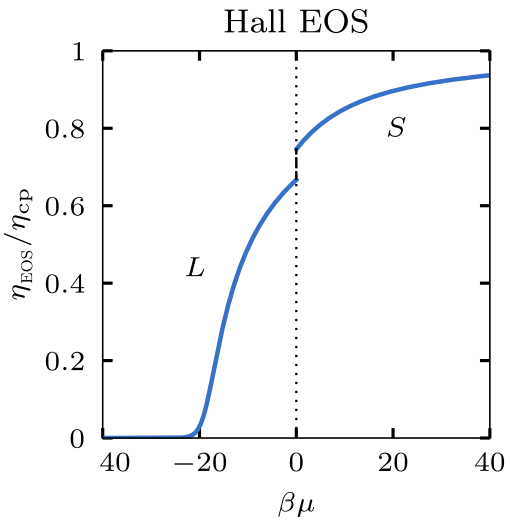


Figure 1.6: Packing fraction $\eta$ relative to close packing $\eta_{\text{cp}}$ as a function of scaled chemical potential $\beta\mu$ for hard spheres according to Hall's EOS [69]. The liquid (L) to crystal (S) phase transition is shifted to $\beta\mu = 0$ without loss of generality.

### Density Functional Theory

Another widely used approach to describe a bulk system is to obtain the bulk equation of state via Density Functional Theory (DFT). Since we are not interested on the detailed dynamics of every single particle in the system, but only the average behaviour of the inhomogeneous system, we resort to a description of the statistical system based on a one-body quantity, the density profile, which is a function of only a single positional coordinate in $D$ dimensions for isotropic particles. With anisotropic particles additional orientational variables characterizing the orientation of the

particle are required.

DFT was developed to find the equilibrium density profile of a many-body system by Kohn, Sham and Hohenberg [73, 74] in quantum systems for zero temperature in 1964 and 1965. The theory was extended to finite temperature by Mermin [75] in the same year. Evans introduced DFT for classical inhomogeneous many-body systems [76] in 1979. DFT is usually formulated in the grand canonical ensemble with its thermodynamic variables being temperature $T$, volume $V$ and chemical potential $\mu$. The central quantity of DFT is the one-body density profile, which for isotropic particles is

$$\rho(\boldsymbol{r}) = \left\langle \sum_i^N \delta(\boldsymbol{r} - \boldsymbol{r}_i) \right\rangle, \tag{1.13}$$

where $\boldsymbol{r}_i$ is the position of particle $i$ and $\langle . \rangle$ is the grand canonical average. The grand canonical potential $\Omega([\rho]; T, V, \mu)$ as a functional of the density profile is then given by

$$\Omega[\rho] = F[\rho] + \int \mathrm{d}\boldsymbol{r}\, \rho(\boldsymbol{r})(V_{\mathrm{ext}}(\boldsymbol{r}) - \mu). \tag{1.14}$$

Here $F[\rho]$ is the Helmholtz free energy functional and $V_{\mathrm{ext}}(\boldsymbol{r})$ is an external potential. DFT states that $\Omega[\rho]$ follows a variational principle and that it is minimal at the equilibrium density $\rho_0(\boldsymbol{r})$. This can be formally expressed by the Euler-Lagrange equation

$$\left.\frac{\delta\Omega[\rho]}{\delta\rho(\boldsymbol{r})}\right|_{\rho=\rho_0} = 0, \quad \text{(min)}, \tag{1.15}$$

associated to the functional. Furthermore, $\Omega[\rho_0]$ yields the value of the equilibrium grand canonical potential $\Omega_0$, i.e.,

$$\Omega[\rho_0] = \Omega_0. \tag{1.16}$$

Inserting Eq. (1.14) into the minimization principle, Eq. (1.15), yields the Euler-Lagrange equation for the free energy functional

$$\left.\frac{\delta F[\rho]}{\delta\rho(\boldsymbol{r})}\right|_{\rho=\rho_0} = \mu - V_{\mathrm{ext}}(\boldsymbol{r}). \tag{1.17}$$

The intrinsic Helmholtz free energy $F[\rho]$ can be split into an ideal contribution $F^{\mathrm{id}}[\rho]$ and an excess contribution $F^{\mathrm{exc}}[\rho]$. The ideal contribution is the free energy of an ideal gas with the same density $\rho(\boldsymbol{r})$ as the interacting system, given exactly by

$$F^{\mathrm{id}}[\rho] = k_{\mathrm{B}}T \int \mathrm{d}\boldsymbol{r}\, \rho(\boldsymbol{r}) \left(\ln\left(\Lambda^D \rho(\boldsymbol{r})\right) - 1\right), \tag{1.18}$$

with the thermal de Broglie wavelength $\Lambda = \sqrt{2\pi\hbar^2/(mk_{\mathrm{B}}T)}$, reduced Planck constant $\hbar$ and particle mass $m$. For an ideal system, inserting the ideal free energy in Eq. (1.18) into the Euler-Lagrange Eq. (1.17) for the free energy yields

$$\rho(\boldsymbol{r}) = \Lambda^{-D} \exp\left(\beta(V_{\mathrm{ext}}(\boldsymbol{r}) - \mu)\right). \tag{1.19}$$

That is, the density of an inhomogeneous ideal gas in presence of an external field and in the grand canonical ensemble.

For some systems with non-vanishing interparticle interaction , there exist exact expressions for the excess free energy $F^{\text{exc}}[\rho]$, but generally $F^{\text{exc}}[\rho]$ is unknown and approximations are used. An example for an exact expression is the one-dimensional system of hard rods of length $\sigma$ where $F^{\text{exc}}[\rho]$ is exactly given by

$$F^{\text{exc}}[\rho] = -k_{\text{B}}T \int \mathrm{d}x\, \rho(x) \ln\left(1 - \int_{x}^{x+\sigma} \mathrm{d}x'\, \rho(x')\right), \tag{1.20}$$

as shown by Percus [77]. We note that in Eq. (1.20) a weighted density in the form of

$$n(x) = \int \mathrm{d}x'\, w(x, x')\rho(x'), \tag{1.21}$$

where $w(x, x')$ is the weight function, appears. The concept of weighted densities was generalized by Nordholm, Johnson, and Freasier for inhomogeneous hard sphere fluids in three dimensions in the Weighted Density Approximation (WDA) [78]. In 1989 Rosenfeld proposed the Fundamental Measure Theory (FMT) [79] for hard sphere fluids which uses as weight functions fundamental geometrical measures of the spheres such as the volume, the surface area, and the radius. Although FMT does not give the exact excess free energy for dimensions larger than one, it is the still the state of the art approximation to $F^{\text{exc}}[\rho]$. Nevertheless, for homogeneous phases the use of simpler functionals, one of which we explore in the next section, can also give accurate results [80] and correctly describe the topology of the bulk phase diagram [81].

### Onsager Theory

To describe mixtures of anisotropic particles we need to generalize the one-body density to

$$\rho(\boldsymbol{r}) \to \rho_i(\boldsymbol{r}, \boldsymbol{\omega}) \tag{1.22}$$

by introducing a dependence on the orientation of the particle, as given by the direction of the unit vector $\boldsymbol{\omega}$, and also on the species of the particle, labeled by the index $i$. Thus $\rho_i(\boldsymbol{r}, \boldsymbol{\omega})$ gives the number of particles of species $i$ per infinitesimal volume and solid angle element at position $\boldsymbol{r}$ and with orientation $\boldsymbol{\omega}$, and it is normalized to the total number of particles of species $i$. That is

$$\int \mathrm{d}\boldsymbol{r} \int \mathrm{d}\boldsymbol{\omega}\, \rho_i(\boldsymbol{r}, \boldsymbol{\omega}) = N_i. \tag{1.23}$$

For a multicomponent mixture of anisotropic particles, the ideal free energy is given exactly by

$$\beta F^{\text{id}}[\{\rho_i\}] = \sum_i \int \mathrm{d}\boldsymbol{r} \int \mathrm{d}\boldsymbol{\omega}\, \rho_i(\boldsymbol{r}, \boldsymbol{\omega}) \left[\ln\left(\rho_i(\boldsymbol{r}, \boldsymbol{\omega})\Lambda_i^3\right) - 1\right], \tag{1.24}$$

where the sum runs over all species and $\Lambda_i$ is the thermal wavelength of species $i$. Since we consider here only phases without positional order, we integrate over all positions $\boldsymbol{r}$ and introduce

the orientational distribution function $\psi_i$ of species $i$ via $\rho_i(\boldsymbol{r}, \boldsymbol{\omega}) = \rho_i \psi_i(\boldsymbol{\omega})$ and normalization $\int \mathrm{d}\boldsymbol{\omega}\, \psi_i(\boldsymbol{\omega}) = 1$. Hence, $\rho_i$ is the bulk number density of species $i$. We obtain

$$\frac{\beta F^{\mathrm{id}}[\{\rho_i\}]}{N} = \sum_i x_i \int \mathrm{d}\boldsymbol{\omega}\, \psi_i(\boldsymbol{\omega}) \left[\ln\left(\psi_i(\boldsymbol{\omega})\rho_i \Lambda_i^3\right) - 1\right], \tag{1.25}$$

where $N$ is the total number of particles in the system and $x_i$ is the composition of species $i$.

Onsager showed that for hard particles the excess free energy functional $F^{\mathrm{exc}}[\{\rho_i\}]$ can be approximated via the excluded volume between two particles as [82]

$$\frac{\beta F^{\mathrm{exc}}[\{\rho_i\}]}{N} = \frac{1}{2}\rho \sum_{i,j} x_i x_j \int \mathrm{d}\boldsymbol{\omega} \int \mathrm{d}\boldsymbol{\omega'}\, \psi_i(\boldsymbol{\omega})\psi_j(\boldsymbol{\omega'}) V_{i,j}^{\mathrm{ex}}(\boldsymbol{\omega}, \boldsymbol{\omega'}), \tag{1.26}$$

with total density $\rho = \sum_i \rho_i$ and $V_{i,j}^{\mathrm{ex}}(\boldsymbol{\omega}, \boldsymbol{\omega'})$ being the excluded volume between particles of species $i$ and $j$ with orientations $\boldsymbol{\omega}$ and $\boldsymbol{\omega'}$, respectively. The excluded volume between two particles is the volume that is inaccessible to one particle due to the presence of the other particle, see Fig. 1.7. For some particles shapes analytic expressions for the excluded volume can be obtained by geometrical considerations [83]. Monte Carlo simulations can also be used to obtain accurate numerical estimates [84, 85].

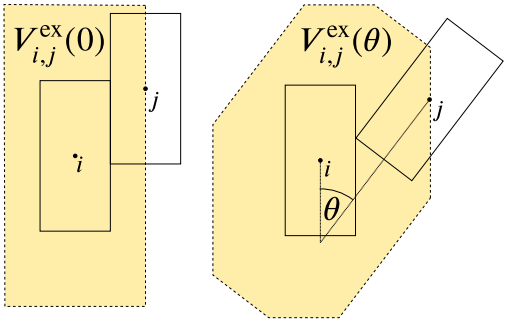


Figure 1.7: Schematic of the excluded area for two identical rectangles, labeled $i$ and $j$, with relative orientations $\theta = 0$ and $\theta > 0$. This is the two-dimensional analog to the excluded volume between two cylinders or two rectangular cuboids. The excluded area depends on the particle dimensions and the relative orientation of the two particles.

In Refs. [1, 2], we model mixtures of rods and plates using hard cylinders for both species to compare with the experiments by van der Kooij and Lekkerkerker [34, 50] on mixtures of boehmite rods and gibbsite plates. The analytical expression for the excluded volume between two cylinders $i$ and $j$ with diameters $d_i$, $d_j$ and lengths $l_i$, $l_j$, respectively, reads [82, 83]

$$\begin{aligned} V_{i,j}^{\mathrm{ex}}(\theta) =& \frac{\pi}{4}(l_i d_i^2 + l_j d_j^2) + \left(\frac{\pi}{4} d_i d_j + l_i l_j\right)(d_i + d_j)\sin\theta + \\ & \frac{\pi}{4}(l_i d_j^2 + l_j d_i^2)|\cos\theta| + (l_i + l_j) d_i d_j E(\sin\theta). \end{aligned} \tag{1.27}$$

Here $\theta$ is the polar angle between the main axes of particles $i$ and $j$, $E(\sin\theta)$ is the elliptic integral of the second kind

$$E(\sin\theta) = \int_0^{\pi/2} \mathrm{d}\varphi \sqrt{1 - \sin^2\theta \sin^2\varphi}, \tag{1.28}$$

and $\varphi$ is the relative azimuthal angle between particles $i$ and $j$. We use prolate cylinder to model hard rods and oblate cylinders for hard disks in the following.

As shown by Parsons [86] and Lee [87], the original excess free energy expression in by Onsager [82] can be improved upon replacing the prefactor $1/2$ in front of the second virial coefficient in Eq. (1.26) by $\Psi(\eta)$, the excess free energy per particle of a reference system. Using a system of hard spheres as a reference system and the corresponding equation of state by Carnahan and Starling [70] yields

$$\Psi(\eta) = \frac{4 - 3\eta}{8(1-\eta)^2}. \tag{1.29}$$

Here $\eta = \rho \sum_i x_i v_i = \sum_i \eta_i$ is the total packing fraction across all species and $v_i$ is the particle volume of species $i$. The rescaled $F^{\text{exc}}[\rho]$ improve substantially the agreement of the transition densities compared to computer simulations [88]. In the low density limit ($\eta \to 0$) the original Onsager expression, based on the second virial coefficient, is recovered since $\Psi(\eta \to 0) = 1/2$. The Parsons-Lee rescaling [86, 87] effectively replaces the virial coefficients higher than the second coefficient by those of the reference system [11, 89, 90].

### 1.3.3 Phase coexistence and bulk phase diagrams

We are interested in the stacking behavior of mixtures under gravity. To use sedimentation path theory to describe the sedimentation-diffusion-equilibrium of mixtures, we first need the bulk phase diagram, as we discussed in Section 1.3.1. To construct the bulk phase diagram, we need to find the points where two or more phases coexist in bulk. At phase coexistence, thermal, mechanical, and chemical equilibrium must be satisfied. That is, the temperature, the (osmotic) pressure and the chemical potential must be the same in all coexisting phases [91]. It is practical to work in a statistical ensemble which already has two of the three conditions satisfied by construction. We choose the isothermal–isobaric (or Gibbs) ensemble and work at fixed temperature and pressure in order to have thermal and mechanical equilibrium satisfied by construction. From the Helmholtz free energy functional $F[\rho]$ we then obtain the Gibbs free energy $G$ per particle by

$$\frac{G[\rho]}{N} = \frac{F[\rho]}{N} + \frac{P}{\rho}. \tag{1.30}$$

In a binary mixture with $N_i$ particles of species $i \in \{1, 2\}$ and total number of particles $N = N_1 + N_2$, the chemical equilibrium can be expressed as a common tangent condition in the plane of composition of the mixture $x = N_1/N$ and Gibbs free energy per particle $g_{\text{b}} = G/N$. Thus two compositions $x_1$ and $x_2$ coexist if there is a common tangent to the function $g_{\text{b}}(x)$ through the points $(x_1, g_{\text{b}}(x_1))$ and $(x_2, g_{\text{b}}(x_2))$.

Repeating the common tangent construction for every pressure $P$ in a given range yields the phase diagram in the plane of composition and pressure. From evaluating the common tangent at $x = 1$ and $x = 0$, we obtain the coexisting chemical potentials $\mu_1$ and $\mu_2$, respectively. For each value of the pressure we obtain a point in the plane of $\mu_1$ and $\mu_2$, and thus the full phase diagram in the plane of chemical potentials can be constructed.

We have summarized the main methods used in this Thesis from the theoretical treatment of bulk binary mixtures, the incorporation of gravity using sedimentation path theory, and extensions

to mass-polydisperse colloidal systems. Next, we give a summary of the publications that form the core of this Thesis highlighting the phenomenology as well as the use of the theories and methods described in this section.

# 2 Overview of the publications

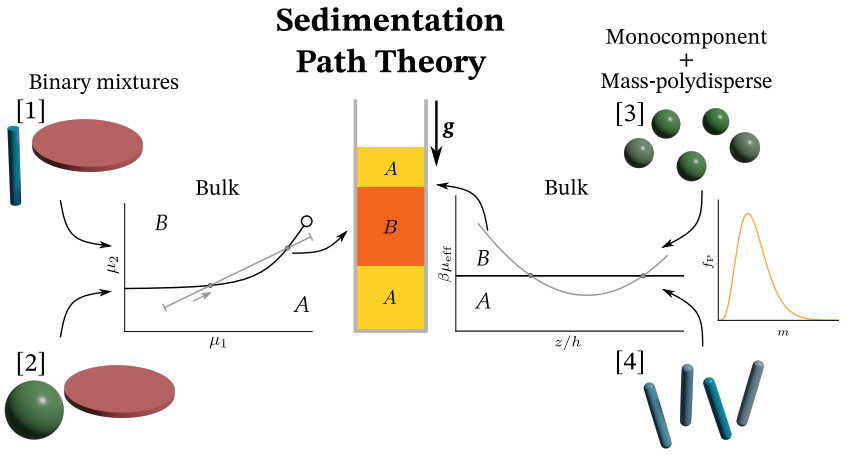


Figure 2.1: Relations between the four publications of this cumulative Thesis. In Refs. [1] and [2], we use DFT to obtain the phase diagram for colloidal mixtures of plates and rods, and plates and spheres, respectively, and sedimentation path theory to compute the stacking sequences and the stacking diagram. In Refs. [3] and [4], we use mass-polydisperse sedimentation path theory to treat a mass-polydisperse suspension of hard spheres and spherocylinders, respectively, using preexisting analytic equations of state.

This chapter gives an overview of the four publications contributing to this cumulative Thesis. Our work is dedicated to the study of sedimentation-diffusion-equilibrium in suspensions of colloidal particles under a gravitational field.

First, we start motivated by the iconic experiments on colloidal plate-rod mixtures by van der Kooij and Lekkerkerker [34, 50] and reinterpret their findings in the light of sedimentation path theory. We reproduce theoretically their results, but also compute the stacking diagram for the experimental plate-rod mixture in the entire plane of particle concentrations, complementing therefore their experimental study. Furthermore, we infer the topology of the bulk phase diagram from four experimental samples reported by van der Kooij and Lekkerkerker [34]. That is, we estimate the positions of the bulk binodals for the transition into columnar and smectic phases from the experimental samples using the corresponding sedimentation paths in the plane of chemical potential. We investigate the evolution of the stable layers in the samples with increasing height for a given partial concentration, and find the introduction and subsequent disappearance of a floating plate-rich nematic.

Next, we solve the inverse problem, i.e. extracting microscopic properties of the colloids from macroscopic images of sedimentation-diffusion-equilibrium experiments. Using sedimentation path theory, we estimate the buoyant mass and concentration of the colloids in experiments of a colloidal mixture of spheres and plates [52]. Solving the inverse problem helps in selecting experimental interesting ranges of particle buoyant masses and colloidal concentration for future sedimentation experiments. We study the effect of an inflection point in the bulk binodal on the stacking diagram and find an $ININ$ stacking sequence with two floating layers.

Motivated by our study of the range of buoyant masses that can correspond to a single stacking sequence in Ref. [2], we extend sedimentation path theory from binary mixtures to mass-polydisperse colloidal systems with an arbitrary distribution of buoyant masses of the colloids. Using statistical mechanics, we are able to map the mass-polydisperse system to an effective monodisperse system with a non-linear local chemical potential in the vertical coordinate. From theoretical considerations we are able to formulate constraints on the possible set of stacking sequences. We find that the topology of the stacking diagram for systems close to density matching is sensitive to mass-polydispersity. However systems far from density matching are insensitive to mass-polydispersity. Although several effects in colloidal systems are due to polydispersity [35–39], we conclude that for systems far from density matching the sedimentation behavior is nearly unaffected by polydispersity in the buoyant mass. This helps to clarify the different roles that polydispersity has in bulk and in sedimentation.

Last, we apply the extended sedimentation path theory to colloidal hard spherocylinders. To study the effect of particle elongation on the sedimentation behavior, we compute the stacking diagram for monodisperse and mass-polydisperse spherocylinders for different aspect ratios. We find complex stacking sequences with up to seven layers and reentrant stacking sequences.

## 2.1 Gravity-induced phase phenomena in plate-rod colloidal mixtures

In this publication [1], we revisit from the perspective of sedimentation path theory the iconic sedimentation-diffusion-equilibrium experiments on colloidal plate-rod mixtures by van der Kooij and Lekkerkerker [34, 50]. They found several complex stacking sequences, including one with five layers of different bulk phases. Sedimentation path theory was introduced by de las Heras and Schmidt [58] for binary mixtures and the underlying ideas are outlined in Section 1.3.1. It is based on the concept of sedimentation paths, which are segments of a straight line in the plane of chemical potentials. The bulk behavior of the binary mixture is treated by DFT and Onsager theory with Parsons-Lee rescaling, as discussed in Section 1.3.2.

Through this approach we reinterpret the findings by van der Kooij and Lekkerkerker in mixtures of plates and rods, arguably one of the best known experiments in this field. We are able to quantitatively reproduce the stacking sequences that they observe in their cuvettes of isotropic, nematic plate-rich and nematic rod-rich phases. We compute the stacking diagram in the plane of chemical potential and also in the, experimentally relevant, plane of average colloidal packing fractions for several sample heights. The stacking diagram predicts the stacking sequence for any packing fraction of plates and rods, and helps to purposely design experiments with the goal of investigation multi-layer stacking phenomena.

Furthermore, we also address the inverse problem of inferring the bulk phase diagram using the experimentally observed stacking sequences. As discussed in Section 1.2, in mono-component systems, the bulk equation of state can be read off a single sedimentation-diffusion-equilibrium experiments. For multi-component mixtures this is no longer possible and a single experiment does not suffice. Nevertheless, we demonstrate how to extract the complete topology of the bulk phase diagram using the macroscopic thicknesses of each layer in only four experimental samples.

We compute the stacking diagrams for two different buoyant mass ratios, which give rise to topologically different stacking diagram. We study how a family of samples with fixed concentration of plates and rods evolves as we vary the sample height. We find different stacking sequences by varying the height, such as e.g. a floating nematic plate-rich layer sandwiched between isotropic layers that vanish with increasing the sample height. Our predictions regarding the effect of the sample height can be tested experimentally since controlling the height is in principle doable experimentally.

The richness in the sedimentation behaviour observed in the experiments by van der Kooij and Lekkerkerker [34] with up to five layers of different bulk phases was initially attributed to polydispersity of the colloidal particles [34, 50]. However, we have demonstrated with sedimentation path theory that the observed stacking behaviour is a gravity induced effect and could also be observed in a purely monodisperse mixture of plates and rods.

## 2.2 Sedimentation of colloidal plate-sphere mixtures and inference of particle characteristics from stacking sequences

In this manuscript [2], we investigate the effect of gravity on a plate-sphere colloidal mixture. We use a Onsager-like density functional with Parsons-Lee rescaling to describe the bulk and sedimentation path theory to incorporate gravity, see Section 1.3.2, respectively. We compare with corresponding sedimentation-diffusion-equilibrium experiments [52] and are able to reproduce theoretically a sequence with a floating nematic layer between two isotropic layers as in the experiments. The authors of Ref. [52] find an inflection point in the bulk binodal, but they model the binary mixture with infinitely thin plates, which could be the reason for such an inflection point. However, we confirm in Ref. [2] the existence of an inflection point in our approach with plates of finite thickness. The presence of an inflection point in bulk enriches the stacking diagram by introducing additional stacking sequences with reentrant and alternating layers of bulk phases.

We present the stacking diagram for several sample heights and both the buoyant mass ratio in the experiment [52] as well as a buoyant mass ratio close to the slope at the inflection point of the bulk binodal. Close to the inflection point we find a four layer stacking sequence ($ININ$) with floating nematic and isotropic layers.

Furthermore, we use the macroscopic layer thicknesses of an experimental sample in Ref. [52] showing a floating nematic layer to obtain microscopic information about the particles. We are able to infer the buoyant mass of the plates and that of the spheres for a given concentration of colloids and vice versa. The thickness of the layers and the shape of the colloidal particles is the only information that we use from the experiments. We identify regions in the plane of

buoyant mass and average packing fraction of both species where no floating nematic layer ($INI$) can occur, and regions where no $INI$ sequence with the experimental layer thicknesses can be observed. For all the samples which show the experimental $INI$ stacking sequence, the average packing fraction of plates falls into a narrow interval of less than $\pm 9\%$. Our findings aid in designing new experiments and determine theoretical bounds for the buoyant mass and concentration of particles for a given stacking sequence. The methodology we have developed can be applied to other colloidal mixtures to extract microscopic particle properties from macroscopic observations in sedimentation experiments.

Moreover, we also study the evolution of the stacking sequence with increasing sample height and find non-trivial behavior where new layers are introduced at the top as well as the bottom of the sample. Our theoretical predictions can be experimentally realized by using a stock solution of colloids and filling multiple samples to different heights, granting deep insights into the sedimentation behavior.

## 2.3 Sedimentation path theory for mass-polydisperse colloidal systems

Natural as well as synthesized colloidal particles always have some degree of polydispersity. Thus, polydispersity is inherent to essentially all colloidal experiments. Several works [35, 37, 38, 92–96] have considered the effects of polydispersity on bulk behavior. However the effects of polydispersity on sedimentation are not well known. Sedimentation path theory, a vehicle to implement gravity on top of bulk behavior, has so far only been used to study sedimentation in colloidal binary mixtures [1, 2, 52–58, 97].

In this publication [3], we extend sedimentation path theory to mass-polydisperse colloidal systems. That is, the colloids have different buoyant masses, but are indistinguishable in their interparticle interactions. This model helps to isolate the interplay between polydispersity and gravity from that of the effects of polydispersity in bulk. Furthermore, our model can represent real experimental systems, e.g. core-shell colloids with different shell thickness, but the same overall size.

Using statistical mechanics, we reduce the mass-polydisperse system to an effective monodisperse system with a local chemical potential which is non-linear in the vertical coordinate along the sample. Thus, in mass-polydisperse systems the sedimentation paths are no longer straight lines but curves, although the curve must be a convex function of the vertical coordinate. The curvature in the sedimentation path enriches the stacking behavior with an increased maximum number of layers in the stacking sequences and the occurrence of reentrant and floating layers of bulk phases. Within the local equilibrium approximation, our expression for the local chemical potential is an exact result and no further approximation need to be made to describe mass-polydisperse. The effective monodisperse system can be treated by standard bulk theories. In our study, we use existing analytic bulk equations of state for simplicity. However any bulk theory or equation of state can be used. Thus our theory for mass-polydisperse systems is general and can be used in the study of any colloidal system.

In Ref. [4], we illustrate the construction of the effective sedimentation path and the stacking diagram for mass-polydisperse systems using a model equation of state. Furthermore, we study

the sedimentation of mass-polydisperse colloidal hard-spheres for various parent distributions of the buoyant mass. In systems near density matching, i.e. with a parent distribution centered around natural buoyancy and thus particles with positive and negative buoyant mass, mass-polydispersity has a major impact on the system. Near density matching the topology of the stacking diagram can change with small modifications in the parent distribution. On the other hand, we identify a host of parent distributions for which the degree of mass-polydispersity has negligible effect on the stacking diagram. For these parent distributions the dominant characteristic is the average buoyant mass, and the system behave like an effective monodisperse system with the corresponding average buoyant mass.

## 2.4 Effect of sample height and particle elongation in the sedimentation of colloidal rods

Hard spherocylinders are arguably one of the most important models for anisotropic colloidal particles. Whereas several works investigated the bulk phase behavior of hard spherocylinders [98–105], not many studies have considered the effects of gravity on colloidal spherocylinders [48].

In this manuscript [4], we apply the extension of sedimentation path theory to mass-polydisperse systems to a colloidal system of monodisperse as well as mass-polydisperse hard spherocylinders. We use an algebraic equation of state for hard spherocylinders proposed by Peters et al. [23] to treat the bulk. To investigate the effects of particle elongation, we compute the stacking diagram of monodisperse systems of hard spherocylinders for four different characteristic aspect ratios. We compare with a theoretical stacking diagram for the aspect ratio $L/D = 5.0$ by Savenko and Dijkstra [48] and find semiquantitative agreement. The small difference can be attributed to differences in the underlying bulk equation of state.

Furthermore, we study the evolution of stable layers with increasing sample height and find simultaneous growth of a top and a bottom layer. To highlight the increased complexity of the stacking diagram for mass-polydisperse system as compared to a monodisperse system, we compute the stacking diagram for a mass-polydisperse system close to density matching. Due to the mass-polydispersity, colloidal particles with positive as well as negative buoyant masses are present in the system. The two competing effects of settling and creaming up dominate the stacking behavior of the system. We find stacking sequences with up to seven layers, where parts of the sequence occur twice, but inverted. Additionally, we observe reentrant stacking sequences, due to the curvature of the sedimentation binodals.

Colloidal suspensions near density matching are experimentally relevant to try to minimize the effects of gravity on the colloidal particles [106, 107]. On the other hand, a controlled density mismatch can be desirable, e.g. in microgravity experiments [108–110]. Close to density matching, mass-polydispersity, which is to some degree unavoidable in experiments, plays an especially important rule and needs to be considered in the interpretation of experiments, as we have demonstrated in Refs. [3, 4].

## 2.5 Author contributions

I helped to design the research concepts, created a complete first version (including both figures and text) and contributed to the final version and the revision of all the publications that form this cumulative Thesis [1–4].

In Ref. [1] I implemented DFT for a colloidal mixture of rods and plates using an Onsager-like free energy functional and constructed the bulk phase diagram of the mixture. Furthermore, I used sedimentation path theory to obtain the density profiles, the stacking sequences, and the stacking diagrams for the experimental samples reported by van der Kooij and Lekkerkerker [50].

In Ref. [2] I performed DFT minimizations for a colloidal mixture of plates and spheres in order to obtain the bulk phase diagram. Using sedimentation path theory I computed the stacking diagram for the mixture. I developed a method to solve the inverse problem of extracting microscopic information from macroscopic pictures of colloidal stacking sequences.

In Ref. [3] I extended sedimentation path theory from binary colloidal mixtures to mass-polydisperse colloidal systems. I applied our novel theory to a model system and to colloidal hard spheres. I designed an algorithm to obtain the stacking diagram for mass-polydisperse colloidal suspensions.

In Ref. [4] I applied sedimentation path theory for monodisperse and mass-polydisperse colloidal systems to hard spherocylinders. I implemented the bulk equation of state for hard spherocylinders proposed by Peters et al. [23] and obtained the stacking diagram for monodisperse and mass-polydisperse systems of spherocylinders with different aspect ratios and sample heights.

# 3 Conclusion and outlook

In this Thesis we have investigated the description of colloidal sedimentation-diffusion-equilibrium experiments via sedimentation path theory. We have applied the theory in conjunction with DFT to binary colloidal mixtures of plates and rods, as well as mixtures of plates and spheres. Without incorporating polydispersity into our theory, we were able to reproduce the experimentally observed stacking behaviour which, so far, was attributed to polydispersity. Furthermore, we identify the sample height as a key variable alongside the average colloidal concentration in both binary mixtures. Sedimentation path theory is equivalent to the approach taken by, e.g. Savenko and Dijkstra [48], and Piazza [111], of using a local equilibrium approximation together with the equilibrium condition

$$\frac{\mathrm{d}P(z)}{\mathrm{d}z} = -mg\rho(z). \tag{3.1}$$

However, working with the local chemical potential, as in sedimentation path theory, can be more convenient, since the chemical potential varies linearly with the vertical coordinate $z$. In addition, the stacking diagram can be easily constructed from the bulk phase diagram in the plane of chemical potentials using the crossings of segments of straight lines with the bulk binodals.

Sedimentation path theory assumes local equilibrium of each horizontal layer of the system. This is a an accurate approximation if the gravitational length of the system is large compared to the characteristic correlation length scale. However, for large colloidal particles or systems with longer correlation lengths, such as gels or aggregates [112], the local equilibrium approximation breaks down and a microscopic theory for the whole system is needed.

Furthermore, we have neglected surface effects in our approach. This includes the sample-air interface on top of the sample as well as the interaction of the sample with the wall of the cuvette. For instance, in experiments a clear formation of a meniscus at the top of the sample due to surface tension can be observed [34, 50]. A theory which encapsulates the sample as a whole including all interfaces would be needed to describe such phenomena. For macroscopic samples this is challenging due to the large number of colloidal layers and thus computer simulations of realistic macroscopic colloidal systems under gravity are demanding due to the large number of particles. Other phenomena such as wetting [113–116] and the effect of surface tension [117–120] are also neglected in sedimentation path theory. Incorporating these surface effects into sedimentation path theory would allow us to capture experiments on sedimentation-diffusion-equilibrium more accurately.

Active colloids [121] are currently receiving much research interest, including among other topics the formation of active nematics [122], active turbulence [123], and sedimentation of active particles [124, 125]. Expanding our investigation of sedimentation in colloidal suspensions to non-equilibrium systems, and in particular to active particles, could give rise to interesting phenomena.

With the extension of sedimentation path theory to mass-polydisperse colloidal systems, we

have predicted interesting stacking behaviour due to mass-polydispersity, such as reentrant layers in the stacking sequences [3] cand reentrant stacking sequences in the stacking diagram [4]. With our model for mass-polydispersity, we have been able to disentangle the effects of polydispersity due to a polydisperse buoyant mass of the particles from the effects of polydispersity on the bulk behaviour. We are currently working on two closely related projects that we describe briefly in the following.

## 3.1 Stacking diagram of hard spheres: a comparison with experiments

On an ongoing collaboration with Matthias Schmidt[1], Danial de las Heras[1], and Stefan U. Egelhaaf[2], we compute the stacking diagram for a mass-polydisperse system of hard spheres in the plane of sample height $h$ and average packing fraction $\bar{\eta}$, see Fig. 3.1. We compare the mass-polydisperse system with a monodisperse system with the same buoyant mass as the mean buoyant mass of the mass-monodisperse system.

Since the system consists purely of particles with positive buoyant mass, we only observe the stacking sequence top liquid and bottom crystal $LS$, besides the pure liquid $L$ and crystal $S$ stacks. The stacking diagram contains two sedimentation binodals corresponding to the sedimentation paths that either end or start at the liquid-crystal bulk binodal. By increasing the sample height, the sedimentation binodals open, moving away from each other. Hence, the stacking sequence $LS$ grows at the expenses of the pure stacks $L$ and $S$, whose occurrence is restricted to either very dilute or very dense samples, respectively (in the limit of high values of the samples height).

We compare our predictions with available experimental data on sedimentation of (quasi) hard sphere suspensions by Paulin and Ackerson [126], Pusey and van Megen [127], and Ackerson et al. [128]. The height and the packing fraction of the experimental samples, together with sketches showing the vertical position of the liquid-crystal interface are shown in Fig. 3.1. We also show sketches of our theoretical predictions including the position of the interfaces. In all cases, we estimate the experimental gravitational lengths by calculating an approximate value of the buoyant masses using the particle size and the mass densities of the solvent and of the colloids, which results in $\xi = 3.1\,\mu\text{m}$ for the sample by Paulin and Ackerson [126], $\xi = 16\,\mu\text{m}$ for the samples by Pusey and van Megen [127], and $\xi = 47\,\mu\text{m}$ for the samples by Ackerson et al. [128]

For the samples reported by Paulin and Ackerson [126] and Ackerson et al. [128] there is an excellent qualitative agreement between the experiments and our theoretical predictions regarding both the stacking sequence and the position of the interface. Experiments and theory agree over a significant range of packing fractions from $\eta/\eta_{\text{cp}} \approx 0.06$ to 0.66 and different values of the sample height (scaled with the gravitational length) ranging from $h/\xi \approx 380$ to $h/\xi \approx 7400$.

We find significant quantitative but also qualitative deviations between the theory and the iconic experiments by Pusey and van Megen [127]. For a packing fraction of $\bar{\eta}/\eta_{\text{cp}} = 0.53$ the reported experimental stacking sequence is a pure liquid stack (sample 2 in Fig. 3.1), whereas the theory predicts a top liquid bottom crystal stacking sequence $LS$. Given that the sample height is three

[1]University of Bayreuth
[2]Heinrich Heine University Düsseldorf

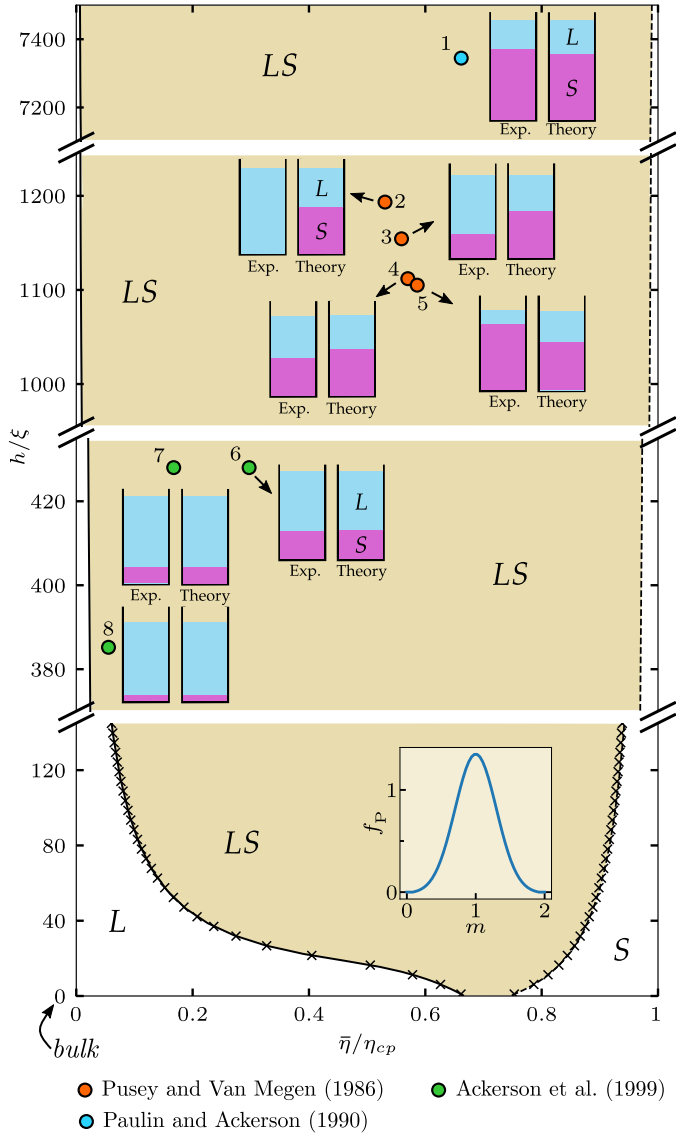


Figure 3.1: Stacking diagram of a mass-monodisperse system of hard spheres using the Hall EOS in the plane of sample height $h$ relative to the gravitational length $\xi$ and packing fraction $\eta$ relative to close packing $\eta_{\mathrm{cp}}$. Note the gaps in the vertical axis. The solid (dashed) line is the sedimentation binodal of the sedimentation paths that end (start) at the bulk liquid-crystal transition. The crosses represent the stacking diagram for a mass-polydisperse system with a Gaussian parent distribution $f_{\mathrm{P}}$ of mean $m = 1$ and cut at $m = 0.1$ and $m = 1.9$ (see inset). The results for eight experimental samples are indicated by closed circles, together with sketches of the experimental and the theoretical stacking sequences: sample 1 by Paulin and Ackerson [126] (spheres of diameter 1.0 µm in a mixture of decaline and tetralin), samples 2 to 5 by Pusey and van Megen [127] (spheres of diameter 0.64 µm in a mixture of decalin and carbon disulphide in volume ratio 2.66:1), and samples 6 to 8 by Ackerson et al. [128] (spheres of diameter 0.39 µm in cis-decalin).

orders of magnitude larger than the gravitational length of the particles, we expect that almost all the colloidal particles sediment to the bottom of the sample, leaving around 53% of the sample as a dense crystal and the rest as a very dilute liquid. This is also predicted by our theory, see sketch of sample 2 in Fig. 3.1. Within their experiment range from $\bar{\eta}/\eta_{\text{cp}} = 0.53$ to 0.64 our theoretical prediction for the percentage of crystalline sample vary only marginally from 54% to 66%. For other samples reported in Ref. [127], theory and experiment agree on the $LS$ stacking sequence (samples 3 to 5 in Fig. 3.1) but there is still a quantitative disagreement on the position of the liquid-crystal interface. For example, for sample 3 the theoretical interface is above the experimental one, and the opposite is true in sample 5. We cannot compare with the rest of the samples in Ref. [127] since they develop an amorphous glassy phase which is not described by the Hall bulk equation of state.

The short waiting times used by Pusey and van Megen (four days in comparison to waiting times between thirty five and fifty days in Refs. [126, 128]) are most likely the reason behind the differences between the theory (which assumes sedimentation-diffusion-equilibrium) and the experiment (which focus on bulk behaviour). Samples 2 to 5 in Fig. 3.1 have not reached sedimentation-diffusion-equilibrium. Note e.g. that sample 8 in Fig. 3.1 corresponds to a $LS$ stacking sequence in a sample with height $h/\xi \approx 380$ and packing fraction $\bar{\eta}/\eta_{\text{cp}} \approx 0.08$. It is therefore not possible that sample 2 with packing fraction $\bar{\eta}/\eta_{\text{cp}} \approx 0.53$ and a much higher sample height in terms of the gravitational length ($h/\xi \approx 1200$) remains in a pure liquid state in sedimentation-diffusion-equilibrium. We conclude that the experimental samples reported by Pusey and van Megen [127] are not in sedimentation-diffusion-equilibrium, but they provide a good representation of bulk phenomena since the internal relaxation times are much faster than the sedimentation relaxation times. After four days, it seems that bulk phase phenomena have already occurred and that sedimentation has only slightly perturbed the samples. This is in line with the observation that "some overall gravitational settling of the particles has occurred, leading to a small layer of crystals at the bottom of sample 2" by Pusey and van Megen [127]. To eliminate the arbitrariness on selecting the waiting time required to observe bulk but not sedimentation phenomena, it is possible to monitor the position of the liquid-crystal interface over time and then extrapolate to time zero [126, 128, 129].

Since all of the previous experiments that we are aware of [126, 128, 129] are in the limit of large sample height compared to the gravitational length, $h/\xi$, new experiments are necessary to make conclusions on the stacking behavior of colloidal hard spheres. Ideally these experiments would cover the region of $h/\xi < 120$ (see lower part of Fig. 3.1), where we could accurately test our theoretical predictions.

## 3.2 Shape polydisperse colloidal systems

After the extension of sedimentation path theory to mass-polydisperse colloidal systems, the natural next step is to extend the theory to fully polydisperse systems. The generalization of sedimentation path theory to polydisperse colloidal system is an ongoing collaboration with Daniel de las Heras, Enrique Velasco[3], and Yuri Martínez-Ratón[4]. The collaboration was initiated

[3] Autonomous University of Madrid
[4] Charles III University of Madrid

during my research stay in Madrid. Our approach to treat polydisperse colloidal systems under gravity, which is based on a local equilibrium approximation on the direct correlation function, is general and can be applied to any existing bulk theory for polydisperse systems.

To demonstrate our approach, we consider an illustrative colloidal system under gravity consisting of hard rounded rectangular colloidal particles in two dimensions [130]. All particles have the same fixed core dimensions, $L$ and $\sigma$, but the thickness of the padding of the particles $l$ is given by a continuous distribution, see the sketch in Fig. 3.2(a). Thus, particles with different padding have different roundness, as well as area and mass.

The bulk of the system is treated by DFT within scaled particle theory [130]. The gravitational potential is incorporated into the theory by a local equilibrium approximation.

We find that polydispersity in the particle shape induces new phenomena such as an inversion of the stacking sequence by increasing the sample height, see Fig. 3.2(b).

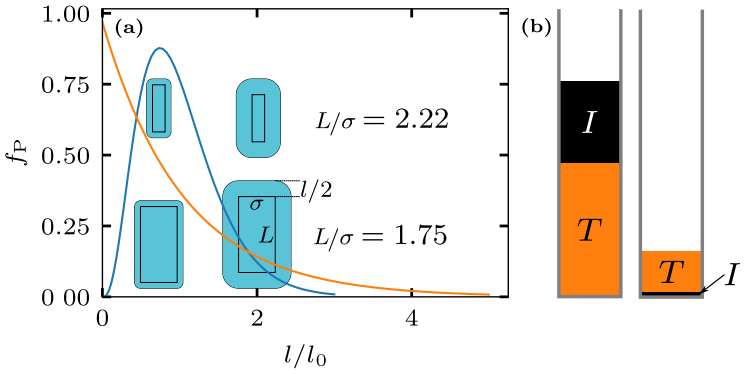


Figure 3.2: (a) Schematics of different hard rounded rectangles with core dimensions $L$ and $\sigma$, and padding thickness $l$. Two illustrative parent distributions $f_P(l)$ which represent two different degrees of polydispersity. (b) Sketches of two samples with the same parent distribution [orange curve in (a)] and average packing fraction, but different sample height (sketch to scale). The larger sample shows an isotropic ($I$) on top of a tetratic layer ($T$), and the smaller sample shows the inverted sequence.

# References


[1]T. Eckert, M. Schmidt, and D. de las Heras, *Gravity-induced phase phenomena in plate-rod colloidal mixtures*, Commun. Phys. **4**, 202 (2021).

[2]T. Eckert, M. Schmidt, and D. de las Heras, *Sedimentation of colloidal plate-sphere mixtures and inference of particle characteristics from stacking sequences*, Phys. Rev. Research **4**, 013189 (2022).

[3]T. Eckert, M. Schmidt, and D. de las Heras, *Sedimentation path theory for mass-polydisperse colloidal systems*, J. Chem. Phys. **157**, 234901 (2022).

[4]T. Eckert, M. Schmidt, and D. de las Heras, *Effect of sample height and particle elongation in the sedimentation of colloidal rods*, Soft Matter **19**, 2214 (2023).

[5]R. Brown, *A brief account of microscopical observations made in the months of June, July and August 1827, on the particles contained in the pollen of plants; and on the general existence of active molecules in organic and inorganic bodies*, Philos. Mag. **4**, 161 (1828).

[6]A. Einstein, *About the movement of suspended particles in liquids at rest as required by the molecular kinetic theory of heat*, Ann. Phys. **322**, 549 (1905).

[7]W. Sutherland, *A dynamical theory of diffusion for non-electrolytes and the molecular mass of albumin*, Philos. Mag. **9**, 781 (1905).

[8]A. D. Dinsmore, E. R. Weeks, V. Prasad, A. C. Levitt, and D. A. Weitz, *Three-dimensional confocal microscopy of colloids*, Applied Optics **40**, 4152 (2001).

[9]V. Prasad, D. Semwogerere, and E. R. Weeks, *Confocal microscopy of colloids*, J. Phys.: Condens. Matter **19**, 113102 (2007).

[10]W. Poon, *Colloids as Big Atoms*, Science **304**, 830 (2004).

[11]L. Mederos, E. Velasco, and Y. Martínez-Ratón, *Hard-body models of bulk liquid crystals*, J. Phys.: Condens. Matter **26**, 463101 (2014).

[12]T. K. Sau and A. L. Rogach, *Nonspherical Noble Metal Nanoparticles: Colloid-Chemical Synthesis and Morphology Control*, Adv. Mater. **22**, 1781 (2010).

[13]Z. Dogic and S. Fraden, *Ordered phases of filamentous viruses*, Curr. Opin. Colloid. In. **11**, 47 (2006).

[14]I. Langmuir, *The Role of Attractive and Repulsive Forces in the Formation of Tactoids, Thixotropic Gels, Protein Crystals and Coacervates*, J. Chem. Phys. **6**, 873 (1938).

[15]J.-C. P. Gabriel, C. Sanchez, and P. Davidson, *Observation of Nematic Liquid-Crystal Textures in Aqueous Gels of Smectite Clays*, J. Phys. Chem. **100**, 11139 (1996).

[16]E. Paineau, A. Philippe, K. Antonova, I. Bihannic, et al., *Liquid–crystalline properties of aqueous suspensions of natural clay nanosheets*, Liq. Cryst. Rev. **1**, 110 (2013).

[17]D. Schneider, P. J. Beltramo, M. Mattarelli, P. Pfleiderer, et al., *Elongated polystyrene spheres as resonant building blocks in anisotropic colloidal crystals*, Soft Matter **9**, 9129 (2013).

[18]Q. Yu, K. Wang, J. Zhang, M. Liu, Y. Liu, and C. Cheng, *Synthesis of anisotropic silica colloids*, RSC Adv. **7**, 37542 (2017).

[19]V. Novotny, *Applications of nonaqueous colloids*, Colloid Surface **24**, 361 (1987).

[20]B. Bahadur, *Liquid Crystals — Applications and Uses* (World Scientific, 1990).

[21]S. Odenbach, ed., *Colloidal Magnetic Fluids* (Springer Berlin Heidelberg, 2008).

[22]M. J. Solomon and P. T. Spicer, *Microstructural regimes of colloidal rod suspensions, gels, and glasses*, Soft Matter **6**, 1391 (2010).

[23]V. F. D. Peters, M. Vis, H. H. Wensink, and R. Tuinier, *Algebraic equations of state for the liquid crystalline phase behavior of hard rods*, Phys. Rev. E **101**, 062707 (2020).

[24]V. A. Belyakov, V. E. Dmitrienko, and V. P. Orlov, *Optics of cholesteric liquid crystals*, Phys.-Uspekhi **22**, 64 (1979).

[25]V. A. Belyakov and V. E. Dmitrienko, *The blue phase of liquid crystals*, Phys.-Uspekhi **28**, 535 (1985).

[26]I. Dierking and S. Al-Zangana, *Lyotropic Liquid Crystal Phases from Anisotropic Nanomaterials*, Nanomaterials **7**, 305 (2017).

[27]P. S. Pershan, *Structure of Liquid Crystal Phases* (World Scientific, 1988).

[28]E. Bianchi, R. Blaak, and C. N. Likos, *Patchy colloids: state of the art and perspectives*, Phys. Chem. Chem. Phys. **13**, 6397 (2011).

[29]G.-R. Yi, D. J. Pine, and S. Sacanna, *Recent progress on patchy colloids and their self-assembly*, J. Phys.: Condens. Matter **25**, 193101 (2013).

[30]J. Russo, J. M. Tavares, P. I. C. Teixeira, M. M. T. da Gama, and F. Sciortino, *Re-entrant phase behaviour of network fluids: A patchy particle model with temperature-dependent valence*, J. Chem. Phys. **135**, 034501 (2011).

[31]D. de las Heras, J. M. Tavares, and M. M. T. da Gama, *Phase diagrams of binary mixtures of patchy colloids with distinct numbers of patches: the network fluid regime*, Soft Matter **7**, 5615 (2011).

[32]E. Matijevic, *Preparation and properties of uniform size colloids*, Chem. Mater. **5**, 412 (1993).

[33]R. P. Murphy, K. Hong, and N. J. Wagner, *Synthetic control of the size, shape, and polydispersity of anisotropic silica colloids*, J. Colloid Interface Sci. **501**, 45 (2017).

[34]F. M. van der Kooij and H. N. W. Lekkerkerker, *Liquid-Crystal Phases Formed in Mixed Suspensions of Rod- and Platelike Colloids*, Langmuir **16**, 10144 (2000).

[35]J. Barrat and J. Hansen, *On the stability of polydisperse colloidal crystals*, J. Phys. **47**, 1547 (1986).

[36]S. Auer and D. Frenkel, *Suppression of crystal nucleation in polydisperse colloids due to increase of the surface free energy*, Nature **413**, 711 (2001).

[37]M. A. Bates and D. Frenkel, *Influence of polydispersity on the phase behavior of colloidal liquid crystals: A Monte Carlo simulation study*, J. Chem. Phys. **109**, 6193 (1998).

[38]Y. Martínez-Ratón and J. A. Cuesta, *Enhancement by Polydispersity of the Biaxial Nematic Phase in a Mixture of Hard Rods and Plates*, Phys. Rev. Lett. **89**, 185701 (2002).

[39]D. Sun, H.-J. Sue, Z. Cheng, Y. Martínez-Ratón, and E. Velasco, *Stable smectic phase in suspensions of polydisperse colloidal platelets with identical thickness*, Phys. Rev. E **80**, 041704 (2009).

[40]W. E. Mell, K. B. McGrattan, and H. R. Baum, *g-Jitter effects on spherical diffusion flames*, Microgravity. Sci. Tec. **15**, 12 (2004).

[41]H. Selig, H. Dittus, and C. Lämmerzahl, *Drop Tower Microgravity Improvement Towards the Nano-g Level for the MICROSCOPE Payload Tests*, Microgravity. Sci. Tec. **22**, 539 (2010).

[42]A. Mialdun, H. Bataller, M. M. Bou-Ali, M. Braibanti, et al., *Preliminary analysis of Diffusion Coefficient Measurements in ternary mIXtures 4 (DCMIX4) experiment on board the International Space Station*, Eur. Phys. J. E **42**, 87 (2019).

[43]J. Perrin, *Atoms* (D. van Nostrand, New York, 1916).

[44]T. Svedberg, *A discussion on: The protein molecule*, Proc. R. Soc. A **170**, 40 (1939).

[45]T. Svedberg, K. O. Pedersen, et al., *The Ultracentrifuge.* (Clarendon Press, Oxford, 1940).

[46]T. Biben, J.-P. Hansen, and J.-L. Barrat, *Density profiles of concentrated colloidal suspensions in sedimentation equilibrium*, J. Chem. Phys. **98**, 7330 (1993).

[47]R. Piazza, T. Bellini, and V. Degiorgio, *Equilibrium sedimentation profiles of screened charged colloids: A test of the hard-sphere equation of state*, Phys. Rev. Lett. **71**, 4267 (1993).

[48]S. V. Savenko and M. Dijkstra, *Sedimentation and multiphase equilibria in suspensions of colloidal hard rods*, Phys. Rev. E **70**, 051401 (2004).

[49]D. van der Beek, T. Schilling, and H. N. W. Lekkerkerker, *Gravity-induced liquid crystal phase transitions of colloidal platelets*, J. Chem. Phys. **121**, 5423 (2004).

[50]F. M. van der Kooij and H. N. W. Lekkerkerker, *Liquid-Crystalline Phase Behavior of a Colloidal Rod-Plate Mixture*, Phys. Rev. Lett. **84**, 781 (2000).

[51]L. Luan, W. Li, S. Liu, and D. Sun, *Phase Behavior of Mixtures of Positively Charged Colloidal Platelets and Nonadsorbing Polymer*, Langmuir **25**, 6349 (2009).

[52]D. de las Heras, N. Doshi, T. Cosgrove, J. Phipps, et al., *Floating nematic phase in colloidal platelet-sphere mixtures*, Sci. Rep. **2**, 789 (2012).

[53]R. Braz Teixeira, D. de las Heras, J. M. Tavares, and M. M. Telo da Gama, *Phase behavior of a binary mixture of patchy colloids: Effect of particle size and gravity*, J. Chem. Phys. **155**, 044903 (2021).

[54]T. Geigenfeind and D. de las Heras, *The role of sample height in the stacking diagram of colloidal mixtures under gravity*, J. Phys.: Condens. Matter **29**, 064006 (2016).

[55]T. Drwenski, P. Hooijer, and R. van Roij, *Sedimentation stacking diagrams of binary mixtures of thick and thin hard rods*, Soft Matter **12**, 5684 (2016).

[56]G. Avvisati, T. Dasgupta, and M. Dijkstra, *Fabrication of Colloidal Laves Phases via Hard Tetramers and Hard Spheres: Bulk Phase Diagram and Sedimentation Behavior*, ACS Nano **11**, 7702 (2017).

[57]T. Dasgupta and M. Dijkstra, *Towards the colloidal Laves phase from binary hard-sphere mixtures via sedimentation*, Soft Matter **14**, 2465 (2018).

[58]D. de las Heras and M. Schmidt, *The phase stacking diagram of colloidal mixtures under gravity*, Soft Matter **9**, 8636 (2013).

[59]A. Imhof and J. K. G. Dhont, *Experimental Phase Diagram of a Binary Colloidal Hard-Sphere Mixture with a Large Size Ratio*, Phys. Rev. Lett. **75**, 1662 (1995).

[60]F. Lado, *Equation of State of the Hard-Disk Fluid from Approximate Integral Equations*, J. Chem. Phys. **49**, 3092 (1968).

[61]K. S. Schweizer and J. G. Curro, *Equation of state of polymer melts: General formulation of a microscopic integral equation theory*, J. Chem. Phys. **89**, 3342 (1988).

[62]Y. C. Chiew, *Percus-Yevick integral-equation theory for athermal hard-sphere chains*, Mol. Phys. **70**, 129 (1990).

[63]J. K. Johnson, J. A. Zollweg, and K. E. Gubbins, *The Lennard-Jones equation of state revisited*, Mol. Phys. **78**, 591 (1993).

[64]R. L. Rowley and M. M. Painter, *Diffusion and viscosity equations of state for a Lennard-Jones fluid obtained from molecular dynamics simulations*, Int. J. Thermophys. **18**, 1109 (1997).

[65]I. Saika-Voivod, F. Sciortino, and P. H. Poole, *Computer simulations of liquid silica: Equation of state and liquid-liquid phase transition*, Phys. Rev. E **63**, 011202 (2000).

[66]R. Span and W. Wagner, *A New Equation of State for Carbon Dioxide Covering the Fluid Region from the Triple-Point Temperature to 1100 K at Pressures up to 800 MPa*, J. Phys. Chem. Ref. Data. **25**, 1509 (1996).

[67]G. Soave, *Equilibrium constants from a modified Redlich-Kwong equation of state*, Chem. Eng. Sci. **27**, 1197 (1972).

[68]D.-Y. Peng and D. B. Robinson, *A New Two-Constant Equation of State*, Ind. Eng. Chem. Res. **15**, 59 (1976).

[69]K. R. Hall, *Another Hard-Sphere Equation of State*, J. Chem. Phys. **57**, 2252 (1972).

[70]N. F. Carnahan and K. E. Starling, *Equation of State for Nonattracting Rigid Spheres*, J. Chem. Phys. **51**, 635 (1969).

[71]E. Thiele, *Equation of state for hard spheres*, J. Chem. Phys. **39**, 474 (1963).

[72]A. Mulero, C. A. Faúndez, and F. Cuadros, *Chemical potential for simple fluids from equations of state*, Mol. Phys. **97**, 453 (1999).

[73]P. Hohenberg and W. Kohn, *Inhomogeneous Electron Gas*, Phys. Rev. **136**, B864 (1964).

[74]W. Kohn and L. J. Sham, *Self-Consistent Equations Including Exchange and Correlation Effects*, Phys. Rev. **140**, A1133 (1965).

[75]N. D. Mermin, *Thermal Properties of the Inhomogeneous Electron Gas*, Phys. Rev. **137**, A1441 (1965).

[76]R. Evans, *The nature of the liquid-vapour interface and other topics in the statistical mechanics of non-uniform, classical fluids*, Adv. Phys. **28**, 143 (1979).

[77]J. K. Percus, *Equilibrium state of a classical fluid of hard rods in an external field*, J. Stat. Phys. **15**, 505 (1976).

[78]S. Nordholm, M. Johnson, and B. Freasier, *Generalized van der Waals theory. III. The prediction of hard sphere structure*, Aust. J. Chem. **33**, 2139 (1980).

[79]Y. Rosenfeld, *Free-energy model for the inhomogeneous hard-sphere fluid mixture and density-functional theory of freezing*, Phys. Rev. Lett. **63**, 980 (1989).

[80]A. J. Archer, B. Chacko, and R. Evans, *The standard mean-field treatment of inter-particle attraction in classical DFT is better than one might expect*, J. Chem. Phys. **147**, 034501 (2017).

[81]R. Roth, *Fundamental measure theory for hard-sphere mixtures: a review*, J. Phys.: Condens. Matter **22**, 063102 (2010).

[82]L. Onsager, *The effects of shape on the interaction of colloidal particles*, Ann. N.Y. Acad. Sci. **51**, 627 (1949).

[83]B. M. Mulder, *The excluded volume of hard sphero-zonotopes*, Mol. Phys. **103**, 1411 (2005).

[84]N. Ibarra-Avalos, A. Gil-Villegas, and A. M. Richa, *Excluded volume of hard cylinders of variable aspect ratio*, Mol. Simulat. **33**, 505 (2007).

[85]T. Geigenfeind and D. de las Heras, *Principal component analysis of the excluded area of two-dimensional hard particles*, J. Chem. Phys. **150**, 184906 (2019).

[86]J. D. Parsons, *Nematic ordering in a system of rods*, Phys. Rev. A **19**, 1225 (1979).

[87]S.-D. Lee, *A numerical investigation of nematic ordering based on a simple hard-rod model*, J. Chem. Phys. **87**, 4972 (1987).

[88]S. Varga, A. Galindo, and G. Jackson, *Global fluid phase behavior in binary mixtures of rodlike and platelike molecules*, J. Chem. Phys. **117**, 7207 (2002).

[89]A. M. Somoza and P. Tarazona, *Nematic-Smectic-A-Smectic-C Transitions in Systems of Parallel Hard Molecules*, Phys. Rev. Lett. **61**, 2566 (1988).

[90]A. M. Somoza and P. Tarazona, *Density functional approximation for hard-body liquid crystals*, J. Chem. Phys. **91**, 517 (1989).

[91]H. B. Callen, *Thermodynamics and an Introduction to Thermostatistics* (Wiley, 1985).

[92]P. Pusey, *The effect of polydispersity on the crystallization of hard spherical colloids*, J. Phys. **48**, 709 (1987).

[93]P. Sollich, *Predicting phase equilibria in polydisperse systems*, J. Phys.: Condens. Matter **14**, R79 (2001).

[94]M. Fasolo and P. Sollich, *Effects of colloid polydispersity on the phase behavior of colloid-polymer mixtures*, J. Chem. Phys. **122**, 074904 (2005).

[95]S. M. Liddle, T. Narayanan, and W. C. K. Poon, *Polydispersity effects in colloid–polymer mixtures*, J. Phys.: Condens. Matter **23**, 194116 (2011).

[96]Y. Martínez-Ratón and E. Velasco, *Effect of combined roundness and polydispersity on the phase behavior of hard-rectangle fluids*, Phys. Rev. E **106**, 034602 (2022).

[97]D. de las Heras, L. L. Treffenstädt, and M. Schmidt, *Reentrant network formation in patchy colloidal mixtures under gravity*, Phys. Rev. E **93**, 030601 (2016).

[98]A. M. Somoza and P. Tarazona, *Nematic and smectic liquid crystals of hard spherocylinders*, Phys. Rev. A **41**, 965 (1990).

[99]J. A. C. Veerman and D. Frenkel, *Relative stability of columnar and crystalline phases in a system of parallel hard spherocylinders*, Phys. Rev. A **43**, 4334 (1991).

[100]A. Poniewierski and T. J. Sluckin, *Phase diagram for a system of hard spherocylinders*, Phys. Rev. A **43**, 6837 (1991).

[101]H. Löwen, *Brownian dynamics of hard spherocylinders*, Phys. Rev. E **50**, 1232 (1994).

[102]S. C. McGrother, D. C. Williamson, and G. Jackson, *A re-examination of the phase diagram of hard spherocylinders*, J. Chem. Phys. **104**, 6755 (1996).

[103]P. Bolhuis and D. Frenkel, *Tracing the phase boundaries of hard spherocylinders*, J. Chem. Phys. **106**, 666 (1997).

[104]G. Cinacchi, L. Mederos, and E. Velasco, *Liquid–crystal phase diagrams of binary mixtures of hard spherocylinders*, J. Chem. Phys. **121**, 3854 (2004).

[105]F. Gámez, R. D. Acemel, and A. Cuetos, *Demixing and nematic behaviour of oblate hard spherocylinders and hard spheres mixtures: Monte Carlo simulation and Parsons–Lee theory*, Mol. Phys. **111**, 3136 (2013).

[106]H. Guo, T. Narayanan, M. Sztuchi, P. Schall, and G. H. Wegdam, *Reversible Phase Transition of Colloids in a Binary Liquid Solvent*, Phys. Rev. Lett. **100**, 188303 (2008).

[107]T. E. Kodger, R. E. Guerra, and J. Sprakel, *Precise colloids with tunable interactions for confocal microscopy*, Sci. Rep. **5**, 14635 (2015).

[108]J. Zhu, M. Li, R. Rogers, W. Meyer, et al., *Crystallization of hard-sphere colloids in microgravity*, Nature **387**, 883 (1997).

[109]D. G. A. L. Aarts, *The interface in demixed colloid–polymer systems: wetting, waves and droplets*, Soft Matter **3**, 19 (2007).

[110]Y. Wang, Y. Wang, D. R. Breed, V. N. Manoharan, et al., *Colloids with valence and specific directional bonding*, Nature **491**, 51 (2012).

[111]R. Piazza, *Settled and unsettled issues in particle settling*, Rep. Prog. Phys. **77**, 056602 (2014).

[112]T. Nicolai and S. Cocard, *Structure of gels and aggregates of disk-like colloids*, Eur. Phys. J. E **5**, 221 (2001).

[113]M. Telo da Gama, *The interfacial properties of a model of a nematic liquid crystal*, Mol. Phys. **52**, 611 (1984).

[114]U.-C. Boehnke, T. Remmler, H. Motschmann, S. Wurlitzer, J. Hauwede, and T. M. Fischer, *Partial Air Wetting on Solvophobic Surfaces in Polar Liquids*, J. Colloid Interface Sci. **211**, 243 (1999).

[115]I. Rodríguez-Ponce, J. M. Romero-Enrique, E. Velasco, L. Mederos, and L. F. Rull, *Interplay between Anchoring and Wetting at a Nematic-Substrate Interface*, Phys. Rev. Lett. **82**, 2697 (1999).

[116]M. Dijkstra, R. van Roij, and R. Evans, *Wetting and capillary nematization of a hard-rod fluid: A simulation study*, Phys. Rev. E **63**, 051703 (2001).

[117]M. Telo da Gama, *The interfacial properties of a model of a nematic liquid crystal*, Mol. Phys. **52**, 585 (1984).

[118]A. J. McDonald, M. P. Allen, and F. Schmid, *Surface tension of the isotropic-nematic interface*, Phys. Rev. E **63**, 010701 (2000).

[119]D. van der Beek, H. Reich, P. van der Schoot, M. Dijkstra, et al., *Isotropic-Nematic Interface and Wetting in Suspensions of Colloidal Platelets*, Phys. Rev. Lett. **97**, 087801 (2006).

[120]D. de las Heras, Y. Martínez-Ratón, and E. Velasco, *Surface and smectic layering transitions in binary mixtures of parallel hard rods*, Phys. Rev. E **81**, 021706 (2010).

[121]J. Elgeti, R. G. Winkler, and G. Gompper, *Physics of microswimmers—single particle motion and collective behavior: a review*, Rep. Progr. Phys. **78**, 056601 (2015).

[122]A. Doostmohammadi, J. Ignés-Mullol, J. M. Yeomans, and F. Sagués, *Active nematics*, Nat. Commun. **9**, 3246 (2018).

[123]M. James, W. J. T. Bos, and M. Wilczek, *Turbulence and turbulent pattern formation in a minimal model for active fluids*, Phys. Rev. Fluids **3**, 061101 (2018).

[124]J. Palacci, C. Cottin-Bizonne, C. Ybert, and L. Bocquet, *Sedimentation and Effective Temperature of Active Colloidal Suspensions*, Phys. Rev. Lett. **105**, 088304 (2010).

[125]S. Hermann and M. Schmidt, *Active ideal sedimentation: exact two-dimensional steady states*, Soft Matter **14**, 1614 (2018).

[126]S. E. Paulin and B. J. Ackerson, *Observation of a phase transition in the sedimentation velocity of hard spheres*, Phys. Rev. Lett. **64**, 2663 (1990).

[127]P. N. Pusey and W. van Megen, *Phase behaviour of concentrated suspensions of nearly hard colloidal spheres*, Nature **320**, 340 (1986).

[128]B. J. Ackerson, S. E. Paulin, B. Johnson, W. van Megen, and S. Underwood, *Crystallization by settling in suspensions of hard spheres*, Phys. Rev. E **59**, 6903 (1999).

[129]S. M. Underwood, J. R. Taylor, and W. van Megen, *Sterically Stabilized Colloidal Particles as Model Hard Spheres*, Langmuir **10**, 3550 (1994).

[130]Y. Martínez-Ratón, E. Velasco, and L. Mederos, *Effect of particle geometry on phase transitions in two-dimensional liquid crystals*, J. Chem. Phys. **122**, 064903 (2005).

# 4 Publications

This chapter contains in chronological order the full versions of the four papers contributing to this cumulative Thesis, including their supplementary material.

| | | |
|---|---|---|
| [1] | *Gravity-induced phase phenomena in plate-rod colloidal mixtures.* T. Eckert, M. Schmidt, and D. de las Heras, Commun. Phys. **4**, 202 (2021) | 41 ff. |
| [2] | *Sedimentation of colloidal plate-sphere mixtures and inference of particle characteristics from stacking sequences.* T. Eckert, M. Schmidt, and D. de las Heras, Phys. Rev. Research **4**, 013189 (2022) | 57 ff. |
| [3] | *Sedimentation path theory for mass-polydisperse colloidal systems.* T. Eckert, M. Schmidt, and D. de las Heras, J. Chem. Phys. **157**, 234901 (2022) | 71 ff. |
| [4] | *Effect of sample height and particle elongation in the sedimentation of colloidal rods.* T. Eckert, M. Schmidt, and D. de las Heras, Soft Matter **19**, 2214 (2023) | 83 ff. |

communications physics

ARTICLE

https://doi.org/10.1038/s42005-021-00706-0 OPEN

# Gravity-induced phase phenomena in plate-rod colloidal mixtures

Tobias Eckert [1], Matthias Schmidt [1✉] & Daniel de las Heras [1✉]

Gravity can affect colloidal suspensions since for micrometer-sized particles gravitational and thermal energies can be comparable over vertical length scales of a few millimeters. In mixtures, each species possesses a different buoyant mass, which can make experimental results counter-intuitive and difficult to interpret. Here, we revisit from a theoretical perspective iconic sedimentation-diffusion-equilibrium experiments on colloidal plate-rod mixtures by van der Kooij and Lekkerkerker. We reproduce their findings, including the observation of five different mesophases in a single cuvette. Using sedimentation path theory, we incorporate gravity into a microscopic theory for the bulk of a plate-rod mixture. We also show how to disentangle the effects of gravity from sedimentation experiments to obtain the bulk behavior and make predictions that can be experimentally tested. These include changes in the sequence by altering the sample height. We demonstrate that both buoyant mass ratio and sample height form control parameters to study bulk phase behavior.

[1] Theoretische Physik II, Physikalisches Institut, Universität Bayreuth, Bayreuth, Germany. ✉email: matthias.schmidt@uni-bayreuth.de; delasheras.daniel@gmail.com

Colloids, i.e., nano- to micrometer-sized particles suspended in a liquid, behave under some circumstances as big atoms[1–5]. Despite their size disparity, molecular and colloidal systems exhibit analogous bulk phases and similar surface phenomena such as wetting[6], capillary waves at the free fluid-fluid interface[7], and the occurrence of topological defects due to frustration[8]. Beyond intrinsic fundamental interest, understanding bulk phase behavior is a prerequisite for the design of new materials. Sedimentation experiments, in which a colloidal suspension is placed in a cuvette under the influence of gravity, are ideal candidates to study the bulk behavior of colloidal systems. One famous example are the experiments on suspensions of nearly hard colloidal spheres[9] that confirmed the fluid-crystal transition predicted decades earlier[10]. Sedimentation experiments also confirmed the entropy-driven formation of liquid crystalline phases in systems of anisotropic particles[11,12], the existence of empty liquids and equilibrium gels[13], and the hexatic phase in two-dimensional colloidal discs[14]. Gravity can play a major role in the colloidal realm and can only be neglected if the relevant length scales of the experiment (e.g., the height of the sample inside the cuvette) are much smaller than the colloidal gravitational length; the latter is the ratio between the thermal energy and the buoyant force acting on a single particle. For typical colloidal systems, the gravitational length is of the order of millimeters, and hence it is smaller or comparable to the sample height.

Depending on the sign of the buoyant mass the colloidal particles sediment towards the bottom or they cream up. In both cases, gravity creates a particle density gradient in the vertical direction. Sedimentation-diffusion-equilibrium is reached once the gravity-induced particle flow is balanced by the diffusive flow originated by the density gradient and the interparticle interactions. As already shown in Perrin's pioneering experiments[15], the resulting height-dependent colloidal density distribution provides direct access to the full equation of state for monocomponent systems of both isotropic[16,17] and anisotropic[18,19] colloidal particles.

It is often an excellent approximation to consider that at each height inside the cuvette, the system is well reproduced by a corresponding homogeneous equilibrium system with a bulk density that is identical to the local density of the inhomogeneous system[20,21]. This local density approximation can be implemented by considering that the chemical potential of the sample varies linearly with the vertical coordinate. The strength of sedimentation-diffusion-equilibrium experiments is that instead of looking at a single state point of a bulk system (i.e., at a fixed chemical potential), one is able to consider set of states with varying chemical potential along the vertical axis. This result is due to the gravity-induced varying density (or equivalently chemical potential) along the vertical axis. Since in many colloidal systems the gravitational length is smaller than the typical height of a cuvette, even sedimentation experiments with samples of few millimeters in height provide in-depth insight into the equation of state and bulk phase phenomenology.

In binary colloidal mixtures, gravity has stronger impact since two, in general distinct, gravitational lengths exist. Counter-intuitive and complex phenomenology arises, making it difficult to draw conclusions about bulk behavior. For example, in their iconic experiments on plate-rod mixtures, van der Kooij and Lekkerkerker[22,23], found hitherto unexpected and rich phenomenology of colloidal mixtures. By changing the colloidal concentrations the authors observed the formation of different stacking sequences, including samples with the sequence: isotropic-nematic-smectic-nematic-columnar, when scanned from top to bottom of the sample. The two nematic layers correspond to different bulk phases rich in either rods (top) or plates (bottom).

In mixtures, it is frequent to observe more than three layers of different bulk phases in a cuvette at different altitudes: Up to six different layers occur in mixtures of positively charged colloidal plates and nonadsorbing polymers[24]. Even the same layer can reenter the stacking sequence, such as e.g., a nematic sandwiched between two isotropic layers in sphere-plate colloidal mixtures[25]. Further experimental studies were aimed at colloidal rod-plate[26,27], plate-sphere[28,29], rod-sphere[30], and sphere-sphere[31,32] mixtures, liquid crystalline binary nanosheet colloids[33], mixtures of thin and thick colloidal rods[34], as well as attractive nanosized spheres and plates[35]. Gravitational effects can be relevant even if the system contains only a few colloidal layers[36], as e.g in the stratification found in drying films of colloidal mixtures[37].

To draw conclusions about bulk phenomena from sedimentation experiments (and vice versa), gravity needs to be considered. However, in mixtures the dimensionality of the phase diagram increases by one unit for each added species. Gravity induces a height-dependent density profile for each component. Therefore the gravity-induced one-dimensional scan along the vertical axis of the sample gives only a one-dimensional slice of the complete phase diagram. The full equation of state and the phase diagram can not be extracted from a single sedimentation profile. Wensink and Lekkerkerker[20] incorporated gravity in a mixture of plates and polymers by treating the mixture as an effective mono-component system with the chemical potential of the polymer fixed. This approach is limited to systems in which the gravitational length of one species (the polymer) is much larger than the sample height. A generalized Archimedes principle[38,39] appropriately describes the behavior a mixture in which both species are colloidal particles and one of them is very diluted.

An alternative approach, valid for any mixture and any colloidal concentration, was formally given by de las Heras and Schmidt[21]. The theory is formulated in terms of sedimentation paths, which represent how the chemical potentials of both species vary linearly with the vertical coordinate due to gravity. The sedimentation paths are straight lines in the plane of chemical potentials, and the crossing between a path and a binodal indicates the formation of an interface in the sample. Different stacking sequences appear depending on which binodals are crossed by the path. The stacking sequences are grouped in a stacking diagram, which is the analog of the bulk phase diagram for systems subject to gravity. So far, the stacking diagrams have been used to theoretically study sedimentation of model colloidal mixtures[21,40–42].

We demonstrate here that this formal approach also opens the door for the rigorous interpretation and the prediction of sedimentation-diffusion-equilibrium experiments in colloidal mixtures. We reinterpret the findings of the arguably best known experimental study in the field, conducted by van der Kooij and Lekkerkerker[22,23], on plate-rod colloidal mixtures. By incorporating gravity into a microscopic theory for the bulk behavior of the mixture we reproduce quantitatively their experimental findings. Furthermore we address the (experimentally relevant) inverse problem. That is, we demonstrate how to infer the bulk phase diagram using the experimentally obtained stacking sequences and the individual heights of their constituent layers. We also make predictions that can be tested experimentally: a different set of stacking sequences emerges by altering the ratio of the buoyant masses of the colloidal particles and complex changes in the stacking sequence occur by simply varying the height of the sample. Both variables, the buoyant mass ratio and the sample height, can be systematically controlled in both experimental and theoretical work. Our demonstration of the important role played by both the buoyant mass ratio and the sample height allows to

design experimental and theoretical studies that exploit these (hitherto largely unexplored) control parameters.

## Results

**Particle model**. To model the experiments[22,23] we consider a mixture of hard rods and hard plates. Depending on composition and packing fraction, the bulk phase is either isotropic ($I$), nematic rich in plates ($N_p$), or nematic rich in rods ($N_r$), see Fig. 1. We use subscripts p and r to designate the plates and the rods, respectively.

The gravitational lengths are $\xi_i = k_B T/(m_i g)$ with $m_i$ the buoyant mass of species $i$, $g$ the gravitational acceleration, $k_B$ the Boltzmann constant, and $T$ absolute temperature. The rods are made of boehmite (mass density 3.03 g/cm$^3$) and the plates of gibbsite (2.35 g/cm$^3$). The particles are sterically stabilized with a polymer coating of a few nanometer thickness and suspended in toluene (0.87 g/cm$^3$). We use cylinders of lengths 200 nm and 10 nm, and diameters 20 nm and 150 nm to model the rods and the plates, respectively. The particles match both the length-to-width aspect ratio and the dimensions of the particles used in the experiments[22,23] within the experimental uncertainty. We subtract the volume of the polymer coating from the total particle volume to estimate the buoyant masses. Using a diameter of 15 nm for the rod's core and a length of 8.7 nm for the plates' core, we obtain $\xi_r = 5.5$ mm, $\xi_p = 1.8$ mm. Hence the buoyant mass ratio is

$$s = \frac{m_p}{m_r} = \frac{\xi_r}{\xi_p} \approx 3. \quad (1)$$

The values of the gravitational lengths and hence that of the buoyant mass ratio are only rough estimates since there is a large uncertainty in the particle dimensions (up to 25%) and in the thickness of the polymer layer[43,44]. Given this uncertainty, the buoyant mass ratio is likely between a minimum value of ~2 and a maximum value of ~5.

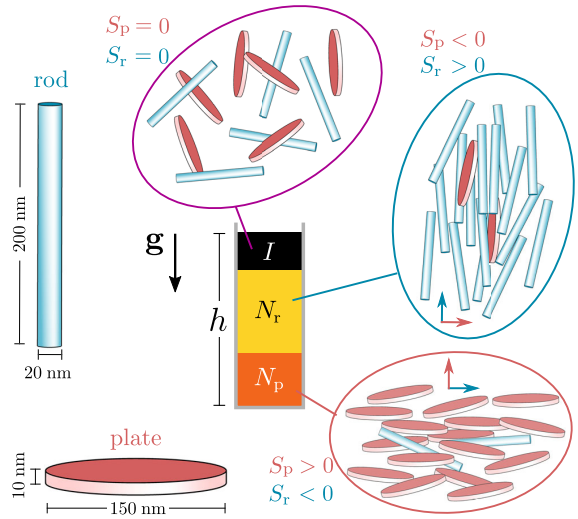


**Fig. 1 Model.** Schematics of colloidal rods (blue) and plates (red), together with schematics of the particles in the isotropic ($I$), the nematic rod-rich ($N_r$) and the nematic plate-rich ($N_p$) layers that appear in a cuvette of height $h$ under the gravitational field **g**. The blue and red arrows indicate the nematic director for rods and plates, respectively. The sign of the uniaxial order parameter of plates $S_p$ and rods $S_r$ in each phase is also indicated (the order parameter is calculated with respect to the director of the dominant species in each phase).

**Bulk**. We use an Onsager-like density functional theory to study the bulk, see Methods. To characterize the phases we use the uniaxial order parameters $S_i$ of each species (see Methods) that take values between −0.5 and 1. The order parameters measure the orientational order with respect to the direction given by the director of the dominant species, see Fig. 1. A positive (negative) value indicates that the alignment of the particles is parallel (perpendicular) to the director. In the isotropic phase both order parameters vanish.

**Sedimentation path theory**. Gravity is incorporated by approximating each horizontal slice of the system at height $z$ by a bulk equilibrium system with local chemical potentials $\mu_i(z)$ given by[21]

$$\mu_i(z) = \bar{\mu}_i - m_i g\left(z - \frac{h}{2}\right), \quad i = \mathrm{r}, \mathrm{p}, \quad (2)$$

with $0 \le z \le h$ the vertical coordinate and $h$ the height of the sample. This constitutes a local density approximation (LDA), which is justified if all correlation lengths are small compared to both gravitational lengths. The LDA is used only to incorporate gravity and it does not affect therefore the description of the bulk. Sophisticated bulk theories, such as fundamental measure theory[45], can be used together with sedimentation path theory to study sedimentation of e.g., crystalline phases.

Due to the gravitational potential, the local chemical potentials depend linearly on the vertical coordinate $z$. Equation (2) formalizes the concept that a sample subject to gravity can be understood as a set of bulk states at different chemical potentials and distributed along the vertical axis. Geometrically, Eq. (2) describes a line segment parametrized by $z$ in the plane of chemical potentials. We refer to such lines as sedimentation paths[21,41]. The constant terms $m_i g h/2$ in Eq. (2) conveniently translate the origin of chemical potentials such that the values of the midpoint of the path are $(\bar{\mu}_r, \bar{\mu}_p)$. Eliminating $z$ for the mixture in Eq. (2) yields

$$\mu_p(\mu_r) = s\mu_r + a, \quad (3)$$

which constitutes the equation of a line segment with a slope given by the buoyant mass ratio $s = m_p/m_r = \xi_r/\xi_p$ and intercept $a = \bar{\mu}_p - s\bar{\mu}_r$. The buoyant masses play therefore a vital role since they determine both the slope $s$ (buoyant mass ratio) and, together with $h$, the length of the sedimentation path in the plane of chemical potentials. The latter is given by $\beta\Delta\mu_i = h/\xi_i$, with $\Delta\mu_i = \mu_i(0) - \mu_i(h)$ being the differences in local chemical potentials between the bottom and the top of the sample.

The sedimentation path provides direct information of the sequence of layers in the sample, i.e., the stacking sequence. An interface between two layers of different bulk phases appears in the sample whenever a sedimentation path crosses a bulk binodal in the plane of chemical potentials, see Fig. 2a. The crossing point between the path and the binodal gives the $z$ position of the interface in the sample via Eq. (2).

**Stacking diagram**. Different stacking sequences occur by varying e.g., the position, the slope, and the length of the sedimentation path. The sequences can be grouped in a stacking diagram. The stacking diagram admits several representations depending on which variables are kept constant. To connect with the experiments we fix the buoyant masses and the sample height $h$. Hence, we work at constant sedimentation path length and fixed buoyant mass ratio $s$.

From the bulk phase diagram we construct the stacking diagram by finding the boundaries between two stacking sequences in the stacking diagram. There exist three types of boundaries formed by three sets of special sedimentation paths[41],

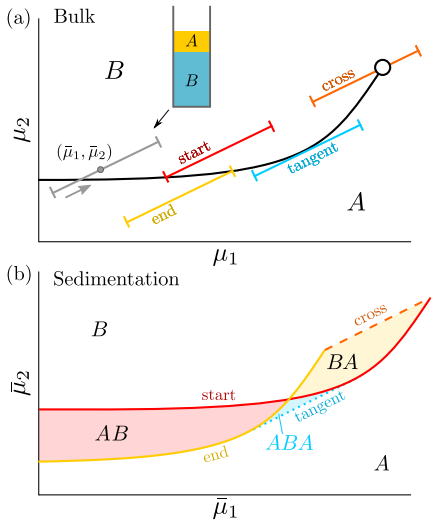


**Fig. 2 Sedimentation path theory. a** Model bulk phase diagram in the plane of chemical potentials $\mu_1 - \mu_2$. Phases *A* and *B* coexist along a binodal (solid line) that ends at a critical point (empty circle). The line segments are sedimentation paths. The gray path that crosses the binodal corresponds to a stacking sequence *AB* (from top to bottom), as schematically represented. The gray arrow indicates the direction of the paths from top to bottom of the sample. Examples of all types of paths that form the boundaries between different stacking sequences are shown: (i) paths that either start (red) or end (yellow) at the binodal, (ii) paths tangent (blue) to the binodal, and (iii) paths crossing (orange) the critical point. An infinitesimal displacement of any of such paths can alter the stacking sequence. **b** Corresponding stacking diagram in the plane of average chemical potentials $\bar{\mu}_1 - \bar{\mu}_2$. Each colored region is a different stacking sequence, as indicated. The boundary lines between sequences are sedimentation binodals of type I (solid lines) or type II (dotted-blue line), and terminal lines (dashed-orange line).

see Fig. 2a. The first type corresponds to sedimentation paths that either start or end at a bulk binodal (red and yellow paths in Fig. 2). These paths represent boundaries, so-called sedimentation binodals of type I, between stacking sequences since an infinitesimal displacement of the path in the $\mu_1 - \mu_2$ plane can alter the stacking sequence by crossing the binodal. Paths that cross an ending point of a binodal, e.g., a triple point or a critical point (orange path in Fig. 2), also form a boundary in the stacking diagram, known as a terminal line. Finally, paths tangent to a binodal (blue path in Fig. 2) form the so-called sedimentation binodal of type II which is also a boundary between different stacking sequences. In each of the three cases, an infinitesimal displacement of the path can alter the stacking sequence.

The coordinates of the midpoint $(\bar{\mu}_r, \bar{\mu}_p)$ for each special path are then represented in the $\bar{\mu}_r - \bar{\mu}_p$ plane to generate the stacking diagram, see Fig. 2b. The experimentally relevant variables are the colloidal packing fractions. Therefore, we transform the stacking diagram from the $\bar{\mu}_1 - \bar{\mu}_2$ to the $\bar{\eta}_1 - \bar{\eta}_2$ plane of average colloidal packing fractions (percentage of the total volume occupied by each species). To this end we average the packing fraction of each species, i.e., $\eta_i = \rho_i v_i$, along the sedimentation path. Here $v_i$ is the particle volume of species *i*. We compute $\eta_i$ for each set of $\mu_i$ along the path (see Methods) and transform the stacking diagram from the $\bar{\mu}_r - \bar{\mu}_p$ to the $\bar{\eta}_r - \bar{\eta}_p$ plane. In both planes each point of the stacking diagram represents a sedimentation path and therefore directly corresponds to an experimental sample in sedimentation-diffusion-equilibrium.

**Comparison with experiments**. In the experiments[22], stacking sequences with isotropic (*I*), nematic rod-rich ($N_r$), and nematic plate-rich ($N_p$) layers are reported. The samples, reproduced in Fig. 3, were initially prepared with packing fractions $(\bar{\eta}_r, \bar{\eta}_p) = (0.02,0.18)$ (a), (0.10,0.08) (b), and (0.10,0.01) (c).

To compare with the experiments, we find the paths for which the average packing fractions $(\bar{\eta}_r, \bar{\eta}_p)$ and sample height match the experimental values. The height is measured form the pictures knowing that the width of the cuvettes is 10 mm. The buoyant mass ratio, and hence the slope of the path, is the same for all samples. There is an uncertainty of ~25% in the experimental particle dimensions[22,23,44] (note small deviations in the diameter of the rods and the height of the plates greatly affect the particle volumes and therefore the packing fractions). Also, solvent evaporation can occur experimentally, affecting the packing fractions[25]. Hence, to find the paths we fix the composition of the mixture to the experimentally reported value and allow a variation in the total packing fraction. This is equivalent to assuming that an unknown percentage of the solvent has been evaporated (alternatively we could allow a variation in the particle sizes). The best agreement between theory and experiment occurs assuming that 25%(a), 50%(b) and 60%(c) of the solvent evaporated during the long equilibration times. These values are consistent with the position of the meniscus in Fig. 3 (the sample heights are (a) 23 mm, (b) 18 mm, and (c) 17 mm) if the samples were filled to the same height initially. The density and nematic order parameter profiles along the sedimentation paths are shown in Fig. 3. Due to gravity the profiles are inhomogeneous (also within a layer of a given mesophase) in contrast to what happens in a bulk state in absence of gravity. The stacking sequence can be read off directly from the nematic order parameter profiles. In the isotropic layers both order parameter vanish, $S_r = S_p = 0$. In the nematic layers rods and plates orient themselves perpendicular to each other (see schematics in Fig. 1): the dominant species has a positive order parameter $S_i > 0$ (particles aligned along the director) and the minority species has a negative order parameter $S_j < 0$ (particles perpendicular to the director).

Despite the complexity of the experiments and the simplicity of the theory, the agreement of the respective results is excellent. All three stacking sequences, namely (from top to bottom) $IN_p$ Fig. 3a, $IN_rN_p$ Fig. 3b and $IN_r$ Fig. 3c are reproduced. Both the phase identity of each layer and their order in the sequence are correctly predicted. Even the vertical positions of the interfaces between layers agree semi-quantitatively. The density profiles show that the $N_p$ and $N_r$ phases are rich in plates and rods, respectively. Interestingly, the isotropic phase can be either dominated by plates, Fig. 3a, or by rods, Fig. 3b, c. This affects the order that the isotropic layer occupies in the stacking sequence for other values of the buoyant mass ratio as we will see below. The experimental results and the theoretical predictions differ in two aspects. In Fig. 3b the theory overestimates the thickness of the $N_r$ layer. The experimentally reported packing fraction of rods is larger than that of plates and the theory predicts almost perfect demixing between the species, see the packing fraction profiles in Fig. 3b. As a result the predicted $N_r$ layer is thicker than the $N_p$ layer. The opposite, however, is observed in the experiments. The other discrepancy between theory and experiments is the prediction of a thin $N_p$ layer at the bottom of sample 3 which is not observed experimentally, see Fig. 3c. This could be due to interfacial effects that are not considered in the sedimentation path theory approximation. The surface tension associated with the emergence of the new interface might prevent such slim layer

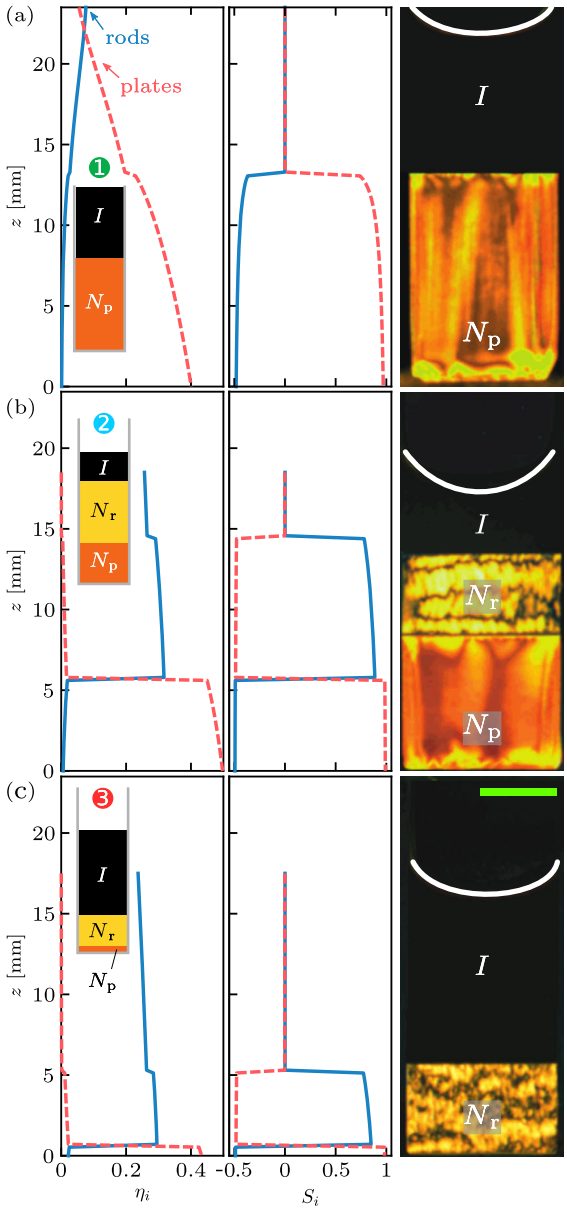


**Fig. 3 Comparison with experiments.** Vertical profiles of the packing fractions $\eta_i$ and the nematic order parameters $S_i$ with $i = r, p$ for rods (solid-blue lines) and plates (dashed-red lines), respectively. Three different samples labeled as 1, 2, and 3 (indicated by the colored circles) are shown. Schematics of the samples showing the isotropic ($I$), nematic rod-rich ($N_p$) and nematic plate-rich ($N_p$) layers are represented in the insets. The average packing fractions ($\bar{\eta}_r, \bar{\eta}_p$) are (0.027, 0.24) (**a**), (0.20, 0.16) (**b**), and (0.25, 0.025) (**c**). The corresponding experimental samples (pictures taken between crossed polarizers) by van der Kooij and Lekkerkerker[22,23] are also shown (adapted with permission[23], Copyright 2000 American Chemical Society). The meniscus is highlighted with a white line. The bright areas are due to light being polarized in layers with orientational order. The scale bar (green) is 5 mm.

to appear in the experiments. Also, for other values of the buoyant mass ratio within the experimental uncertainty, the bottom $N_p$ layer is not present (see Supplementary Fig. 1). Nevertheless, the discrepancies found are certainly not surprising given the simple microscopic theory we use to describe the bulk, the experimental uncertainties in both particle dimensions and masses, as well as other bulk factors not taken into account such as polydispersity.

Recall that we adjust only the amount of solvent evaporated to find the best agreement between theory and experiment. Any value of the buoyant mass ratio within the experimental uncertainties reproduces the experimental stacking sequences using only the evaporation as a free parameter in the theory (see Supplementary Fig. 1).

**Bulk and stacking diagrams**. We discuss now the intricate connection between the stacking sequences under gravity and the bulk phase diagram of the mixture. The bulk phase diagram according to our microscopic theory is shown in Fig. 4a, b in the planes of chemical potentials and packing fractions, respectively. To reassure the validity of the theory, we compare the chemical potentials of the $I - N_p$ and $I - N_r$ transitions in mono-component systems (i.e., $\mu_r \to -\infty$ or $\mu_p \to -\infty$) with those of parallel hard spherocylinders[46,47] and hard cut spheres[48] according to simulations, see the violet arrows in Fig. 4a. We expect that both spherocylinders and cut spheres behave similarly to our cylindrical particles at the relatively low density of the isotropic-nematic transition and large particle anisotropies considered here.

The sedimentation paths of the samples in Fig. 3 are depicted in Fig. 4a. The stacking sequences can be read off by simply following the direction, and observing the binodals or the phase regions crossed by each path. For example, the stacking sequence of sample 1 is $IN_p$ from top to bottom since the path crosses only the $I - N_p$ binodal.

The experimentally observed layers in a stacking sequence do not represent coexisting phases in bulk[21]. For example, the sequence $IN_rN_p$ shown in Fig. 3b should not be interpreted as a triple thermodynamic coexistence between $I$, $N_r$, and $N_p$ bulk phases. In reality the three phases might or might not coexist in bulk, i.e., in the absence of gravity. This is because due to gravity, the sample does not represent a state point in bulk but a set of state points along the sedimentation path. Note also that for typical colloidal particles and sample heights, the paths cover a large region of the bulk phase diagram, see e.g., the paths in Fig. 4a. Therefore, the observation of more than three layers in a stacking sequence does not imply violation of the Gibbs phase rule. Observing a single sample, we can conclude that any two consecutive phases in the sample (e.g., $IN_r$ and $N_rN_p$ in the sequence $IN_rN_p$) coexist in bulk since the path crosses a bulk binodal at the position of the interfaces between two consecutive layers. However, one cannot conclude whether or not two non-consecutive layers (e.g., $I$ and $N_p$ in the sequence $IN_rN_p$) coexist in bulk.

As discussed above, it is useful to group the stacking sequences in a finite height stacking diagram[41]. Figure 4 shows the stacking diagrams for samples with heights $h = 5$ mm (c,d) and 18 mm (e,f) in the plane of average chemical potentials (c,e) and average packing fractions (d,f) along the path. In bulk three binodals meet at a triple point, see Fig. 4a. The stacking diagrams contain sedimentation binodals of type I due to paths that either start or end at a bulk binodal plus one terminal line due to paths crossing the bulk triple point. Six different

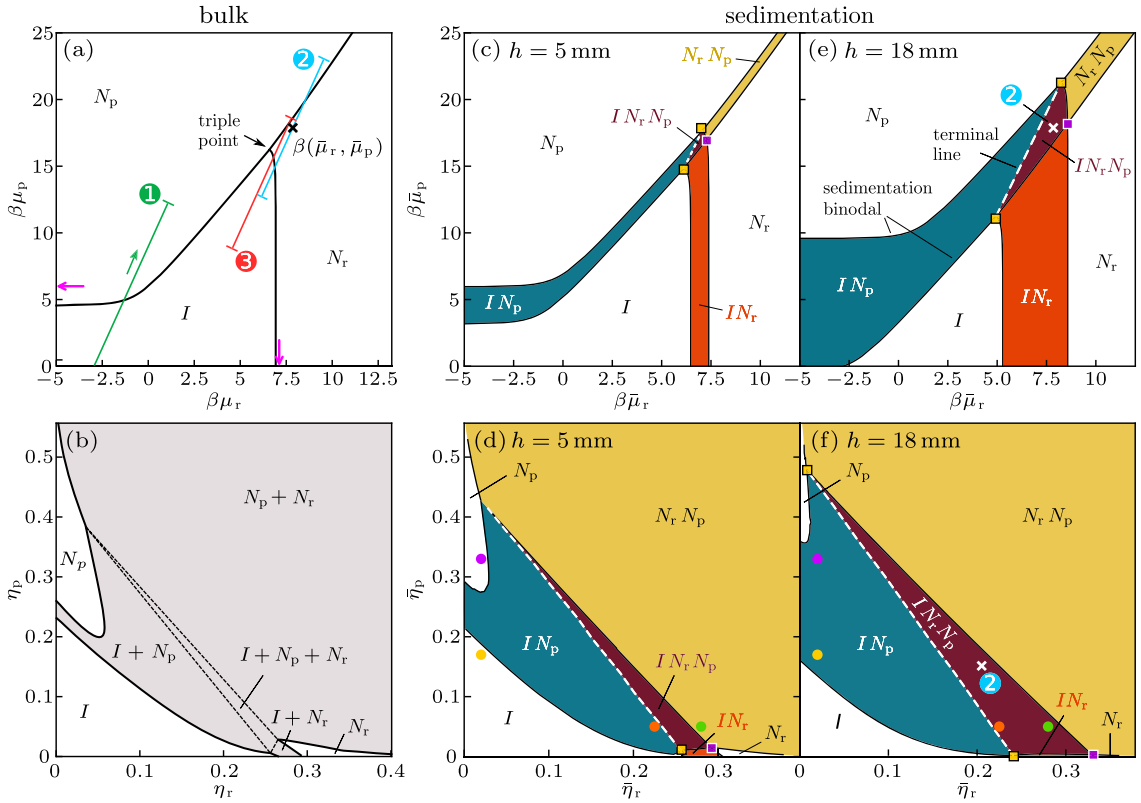


**Fig. 4 Bulk and stacking diagrams.** Bulk phase diagram in the plane of chemical potentials of rods $\mu_r$ and plates $\mu_p$ (**a**) and also in the plane of packing fractions of rods $\eta_r$ and plates $\eta_p$ (**b**). The chemical potentials are scaled with the inverse temperature $\beta = 1/(k_BT)$. Solid lines are the binodals. The stable phases are isotropic ($I$), nematic plate-rich ($N_p$), and nematic rod-rich ($N_r$). The violet arrows in (**a**) mark the $I - N_p$ and $I - N_r$ transitions of pure systems of plates (horizontal arrow) and rods (vertical) obtained by simulations[46–48]. The line segments are the sedimentation paths of samples 1, 2, and 3. The green arrow illustrates the direction of the paths from top to bottom. The shadow region in (**b**) is the two phase region and the dashed lines are the tie lines of the triple point. Stacking diagrams for heights $h = 5$ mm (**c**, **d**) and 18 mm (**e**, **f**) in the plane of average chemical potentials of the sedimentation paths for rods $\bar{\mu}_r$ and plates $\bar{\mu}_p$ (**c**, **e**) and average packing fractions of rods $\bar{\eta}_r$ and of plates $\bar{\eta}_p$ in the samples (**d**, **f**). Black solid (white dashed) lines are sedimentation binodals (terminal lines). Each stacking sequence is denoted from top to bottom and colored differently (except for the white regions that represent sequences with only one layer). The midpoint of the path for sample 2 is marked with a black cross in (**a**). The position of this sample is also marked in the stacking diagrams with crosses in (**e**) and (**f**). The colored squares indicate the points at which four stacking sequences meet due to the crossing between two sedimentation binodals (violet squares) or the intersection of sedimentation binodals and a terminal line (yellow squares). The colored circles in (**d**) and (**f**) mark samples with the same colloidal packing fractions in both stacking diagrams.

sequences occur: $I$, $N_p$, $N_r$, $IN_p$, $IN_r$, and $IN_rN_p$. If present in the sequence, the $N_p$ layer is always the bottom layer due to the slope of the path (buoyant mass ratio) being steeper than the slope of each bulk binodal. This behavior is not surprising since the plates are heavier than the rods and hence dominate the bottom phases. The total mass density profile, i.e., the sum of the mass density of the particles and the solvent (see Methods), monotonically increases towards the bottom of the sample in all cases (also if the buoyant masses are negative in which case the particles cream up). This is consistent with Archimedes' principle, although it should be noticed that denser particles can also float on top of a lighter fluid[38,39]. Analog to bulk points at which several phases coexists, such as triple points, there exist points in the stacking diagram at which several stacking sequences meet (due to e.g., the crossing of two sedimentation binodals). A discussion about these points is provided in Supplementary Note 1.

The length of the path in the $\mu_r - \mu_p$ plane is relevant to determine the stacking sequence. For example, varying the length of path 2 in Fig. 4a can alter the stacking sequence from $IN_rN_p$ to $I$, $IN_r$, $N_r$, $N_rN_p$, or $N_p$. Therefore the stacking diagrams are calculated at fixed sample height since the length of the path is proportional to $h$. It is worth noting that for infinitely small sample height the sedimentation path has vanishing length and it is a point in the plane of chemical potentials. Hence, the stacking diagram for $h \to 0$ coincides with the bulk phase diagram. In Fig. 4 it is apparent how the stacking diagram tend to the bulk diagram by decreasing $h$. By increasing $h$ the regions with a single layer sequence shrink in size at the expenses of the regions with multiple layer sequences that are enlarged. This reflects that the longer the path is the more likely it crosses additional binodals. To highlight the importance of the sample height, we indicate by colored circles pairs of illustrative samples with the same colloidal packing fractions but different heights in Fig. 4d and f. In all cases the stacking sequences change upon changing the sample height. For example, for packing fractions $(\bar{\eta}_r, \bar{\eta}_p) = (0.225, 0.05)$ the stacking sequence changes from $IN_p$ if $h = 5$ mm to $IN_rN_p$ if $h = 18$ mm. Therefore, the stacking sequence is not only

determined by the colloidal concentration since the occurring layers also depend on the sample height.

For this buoyant mass ratio ($s = m_p/m_r = 3$) the topologies of the stacking and the bulk diagrams are the same in the sense that there is a one-to-one correspondence between bulk regions and stacking sequences for any sample height. For example, the triple point region $I + N_p + N_r$ in Fig. 4b and the region of the stacking sequence $IN_rN_p$ in Fig. 4d, f correspond to each other, although they are different objects. Recall that bulk phases and stacking sequences differ substantially since (i) the order of the layers plays a role in the stacking diagram but not in bulk, and (ii) bulk phases are homogeneous while layers in a stacking diagram are not, see density profiles in Fig. 3. This one-to-one correspondence is not a general feature since the topology of the stacking diagram changes with the buoyant mass ratio.

**Inferring bulk behavior from sedimentation experiments**. Above we have incorporated gravity into a theoretical calculation of bulk phase behavior and compared with experimental samples. Here, we address the experimentally relevant inverse problem. van der Kooij and Lekkerkerker reported also four samples containing layers with liquid-crystalline positional order[23]. These stacking sequences, reproduced in Fig. 5a, contain plate-rich columnar ($C$) and (most likely[23]) rod-rich smectic ($X$) layers. In addition to the orientational order, in the columnar (smectic) mesophase the particles are positionally ordered along two (one) spatial directions. Complex stacking sequences with five distinct layers such as $IN_rXN_pC$ occur. The experimental particles are highly polydisperse which heavily alters the bulk transition densities of phases with positional order[49,50]. Therefore, attempting to extend the density functional to incorporate smectic and columnar phases[51,52] is not a promising route to reproduce the experimental results involving phases with positional order. Instead, we use the experimental sequences to construct the bulk binodals of phases with positional order. Roughly speaking, we disentangle the effects that gravity has on the samples to find the bulk behavior (in absence of gravity).

The slope of the paths remains unchanged and their lengths are obtained by measuring the sample height from the experimental pictures, Fig. 5a. We then construct a bulk phase diagram, see Fig. 5b, with the approximated location of two new binodals, $N_p - C$ and $N_r - X$. We assume the simplest form for the binodals, i.e., horizontal or vertical lines, which is justified since (i) the binodals connect pure transitions in the monocomponent systems to other binodals and (ii) at high density the mixture is expected to be completely segregated. Then, we find the binodal location in the bulk phase diagram together with the position of the sedimentation paths such that both the experimental stacking sequences and the thicknesses of the individual layers are best reproduced. The resulting theoretical stacking sequences are depicted in Fig. 5a for direct comparison with the experiments. All the experimental sequences are reproduced and we can infer the topology of the bulk phase diagram from the given set of sedimentation experiments. Note that any change in the bulk topology (e.g., interchanging the position of the predicted $N_r - N_p - X$ and $N_p - X - C$ triple points) produces a different set of stacking sequences. The thicknesses of the individual layers can be also reproduced quantitatively in most cases. Small deviations occur, especially if the sedimentation path is close to a bulk triple point, due to the simple approximation we use for the binodals. Near triple points the curvatures of the binodals can be large, c.f. the $I - N_p - N_r$ triple point in Fig. 5b, and a straight line is a crude approximation. Nevertheless, with a larger number of samples it might be possible to reproduce the curvature of the bulk binodals and gain further insight into the phase transition.

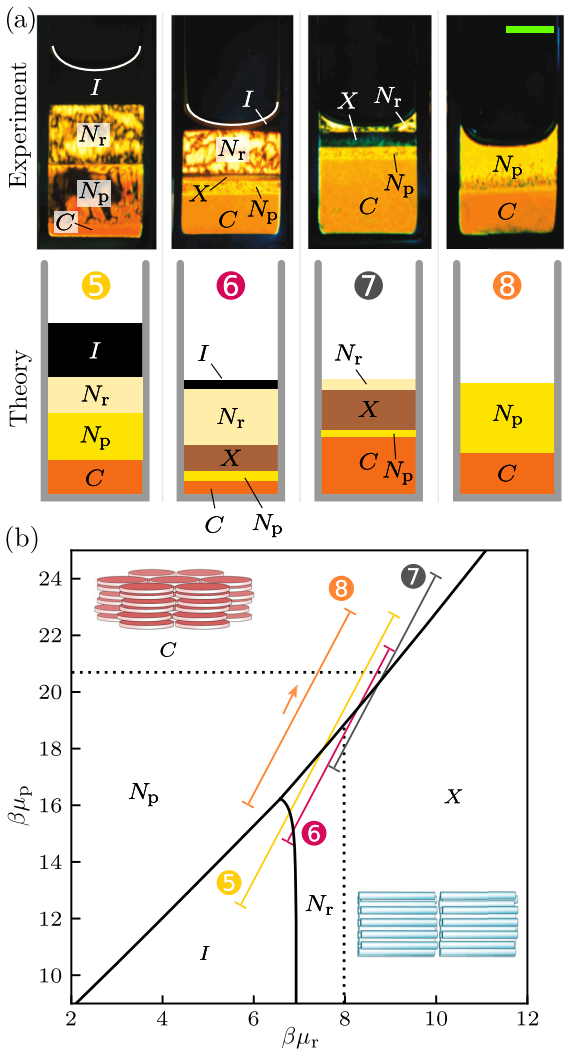


**Fig. 5 Positionally ordered phases. a** Experimental samples and corresponding theoretical predictions of sequences containing isotropic ($I$), nematic plate-rich ($N_p$), and nematic rod-rich ($N_r$) fluid layers as well as layers with positional order: $C$ (columnar plate-rich) and $X$ (smectic rod-rich). The white line indicates the position of the meniscus. The photographs of the experimental samples (adapted with permission[23], Copyright 2000 American Chemical Society) were taken from crossed polarizers. The scale bar (green) is 5 mm. **b** Bulk phase diagram in the plane of chemical potential of rods $\mu_r$ and plates $\mu_p$ for the region next to the triple point. The chemical potentials are scaled with the inverse temperature $\beta = 1/(k_BT)$. Solid lines are the binodals involving isotropic and nematic phases obtained with density functional theory. Dotted lines are the inferred location of the $N_p - C$ (horizontal line) and $N_r - X$ binodals. Schematics of particle arrangement in the $C$ and $X$ phases are shown. The sedimentation paths correspond to the samples shown in (a). The orange arrow in sample 8 indicates the direction of the paths from top to bottom.

Note that the curvature of a binodal in the $\mu_r - \mu_p$ plane is given by the ratio between the density jumps of each species at the phase transition.

Isotropic and columnar phases do not coexist in bulk, Fig. 5b. However, in samples 5 and 6 in Fig. 5a (sequences

$IN_rN_pC$ and $IN_rXN_pC$, respectively) both an isotropic and a (non-adjacent) columnar layer are present. This illustrates that simultaneously occurring layers in a stacking sequence do not need to imply bulk coexistence between the respective phases.

**Changing the buoyant mass ratio**. The topologies of the bulk and the stacking diagrams in Fig. 4b and d are the same (there is a one-to-one correspondence between bulk regions and stacking sequences) for the particular value of the buoyant mass ratio $s = m_p/m_r = 3$. Changing the buoyant mass ratio does not alter the bulk phase diagram but it can modify the topology of the stacking diagram. A change in the buoyant masses can be achieved experimentally by changing the material (inner core[53], coating[54]) of the colloidal particles, and also by changing the solvent density.

To illustrate the effect of changing the buoyant mass ratio, we calculate first the stacking diagram for the idealized case of samples with infinite height[21]. In this limit a sedimentation path is a straight line (not a segment) that can be described with two variables: slope $s$ and intercept $a$ in Eq. (3). A stacking diagram in the $s-a$ plane can be calculated, see Fig. 6a, by locating the paths that form the boundaries between different stacking sequences[21]. These are: paths tangent to bulk binodals, paths that cross triple points, and paths that are parallel to the binodals in the limits $\mu_i \to \pm\infty$. The stacking sequences for finite samples are then given by those in the infinite sample height limit and also by their subsequences formed by removing layers at the top/bottom of the sequence. It becomes apparent from the case of infinite height that the precise value of $s$ is not critical in the sense that it is possible to vary $s$ in a certain range without altering the sequences qualitatively. For example, no qualitative change occurs for buoyant mass ratios $s \gtrsim 2$, see Fig. 6a. This is particularly relevant considering that due to the experimental uncertainties[22], we estimate that the buoyant mass ratio lies within the confidence interval $s \in [2, 5]$ (see Supplementary Fig. 1).

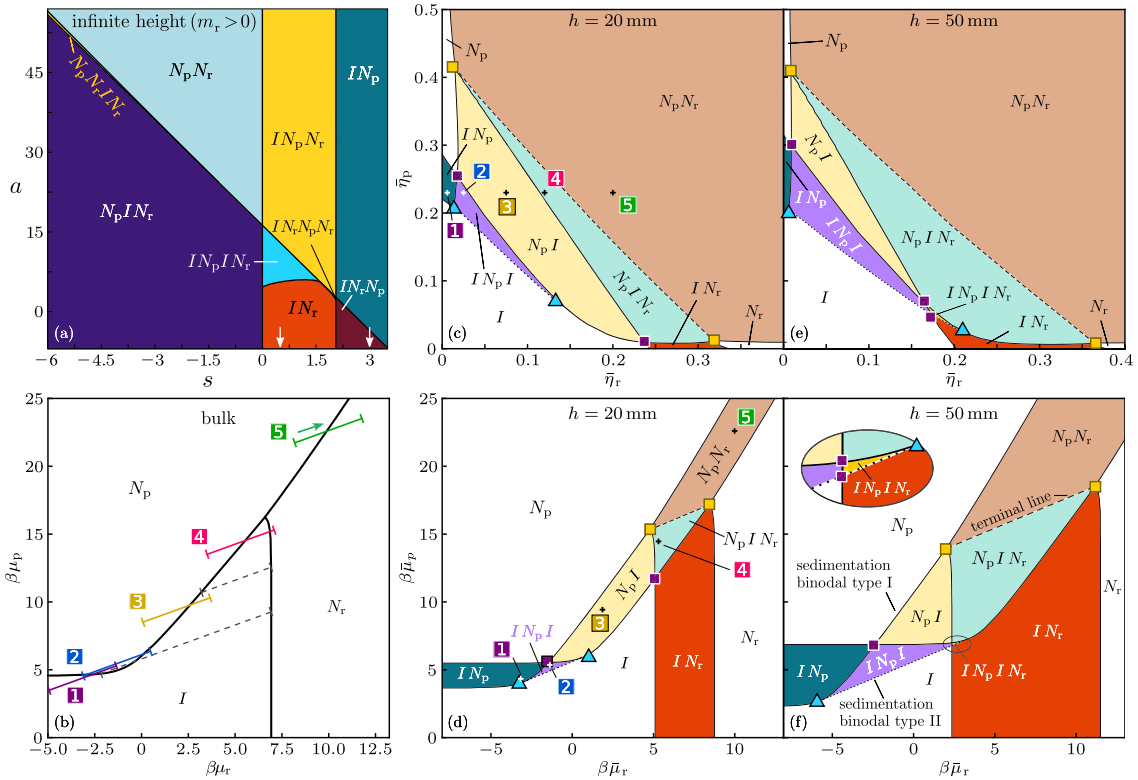


**Fig. 6 Changing the buoyant mass ratio. a** Stacking diagram for samples in the limit of infinite height and positive buoyant mass of rods ($m_r > 0$) in the plane of slope $s = m_p/m_r$ and intercept $a$ of the sedimentation paths. Each region represents a sequence, labeled from top to bottom (the reverse sequences appear if $m_r < 0$). The white arrows highlight the slopes $s = 0.5$ and 3 used here. Bulk phase diagram if the plane of chemical potential of rods $\mu_r$ and plates $\mu_p$ (**b**) with the paths of samples 1 to 5 with $s = 0.5$ and height $h = 20$ mm (solid lines). The chemical potentials are scaled with the inverse temperature $\beta = 1/(k_BT)$. The stable phases are isotropic ($I$), nematic rod-rich ($N_r$), and nematic plate-rich ($N_p$). The green arrow in sample 5 indicates the direction of all paths from top to bottom. Stacking diagrams for heights $h = 20$ mm (**c**, **d**) and 50 mm (**d**, **e**) in the plane of average packing fractions of rods $\bar{\eta}_r$ and plates $\bar{\eta}_p$ (**c**, **e**) and average chemical potentials of rods $\beta\bar{\mu}_r$ and plates $\beta\bar{\mu}_p$ (**d**, **f**). Black solid lines are sedimentation binodals of type I (paths that either end or start at a binodal), black-dashed lines are terminal lines (paths crossing the triple point), and black-dotted lines are sedimentation binodals of type II (paths tangent to binodals). Each sequence is denoted from top to bottom and colored differently (except for the white regions that represent sequences with only one layer). The inset in (**f**) is a close view of a small region. The samples 1 to 5 in (**b**) are also shown in (**c**) and (**d**), as indicated. The blue triangles indicate points at which three stacking sequences meet due to the bifurcation of a sedimentation binodal of type II from one of type I. The colored squares in panels (**c**, **d**, **e**, **f**) indicate the points at which four stacking sequences meet due to the crossing between two sedimentation binodals (violet squares) or the intersection of sedimentation binodals and a terminal line (yellow squares). Two sedimentation binodals cross (violet squares) whenever a sedimentation path in bulk simultaneously start and end at a binodal, as illustrated by two gray-dashed paths in (**b**).

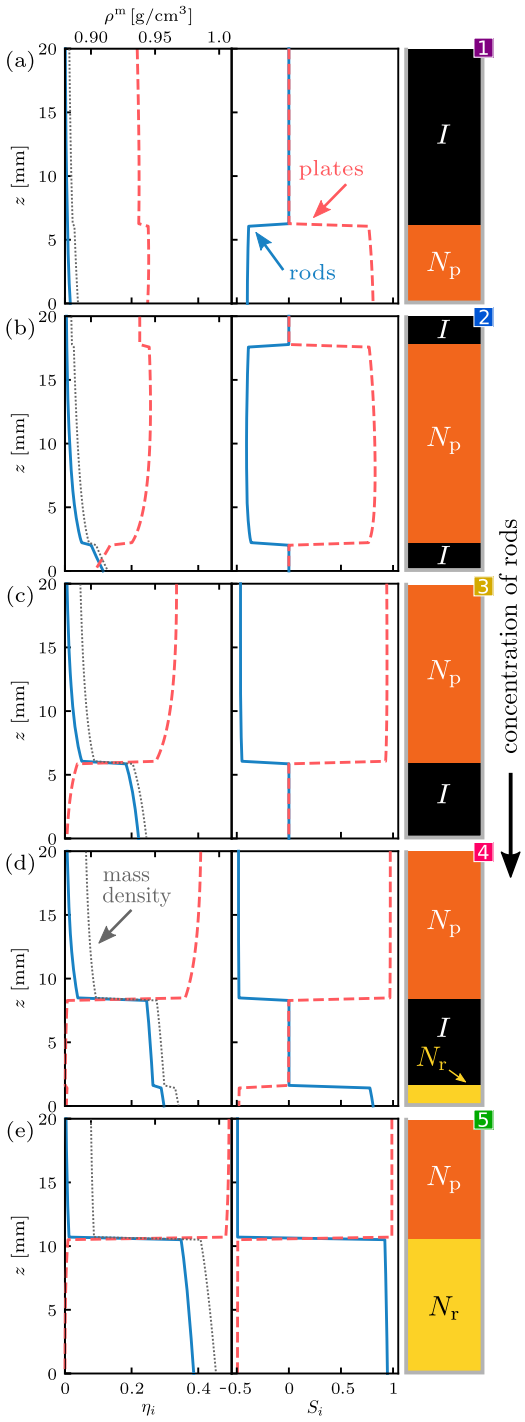


**Fig. 7 Changing the concentration of rods.** Packing fraction $\eta_i$ ($i = r, p$ for rods and plates, respectively) and total mass density $\rho^m$ profiles, uniaxial order parameter $S_i$, $i = r, p$ profiles, and schematics as a function of the vertical coordinate $z$ for samples of height $h = 20$ mm, fixed concentration of plates $\bar{\eta}_p = 0.23$ and varying concentration of rods $\bar{\eta}_r = 0.006$ (**a**), 0.025 (**b**), 0.075 (**c**), 0.12 (**d**), and 0.20 (**e**). The slope of the sedimentation path is $s = 0.5$. The corresponding sedimentation paths are depicted in Fig. 6b. The samples are also marked in the stacking diagrams of Fig. 6c, d using the same labels as here (colored squares with a number from 1 to 5).

The value $s = m_p/m_r = 1$ corresponds to the equality of buoyant masses of plates and rods and hence delimits which species is heavier: rods ($s < 1$) or plates ($s > 1$). Interestingly, the stacking diagram for infinite height, Fig. 6a, reveals that which species is the heavier does not play a decisive role since no qualitative change occurs at $s = 1$.

A buoyant mass ratio in the interval $s \in [0, 1.75]$ produces richer phenomenology than $s = 3$ (three vs. two distinct stacking sequences). We select a value in that interval, $s = 0.5$, and calculate the experimentally relevant stacking diagrams for finite height. Selected paths with slope $s = 0.5$ are represented in Fig. 6b. The paths correspond to a suspension in toluene of the same rods as before but lighter plates with gravitational length $\xi_p = 11$ mm. The slope is such that there are paths tangent to the $I - N_p$ bulk binodal. Those paths create a new boundary in the stacking diagram that increases significantly the number of stacking sequences. We show stacking diagrams in Fig. 6c, d for samples with $h = 20$ mm and in Fig. 6e, f for samples with $h = 50$ mm. Both cases are much richer than the stacking diagrams for $s = 3.0$, cf. Fig. 4. The one-to-one correspondence between bulk regions, Fig. 4b, and stacking sequences, Fig. 6c, e, is lost, emphasizing that bulk and stacking diagrams are fundamentally different objects.

Moreover, the topology of the stacking diagram changes by increasing the sample height due to the occurrence of the complex stacking sequence $IN_pIN_r$ in samples with $h = 50$ mm, Fig. 6e, f. Such a four-layer sequence only occurs for significantly long paths. The path needs to cross the bulk $I - N_p$ binodal twice (only possible if $s \in [0, 1.64]$) and the $I - N_r$ binodal, see the bulk diagram in Fig. 6b. This gives a lower limit of $h \gtrsim 48$ mm for the occurrence of the four-layer sequence if $s = 0.5$. The topological change of the stacking diagram is driven by a change in the sample height. The complex sequence $IN_pIN_r$ illustrates that the same phase ($I$) can reenter the sequence[25] even though there is no $I - I$ demixing in bulk. Instead, the path crosses the $I - N_p$ binodal twice.

**Parametric study of stacking sequences and different representations of the stacking diagram**. We investigate five selected samples with the same height, $h = 20$ mm, and packing fraction of plates, $\bar{\eta}_p = 0.23$, but different packing fraction of rods. Their paths are depicted in Fig. 6b and the corresponding state points in the stacking diagram are indicated in Fig. 6c, d. The density and uniaxial profiles are shown in Fig. 7 together with schematics of the stacking sequences.

By increasing $\bar{\eta}_r$ we observe five different stacking sequences $IN_p$, $IN_pI$, $N_pI$, $N_pIN_r$ and $N_pN_r$. These sequences include the formation of bottom isotropic layers, Fig. 7a, b, a floating isotropic layer between two nematic layers, Fig. 7d, and a floating nematic between two isotropic layers, Fig. 7b. The inversion of the sequence $IN_p$ to $N_pI$, see Fig. 7a, c, also occurs by increasing $\bar{\eta}_r$. Such inversion was experimentally observed in a polydisperse suspension of plates[55] by changing the colloidal concentration, and attributed to a pronounced fractionation with respect to plate thickness. The total colloidal packing fraction (or number density) in the isotropic layers is always smaller than it is in the nematic layers, see the density profiles of Fig. 7. However, depending on the bulk region covered by the path, the mass

density can be greater in the isotropic layer than in the nematic layer which facilitates the occurrence of bottom isotropic layers. In all cases the total mass density (see Methods) increases monotonically towards the bottom of the sample, see Fig. 7.

A detailed investigation of this complex evolution of sequences can be performed with a representation of the stacking diagram in the plane of packing fraction of rods and vertical coordinate, see Fig. 8a. The diagram indicates the occurrent layer at a given vertical position and concentration of rods. Both the height $h = 20$ mm and the plate concentration $\eta_p = 0.23$ are fixed. Figure 8a shows the introduction of the bottom isotropic layer closely followed by the elimination of the top isotropic layer by increasing $\bar{\eta}_r$. Then, an $N_r$ layer is introduced which eventually replaces the $I$ layer at the bottom entirely. At high packing fraction of rods, only nematic layers appear and the thickness of the $N_r$ layer increases by increasing $\bar{\eta}_r$, as expected.

The stacking diagram in the plane of sample height and vertical coordinate at fixed concentrations, $\bar{\eta}_r \approx 0.18$ and $\bar{\eta}_p \approx 0.05$, is shown in Fig. 8b. This stacking diagram is relevant for experimental realizations since it represents the creation of several samples that differ only in the sample height. For $h = 47$ mm we observe the sequence $N_pI$ which upon increasing $h$ transforms first into a floating isotropic $N_pIN_r$, followed by the four-layer sequence $IN_pIN_r$. Finally at $h = 53.7$ mm the two isotropic layers merge into a single layer due to the elimination of the $N_p$ layer, which gives rise to the sequence $IN_r$. See schematics of the evolution in Fig. 8c. Such complex behavior involving four different sequences is observed by varying the sample height only by 17%, from 47 mm to 55 mm. Interestingly, in the $h - z$ plane, Fig. 8b, the lower $I - N_p$ boundary is parallel to the top sample-air boundary, whereas the upper $I - N_p$ boundary is horizontal.

It is worth pointing out that varying the sample height at fixed concentrations not only changes the length of the sedimentation path but also its position in the $\mu_r - \mu_p$ plane. This change gives rise to the observed nontrivial dependence of the stacking sequence on the sample height.

## Discussion

To demonstrate the validity of the concept of sedimentation paths[21] we have studied sedimentation-diffusion-equilibrium of a colloidal plate-rod mixture and found excellent quantitative agreement with the well-known experiments conducted by van der Kooij and Lekkerkerker[22,23]. We have shown how to systematically analyze and interpret the stacking sequences observed experimentally, group these sequences in a stacking diagram, and predict the stacking diagram from the bulk phase diagram of the system. Moreover, we have also shown how to infer the bulk phase behavior of the mixture from the experimental results under gravity and have also predicted both a different set of stacking sequences and a complex evolution of the sequences by simply changing the height of the samples. All predictions can be verified experimentally by altering the buoyant masses of the particles and systematically varying the height of the samples.

Some gravity-induced effects, like the formation of a sequence with five layers, were attributed to polydispersity[22] since the occurrence of more than three layers was understood as an apparent violation of the Gibbs phase rule. However, due to gravity it can only be guaranteed that any two consecutive layers that share an interface in the sample coexist in bulk. Hence, as pointed out in other works[21,40], the occurrence of say five layers in a stacking sequence does not imply the existence of a quintuple point in the bulk phase diagram. Such multi-phase bulk coexisting points can exist in binary mixtures[56,57] for specific interparticle interactions but are unrelated to the occurrence of several layers in sedimentation.

Even though polydispersity is almost unavoidable in experiments, our theory reproduces here the observed stacking sequences semi-quantitatively. Adding polydispersity to sedimentation path theory is, in principle, possible provided that the theoretical description of the bulk also incorporates polydispersity, e.g., via a distribution of particle sizes[49,58].

Our results indicate a nontrivial dependence of the stacking sequences on the sample height. Controlling and varying the sample height is, in principle, simple in experimental realizations and it opens a route to find interesting phenomenology and gain insight into the bulk phase behavior. Analytical ultracentrifugation[59], in which centrifugal forces change the strength of gravity, can be also described with our theory. Changing the strength of gravity is an alternative method to vary the length of the sedimentation path leaving the buoyant mass ratio unaltered.

The topology of the stacking diagrams can change with the buoyant mass ratio. However no qualitative change occurs here around a buoyant mass ratio $s$ of unity (which delimits which species is the heavier). This is likely the case in other asymmetric

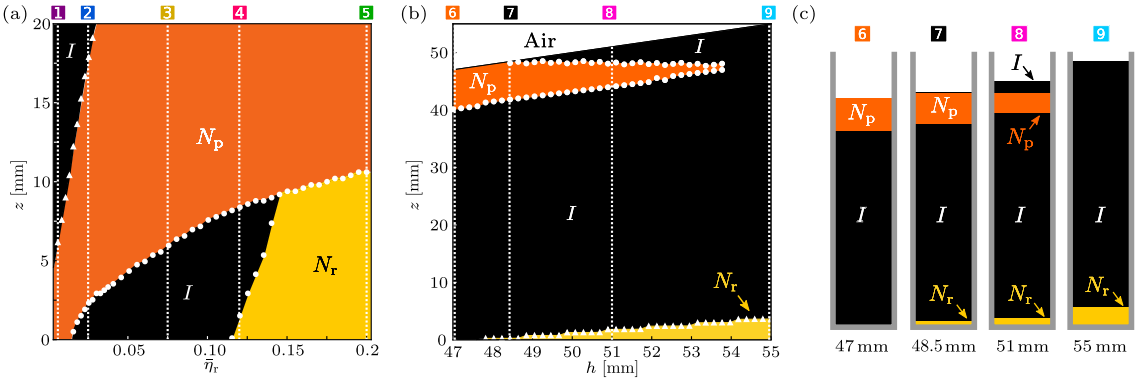


**Fig. 8 Effect of sample height. a** Stable layer at elevation $z$ as a function of the packing fraction of rods $\bar{\eta}_r$ for samples with fixed height $h = 20$ mm and packing fraction of plates $\bar{\eta}_p = 0.23$. **b** Stable layer at elevation $z$ as a function of the total sample height $h$ for samples with fixed concentrations $(\bar{\eta}_r, \bar{\eta}_p) = (0.177, 0.051)$. The vertical dotted white lines indicate the position in the diagrams of selected samples, labeled by colored squares. **c** Schematics of four selected samples of different heights but identical colloidal concentrations that develop qualitatively different stacking sequences. The layers are isotropic ($I$), nematic plate-rich ($N_p$), and nematic rod-rich ($N_r$).

mixtures. Symmetric mixtures are a special case where $s = 1$ can play a special role.

The stacking diagram admits several representations. We have shown two experimentally relevant representations in the plane of vertical interface position between layers, $z$, and either average packing fraction, $\bar{\eta}$, or the overall sample height, $h$. Although these axes are motivated by sedimentation experiments, the $z - h$ plane can be also conceived as a transformation of the bulk phase diagram in the plane of chemical potentials: The vertical position is a linear parameterization of the chemical potential, Eq. (2), and the change in overall height moves nontrivially the path in the plane of chemical potentials implicitly via the constraint of fixed average packing fractions. The inversion of this non-linear integral relationship between average chemical potentials, i.e., the position of the sedimentation path, and the average packing fraction might be another route to obtain the bulk phase diagram from sedimentation experiments.

We expect similar gravity-induced phenomena to occur in other types of mixtures over length scales of a few centimeters provided that the size of at least one species is of the order of 100 nm or larger and there is a significant density difference between the solvent and the particles. For colloidal particles of a few nanometer and micro-emulsions, gravitational effects will be apparent at lengths scales comparable to the gravitational length, which can be of the order of meters. Gravity-induced density gradients also occur in sufficiently large molecular systems and can be also described with sedimentation path theory.

The sedimentation path theory excludes surface effects that occur at the interfaces between two layers and also between the suspension and the bottom/top of the cuvette. Surface effects can be incorporated via a full, spatially resolved, density functional minimization of the inhomogeneous mixture in a gravitational field (see Methods) and might introduce small changes in the position of the boundary lines in the stacking diagram.

The sedimentation path theory and the methodology presented here are general and constitute the basis for carrying out and interpreting sedimentation experiments on both colloid-colloid and polymer-colloid mixtures[60]. Carrying out new experiments to investigate the role of the sample height and that of the buoyant mass ratio would be particularly valuable and enlightening.

## Methods

**Bulk phase behavior**. We use classical density functional theory (DFT)[61] to obtain the bulk phase diagram of the plate-rod mixture. The total free energy $F$ is the sum of the ideal and the excess part ($F = F^{\mathrm{id}} + F^{\mathrm{exc}}$). The ideal contribution to the intrinsic Helmholtz free energy at temperature $T$ for a mixture is given exactly by

$$\beta F^{\mathrm{id}} = \sum_i \int \mathrm{d}\mathbf{r} \int \mathrm{d}\boldsymbol{\omega} \rho_i(\mathbf{r}, \boldsymbol{\omega}) \left[\ln\left(\rho_i(\mathbf{r}, \boldsymbol{\omega})\Lambda_i^3\right) - 1\right], \tag{4}$$

where $\beta = 1/(k_{\mathrm{B}}T)$ with Boltzmann's constant $k_{\mathrm{B}}$, the sum runs over both species, $\Lambda_i$ is the thermal wavelength of species $i = \mathrm{r}, \mathrm{p}$, and $\rho_i(\mathbf{r}, \boldsymbol{\omega})$ is the one-body density profile of species $i$ at position $\mathbf{r}$ and orientation specified by the unit vector $\boldsymbol{\omega}$. Since we consider only phases without positional order we average out all positions $\mathbf{r}$ and introduce the angular distribution function $\psi_i$ of species $i$ via $\rho_i(\mathbf{r}, \boldsymbol{\omega}) = \rho_i \psi_i(\boldsymbol{\omega})$ and normalization $\int \mathrm{d}\boldsymbol{\omega} \psi_i(\boldsymbol{\omega}) = 1$. Hence, $\rho_i$ is the number density of species $i$ and we obtain

$$\frac{\beta F^{\mathrm{id}}}{N} = \sum_i x_i \int \mathrm{d}\boldsymbol{\omega} \psi_i(\boldsymbol{\omega}) \left[\ln\left(\psi_i(\boldsymbol{\omega})\rho_i\Lambda_i^3\right) - 1\right], \tag{5}$$

where $N$ is the total number of particles in the system and $x_i$ is the composition of species $i$.

We use an extended Onsager approximation for the excess (over ideal) contribution to the free energy

$$\frac{\beta F^{\mathrm{exc}}}{N} = \Psi(\eta)\rho \sum_{i,j} x_i x_j \int \mathrm{d}\boldsymbol{\omega} \int \mathrm{d}\boldsymbol{\omega}' \psi_i(\boldsymbol{\omega})\psi_j(\boldsymbol{\omega}') V_{ij}^{\mathrm{ex}}(\boldsymbol{\omega}, \boldsymbol{\omega}'), \tag{6}$$

with total density $\rho = \sum_i \rho_i$ and $V_{ij}^{\mathrm{ex}}(\boldsymbol{\omega}, \boldsymbol{\omega}')$ being the excluded volume (i.e., the volume inaccessible to one particle due to the presence of another particle) between particles of species $i$ and $j$ with orientations $\boldsymbol{\omega}$ and $\boldsymbol{\omega}'$, respectively. Both rods and plates are modeled as hard cylinders (see Fig. 1) for which analytical expressions for the excluded volume exists[62,63]. To speed up the computation, the azimuthal angle $\varphi$ of both species is averaged over in advance and only the polar dependence, $V_{ij}^{\mathrm{ex}}(\theta, \theta')$, is retained. Accordingly, we consider only the polar dependence of the angular distribution function $\int_0^{2\pi} d\varphi \psi_i(\boldsymbol{\omega}) = 2\pi\psi_i(\theta)$. This prevents the study of biaxial phases that, on the other hand, are not stable for the particle aspect ratios considered here[64] and are also not observed in the experiments[22,23].

Following Parsons[65] and Lee[66], we replace the prefactor 1/2 in front of the second virial coefficient in Onsager's original expression[62] by

$$\Psi(\eta) = \frac{4 - 3\eta}{8(1 - \eta)^2}, \tag{7}$$

in Eq. (6), which corresponds to the excess free energy per particle of a system of hard spheres according to the Carnahan-Starling equation of state[67]. Here $\eta = \rho \sum_i x_i v_i = \sum_i \eta_i$ is the total packing fraction across all species with $v_i$ being the particle volume of species $i$. The scaling, Eq. (7), does not alter the topology of the phase diagram and serves to improve substantially the agreement of the transition densities compared to computer simulations[64]. In the low density limit ($\eta \to 0$) the original Onsager expression, based on the second virial coefficient, is recovered since $\Psi(\eta \to 0) = 1/2$.

**Minimization**. We perform a free minimization of the functional discretizing $\psi_i(\theta)$ on a one dimensional grid with 160 bins and calculate the uniaxial order parameter of species $i$ according to

$$S_i = \int \mathrm{d}\theta \frac{3\cos^2(\theta) - 1}{2} \psi_i(\theta), \tag{8}$$

where the angle $\theta$ is measured with respect to the director of one of the species.

**Bulk coexistence**. The bulk phase diagram is obtained via numerical minimization of the Gibbs free energy per particle

$$g_{\mathrm{b}} = \frac{F}{N} + \frac{P}{\rho}, \tag{9}$$

where $P$ is the osmotic pressure and the total number density is $\rho = \rho_{\mathrm{r}} + \rho_{\mathrm{p}}$ with $\rho_i$ the number density of species $i = \mathrm{r}, \mathrm{p}$. Mechanical and thermal phase equilibria are fulfilled in the Gibbs ensemble by construction ($P$ and $T$ are fixed). To find chemical equilibrium and hence phase coexistence we search for a common-tangent construction on $g_{\mathrm{b}}(x_{\mathrm{r}})$, with $x_i = \rho_i/\rho$ the composition of species $i$. The common tangent is equivalent to the equality of chemical potentials of both species in the coexisting phases since $g_{\mathrm{b}} = \mu_{\mathrm{r}} x_{\mathrm{r}} + \mu_{\mathrm{p}} x_{\mathrm{p}}$, with $\mu_i$ the chemical potential species $i$. Hence, for fixed values of $P$, $T$, and $x_{\mathrm{r}}$ (which also fixes $x_{\mathrm{p}}$ since $x_{\mathrm{p}} = 1 - x_{\mathrm{r}}$), we numerically minimize the Gibbs free energy per particle with respect to the total density and the orientational distribution functions of both species and then search for a common tangent.

**Average packing fractions along a path**. To obtain $\eta_i$ along a sedimentation path we minimize the grand canonical potential $\Omega$ per unit of volume

$$\frac{\Omega}{V} = \frac{F}{V} - \rho \sum_i \mu_i x_i, \tag{10}$$

at fixed chemical potentials, $\mu_i$, with respect to the variables $\psi_i$, $x_i$ and $\rho$.

Given the coordinates $\bar{\mu}_i$ of a path, it is straight forward to obtain the corresponding $\bar{\eta}_i$. The opposite procedure, which we use to find the paths that correspond to the experimental samples in Fig. 3, is however involved. Provided with the average packing fractions of a given sample, $\bar{\eta}_i$ we numerically solve a set of non-linear equations to find the corresponding sedimentation path in the plane of chemical potentials.

**Full minimization of the grand potential**. As an alternative to the sedimentation path theory, it would be possible find the solution to the full inhomogeneous system by minimizing the grand potential functional

$$\Omega[\{\rho_i\}] = F[\{\rho_i\}] - \sum_i \int \mathrm{d}\mathbf{r} \int \mathrm{d}\boldsymbol{\omega} \rho_i(\mathbf{r}, \boldsymbol{\omega})(V_i^{\mathrm{ext}}(\mathbf{r}, \boldsymbol{\omega}) - \mu_i), \tag{11}$$

with respect to the density profiles of both species $\rho_p(\mathbf{r}, \boldsymbol{\omega})$ and $\rho_r(\mathbf{r}, \boldsymbol{\omega})$. Here, $F[\{\rho_i\}]$ is the intrinsic free energy functional of the inhomogeneous system. For a gravitational field, the external field is simply $V_i^{\mathrm{ext}} = m_i g z$.

Within the sedimentation path theory, instead of minimizing Eq. (11), we minimize at each value of $z$ along the sedimentation path a corresponding bulk system, Eq. (10), with a height dependent chemical potential given by Eq. (2). The linear dependence of the local chemical potential with the vertical coordinate, Eq. (2), is a direct consequence of the linear dependency of the external potential on $z$. Note, however, that the dependence of the local chemical potentials on other variables such as the composition is more complex since it ultimately depends on the interparticle interactions via the free energy $F$.

**Total mass density**. The total mass density profile, $\rho^{m}(z)$ is the sum of the mass density of each species plus the density of the solvent. Using the buoyant masses $m_i$, the total mass density is simply[68]

$$\rho^{m}(z) = \sum_i m_i \rho_i(z) + \rho_s, \quad (12)$$

where $\rho_i(z)$ is the number density of species $i$ at position $z$ and $\rho_s$ is the mass density of the solvent.

## Data availability

All the data supporting the findings are available from the corresponding author upon reasonable request.

Received: 20 April 2021; Accepted: 10 August 2021;
Published online: 07 September 2021

## References

1. Poon, W., Pusey, P. & Lekkerkerker, H. N. W. Colloids in suspense. *Phys. World* **9**, 27–34 (1996).
2. Frenkel, D. Playing tricks with designer "atoms". *Science* **296**, 65 (2002).
3. Poon, W. Colloids as big atoms. *Science* **304**, 830 (2004).
4. Manoharan, V. N. Colloidal matter: Packing, geometry, and entropy. *Science* **349**, 1253751 (2015).
5. Wang, Y. et al. Colloids with valence and specific directional bonding. *Nature* **491**, 51 (2012).
6. Wijting, W. K., Besseling, N. A. M. & Cohen Stuart, M. A. Wetting in a colloidal liquid-gas system. *Phys. Rev. Lett.* **90**, 196101 (2003).
7. Aarts, D. G. A. L., Schmidt, M. & Lekkerkerker, H. N. W. Direct visual observation of thermal capillary waves. *Science* **304**, 847 (2004).
8. Wittmann, R., Cortes, L. B., Löwen, H. & Aarts, D. G. A. L. Particle-resolved topological defects of smectic colloidal liquid crystals in extreme confinement. *Nat. Commun.* **12**, 623 (2021).
9. Pusey, P. N. & Van Megen, W. Phase behaviour of concentrated suspensions of nearly hard colloidal spheres. *Nature* **320**, 340 (1986).
10. Hoover, W. G. & Ree, F. H. Melting transition and communal entropy for hard spheres. *J. Chem. Phys.* **49**, 3609 (1968).
11. Dogic, Z. & Fraden, S. Smectic phase in a colloidal suspension of semiflexible virus particles. *Phys. Rev. Lett.* **78**, 2417 (1997).
12. van der Kooij, F. M., Kassapidou, K. & Lekkerkerker, H. N. W. Liquid crystal phase transitions in suspensions of polydisperse plate-like particles. *Nature* **406**, 868–871 (2000).
13. Ruzicka, B. et al. Observation of empty liquids and equilibrium gels in a colloidal clay. *Nat. Mater.* **10**, 56 (2011).
14. Thorneywork, A. L., Abbott, J. L., Aarts, D. G. A. L. & Dullens, R. P. A. Two-dimensional melting of colloidal hard spheres. *Phys. Rev. Lett.* **118**, 158001 (2017).
15. Perrin, J. *Atoms* (D. Van Nostrand, New York, 1916).
16. Biben, T., Hansen, J.-P. & Barrat, J.-L. Density profiles of concentrated colloidal suspensions in sedimentation equilibrium. *J. Chem. Phys.* **98**, 7330–7344 (1993).
17. Piazza, R., Bellini, T. & Degiorgio, V. Equilibrium sedimentation profiles of screened charged colloids: A test of the hard-sphere equation of state. *Phys. Rev. Lett.* **71**, 4267–4270 (1993).
18. Savenko, S. V. & Dijkstra, M. Sedimentation and multiphase equilibria in suspensions of colloidal hard rods. *Phys. Rev. E* **70**, 051401 (2004).
19. van der Beek, D., Schilling, T. & Lekkerkerker, H. N. W. Gravity-induced liquid crystal phase transitions of colloidal platelets. *J. Chem. Phys.* **121**, 5423–5426 (2004).
20. Wensink, H. H. & Lekkerkerker, H. N. W. Sedimentation and multi-phase equilibria in mixtures of platelets and ideal polymer. *EPL* **66**, 125–131 (2004).
21. de las Heras, D. & Schmidt, M. The phase stacking diagram of colloidal mixtures under gravity. *Soft Matter* **9**, 8636–8641 (2013).
22. van der Kooij, F. M. & Lekkerkerker, H. N. W. Liquid-crystalline phase behavior of a colloidal rod-plate mixture. *Phys. Rev. Lett.* **84**, 781–784 (2000).
23. van der Kooij, F. M. & Lekkerkerker, H. N. W. Liquid-crystal phases formed in mixed suspensions of rod- and platelike colloids. *Langmuir* **16**, 10144–10149 (2000).
24. Luan, L., Li, W., Liu, S. & Sun, D. Phase behavior of mixtures of positively charged colloidal platelets and nonadsorbing polymer. *Langmuir* **25**, 6349–6356 (2009).
25. de las Heras, D. et al. Floating nematic phase in colloidal platelet-sphere mixtures. *Sci. Rep.* **2**, 789 (2012).
26. Wensink, H. H., Vroege, G. J. & Lekkerkerker, H. N. W. Isotropic-nematic phase separation in asymmetrical rod-plate mixtures. *J. Chem. Phys.* **115**, 7319–7329 (2001).
27. Woolston, P. & van Duijneveldt, J. S. Three-phase coexistence in colloidal rod–plate mixtures. *Langmuir* **31**, 9290–9295 (2015).
28. Kleshchanok, D., Meijer, J.-M., Petukhov, A. V., Portale, G. & Lekkerkerker, H. N. W. Sedimentation and depletion attraction directing glass and liquid crystal formation in aqueous platelet/sphere mixtures. *Soft Matter* **8**, 191 (2012).
29. Chen, M. et al. Observation of isotropic–isotropic demixing in colloidal platelet–sphere mixtures. *Soft Matter* **11**, 5775–5779 (2015).
30. Bakker, H. E. et al. Phase diagram of binary colloidal rod-sphere mixtures from a 3d real-space analysis of sedimentation-diffusion equilibria. *Soft Matter* **12**, 9238 (2016).
31. Bartlett, P., Ottewill, R. H. & Pusey, P. N. Freezing of binary mixtures of colloidal hard spheres. *J. Chem. Phys.* **93**, 1299 (1990).
32. Baumgartl, J., Dullens, R. P. A., Dijkstra, M., Roth, R. & Bechinger, C. Experimental observation of structural crossover in binary mixtures of colloidal hard spheres. *Phys. Rev. Lett.* **98**, 198303 (2007).
33. Nakato, T., Yamashita, Y., Mouri, E. & Kuroda, K. Multiphase coexistence and destabilization of liquid crystalline binary nanosheet colloids of titanate and clay. *Soft Matter* **10**, 3161 (2014).
34. Purdy, K. R., Varga, S., Galindo, A., Jackson, G. & Fraden, S. Nematic phase transitions in mixtures of thin and thick colloidal rods. *Phys. Rev. Lett.* **94**, 057801 (2005).
35. Mo, S., Shao, X., Chen, Y. & Cheng, Z. Increasing entropy for colloidal stabilization. *Sci. Rep.* **6**, 36836 (2016).
36. Royall, C. P., Dzubiella, J., Schmidt, M. & van Blaaderen, A. Nonequilibrium sedimentation of colloids on the particle scale. *Phys. Rev. Lett.* **98**, 188304 (2007).
37. Fortini, A. et al. Dynamic stratification in drying films of colloidal mixtures. *Phys. Rev. Lett.* **116**, 118301 (2016).
38. Piazza, R., Buzzaccaro, S., Secchi, E. & Parola, A. What buoyancy really is. a generalized Archimedes' principle for sedimentation and ultracentrifugation. *Soft Matter* **8**, 7112–7115 (2012).
39. Piazza, R., Buzzaccaro, S., Secchi, E. & Parola, A. On the general concept of buoyancy in sedimentation and ultracentrifugation. *Phys. Biol.* **10**, 045005 (2013).
40. Drwenski, T., Hooijer, P. & van Roij, R. Sedimentation stacking diagrams of binary mixtures of thick and thin hard rods. *Soft Matter* **12**, 5684 (2016).
41. Geigenfeind, T. & de las Heras, D. The role of sample height in the stacking diagram of colloidal mixtures under gravity. *J. Phys. Condens. Matter* **29**, 064006 (2016).
42. Avvisati, G., Dasgupta, T. & Dijkstra, M. Fabrication of colloidal laves phases via hard tetramers and hard spheres: Bulk phase diagram and sedimentation behavior. *ACS Nano* **11**, 7702 (2017).
43. van der Kooij, F. M., Vogel, M. & Lekkerkerker, H. N. W. Phase behavior of a mixture of platelike colloids and nonadsorbing polymer. *Phys. Rev. E* **62**, 5397–5402 (2000).
44. van der Kooij, F. M., Boek, E. S. & Philipse, A. P. Rheology of dilute suspensions of hard platelike colloids. *J. Colloid Interface Sci.* **235**, 344–349 (2001).
45. Roth, R. Fundamental measure theory for hard-sphere mixtures: a review. *J. Phys. Condens. Matter* **22**, 063102 (2010).
46. Veerman, J. A. C. & Frenkel, D. Relative stability of columnar and crystalline phases in a system of parallel hard spherocylinders. *Phys. Rev. A* **43**, 4334–4343 (1991).
47. Bolhuis, P. & Frenkel, D. Tracing the phase boundaries of hard spherocylinders. *J. Chem. Phys.* **106**, 666–687 (1997).
48. Veerman, J. A. C. & Frenkel, D. Phase behavior of disklike hard-core mesogens. *Phys. Rev. A* **45**, 5632–5648 (1992).
49. Sun, D., Sue, H.-J., Cheng, Z., Martínez-Ratón, Y. & Velasco, E. Stable smectic phase in suspensions of polydisperse colloidal platelets with identical thickness. *Phys. Rev. E* **80**, 041704 (2009).
50. Martínez-Ratón, Y. & Cuesta, J. A. Enhancement by polydispersity of the biaxial nematic phase in a mixture of hard rods and plates. *Phys. Rev. Lett.* **89**, 185701 (2002).
51. Somoza, A. M. & Tarazona, P. Nematic and smectic liquid crystals of hard spherocylinders. *Phys. Rev. A* **41**, 965–970 (1990).
52. Cinacchi, G., Mederos, L. & Velasco, E. Liquid–crystal phase diagrams of binary mixtures of hard spherocylinders. *J. Chem. Phys.* **121**, 3854–3863 (2004).
53. Velikov, K. P. & van Blaaderen, A. Synthesis and characterization of monodisperse core-shell colloidal spheres of zinc sulfide and silica. *Langmuir* **17**, 4779 (2001).
54. Graf, C., Vossen, D. L. J., Imhof, A. & van Blaaderen, A. A general method to coat colloidal particles with silica. *Langmuir* **19**, 6693–6700 (2003).
55. van der Kooij, F. M., van der Beek, D. & Lekkerkerker, H. N. W. Isotropic–nematic phase separation in suspensions of polydisperse colloidal platelets. *J. Phys. Chem. B* **105**, 1696 (2001).
56. Álvaro, G. G. et al. Depletion-driven four-phase coexistences in discotic systems. *Mol. Phys.* **116**, 2757 (2018).

57. Peters, V. F. D., Vis, M., García, A. G., Wensink, H. H. & Tuinier, R. Defying the gibbs phase rule: Evidence for an entropy-driven quintuple point in colloid-polymer mixtures. *Phys. Rev. Lett.* **125**, 127803 (2020).
58. Clarke, N., Cuesta, J. A., Sear, R., Sollich, P. & Speranza, A. Phase equilibria in the polydisperse Zwanzig model of hard rods. *J. Chem. Phys.* **113**, 5817–5829 (2000).
59. Planken, K. L. & Cölfen, H. Analytical ultracentrifugation of colloids. *Nanoscale* **2**, 1849 (2010).
60. Lekkerkerker, H. N. W. & Tuinier, R. *Depletion Interaction* (pp. 57–108. Springer Netherlands, Dordrecht, 2011).
61. Evans, R. The nature of the liquid-vapour interface and other topics in the statistical mechanics of non-uniform, classical fluids. *Adv. Phys.* **28**, 143 (1979).
62. Onsager, L. The effects of shape on the interaction of colloidal particles. *Ann. N. Y. Acad. Sci.* **51**, 627 (1949).
63. Mulder, B. M. The excluded volume of hard sphero-zonotopes. *Mol. Phys.* **103**, 1411–1424 (2005).
64. Varga, S., Galindo, A. & Jackson, G. Global fluid phase behavior in binary mixtures of rodlike and platelike molecules. *J. Chem. Phys.* **117**, 7207–7221 (2002).
65. Parsons, J. D. Nematic ordering in a system of rods. *Phys. Rev. A* **19**, 1225–1230 (1979).
66. Lee, S. A numerical investigation of nematic ordering based on a simple hard-rod model. *J. Chem. Phys.* **87**, 4972–4974 (1987).
67. Carnahan, N. F. & Starling, K. E. Equation of state for nonattracting rigid spheres. *J. Chem. Phys.* **51**, 635–636 (1969).
68. Piazza, R. Settled and unsettled issues in particle settling. *Rep. Prog. Phys.* **77**, 056602 (2014).


## Acknowledgements

This work is supported by the German Research Foundation (DFG) via project number 436306241.

## Author contributions

T.E. carried out the calculations. T.E., M.S., and D.d.l.H. conceived and designed the concept, and wrote the manuscript.

## Funding

Open Access funding enabled and organized by Projekt DEAL.

## Competing interests

The authors declare no competing interests.

## Additional information

**Supplementary information** The online version contains supplementary material available at https://doi.org/10.1038/s42005-021-00706-0.

**Correspondence** and requests for materials should be addressed to M.S. or D.d.l H.

**Peer review information** *Communications Physics* thanks the anonymous reviewers for their contribution to the peer review of this work. Peer reviewer reports are available.

**Reprints and permission information** is available at http://www.nature.com/reprints

**Publisher's note** Springer Nature remains neutral with regard to jurisdictional claims in published maps and institutional affiliations.

# Supplementary information
# Gravity-induced phase phenomena in plate-rod colloidal mixtures

Tobias Eckert,[1] Matthias Schmidt,[1] and Daniel de las Heras[1]

[1] *Theoretische Physik II, Physikalisches Institut, Universität Bayreuth, D-95440 Bayreuth, Germany*

## I. SUPPLEMENTARY NOTE 1: BIFURCATION OF STACKING SEQUENCES

We discuss here the analogue to thermodynamic bulk coexistence for the stacking diagram. Two phases coexist in bulk along a binodal line and three phases coexist at a triple point. Fine tuning the interparticle potential, e.g. changing the colloidal shape in hard models, it is even possible to find higher order points at which more than three phases coexist in binary systems [1, 2]. In the stacking diagram, the analogue of bulk two-phase coexistence occurs along any of the boundary lines of the stacking diagram. At these lines, and within our LDA approach, one stacking sequence bifurcates from another one. That is, one layer of the sequence either starts to grow or vanishes when the boundary line is crossed in the stacking diagram (depending on which direction the line is crossed).

There are points in the stacking diagram at which three sequences bifurcate. These points arise from paths that are tangent to a bulk binodal and that simultaneously start or end at the point of tangency. At these points a sedimentation binodal of type II (paths tangent to a bulk binodal) bifurcates from a sedimentation binodal of type I (paths starting or ending at the bulk binodal). These points are marked by blue triangles in the stacking diagrams of Fig. 6 of the main text.

Bifurcation of four stacking sequences occurs at two types of special points in the stacking diagram. First, there are points where three sedimentation binodals and a terminal line meet. This occurs whenever a path either starts or ends at the triple point, which is always possible if a triple point exists in bulk, see the yellow squares in the stacking diagrams of Figs. 4 and 6 of the main text. The second special point occurs if two sedimentation binodals cross each other (violet squares in the stacking diagrams of Figs. 4 and 6 of the main text), which happens whenever a path simultaneously starts and ends at bulk binodals in the bulk phase diagram. See examples of such paths in Fig. 6b of the main text. Hence, the occurrence of these points highly depends on the topology of the bulk phase diagram, the precise curvature of the bulk binodals, and both the slope and the length of the sedimentation path. In the present system the number of such special points depends on the slope of the path. For $s = 3$ two sedimentation binodals cross at a point only once vs twice for the case $s = 0.5$. Due to the decreased slope of $s = 0.5$ and the curvature of the binodal there is an additional special point generated by the path that both start and end at the $I - N_\mathrm{p}$ binodal in bulk, see Fig. 6b of the main text.

Five sequences bifurcating from one point is also a possible scenario for finely tuned combinations of the sample height and the slope of the path. For example, for a specific value of the height $h \lesssim 50\,\mathrm{mm}$ and the slope $s = 0.5$ the sequence $IN_\mathrm{p}IN_\mathrm{r}$ in Fig. 6f of the main text disappears, leading to the bifurcation of five stacking sequences. This highly special point corresponds to the path that is tangent to the $I - N_\mathrm{p}$ binodal and that both starts at the $I - N_\mathrm{p}$ binodal and ends at the $I - N_\mathrm{r}$ binodal. In general, bifurcation of six stacking sequences from a point in the stacking diagram is also possible if three boundary lines intersect in the stacking diagram.

According to our local density approximation, the bifurcation of a sequence into another sequence occurs via the formation of a new infinitely thin layer. However, surface effects might prevent the formation of such a layer due to the energetic cost of the new interfaces that must be formed. Considering surface effects two scenarios are possible: The creation of a new layer can proceed continuously (via the formation of microdroplets instead of a complete layer) or discontinuously (a complete new layer appears abruptly once the thickness is large enough to compensate for the surface tensions of the associated interfaces). A set of sedimentation-diffusion-equilibrium experiments performed near the bifurcation points or boundary lines of the stacking diagram would be very valuable to shed light on this fundamental process. Also, a study of the time evolution from an initially homogeneous sample to the final equilibrium sequence can help to understand how stacking sequences evolves into each other.

[1] Álvaro González García, R. Tuinier, J. V. Maring, J. Opdam, H. H. Wensink, and H. N. W. Lekkerkerker, Depletion-driven four-phase coexistences in discotic systems, Mol. Phys. **116**, 2757 (2018).

[2] V. F. D. Peters, M. Vis, A. G. García, H. H. Wensink, and R. Tuinier, Defying the gibbs phase rule: Evidence for an entropy-driven quintuple point in colloid-polymer mixtures, Phys. Rev. Lett. **125**, 127803 (2020).

[3] F. M. van der Kooij and H. N. W. Lekkerkerker, Liquid-crystalline phase behavior of a colloidal rod-plate mixture, Phys. Rev. Lett. **84**, 781 (2000).

[4] F. M. van der Kooij and H. N. W. Lekkerkerker, Liquid-crystal phases formed in mixed suspensions of rod- and platelike colloids, Langmuir **16**, 10144 (2000).

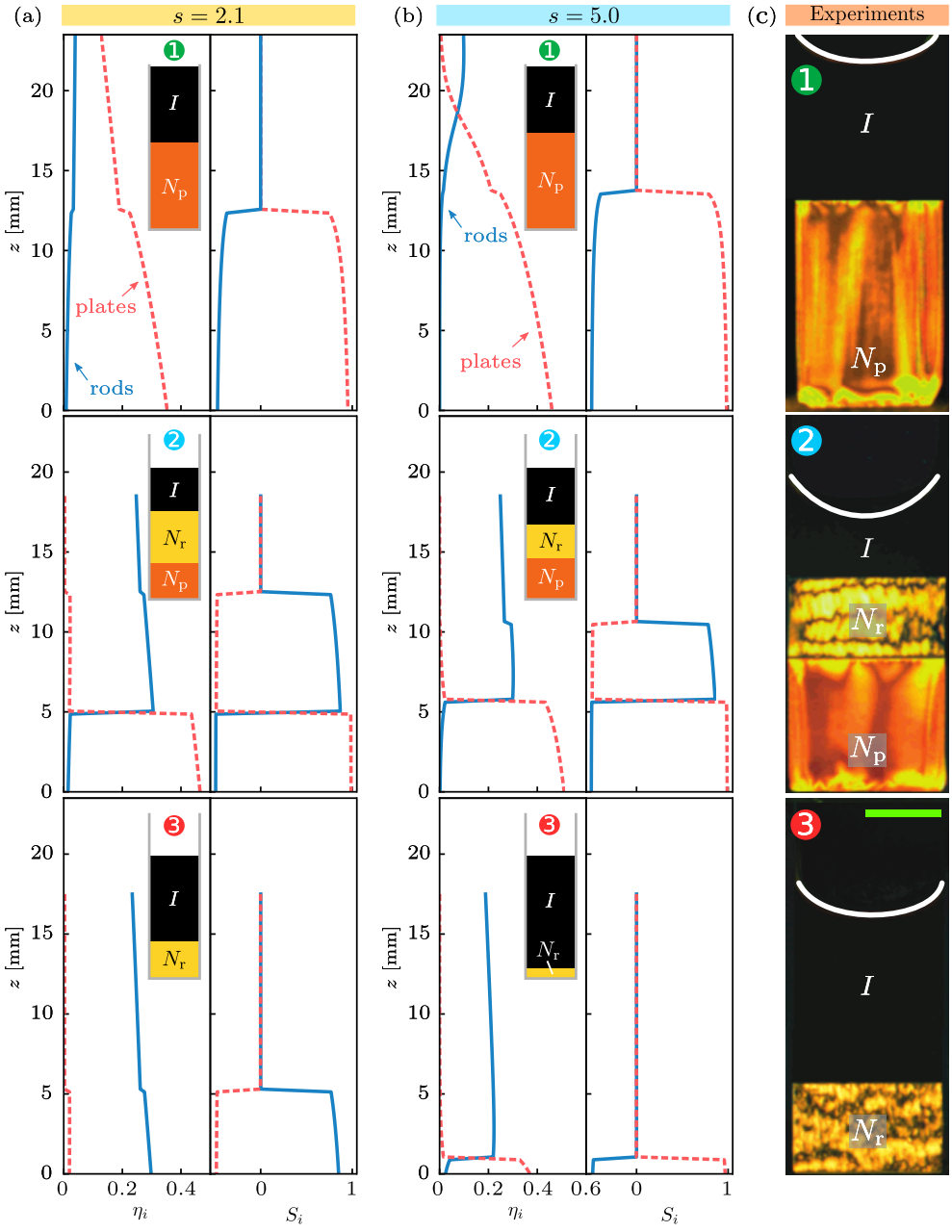


Supplementary Figure 1. Vertical profiles of the packing fractions $\eta_i$ and the nematic order parameters $S_i$ (with $i = \{\mathrm{r}, \mathrm{p}\}$) for rods (solid-blue lines) and plates (dashed-red lines) in three different samples, labeled as 1,2, and 3 (as indicated by the colored circles). The layers are isotropic ($I$), rod-rich nematic ($N_\mathrm{r}$), and plate-rich nematic ($N_\mathrm{p}$). The buoyant mass ratio is fixed to $s = 2.1$ in (a) and $s = 5.0$ in (b) which are the limiting cases of the experimental uncertainty. In both cases we change $s$ by varying the gravitational length of the plates $\xi_\mathrm{p}$ while keeping that of the rods constant, $\xi_\mathrm{r} = 5.5\,\mathrm{mm}$. Schematics of the samples are represented in the insets. The amount of solvent evaporated (only parameter used to find the best agreement between theory and experiments) is 22% (a) and 30% (b) in sample 1, 48% (a) and 47% (b) in sample 2, 60% (a) and 50% (b) in sample 3. The corresponding experimental samples (pictures taken between crossed polarizers) by van der Kooij and Lekkerkerker [3, 4] are shown in (c) (adapted with permission from [4], Copyright 2000 American Chemical Society). The meniscus is highlighted with a white line for clarity. The bright areas are due to light being polarized in layers with orientational order. The scale bar (green) is 5 mm.

# Sedimentation of colloidal plate-sphere mixtures and inference of particle characteristics from stacking sequences

Tobias Eckert, Matthias Schmidt,* and Daniel de las Heras†
*Theoretische Physik II, Physikalisches Institut, Universität Bayreuth, D-95440 Bayreuth, Germany*

(Received 22 December 2021; accepted 9 February 2022; published 8 March 2022)

We investigate theoretically the effect of gravity on a plate-sphere colloidal mixture by means of an Onsager-like density functional to describe the bulk, and sedimentation path theory to incorporate gravity. We calculate the stacking diagram of the mixture for two sets of buoyant masses and different values of the sample height. Several stacking sequences appear due to the intricate interplay between gravity, the sample height, and bulk phase separation. These include the experimentally observed floating nematic sequence, which consists of a nematic layer sandwiched between two isotropic layers. The values of the thicknesses of the layers in a complex stacking sequence can be used to obtain microscopic information of the mixture. Using the thicknesses of the layers in the floating nematic sequence we are able to infer the values of the buoyant masses from the colloidal concentrations and vice versa. We also predict new phenomena that can be experimentally tested, such as a nontrivial evolution of the stacking sequence by increasing the sample height in which new layers appear either at the top or at the bottom of the sample.

DOI: 10.1103/PhysRevResearch.4.013189

## I. INTRODUCTION

With remarkable exceptions [1–3], experiments on colloidal science are performed on Earth. Hence, the colloidal particles are subject to a gravitational field that can have a strong effect on the system. The effect of gravity is particularly strong if the suspension contains particles with significantly different buoyant masses, such as e.g., the case of strongly polydisperse and multicomponent colloidal systems. On the other hand, theoretical studies of colloidal systems are often focused on bulk properties and disregard the effect of gravity on the system.

This paper aims at bridging the gap between sedimentation-diffusion-equilibrium experiments and theoretical studies of bulk phenomena in colloidal plate-sphere mixtures. Experimental works include studies on the structure [4] and the rheology [5] of mixtures of silica nanospheres and kaolinite plates, the observation of a slowdown of the crystallization transition of spheres due to the addition of plates [6], the occurrence of isotropic-columnar coexistence in charged mixtures of gibbsite plates and silica spheres [7,8], enhanced density fluctuations of the spheres due to the addition of plates in dilute suspensions [9], the formation of an arrested glass state in gibbsite platelets and silica sphere mixtures [10], and several sedimentation experiments in which a floating nematic layer sandwiched between two isotropic layers [11–13] was observed. From a theoretical point of view, the bulk properties of plate-sphere mixtures have been investigated via free-volume theory [14], density functional theory in the Onsager approximation with [15–17] and without [18] rescaling of the second virial coefficient as well as using fundamental measure density functional theory [15,19–21], with explicit approximations to the configurational partition function [22], and via a density expansion on the work required to insert particles to the mixture [23].

The effect of gravity on a colloidal plate-sphere mixture has received little theoretical attention, with notable exceptions that have analysed the floating nematic stacking sequence [11,24,25]. We use here sedimentation path theory [26] to connect bulk and sedimentation phenomena in colloidal plate-sphere mixtures. The theory is based on the so-called sedimentation paths, which are straight lines in the plane of chemical potentials. The paths represent the linearly varying local chemical potentials along the vertical axis in a sample that is subject to gravity. An interface between two layers of different bulk phases appears in a cuvette if a sedimentation path crosses a bulk binodal. Several stacking sequences can occur by varying the control parameters of the mixture such as the colloidal concentrations and compositions but also as a result of changing the sample height [27,28]. The set of stacking sequences for a given mixture can be grouped in a stacking diagram, which depicts all possible stacking sequences in the plane of experimentally relevant quantities, such as the overall packing fraction for each species. The stacking diagram is in sedimentation-diffusion-equilibrium, the analog of the bulk phase diagram in equilibrium.

*Matthias.Schmidt@uni-bayreuth.de
†delasheras.daniel@gmail.com; www.danieldelasheras.com

The stacking diagrams of several colloidal mixtures have been calculated with sedimentation path theory using both the infinite sample height limit [26,29–32] and also the case of finite sample height [27–29]. The later allows to carry out a direct comparison with experimental findings. Excellent agreement of results from the sedimentation path theory and the experimental observations by van der Kooij and Lekkerkerker [33,34] has been recently found in mixtures of plates and rods [28].

Here, we use sedimentation path theory to study theoretically the effect of gravity on a colloidal plate-sphere mixture and compare with corresponding sedimentation experiments [11]. In the experiments [11] only isotropic and uniaxial phases were reported. We hence restrict the bulk study to phases without positional order using a simple microscopic density functional theory. The isotropic-nematic bulk binodal has an inflection point in the plane of chemical potentials. The occurrence of an inflection point affects the sedimentation-diffusion equilibrium by enriching the set of possible stacking sequences. We study how the stacking diagram changes by varying both the buoyant masses of the species and the height of the sample. We also demonstrate how to use the macroscopically observed stacking sequences in the experiments to infer microscopic information about the colloidal particles, such as their buoyant masses. Our methodology is general and can be used in other colloidal mixtures to both obtain the stacking diagram and infer particle characteristics from macroscopic stacking behavior.

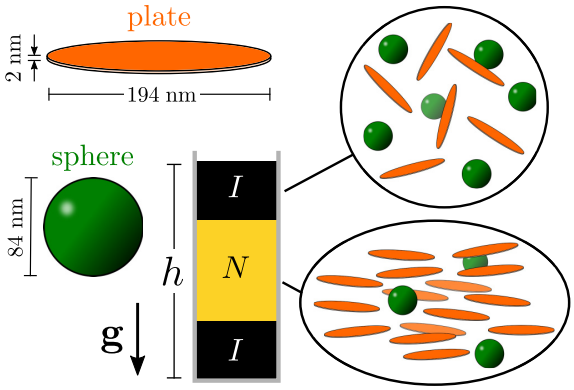


FIG. 1. Dimensions of the hard spheres (green) and hard cylinders (orange) used to model the colloidal plate-sphere mixture, together with a sketch of a cuvette of height $h$ under a gravitational field $\boldsymbol{g}$. The stacking sequence is a floating nematic phase $INI$, i.e., top isotropic, middle nematic, and bottom isotropic. Both the stacking sequence and the thickness of the layers are consistent with one of the experimental samples reported in Ref. [11]. Schematics of the particles in the isotropic (no orientational order $S_\mathrm{p} = 0$) and in the uniaxial nematic (orientational order $S_\mathrm{p} > 0$) phases are also shown.

## II. THEORY

### A. Plate-sphere particle model

Lyotropic liquid crystals are often modelled using hard particles [35] for which the pairwise interparticle potential is infinite if two particles overlap and zero otherwise. We use here a mixture of hard plates and hard spheres to model the experimental colloidal particles of Ref. [11]. In the experiments only isotropic ($I$) and uniaxial nematic ($N$) bulk phases were reported. Hence, we restrict the bulk study to phases without positional order. The nematic phase is rich in the anisotropic particles, i.e., the plates. A schematic of both phases is shown in Fig. 1. The uniaxial order parameters $S_\mathrm{p}$ of the plates (see Appendix A) characterizes the isotropic ($S_\mathrm{p} = 0$) and the nematic ($S_\mathrm{p} > 0$) phases. In what follows, we use subscripts p and s to designate the plates and the spheres, respectively.

The gravitational length of species $i = \mathrm{p}, \mathrm{s}$ is $\xi_i = k_\mathrm{B}T/(m_i g)$ with $m_i$ the buoyant mass of the species, $g$ the gravitational acceleration, $k_\mathrm{B}$ Boltzmann's constant, and $T$ absolute temperature. In the experimental study [11], the plates were made of gibbsite (mass density $2.42\,\mathrm{g/cm^3}$) and the spheres of alumina-coated silica ($2.30\,\mathrm{g/cm^3}$). The particles were sterically stabilized with a polymer coating of a few nanometer thickness and suspended in an aqueous solvent ($1.00\,\mathrm{g/cm^3}$). Here we use cylinders of diameter 184 nm and thickness 2 nm together with spheres of diameter 74 nm to model the cores of the plates and of the spheres, respectively. The core dimensions are relevant to calculate the buoyant masses, and thus the gravitational lengths. The effective dimensions of the coated particles are obtained by adding 10 nm to the core dimensions, as estimated experimentally by neutron scattering [11]. Hence, we use plates of diameter 194 nm and spheres of diameter 84 nm for the hard particle-particle interactions, see Fig. 1. Gibbsite plates are usually polydisperse. For example, in a similar system, the uncertainty in the thickness of the plates is approximately 20% [33,34]. We therefore use the effective plate thickness as an adjustable parameter to match the properties of the isotropic-nematic transition of the monocomponent system of plates between theory and experiments. In the experimental study [11] the packing fractions at the isotropic-nematic coexistence in a pure system of plates are 0.045 and 0.049, respectively. We study the bulk of the mixture with an Onsager-like [36] classical density functional theory [37], see details in Appendix A. We find an effective plate thickness of 2 nm to be the optimal value such that the average between the isotropic and the nematic coexisting densities of a pure system of plates are the same in the theory and in the experiments. The theory however overestimates the density jump at the transition: The predicted coexisting isotropic-nematic packing fractions are 0.042 and 0.052.

We estimate the buoyant masses using only the volumes of the cores. That is, we neglect the effects of the polymer coating since its mass density ($1.02\,\mathrm{g/cm^3}$) is close to the density of the aqueous solvent. With the above values of the mass densities and particle dimensions of plates and spheres, we obtain the gravitational lengths $\xi_\mathrm{p} = 5.34$ mm and $\xi_\mathrm{s} = 1.49$ mm. Hence, the buoyant mass ratio in our system is

$$s = \frac{m_\mathrm{s}}{m_\mathrm{p}} = \frac{\xi_\mathrm{p}}{\xi_\mathrm{s}} \approx 3.58. \tag{1}$$

Our estimate of the gravitational length of the plates (5.34 mm) is larger than that in Ref. [11] (2.92 mm) due to the adjustable value of the plate thickness. Recall that the effective plate thickness is the only adjustable parameter that we use in our theoretical study. The remaining particle dimensions as well as the mass densities are directly taken as reported in the experimental study [11].

### B. Sedimentation path theory

To incorporate gravity we employ a local density approximation (LDA) that approximates each horizontal slice of the system at height $z$ by a bulk equilibrium system with local chemical potentials $\mu_i(z)$ given by [26,27,29]

$$\mu_i(z) = \bar{\mu}_i - m_i g\left(z - \frac{h}{2}\right), \quad i = \mathrm{p}, \mathrm{s}. \tag{2}$$

Here $0 \leqslant z \leqslant h$ is the vertical coordinate measured from the bottom of the sample, $h$ is the height of the sample, $\bar{\mu}_i$ with $i = \mathrm{p}, \mathrm{s}$ are the chemical potentials in the absence of gravity, and $m_i g z$ are the gravitational potentials (linear in $z$). The LDA is justified if all correlation lengths are small compared to both gravitational lengths, which is the case in many colloidal systems including the current one. Note that the LDA is used here only to incorporate gravity to the underlying bulk theory. Hence, the LDA does not affect the theoretical treatment of the bulk. The description of the bulk can be done with a simple Onsager theory like we use here, but also with more sophisticated density functional theories [35,38] and other approaches such as perturbation theory [39].

Equation (2) describes a line segment in the plane of chemical potentials. The position (i.e., the statepoint) along the line segment is parameterized by $z$. We refer to such line segments as sedimentation paths [26,27]. Eliminating $z$ for the binary mixture in Eq. (2) yields

$$\mu_\mathrm{s}(\mu_\mathrm{p}) = s\mu_\mathrm{p} + a = s(\mu_\mathrm{p} - b), \tag{3}$$

which is the equation of a line segment in the plane of $\mu_\mathrm{p}$ and $\mu_\mathrm{s}$ with slope given by the buoyant mass ratio $s = m_\mathrm{s}/m_\mathrm{p} = \xi_\mathrm{p}/\xi_\mathrm{s}$, intersect $a = \bar{\mu}_\mathrm{s} - s\bar{\mu}_\mathrm{p}$, and root $b = \bar{\mu}_\mathrm{p} - \bar{\mu}_\mathrm{s}/s$ [see Fig. 2(a)]. The midpoint of the sedimentation path is $(\bar{\mu}_\mathrm{p}, \bar{\mu}_\mathrm{s})$, conveniently translated by the constant terms $m_i g h/2$ in Eq. (2). The length of the path in the plane of $\mu_\mathrm{p}$ and $\mu_\mathrm{s}$ is $\beta\Delta\mu_i = h/\xi_i$, with $\Delta\mu_i = \mu_i(0) - \mu_i(h)$ and $\beta = 1/(k_\mathrm{B}T)$.

The significance of the sedimentation path is that whenever a path crosses a bulk binodal, an interface between the two bulk phases that coexist at the binodal appears in the cuvette, see Fig. 2(a). The crossings between the sedimentation path and the binodal provide therefore the sequence of layers in the sample, i.e., the stacking sequence. Moreover, the value of the parameter $z$ at the crossing dictates the vertical position of the interface in the sample.

### C. Stacking diagram

Depending on the position, the slope, the length, and the direction of the sedimentation path, different stacking sequences

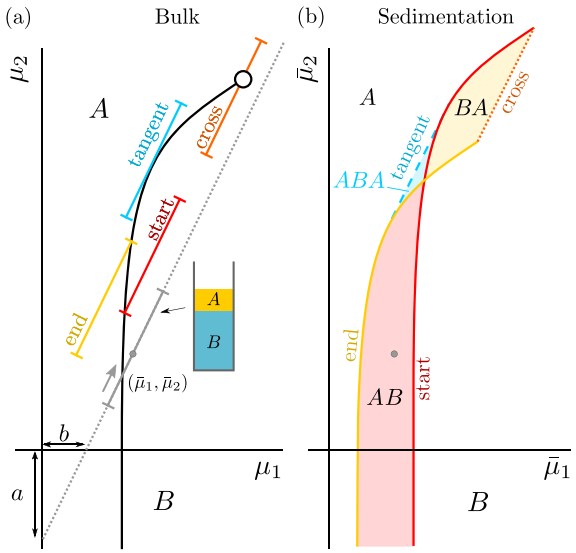


FIG. 2. (a) Model bulk phase diagram in the plane of chemical potentials $\mu_1$ and $\mu_2$. The phases $A$ and $B$ coexist along a binodal (black-solid line) that ends at a critical point (empty circle). The line segments are finite sedimentation paths. The gray path crosses the binodal and corresponds to a stacking sequence $AB$ (from top to bottom). The grey arrow indicates the direction of all paths from top to bottom. Illustrative examples of paths that form boundaries between different stacking sequences are depicted: (i) paths that start (red) or end (yellow) at the binodal, (ii) paths tangent (blue) to the binodal, and (iii) paths that cross (orange) the critical point. A displacement of any of such paths can alter the stacking sequence. The dotted-gray line is a sedimentation path in the limit of infinite height ($a$ and $b$ are the intersects of the path with the $\mu_2$ and the $\mu_1$ axes, respectively). (b) Stacking diagram, plane of average chemical potentials $\bar{\mu}_1$ and $\bar{\mu}_2$, of the bulk phase diagram depicted in (a). Each region is a different stacking sequence, as indicated. The boundary lines between sequences are sedimentation binodals of type I (solid lines) or type II (dashed-blue line), and a terminal line (dotted-orange line). A sedimentation path in (a) is a point in (b) given by the coordinates of the average chemical potentials along the path. See, e.g., the grey circle in (b) that corresponds to the gray sedimentation path (finite height) in (a).

can occur. The stacking sequences can be grouped in a stacking diagram. Similar to the bulk phase diagram, the stacking diagram admits several representations that differ in the variables that are kept constant. To compare with experiments we fix the buoyant mass ratio $s$ and the path length, i.e., we fix the buoyant masses of both species and the sample height $h$.

To illustrate the construction of a stacking diagram, we plot in Fig. 2 a hypothetical bulk diagram and its corresponding stacking diagram. In bulk, two phases $A$ and $B$ coexist along a binodal that ends at a critical point, Fig. 2(a). We construct the stacking diagram by finding the sedimentation paths in the bulk phase diagram that form the boundaries between two stacking sequences in the stacking diagram. There exist three types of boundaries [27,28]. The first type, so-called sedimentation binodals of type I, corresponds to sedimentation paths

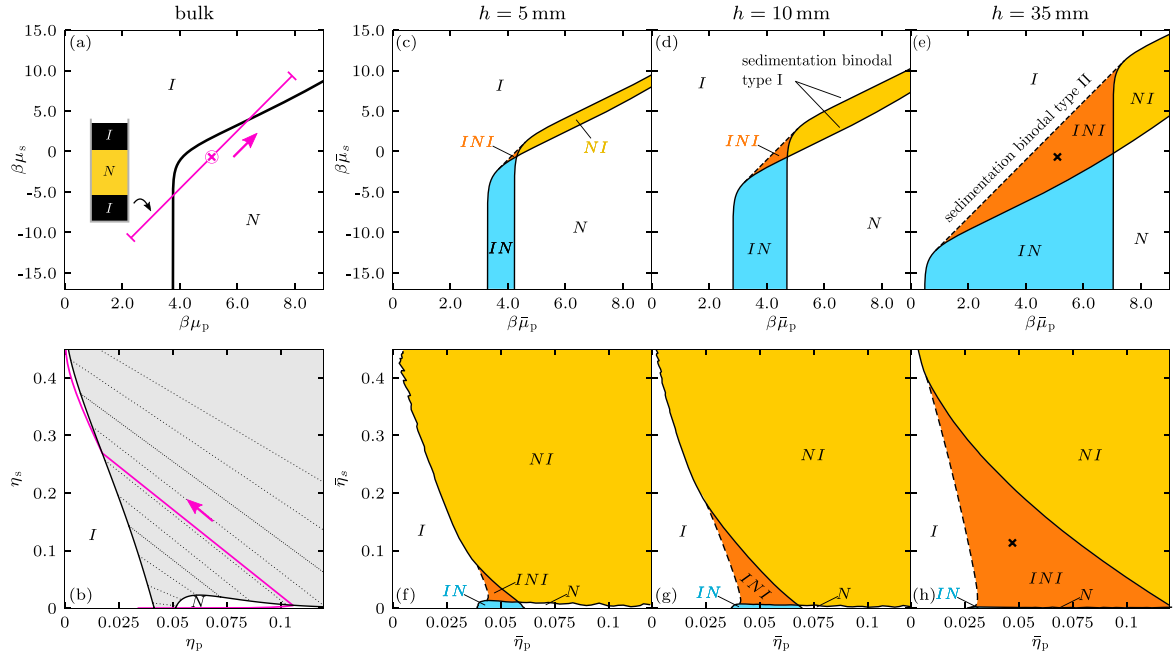


FIG. 3. Bulk phase diagram in the plane of chemical potential of plates $\mu_p$ and spheres $\mu_s$ (a), and also in the plane of packing fractions of plates $\eta_p$ and spheres $\eta_s$ (b). The solid-black line in (a) is the binodal at which the isotropic $I$ and the nematic $N$ phases coexist. Dotted lines in (b) are tie lines connecting coexisting points along the binodal (solid-black line). The grey area is the two-phase region. The pink line in (a) is a sedimentation path corresponding to the $INI$ stacking sequence with layer thicknesses of 9.3 mm, 16.5 mm, and 9.6 mm as found experimentally in Ref. [11]. The pink curve in (b) is the same sedimentation path in the plane of packing fractions. The pink arrows indicate the direction of the path from the top to the bottom of the sample. Stacking diagram in the plane of average chemical potential of plates $\bar{\mu}_p$ and spheres $\bar{\mu}_s$ [(c)–(e)], and in the plane of average packing fractions of plates $\bar{\eta}_p$ and spheres $\bar{\eta}_s$ [(f)–(h)] for three different sample heights: $h = 5$ mm [(c),(f)], 10 mm [(d),(g)], and 30 mm [(e),(h)]. Each colored region correspond to a different stacking sequence (except the pure sequences $I$ and $N$ depicted in white). The sequences are labeled from the top to the bottom of the sample. The black crosses in panels (e) and (h) indicate the position of the sedimentation path plotted in panels (a) and (b). In the stacking diagram, sedimentation binodals of type I (type II) are represented with solid (dashed)-black lines.

that either start or end at a bulk binodal [red and yellow paths in Fig. 2(a)]. Paths that cross an ending point of a binodal, e.g., a triple point or a critical point [orange path in Fig. 2(a)], also form a boundary in the stacking diagram, known as a terminal line. The third type, known as sedimentation binodal of type II, corresponds to paths tangent to a binodal, see the blue path in Fig. 2(a). An infinitesimal displacement of the midpoint $(\bar{\mu}_1, \bar{\mu}_2)$ of the path can alter the stacking sequence in each of the three cases.

The coordinates $(\bar{\mu}_1, \bar{\mu}_2)$ for each of these special paths are then represented in a diagram to produce the stacking diagram in the plane of $\bar{\mu}_1$ and $\bar{\mu}_2$, see Fig. 2(b). However, in the experiments the relevant quantities are usually the colloidal packing fractions. Hence, in our plate-sphere mixture we transform the stacking diagram in the plane of $\bar{\mu}_p$ and $\bar{\mu}_s$ by averaging the packing fraction of each species, i.e., $\eta_i = \rho_i v_i$, along the sedimentation path to obtain $(\bar{\eta}_p, \bar{\eta}_s)$. Here $v_i$ is the particle volume of species $i$. For this transformation we need to compute $\eta_i$ for each point $(\mu_p, \mu_s)$ along the path (see [Appendix A]). In both planes, the $\bar{\mu}_p\bar{\mu}_s$-plane and the $\bar{\eta}_p\bar{\eta}_s$-plane, each point of the stacking diagram represents a sedimentation path, i.e., one sample in sedimentation-diffusion-equilibrium.

## III. RESULTS

### A. Bulk and stacking diagrams

The bulk phase diagram according to our microscopic density functional theory is shown in Figs. 3(a) and 3(b) in the planes of chemical potentials and packing fractions, respectively. We restrict the study to phases without positional order. Two phases occur: isotropic ($I$) with no orientational order of the plates ($S_p = 0$) and uniaxial nematic ($N$) with plates aligned on average along the director ($S_p > 0$). The mixture does not show any critical behavior, nor does it show isotropic-isotropic demixing. Critical and triple points are therefore not present in the bulk phase diagram. The curvature of the binodal in the plane of chemical potentials changes, leading to an inflection point. We see below how the inflection point affects the sedimentation-diffusion-equilibrium of the mixture.

A sedimentation path ($h = 35$ mm and $s = 3.58$) corresponding to a floating nematic stacking sequence $INI$ is depicted in the chemical potential representation of the bulk diagram, see Fig. 3(a). To illustrate the advantage of using the chemical potentials in the description of sedimentation-diffusion equilibrium, we also depict the path in the plane of

packing fractions, see Fig. 3(b). The simple form of the path in the plane of chemical potentials (line segments) is lost in other representations of the bulk diagram. In the plane of $\bar{\eta}_p$ and $\bar{\eta}_s$ the path discontinuously jumps from the isotropic to the nematic phase, and vice-versa, along the tie lines that connect coexisting points in bulk. For a detailed study of sedimentation paths in the plane of packing fractions see Ref. [31].

The finite height stacking diagram in the plane of chemical potentials and also in the plane of packing fractions is shown in Figs. 3(c)–3(e) and Figs. 3(f)–3(h), respectively, for three sample heights: 5 mm, 10 mm, and 35 mm. In all cases the buoyant mass ratio is fixed to $s = 3.58$. There are five different stacking sequences, namely $I$, $N$, $IN$, $NI$, and $INI$. We label the sequences from the top to the bottom of the sample. For example, $NI$ indicates a top nematic layer and a bottom isotropic layer. The occurring sequences are all possible ordered subsets of the sequence $INI$. We can arrive at the sequence $I$ by removing from the sequence $INI$ the two top layers, the two bottom layers, or the middle $N$ layer. Since no isotropic-isotropic demixing is observed, the resulting sequence ($I$) through any of these routes is the same. Note that the observation of two isotropic layers in the $INI$ sequence does not imply the occurrence of isotropic-isotropic demixing in bulk.

There is no topological change by varying the sample height from 5 mm to 35 mm. However, the region occupied by a given stacking sequence changes with $h$. Hence, the stacking sequence of two sedimentation-diffusion-equilibrium samples that share either the same $(\bar{\mu}_p, \bar{\mu}_s)$ or the same $(\bar{\eta}_p, \bar{\eta}_s)$ can change with the sample height $h$. All regions corresponding to stacking sequences with multiple layers grow in the plane of $\bar{\mu}_p$ and $\bar{\mu}_s$ with increasing $h$. In contrast, in the plane of $\bar{\eta}_p$ and $\bar{\eta}_s$ only the $INI$ region grows in size. All the other regions shrink with increasing $h$. In the limit of $h \to \infty$ only the stacking sequences $I$ and $INI$ remain. This is confirmed by the calculation of the stacking diagram in the infinite height limit, see Sec. III E. That only two sequences remain if $h \to \infty$ can be also concluded from the bulk diagram in Fig. 3(a) by lengthening the depicted sedimentation path. The resulting path either lies entirely in the $I$ phase or it transitions into the $N$ phases and hence cuts the binodal twice giving rise to the $INI$ sequence (note that the binodal does not end at a critical point and that the path is an infinite line in the limit $h \to \infty$).

### B. Reading microscopic information from experimental photographs

A prominent result of sedimentation-diffusion-equilibrium experiments is the stacking sequence. Sometimes, the sequence can be easily read from direct visual inspection of the sample using crossed polarizers. Between crossed polarizers, isotropic layers appear dark whereas layers in which the particles posses orientational order are bright. Even two layers of different phases with orientational order, such as, e.g., nematic and columnar, can be differentiated by their relative brightness and color [34,40]. We explore here the possibility of obtaining microscopic information about the particles by using from the experiments only the stacking sequence and the thicknesses of the occurring layers.

The thicknesses of the layers in stacking sequences provide information to locate the corresponding sedimentation path in the plane of chemical potentials. To contain sufficient amount of information and hence be useful for the analysis, such sequences need to possess at least three layers. That is, at least two crossings between the corresponding path and the bulk binodal(s) are required. For example, in Fig. 3(a) we construct the sedimentation path such that its slope is $s = 3.58$ and its stacking sequence is $INI$ with layer thicknesses of 9.3 mm (bottom isotropic), 16.5 mm (middle nematic), and 9.6 mm (top isotropic). The values of the thicknesses are chosen to reproduce the experimental sample in Ref. [11] with 74 nm spheres and average packing fractions $(\bar{\eta}_s, \bar{\eta}_p) = (0.05, 0.05)$.

A path is defined by four values and its direction (given by the sign of the buoyant mass of one species). For example, a path is defined by the position of the two endpoints in the plane of chemical potentials, or by the set of variables $s$, $\Delta\mu_p$, $\bar{\mu}_p$, and $\bar{\mu}_s$. The slope and the value of the three layer thicknesses in the $INI$ sequence give in total four constrains, and hence properly define a unique sedimentation path, see Fig. 3(a).

To locate the path in the previous example, we used fixed values of the buoyant masses. The buoyant masses determine the slope and, together with the sample height, the length of the sedimentation path. Determining experimentally the buoyant masses might be a difficult task since it requires detailed measurements of the particle dimensions and mass densities. We show next that using as input only the experimentally reported thicknesses of the layers in the $INI$ stacking sequence, one can infer a range of gravitational lengths (and also a range of average colloidal concentrations) in which such sample can exists. We therefore pretend that the gravitational lengths are unknown, and consider a wide range of candidate values for both $\xi_p$ and $\xi_s$. For each pair of $\xi_p$ and $\xi_s$, we find the sedimentation path that produces the $INI$ sequence with layer thicknesses equal to those in the experiments, see sketch in the inset of Fig. 4(a). The gravitational lengths fix the length and the slope of the path. Hence, we only vary the position of the path $(\bar{\mu}_p, \bar{\mu}_s)$ until the correct layer thicknesses are reproduced. If a solution exists, the path is unique.

The results are summarized in Fig. 4. Each point corresponds to a path with the sequence $INI$ and layer thicknesses 9.3 mm, 16.5 mm, and 9.6 mm. Illustrative paths of different slope and length in the plane of $\mu_p$ and $\mu_s$ are shown in the inset of Fig. 4(a). All the paths give rise to the desired $INI$ stacking sequence with the correct layer thicknesses. Note that paths of different lengths in the plane of chemical potentials can represent samples with the same height if the paths have different gravitational lengths since $h = \beta\Delta\mu_i\xi_i$.

Once a sedimentation path with the right sequence and layer thicknesses is found, we calculate the corresponding overall packing fractions by integrating the local packing fraction along the path. Figures 4(a) and 4(b) show for each pair $(\xi_p, \xi_s)$ the corresponding values of $\bar{\eta}_p$ and $\bar{\eta}_s$ (see color bars). Above the red-dotted line it is not possible to find an $INI$ sequence because the paths there are too flat (small slope) to cross the bulk binodal twice. From the slope of the bulk binodal at its inflection point, we determine the minimum slope for an $INI$ sequence to occur to be $s_{min} \approx 1.7$. For slopes $s > s_{min}$ it is always possible to find an $INI$ sequence, but

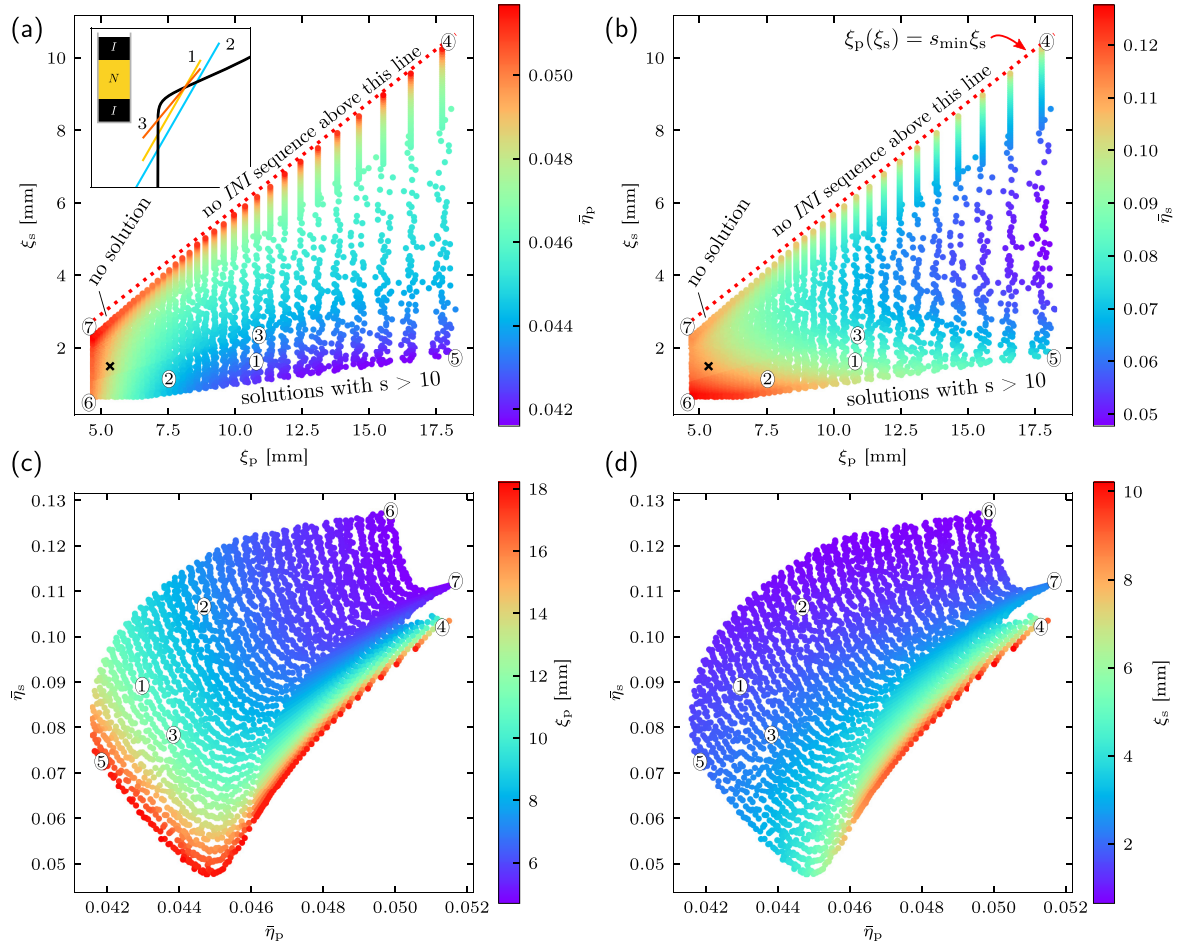


FIG. 4. Average packing fraction of plates $\bar{\eta}_p$ (a) and spheres $\bar{\eta}_s$ (b) indicated by the color map as a function of the gravitational lengths of plates $\xi_p$ and spheres $\xi_s$. Each point in the diagrams represents a sedimentation path that produces an isotropic-nematic-isotropic (*INI*) stacking sequence with layer thicknesses of 9.3 mm, 16.5 mm, and 9.6 mm, from top to bottom. Illustrative paths together with a sketch of the sample are shown in the inset of panel (a). No solution exists above the red-dotted line in panels (a) and (b) due to the path being too flat to cross the binodal twice. The inverse relations, i.e., gravitational lengths as a function of average packing fractions, are depicted in panels (c) and (d). The samples labeled 1 – 3 correspond to the paths shown in the inset of panel (a). The samples labeled 4 – 7 are close to the boundaries of the diagrams shown in panels (a) and (b). The black crosses in (a) and (b) indicate the value of the gravitational lengths used here.

there is a small region in which there is no *INI* sequence with the desired thicknesses (region indicated as "no solution" in Fig. 4). For the remaining values of gravitational lengths an *INI* sequence with the desired thicknesses always exists. In Fig. 4 we show only solutions for $s < 10$, which covers a vast range of experimentally realisable buoyant mass ratios. For $s > 10$ the path is almost parallel to the vertical region of the binodal, which makes it difficult to numerically find the solution. The region in which solutions with $s > 10$ can occur is indicated in Figs. 4(a) and 4(b)

The inverse relation to Figs. 4(a) and 4(b) is shown in Figs. 4(c) and 4(d). There, for each pair $(\bar{\eta}_p, \bar{\eta}_s)$ the gravitational lengths, $\xi_p$ and $\xi_s$, required to obtain the correct layer heights are depicted via a color map. This representation clearly shows that given a specific set of layer thicknesses, not every combination of packing fractions is possible. Also, the set of possible values of $\bar{\eta}_p$ is limited to the narrow range $[0.0415, 0.052]$. The possible concentration of spheres varies in a wider range of approximately $[0.05, 0.13]$. We expect these ranges to slightly increase if solutions with $s > 10$ are also considered.

The four-sided shape of the point cloud in the plane of $\xi_p$ and $\xi_s$ in Fig. 4(a) is deformed when transformed into the plane of $\bar{\eta}_p$ and $\bar{\eta}_s$ in Fig. 4(c). A nonlinear function governs this transformation from gravitational lengths to average packing fractions. Despite the nonlinearity, the clockwise order of the points labeled 4 – 7 is preserved under this transformation.

Using the experimental values for the layer thicknesses in the *INI* sequence together with the values of the gravitational

lengths known from the synthesis of the particles, we can use Figs. 4(a) and 4(b) to infer the values of the packing fractions. The opposite also holds: If the packing fractions are known from the preparation of the samples, but the microscopic gravitational lengths are unknown, we can use Figs. 4(c) and 4(d) to infer their values.

For the gravitational lengths calculated with our particle model, $\xi_p = 5.34\,\text{mm}$ and $\xi_s = 1.49\,\text{mm}$ [marked in Figs. 4(a) and 4(b) with black crosses], we predict using Figs. 4(a) and 4(b) that the average packing fractions of the sample are $\bar{\eta}_p = 0.047$ and $\bar{\eta}_s = 0.11$. This is in almost perfect agreement for the plates (the packing fraction used in the experimental study [11] is $\bar{\eta}_p = 0.05$). For the spheres, our predicted concentration differs by a factor of two (in the experimental study [11] $\bar{\eta}_s = 0.05$). The difference might be due to our simple theoretical description of the bulk and also to intrinsic characteristics of the experiments, such as polydispersity and the uncertainties in the dimensions of both the particles' cores and the thickness of the coating polymer layer. Note that our discrepancy of a factor of two in the packing fraction of the spheres can be explained with a change in the diameter of the spheres of approximately $\sqrt[3]{2} \approx 1.26$. This value is compatible with the variance in the distribution of the diameter of the spheres (26%) due to polydispersity [9].

Using the stacking diagram, e.g., Figs. 3(g)–3(i), we can choose the packing fractions that produce a given stacking sequence for fixed buoyant mass ratio $s$. The type of analysis done in Fig. 4 allows us to choose the parameters that produce not only the sequence but also the desired layer thicknesses within the sequence.

### C. Effects of a bulk inflection point on the stacking diagram

The Onsager-like density functional theory used here predicts that in the plane of chemical potentials the isotropic-nematic bulk binodal presents an inflection point. The fundamental measure theory applied to a mixture of infinitely thin plates and spheres [15,20] also predicts the occurrence of an inflection point [11], which therefore seems to be a robust feature of the system.

The inflection point does not have any qualitative effects on the stacking diagram for a slope of $s = 3.58$. However, for slopes of the path comparable to the slope of the bulk binodal at the inflection point, the inflection point induces topological changes to the stacking diagram due to the occurrence of new sequences.

The maximum number of layers that can appear in a stacking sequence is [26]

$$l_{\max} = 3 + 2(n_b - 1) + n_i, \tag{4}$$

with $n_b$ the number of bulk binodals and $n_i$ the total number of inflection points in all the binodals. The occurrence of several layers in sedimentation-diffusion-equilibrium is unrelated to bulk coexistence in which the Gibbs phase rule dictates the maximum number of phases that can coexist simultaneously (with the notable exceptions found recently in colloid-polymer mixtures [41–43] in which by fine-tuning the interparticle interactions it is possible to find bulk multiphase coexistence involving more than three different phases). Under gravity, the maximum number of layers in a sequence, Eq. (4), is achieved if a path crosses each binodal for the maximum number of possible times (i.e., two plus the number of inflection points of the binodal). Whether or not a sequence with $l_{\max}$ layers can actually occur depends on the position of the binodals relative to each other in bulk. Here $n_b = 1$ and $n_i = 1$, which yields $l_{\max} = 4$. To confirm the general argument presented above, we see below that in our mixture the sequence with $l_{\max}$ layers is $ININ$. This sequence occurs in the range of buoyant mass ratios $s \in [1.7, 2.5]$ provided that the path is long enough. The slope must be larger than the slope of the binodal at the inflection point ($s \gtrsim 1.7$) but also smaller than the slope of the binodal in the limit as both chemical potentials approach infinity ($s \lesssim 2.5$).

We choose a buoyant mass ratio of $s = 2$, i.e., slightly above the slope of the binodal at the inflection point. The stacking diagram in the plane of average chemical potentials and average packing fractions for sample heights 20 mm, 32 mm, and 40 mm is shown in Fig. 5. A prominent feature is the presence of the four layer stacking sequence $ININ$ [11,24] for the sample heights 32 mm and 40 mm. This sequence can only occur for sufficiently large samples ($h \gtrsim 30\,\text{mm}$) since the sedimentation path needs to start in the $I$ phase, enter the $N$, reenter the $I$ phase again, and finally end in the $N$ phase. For $h = 20\,\text{mm}$ the path is not long enough and it can either start in the $I$ phase but not reach the ultimate $N$ phase (giving rise to the sequence $INI$) or end in the $N$ phase without having started in the $I$ phase (resulting in $NIN$).

Hence, from $h = 20\,\text{mm}$ to $h = 32\,\text{mm}$ a topological change in the stacking diagram occurs. The type I sedimentation binodal that separates the sequences $NI$ from $INI$, and the type I sedimentation binodal that separates $NI$ from $NIN$ cross each other, c.f. panels (d) and (e) in Fig. 5. This gives rise to the $ININ$ sequence. The same two sedimentation binodals no longer cross for $h = 40\,\text{mm}$, which eliminates the sequence $NI$ entirely in favor of $ININ$, cf. panels (e) and (f) in Fig. 5. Both topological changes can also be observed in the plane of $\bar{\mu}_p$ and $\bar{\mu}_s$. For $h = 20\,\text{mm}$ the two type I sedimentation binodals (same shape as the bulk binodal) intersect each other twice due to the inflection point, see Fig. 5(a). For $h = 32\,\text{mm}$ one of the intersection points has moved over to the other side of one of the points of tangency, see inset of Fig. 5(b), and the $ININ$ stacking sequence appears. The two intersections between the two sedimentation binodals of type I merge approximately for $h = 40\,\text{mm}$ into a single point, see Fig. 5(c). As a consequence the $NI$ stacking sequence disappears. The transition from $h = 20\,\text{mm}$ to $h = 40\,\text{mm}$ replaces therefore the sequence $IN$ by $ININ$ but leaves the other sequences unaltered (except for changes in the shape of the regions occupied by each sequence that are inherent to changes in the height).

Another notable feature of the stacking diagram is the presence of a reentrant $IN$ stacking sequence. This sequence (blue in Fig. 5) appears in significantly different and disconnected regions of the stacking diagram corresponding to low and high average packing fractions of colloids. The two $IN$ regions share in common a direct connection to both the $I$ and the $N$ regions. This is clearly visible in the chemical potential representation of the stacking diagram, see Figs. 5(a)–5(c). Reentrant phenomena can occur in the bulk of mono- [44,45] and multicomponent [46,47] systems, but also, as in the present case, induced by external fields [48–50].

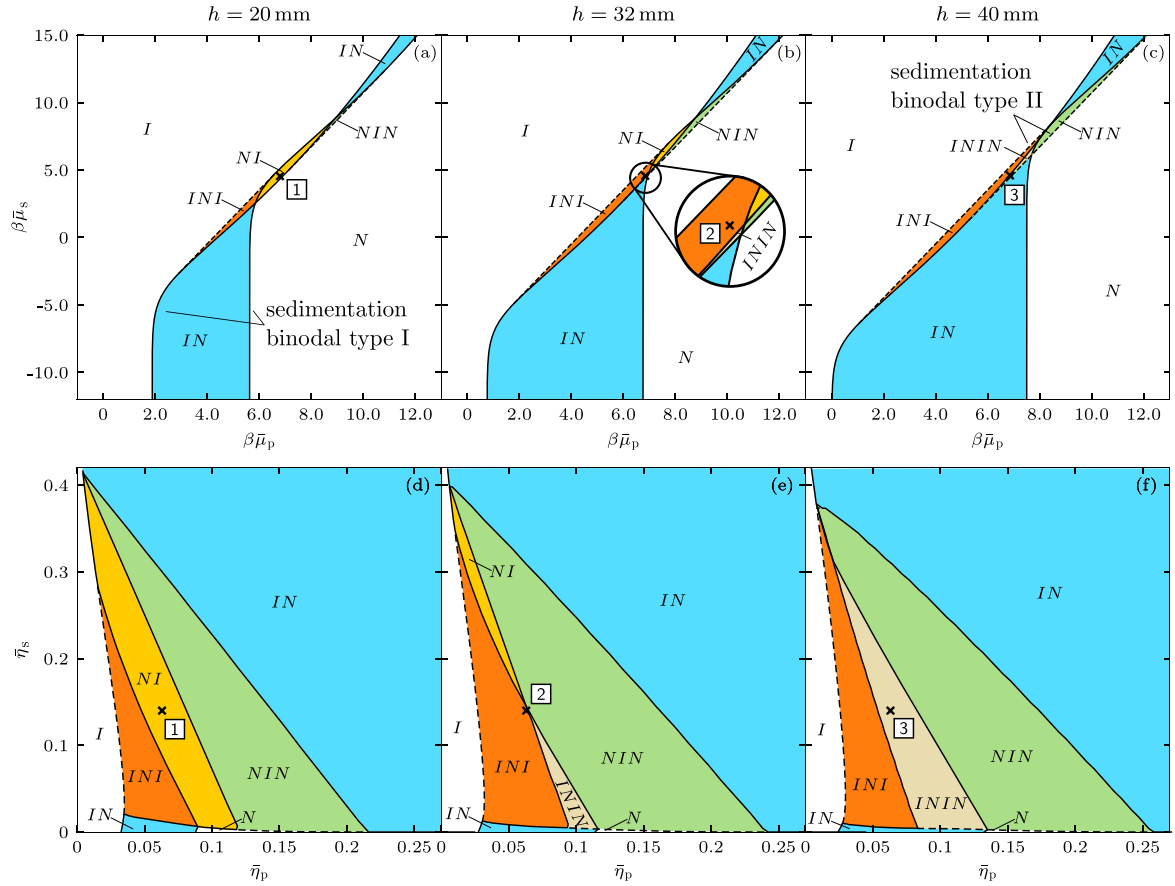


FIG. 5. Stacking diagram in the plane of average chemical potential of plates $\bar{\mu}_p$ and spheres $\bar{\mu}_s$ [(a)–(c)] and also in the plane of average packing fractions of plates $\bar{\eta}_p$ and spheres $\bar{\eta}_s$ [(d)–(f)] for sample heights of $h = 20$ mm [(a), (d)], 32 mm [(b), (e)], and 40 mm [(c), (f)]. The buoyant mass ratio is $s = 2$ in all cases. The crosses indicate at each height the location of the samples with average packing fractions $(\bar{\eta}_p, \bar{\eta}_s) = (0.063, 0.14)$ labeled with white squares as samples 1, 2, and 3. The stacking sequences are labeled from top to bottom of the sample. The inset in (b) is a close view of a small region of the stacking diagram. Sedimentation binodals of type I (type II) are represented with solid (dashed)-black lines.

### D. Dependency on sample height

The stacking diagram for buoyant mass ratio $s = 2$ shows a strong dependency on the sample height. To further investigate the influence of the sample height on the stacking sequence, we consider a set of samples with the same average colloidal packing fractions, $(\bar{\eta}_p, \bar{\eta}_s) = (0.063, 0.14)$, but different heights. This corresponds to an experimental setup with a solution prepared with the desired concentrations, which is then distributed into cuvettes filled to a different height. Only a single colloidal solution needs to be prepared, and even if there is a large uncertainty in the colloidal concentrations, it is at least guaranteed that the concentrations are the same throughout all cuvettes.

Here, we compute for each height $h$ in a range from 2 mm to 42 mm the stable phase ($I$ or $N$) that would be observed in an experiment as a function of the elevation $z$. We then plot the results in the plane of $z$ and $h$, see Fig. 6. This is a different representation of the stacking diagram in which the colloidal concentrations are kept constant. Samples from 2 mm to 30 mm always show the same $NI$ stacking sequence. At 30 mm an additional isotropic layer evolves at the top of the sample, followed by the emergence of a nematic layer at the bottom of the sample from 38 mm onwards. In total two additional layers form, one at the bottom ($N$) and one at the top ($I$) of the sample, as compared to the initial $NI$ sequence for low heights.

### E. Stacking diagram for samples with infinite height

So far, we have studied the stacking diagram for finite height samples and for two fixed values of the buoyant mass ratio, $s = 3.58$ and $s = 2$. We end the results section showing that these two illustrative values of the buoyant mass ratio give rise to the stacking diagrams with the two largest possible number of stacking sequences. To this end, we use sedimentation path theory for samples with infinite height [26,29]. In

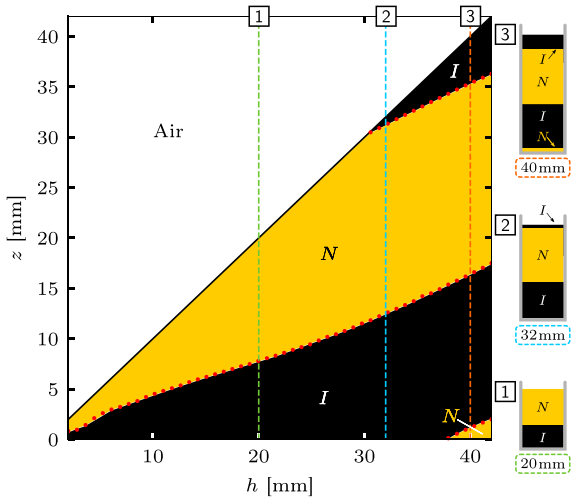


FIG. 6. Stacking diagram at fixed colloidal concentrations. Stable layer at elevation $z$ as a function of the total sample height $h$ for samples with fixed concentrations $(\bar{\eta}_p, \bar{\eta}_s) = (0.063, 0.14)$. The buoyant mass ratio is $s = 2$. The vertical-dashed lines mark the samples 1, 2, and 3 with heights 20 mm, 32 mm, and 40 mm. The same samples are also labeled and marked with crosses in Fig. 5. The solid-black line indicates the sample-air interface.

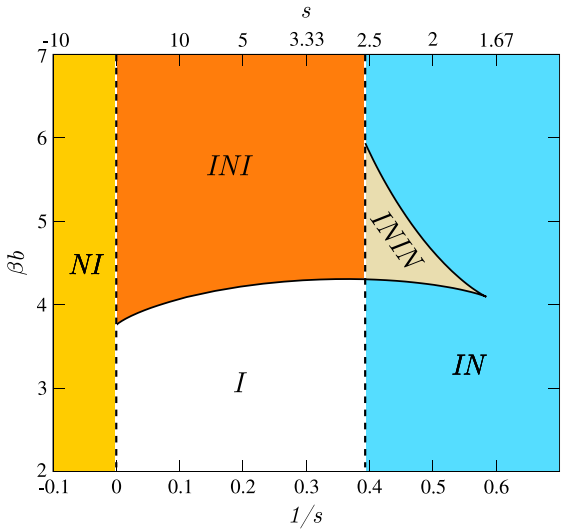


FIG. 7. Stacking diagram for samples in the limit of infinite height in the plane of inverse slope $1/s$ and root $b$ of the sedimentation path. The auxiliary-horizontal axis indicates the value of the slope $s$. Each region corresponds to a different stacking sequence in the limit of infinite height. Sequences are labeled from top to bottom of the sample if $m_p > 0$ and from bottom to top if $m_p < 0$. Black-solid lines are sedimentation binodals formed by the paths that are tangent to the bulk binodal. Vertical-dashed lines are asymptotic terminal lines formed by the two sets of paths that are parallel to the bulk binodal in the limits $\mu_s \to -\infty$ $(1/s = 0)$ and $\mu_s \to +\infty$ $(1/s \approx 0.39)$.

the limit of infinite height, a sedimentation path is a straight line (not a segment as in the finite case) that can therefore be described using only the slope $s$, the root $b$ [see Eq. (3) and Fig. 2] and the direction of path.

Similarly to the finite height case, there exist special paths that are boundaries between two different stacking sequences [26,29]: paths tangent to a binodal, paths crossing an ending point of a binodal, and paths parallel to the asymptotic behavior of the binodal at $\mu_i \to \pm\infty$. Plotting the coordinates of the special paths results in a stacking diagram for infinite height, which gives a global overview of sedimentation phenomena for all possible buoyant mass ratios.

For the plate-sphere mixture considered here, the stacking diagram for infinite height in the plane of $1/s$ and $\beta b$ is shown in Fig. 7. Note that we use $1/s$ to represent the slope, since paths parallel to the binodal in the limit $\mu_s \to -\infty$ are vertical, i.e., $s \to \infty$. For convenience, we also indicate the slope $s$ in the auxiliary $x$ axis of Fig. 7.

From $s \approx 1.7$ to $s \approx 2.5$ we find the four layer stacking sequence $ININ$, which we investigated in detail for the illustrative slope $s = 2$ in Fig. 5. For all negative slopes $(s < 0)$ the sequence $NI$ is the only possible stacking sequence. Positive slopes up to $s \approx 1.7$ exclusively produce the $IN$ stacking sequence. For $s \gtrsim 2.5$ we find the stacking sequences $INI$ and $I$, depending on the root of the sedimentation path.

The stacking sequences that occur in finite samples are always subsequences of the infinite height limit. Hence, we conclude from Fig. 7 that $s = 2$ and $s = 3.58$ capture the essence and all the interesting phenomenology of the binary mixture of plates and spheres. This includes, among others, floating nematic phases $INI$, a four-layer stacking sequence $ININ$, and the occurrence of an $IN$ reentrant sequence.

## IV. CONCLUSIONS

We have studied the sedimentation-diffusion-equilibrium of a simple binary mixture with only one anisotropic species and restricting the bulk to isotropic and uniaxial nematic phases (i.e., no positional order). The corresponding stacking diagram is substantially richer than the bulk phase diagram, with stacking sequences made of up to four layers and the occurrence of reentrant sequences. The topology of the stacking diagram depends on the sample height and on the buoyant mass ratio. An analysis of the stacking diagram in the limit of samples with infinite height reveals that the two buoyant mass ratios considered here, $s = 2$ and $s = 3.58$, capture most of the sedimentation phenomenology of the mixture. Experimentally, it might be possible to alter the buoyant mass ratio by changing the material of the colloidal cores and/or the solvent mass density. Alternatively, using magnetic colloidal spheres [51,52] and an external magnetic field parallel to the gravitational field should effectively have the same effect as varying the buoyant mass ratio of the mixture.

Analysing the effect of the sample height, we have seen that layers appear in a stacking sequence at both the top and the bottom of the sample by increasing the height while keeping the colloidal concentrations constant. Layers can also disappear from the sequence in the middle of a sample [28] such that formerly separated layers merge by changing the sample height. The vanishing of a middle layer has not been

observed here for the considered heights and buoyant mass ratios. The phenomenology found here is therefore complementary to the observation in Ref. [28] and highlights again the relevance of the sample height in sedimentation experiments [27]. Moreover, it shows that *a priori* one does not know where the next layer will form or vanish when transitioning from one sequence to another.

Stacking sequences with three or more layers are often found in sedimentation experiments on colloidal mixtures [11,33,34,53,54]. If both the buoyant masses and the bulk of the mixture are known, the value of the thicknesses of the layers in one of such multi layer sample is enough to uniquely locate the corresponding sedimentation path [11,28]. Knowledge of the particle dimensions is required to construct a theory for the bulk. We have shown here that it is also possible to use the layer thicknesses and the bulk diagram to find the set of all possible sedimentation paths associated to the sample. The set of paths can then be used to estimate the buoyant masses via the colloidal concentrations and vice versa. Including the dimensions of the particles as additional free parameters (i.e., allowing the bulk behavior of the mixture to change) is also possible. Then, a set of experimental samples that differ in their sample heights could provide sufficient information to estimate microscopic parameters such as the particle dimensions and buoyant masses. The required information from the experiments would simply consist of the layer thicknesses, which might be directly measured from the sample images.

The hard particle models used here for both the spheres and the plates are monodisperse. However, size- and therefore mass-polydispersity are inherent to essentially any colloidal system. Several works have considered the effect of polydispersity on the bulk phenomena of a system, see, e.g., Ref. [55] for a review. In contrast, very little is known about the interplay between polydispersity and gravity in sedimentation-diffusion-equilibrium. We will report on the extension of sedimentation path theory to polydisperse colloidal systems in a future publication.

Sedimentation path theory is based on a local equilibrium condition. A sample under gravity is described as a collection of bulk systems with local chemical potentials fixed according to the value of the vertical coordinate. The theory can be used to describe sedimentation in any colloidal mixture, including polymer-colloid mixtures. The addition of polymers to a colloidal suspension can be used to tune the bulk phase behavior of the colloids [56,57] and therefore also the stacking diagram.

An approach conceptually similar to sedimentation path theory that also relies on local equilibrium conditions has been recently used to study sedimentation profiles of molecular systems in centrifugal fields [58]. Even though the gravitational field is not constant under centrifugation, the sedimentation paths are still lines in the space of chemical potentials. Hence, following the ideas of sedimentation path theory it should be possible to construct the stacking diagrams of both colloidal [59] and molecular mixtures under centrifugation.

## ACKNOWLEDGMENTS

This work is supported by the German Research Foundation (DFG) via Project No. 436306241. Publication costs partially funded by the DFG Project No. 491183248 and the Open Access Publishing Fund of the University of Bayreuth.

## APPENDIX: METHODS

**Bulk phase behaviour**. We use classical density functional theory (DFT) [37] to obtain the thermodynamic bulk equilibrium states of our plate-sphere mixture. The total Helmholtz free energy $F$ is comprised of the ideal and the excess contributions ($F = F^{\mathrm{id}} + F^{\mathrm{exc}}$). The ideal contribution to $F$ at temperature $T$ for a mixture is given exactly by

$$\beta F^{\mathrm{id}} = \sum_i \int dr \int d\boldsymbol{\omega} \rho_i(\boldsymbol{r}, \boldsymbol{\omega}) \left[\ln\left(\rho_i(\boldsymbol{r}, \boldsymbol{\omega})\Lambda_i^3\right) - 1\right], \quad \text{(A1)}$$

where the sum runs over both species, $\Lambda_i$ is the thermal wavelength of species $i = \mathrm{p}, \mathrm{s}$, and $\rho_i(\boldsymbol{r}, \boldsymbol{\omega})$ is the one-body density profile of species $i$ at position $\boldsymbol{r}$ and orientation specified by the unit vector $\boldsymbol{\omega}$. Since we consider only phases without positional order, we average out all positions $\boldsymbol{r}$ and introduce the angular distribution function $\psi_i(\boldsymbol{\omega})$ of species $i$ via $\rho_i(\boldsymbol{r}, \boldsymbol{\omega}) = \rho_i \psi_i(\boldsymbol{\omega})$ and normalization $\int d\boldsymbol{\omega} \psi_i(\boldsymbol{\omega}) = 1$. For spheres the general formalism simplifies by using a uniform angular distribution function $\psi_{\mathrm{s}} = 1/(4\pi)$. Hence, $\rho_i$ is the number density of species $i$ and we obtain

$$\frac{\beta F^{\mathrm{id}}}{N} = \sum_i x_i \int d\boldsymbol{\omega} \psi_i(\boldsymbol{\omega}) \left[\ln\left(\psi_i(\boldsymbol{\omega})\rho_i\Lambda_i^3\right) - 1\right], \quad \text{(A2)}$$

where $N$ is the total number of particles in the system and $x_i$ is the composition of species $i$.

For the excess (over ideal) contribution to the free energy $F^{\mathrm{exc}}$, we use an Onsager-like approximation with Parsons-Lee [60,61] rescaling:

$$\frac{\beta F^{\mathrm{exc}}}{N} = \Psi(\eta)\rho \sum_{i,j} x_i x_j \int d\boldsymbol{\omega} \int d\boldsymbol{\omega}' \times \psi_i(\boldsymbol{\omega})\psi_j(\boldsymbol{\omega}') V_{i,j}^{\mathrm{ex}}(\boldsymbol{\omega}, \boldsymbol{\omega}'), \quad \text{(A3)}$$

with total density $\rho = \sum_i \rho_i$ and $V_{i,j}^{\mathrm{ex}}(\boldsymbol{\omega}, \boldsymbol{\omega}')$ being the excluded volume (i.e., the volume inaccessible to one particle due to the presence of another particle) between particles of species $i$ and $j$ with orientations $\boldsymbol{\omega}$ and $\boldsymbol{\omega}'$, respectively. Here $\Psi(\eta)$ is a scalar function of the total packing fraction $\eta = \rho \sum_i x_i v_i = \sum_i \eta_i$, with $v_i$ being the particle volume of species $i$.

The plates are modelled using hard cylinders (see Fig. 1). For all types of interparticle interactions, (i.e., cylinder-cylinder, cylinder-sphere, and sphere-sphere) there exist analytical expressions for the excluded volumes [17,36,62]. The excluded volume between a cylinder and a sphere, and that between two spheres are independent of the orientation of the particles.

We restrict ourselves to uniaxial situations as reported in the experimental study [11]. Also, in the closely related system of hard cut spheres, the uniaxial nematic is the only stable nematic phase for thickness-to-diameter aspect ratios $\leqslant 0.1$ [63] (note that in our system the aspect ratio is 0.001). Only for aspect ratios $\geqslant 0.15$ the cubatic phase was found to be

more stable than the uniaxial nematic [63]. Hence, the angular distribution function of plates depends only on the polar angle $\theta$ (measured with respect to the director)

$$\psi_{\rm p}(\theta) = \frac{1}{2\pi}\int_0^{2\pi} d\varphi \psi_{\rm p}(\boldsymbol{\omega}). \tag{A4}$$

We, therefore, average in advance the excluded volume over the azimuthal angle $\varphi$ and only retain the polar dependency, $V_{i,j}^{\rm ex}(\theta,\theta')$.

The prefactor $\Psi(\eta)$ in front of the excess free energy in Eq. (A3) rescales the second virial coefficient in the original Onsager's expression [36] by the Carnahan-Starling equation of state [64] of a reference system of hard spheres at the same packing fraction

$$\Psi(\eta) = \frac{4-3\eta}{8(1-\eta)^2}. \tag{A5}$$

The topology of the bulk phase diagram does not change with the scaling, which serves to improve the agreement of the $I-N$ transition densities compared to computer simulations [65]. Note that in the low density limit we recover the second virial coefficient, like in the original Onsager expression [36], since $\Psi(\eta\to 0) = 1/2$. Onsager-like density functional theories rely on two-body correlations and can fail to describe the bulk if the symmetries of the stable bulk phases are the result of three- and higher-body correlations [66]. This is not the case here since the excluded volume between two cylinders is minimal if both particles are parallel to each other, i.e., like in the uniaxial nematic phase. We therefore expect the functional to properly describe the topology of the bulk phase diagram.

**Minimization of the functional.** We perform a numerical Picard [67] iteration to minimize the total Helmholtz free energy with respect to the discretized angular distribution function of plates $\psi_{\rm p}(\theta)$ on a one dimensional grid with 160 points.

We calculate the uniaxial order parameter according to

$$S_{\rm p} = \int d\theta \frac{3\cos^2(\theta)-1}{2}\psi_{\rm p}(\theta). \tag{A6}$$

**Bulk Coexistence.** To obtain the bulk phase diagram we use the Gibbs ensemble and numerically minimize the Gibbs free energy per particle

$$g_{\rm b} = \frac{F}{N} + \frac{P}{\rho}, \tag{A7}$$

where $P$ is the osmotic pressure and $\rho = \rho_{\rm p} + \rho_{\rm s}$ is the total number density. For phase coexistence we need mechanical, thermal and chemical equilibrium. The first two conditions are fulfilled in the Gibbs ensemble by construction ($P$ and $T$ are fixed). To find chemical equilibrium we search for a common-tangent construction on $g_{\rm b}(x_{\rm s})$, with $x_{\rm s} = \rho_{\rm s}/\rho$ the composition of spheres. Hence, we numerically minimize the Gibbs free energy per particle $g_{\rm b}$ with respect to the total density $\rho$ and the orientational distribution function of plates $\psi_{\rm p}(\theta)$ for fixed values of $P$, $T$, and $x_{\rm s}$, and then search for a common tangent.

**Average colloidal packing fractions in a sample.** To find the colloidal packing fractions along a sedimentation path we work in the grand canonical ensemble since the paths are lines in the plane of chemical potentials. We minimize the grand canonical potential $\Omega$ per unit of volume

$$\frac{\Omega}{V} = \frac{F}{V} - \rho\sum_i \mu_i x_i, \tag{A8}$$

with respect to $\psi_{\rm p}(\theta)$, $x_i$, and $\rho$ at fixed values of the chemical potentials. We repeat the minimization for each point along the sedimentation path. From the values of the packing fractions $\eta_i = x_i v_i \rho$ at each point along the path we obtain the average packing fractions $\bar{\eta}_i$, $i = {\rm p}, {\rm s}$ in the corresponding sample.


[1] C. T. Lant, A. E. Smart, D. S. Cannell, W. V. Meyer, and M. P. Doherty, Physics of hard spheres experiment: A general-purpose light-scattering instrument, Appl. Opt. **36**, 7501 (1997).

[2] Z. Cheng, P. M. Chaikin, J. Zhu, W. B. Russel, and W. V. Meyer, Crystallization Kinetics of Hard Spheres in Microgravity in the Coexistence Regime: Interactions between Growing Crystallites, Phys. Rev. Lett. **88**, 015501 (2001).

[3] A. E. Bailey, W. C. K. Poon, R. J. Christianson, A. B. Schofield, U. Gasser, V. Prasad, S. Manley, P. N. Segre, L. Cipelletti, W. V. Meyer, M. P. Doherty, S. Sankaran, A. L. Jankovsky, W. L. Shiley, J. P. Bowen, J. C. Eggers, C. Kurta, T. Lorik, P. N. Pusey, and D. A. Weitz, Spinodal Decomposition in a Model Colloid-Polymer Mixture in Microgravity, Phys. Rev. Lett. **99**, 205701 (2007).

[4] J. Baird and J. Walz, The effects of added nanoparticles on aqueous kaolinite suspensions, J. Colloid Interface Sci. **297**, 161 (2006).

[5] J. Baird and J. Walz, The effects of added nanoparticles on aqueous kaolinite suspensions: II. Rheological effects, J. Colloid Interface Sci. **306**, 411 (2007).

[6] S. M. Oversteegen, C. Vonk, J. E. G. J. Wijnhoven, and H. N. W. Lekkerkerker, Crystallization in settling mixtures of colloidal spheres and plates, Phys. Rev. E **71**, 041406 (2005).

[7] D. Kleshchanok, A. V. Petukhov, P. Holmqvist, D. V. Byelov, and H. N. W. Lekkerkerker, Structures and phase behavior in mixtures of charged colloidal spheres and platelets, Langmuir **26**, 13614 (2010).

[8] D. Kleshchanok, J.-M. Meijer, A. V. Petukhov, G. Portale, and H. N. W. Lekkerkerker, Sedimentation and depletion attraction directing glass and liquid crystal formation in aqueous platelet/sphere mixtures, Soft Matter **8**, 191 (2012).

[9] N. Doshi, G. Cinacchi, J. S. van Duijneveldt, T. Cosgrove, S. W. Prescott, I. Grillo, J. Phipps, and D. I. Gittins, Structure of colloidal sphere–plate mixtures, J. Phys.: Condens. Matter **23**, 194109 (2011).

[10] D. Kleshchanok, J.-M. Meijer, A. V. Petukhov, G. Portale, and H. N. W. Lekkerkerker, Attractive glass formation in aqueous mixtures of colloidal gibbsite platelets and silica spheres, Soft Matter **7**, 2832 (2011).

[11] D. de las Heras, N. Doshi, T. Cosgrove, J. Phipps, D. I. Gittins, J. S. V. Duijneveldt, and M. Schmidt, Floating nematic phase in colloidal platelet-sphere mixtures, Sci. Rep. **2**, 789 (2012).

[12] M. Chen, H. Li, Y. Chen, A. F. Mejia, X. Wang, and Z. Cheng, Observation of isotropic–isotropic demixing in colloidal platelet–sphere mixtures, Soft Matter **11**, 5775 (2015).

[13] M. Chen, M. He, P. Lin, Y. Chen, and Z. Cheng, Staged phase separation in the I–I–N tri–phase region of platelet–sphere mixtures, Soft Matter **13**, 4457 (2017).

[14] S. M. Oversteegen and H. N. W. Lekkerkerker, Phase diagram of mixtures of hard colloidal spheres and discs: A free-volume scaled-particle approach, J. Chem. Phys. **120**, 2470 (2004).

[15] D. de las Heras and M. Schmidt, Bulk fluid phase behaviour of colloidal platelet–sphere and platelet–polymer mixtures, Philos. Trans. R. Soc. A **371**, 20120259 (2013).

[16] F. Gámez, R. D. Acemel, and A. Cuetos, Demixing and nematic behaviour of oblate hard spherocylinders and hard spheres mixtures: Monte Carlo simulation and Parsons-Lee theory, Mol. Phys. **111**, 3136 (2013).

[17] R. Aliabadi, M. Moradi, and S. Varga, Tracking three-phase coexistences in binary mixtures of hard plates and spheres, J. Chem. Phys. **144**, 074902 (2016).

[18] L. Harnau and S. Dietrich, Depletion potential in colloidal mixtures of hard spheres and platelets, Phys. Rev. E **69**, 051501 (2004).

[19] L. Harnau and S. Dietrich, Bulk and wetting phenomena in a colloidal mixture of hard spheres and platelets, Phys. Rev. E **71**, 011504 (2005).

[20] A. Esztermann, H. Reich, and M. Schmidt, Density functional theory for colloidal mixtures of hard platelets, rods, and spheres, Phys. Rev. E **73**, 011409 (2006).

[21] L. Harnau and S. Dietrich, in *Inhomogeneous Platelet and Rod Fluids* (Wiley-VCH, Weinheim, 2014), pp. 159–160.

[22] S. D. Peroukidis, A. G. Vanakaras, and D. J. Photinos, Liquid crystalline phases and demixing in binary mixtures of shape-anisometric colloids, J. Mater. Chem. **20**, 10495 (2010).

[23] G. Cinacchi, N. Doshi, S. W. Prescott, T. Cosgrove, I. Grillo, P. Lindner, J. S. Phipps, D. Gittins, and J. S. van Duijneveldt, The effect of size ratio on the sphere structure factor in colloidal sphere-plate mixtures, J. Chem. Phys. **137**, 204909 (2012).

[24] J. Sui, M. Doi, and Y. Ding, Dynamics of the floating nematic phase formation in platelet suspension with thickness polydispersity by sedimentation, Soft Matter **14**, 8956 (2018).

[25] J. Sui, Stratification in the dynamics of sedimenting colloidal platelet–sphere mixtures, Soft Matter **15**, 4714 (2019).

[26] D. de las Heras and M. Schmidt, The phase stacking diagram of colloidal mixtures under gravity, Soft Matter **9**, 8636 (2013).

[27] T. Geigenfeind and D. de las Heras, The role of sample height in the stacking diagram of colloidal mixtures under gravity, J. Phys.: Condens. Matter **29**, 064006 (2017).

[28] T. Eckert, M. Schmidt, and D. de las Heras, Gravity-induced phase phenomena in plate-rod colloidal mixtures, Commun. Phys. **4**, 202 (2021).

[29] D. de las Heras and M. Schmidt, Sedimentation stacking diagram of binary colloidal mixtures and bulk phases in the plane of chemical potentials, J. Phys.: Condens. Matter **27**, 194115 (2015).

[30] G. Avvisati, T. Dasgupta, and M. Dijkstra, Fabrication of colloidal laves phases via hard tetramers and hard spheres: Bulk phase diagram and sedimentation behavior, ACS Nano **11**, 7702 (2017).

[31] T. Drwenski, P. Hooijer, and R. van Roij, Sedimentation stacking diagrams of binary mixtures of thick and thin hard rods, Soft Matter **12**, 5684 (2016).

[32] R. Braz Teixeira, D. de las Heras, J. M. Tavares, and M. M. Telo da Gama, Phase behavior of a binary mixture of patchy colloids: Effect of particle size and gravity, J. Chem. Phys. **155**, 044903 (2021).

[33] F. M. van der Kooij and H. N. W. Lekkerkerker, Liquid-Crystalline Phase Behavior of a Colloidal Rod-Plate Mixture, Phys. Rev. Lett. **84**, 781 (2000).

[34] F. M. van der Kooij and H. N. W. Lekkerkerker, Liquid-crystal phases formed in mixed suspensions of rod- and platelike colloids, Langmuir **16**, 10144 (2000).

[35] L. Mederos, E. Velasco, and Y. Martínez-Ratón, Hard-body models of bulk liquid crystals, J. Phys.: Condens. Matter **26**, 463101 (2014).

[36] L. Onsager, The effects of shape on the interaction of colloidal particles, Ann. N.Y. Acad. Sci. **51**, 627 (1949).

[37] R. Evans, The nature of the liquid-vapour interface and other topics in the statistical mechanics of non-uniform, classical fluids, Adv. Phys. **28**, 143 (1979).

[38] R. Roth, Fundamental measure theory for hard-sphere mixtures: A review, J. Phys.: Condens. Matter **22**, 063102 (2010).

[39] S.-D. Zhang, P. A. Reynolds, and J. S. van Duijneveldt, Phase behavior of mixtures of colloidal platelets and nonadsorbing polymers, J. Chem. Phys. **117**, 9947 (2002).

[40] H. Reich and M. Schmidt, Sedimentation equilibrium of colloidal platelets in an aligning magnetic field, J. Chem. Phys. **132**, 144509 (2010).

[41] Á. González García, R. Tuinier, J. V. Maring, J. Opdam, H. H. Wensink, and H. N. W. Lekkerkerker, Depletion-driven four-phase coexistences in discotic systems, Mol. Phys. **116**, 2757 (2018).

[42] V. F. D. Peters, M. Vis, A. G. García, H. H. Wensink, and R. Tuinier, Defying the Gibbs Phase Rule: Evidence for an Entropy-Driven Quintuple Point in Colloid-Polymer Mixtures, Phys. Rev. Lett. **125**, 127803 (2020).

[43] V. F. D. Peters, Á. González García, H. H. Wensink, M. Vis, and R. Tuinier, Multiphase coexistences in rod–polymer mixtures, Langmuir **37**, 11582 (2021).

[44] T. Tlusty and S. Safran, Defect-induced phase separation in dipolar fluids, Science **290**, 1328 (2000).

[45] J. Russo, J. M. Tavares, P. I. C. Teixeira, M. M. Telo da Gama, and F. Sciortino, Reentrant Phase Diagram of Network Fluids, Phys. Rev. Lett. **106**, 085703 (2011).

[46] T. Narayanan and A. Kumar, Reentrant phase transitions in multicomponent liquid mixtures, Phys. Rep. **249**, 135 (1994).

[47] E. Zaccarelli, H. Löwen, P. P. F. Wessels, F. Sciortino, P. Tartaglia, and C. N. Likos, Is There a Reentrant Glass in Binary Mixtures? Phys. Rev. Lett. **92**, 225703 (2004).

[48] D. de las Heras, E. Velasco, and L. Mederos, Capillary Smectization and Layering in a Confined Liquid Crystal, Phys. Rev. Lett. **94**, 017801 (2005).

[49] B. K. McCoy, Z. Q. Liu, S. T. Wang, V. P. Panov, J. K. Vij, J. W. Goodby, and C. C. Huang, Surface-induced multiple reentrant transitions, Phys. Rev. E **73**, 041704 (2006).

[50] S. Mandal, S. Lang, M. Gross, M. Oettel, D. Raabe, T. Franosch, and F. Varnik, Multiple reentrant glass transitions in confined hard-sphere glasses, Nat. Commun. **5**, 4435 (2014).
[51] P. Tierno, F. Sagués, T. H. Johansen, and T. M. Fischer, Colloidal transport on magnetic garnet films, Phys. Chem. Chem. Phys. **11**, 9615 (2009).
[52] P. Tierno, Recent advances in anisotropic magnetic colloids: realization, assembly and applications, Phys. Chem. Chem. Phys. **16**, 23515 (2014).
[53] L. Luan, W. Li, S. Liu, and D. Sun, Phase behavior of mixtures of positively charged colloidal platelets and nonadsorbing polymer, Langmuir **25**, 6349 (2009).
[54] P. Woolston and J. S. van Duijneveldt, Three-phase coexistence in colloidal rod–plate mixtures, Langmuir **31**, 9290 (2015).
[55] P. Sollich, Predicting phase equilibria in polydisperse systems, J. Phys.: Condens. Matter **14**, R79 (2002).
[56] H. N. W. Lekkerkerker and R. Tuinier, *Colloids and the Depletion Interaction* (Springer Netherlands, Dordrecht, 2011).
[57] F. M. van der Kooij, M. Vogel, and H. N. W. Lekkerkerker, Phase behavior of a mixture of platelike colloids and nonadsorbing polymer, Phys. Rev. E **62**, 5397 (2000).
[58] S. Stemplinger, S. Prévost, T. Zemb, D. Horinek, and J.-F. Dufrêche, Theory of ternary fluids under centrifugal fields, J. Phys. Chem. B **125**, 12054 (2021).
[59] C. S. Plüisch, R. Stuckert, and A. Wittemann, Direct measurement of sedimentation coefficient distributions in multimodal nanoparticle mixtures, Nanomaterials **11**, 1027 (2021).
[60] J. D. Parsons, Nematic ordering in a system of rods, Phys. Rev. A **19**, 1225 (1979).
[61] S. Lee, A numerical investigation of nematic ordering based on a simple hard-rod model, J. Chem. Phys. **87**, 4972 (1987).
[62] B. M. Mulder, The excluded volume of hard sphero-zonotopes, Mol. Phys. **103**, 1411 (2005).
[63] P. D. Duncan, M. Dennison, A. J. Masters, and M. R. Wilson, Theory and computer simulation for the cubatic phase of cut spheres, Phys. Rev. E **79**, 031702 (2009).
[64] N. F. Carnahan and K. E. Starling, Equation of state for nonattracting rigid spheres, J. Chem. Phys. **51**, 635 (1969).
[65] S. Varga, A. Galindo, and G. Jackson, Global fluid phase behavior in binary mixtures of rodlike and platelike molecules, J. Chem. Phys. **117**, 7207 (2002).
[66] Y. Martínez-Ratón and E. Velasco, Failure of standard density functional theory to describe the phase behavior of a fluid of hard right isosceles triangles, Phys. Rev. E **104**, 054132 (2021).
[67] E. Picard, Sur l'application des méthodes d'approximations successives á l'étude de certaines équations différentielles ordinaires, J. Math. Pures Appl. **9**, 217 (1893).

The Journal of Chemical Physics ARTICLE scitation.org/journal/jcp

# Sedimentation path theory for mass-polydisperse colloidal systems

Cite as: J. Chem. Phys. 157, 234901 (2022); doi: 10.1063/5.0129916
Submitted: 7 October 2022 • Accepted: 28 November 2022 •
Published Online: 15 December 2022



Tobias Eckert, Matthias Schmidt,[a] and Daniel de las Heras[b]

AFFILIATIONS

Theoretische Physik II, Physikalisches Institut, Universität Bayreuth, D-95440 Bayreuth, Germany

[a]Matthias.Schmidt@uni-bayreuth.de
[b]Author to whom correspondence should be addressed: delasheras.daniel@gmail.com. URL: https://www.danieldelasheras.com

ABSTRACT

Both polydispersity and the presence of a gravitational field are inherent to essentially any colloidal experiment. While several theoretical works have focused on the effect of polydispersity on the bulk phase behavior of a colloidal system, little is known about the effect of a gravitational field on a polydisperse colloidal suspension. We extend here the sedimentation path theory to study sedimentation–diffusion–equilibrium of a mass-polydisperse colloidal system: the particles possess different buoyant masses but they are otherwise identical. The model helps to understand the interplay between gravity and polydispersity on sedimentation experiments. Since the theory can be applied to any parent distribution of buoyant masses, it can also be used to study the sedimentation of monodisperse colloidal systems. We find that mass-polydispersity has a strong influence in colloidal systems near density matching for which the bare density of the colloidal particles equals the solvent density. To illustrate the theory, we study crystallization in sedimentation–diffusion–equilibrium of a suspension of mass-polydisperse hard spheres.



## I. INTRODUCTION

A certain degree of polydispersity in the size and the shape of the particles, for example, is inherent to all natural colloids. Even though modern synthesis techniques allow the preparation of almost monodisperse colloidal particles,[1–4] a small degree of polydispersity is unavoidable. Understanding bulk phase equilibria in polydisperse systems is a significant challenge.[5] Polydispersity alters the relative stability between bulk phases.[6–10] Phases that are metastable in the corresponding monodisperse system can become stable due to polydispersity. Examples are the occurrence of hexatic columnar[11] and smectic phases[12] in polydisperse discotic liquid crystals, as well as macrophase separation in diblock copolymer melts.[13] The opposite phenomenon can also occur. For example, crystallization in a suspension of hard-spheres is suppressed above a terminal polydispersity.[14–16] Also, fractionation into several phases appears if the degree of polydispersity is high enough.[17–19] A smectic phase of colloidal rods is no longer stable above a terminal polydispersity in the length of the particles.[20] Dynamical processes, such as shear-induced crystallization,[21] are also affected by polydispersity. During drying, a strong stratification occurs in polydisperse colloidal suspensions,[22,23] and the dynamics of large and small particles is different if the colloidal concentration is large enough.[24,25]

Sedimentation–diffusion–equilibrium experiments are a primary tool to investigate bulk phenomena in colloidal suspensions. However, the effect of the gravitational field on the suspension is far from trivial[26–30] and it needs to be understood in order to draw correct conclusions about the bulk.[31] Gravity adds another level of complexity to the already intricate bulk phenomena of a polydisperse suspension. To understand the interplay between sedimentation and polydispersity, we introduce here a mass-polydisperse colloidal suspension: a collection of colloidal particles with the same size and shape (and also identical interparticle interactions) but with buoyant masses that follow a continuous distribution. Since the interparticle interactions are identical, mass-polydispersity does not have any effect in the bulk phase behavior. Hence, our model isolates the effects of a gravitational field on a polydisperse colloidal system from the effects that shape- and size-polydispersity generate in bulk.

We formulate a theory for mass-polydisperse colloidal systems in sedimentation–diffusion–equilibrium. The theory is based

on sedimentation path theory[32,33] that incorporates the effect of gravity on top of the bulk description of the system. Sedimentation path theory uses a local equilibrium approximation to describe how the chemical potential of a sample under gravity changes with the altitude. So far, sedimentation path theory has been used to study sedimentation in colloidal binary mixtures.[28,31–39] In this work, we extend sedimentation path theory to mass-polydisperse systems. Using statistical mechanics, we obtain the exact expression for the sedimentation path of the mass-polydisperse suspension combining the individual paths of all particles in the distribution. We use a model bulk system to illustrate and highlight the key concepts of the theory, such as the construction of the sedimentation path and that of the stacking diagram (which is the analog of the bulk phase diagram in sedimentation). The theory is general and can be applied to any colloidal system in sedimentation–diffusion–equilibrium. Moreover, the theory contains the description of a monodisperse system as a special limit (delta distribution of the buoyant masses). As a proof of concept, we study sedimentation of a suspension of mass-polydisperse hard-spheres with different buoyant mass distributions. We find that mass-polydispersity plays a major role in systems near density matching. For example, near density matching the packing fraction and the height of the sample at which crystallization is observed in sedimentation–diffusion–equilibrium are strongly influenced by the details of the mass distribution.

## II. THEORY

### A. Bulk

We use classical statistical mechanics to describe the thermodynamic bulk equilibrium of our mass-polydisperse colloidal system. The term bulk refers here to an infinitely large system in which boundary effects can be neglected and that is not subject to any external field. The particles differ only in their buoyant masses. Since the buoyant mass does not play any role in bulk, the bulk phenomenology of our model is identical to that of a monocomponent system in which only one buoyant mass is present. Only when gravity is incorporated into both systems the buoyant mass becomes a relevant parameter and the behavior of the mass-polydisperse and the monodisperse colloidal systems will differ from each other.

The total Helmholtz free energy $F$ is the sum of the ideal and the excess contributions, i.e., $F = F^{\mathrm{id}} + F^{\mathrm{exc}}$. In a mass-polydisperse system, the free energy is a functional of $\rho_m$, the density distribution of species with buoyant mass $m$. For simplicity, we work with a scaled, dimensionless, buoyant mass $m = m_b/m_0$, where $m_b$ is the actual buoyant mass of a particle and $m_0$ is a reference buoyant mass. Sensible choices relate $m_0$ to, e.g., the average buoyant mass of the distribution or its standard deviation. The concrete definition of $m_0$ is given below in each considered system.

The ideal contribution to the free energy is a functional of $\rho_m$ and is given exactly by

$$F^{\mathrm{id}}[\rho_m] = k_{\mathrm{B}}T \int \mathrm{d}m\, \rho_m(\ln(\rho_m) - 1), \tag{1}$$

where $k_{\mathrm{B}}$ is the Boltzmann's constant and $T$ is the absolute temperature. Without loss of generality, we measure $\rho_m$ relative to the thermal de Broglie wavelengths $\Lambda_m = \sqrt{2\pi\hbar^2/(m_b k_{\mathrm{B}}T)}$ with reduced Planck's constant $\hbar$. Note that the value of $\Lambda_m$ does not play any role here since altering $\Lambda_m$ simply adds a term to the free energy that is proportional to the total number of particles with buoyant mass $m$. Such term can be reinterpreted as a change of the origin of the chemical potential of the species with buoyant mass $m$.

The integration over $m$ in Eq. (1) reflects the fact that due to the mass-polydispersity, the buoyant mass is a continuous variable. For the sake of simplicity, we omit the positional argument $\boldsymbol{r}$ in the density distribution as well as its corresponding space integral that appear in bulk-phases with positional order such as crystalline phases.

The ideal free energy [Eq. (1)] accounts for the entropy of mixing of our mass-polydisperse system. The overall density across all species $\rho$ follows directly from the density distribution of buoyant masses

$$\rho = \int \mathrm{d}m\, \rho_m. \tag{2}$$

Since the interparticle interaction is independent of the buoyant masses of the particles, only the density across all species $\rho$ enters into the excess (over ideal) free energy. Hence, the excess free energy functional must satisfy

$$F^{\mathrm{exc}}[\rho_m] = F^{\mathrm{exc}}[\rho]. \tag{3}$$

The grand potential is also a functional of $\rho_m$ given by

$$\Omega[\rho_m] = F^{\mathrm{id}}[\rho_m] + F^{\mathrm{exc}}[\rho] - \int \mathrm{d}m\, \rho_m \mu_m, \tag{4}$$

where $\mu_m$ is the chemical potential of the species with buoyant mass $m$. In equilibrium $\Omega[\rho_m]$ is minimal with respect to the mass-density distribution, i.e.,

$$\frac{\delta\Omega[\rho_m]}{\delta\rho_{m'}} = 0. \tag{5}$$

The Euler–Lagrange equation associated with Eq. (5) (see derivation in the Appendix) reads

$$\ln(\rho_m) - \ln(\rho) + \beta\mu - \beta\mu_m = 0, \tag{6}$$

where $\mu$ is the chemical potential of a monodisperse system with overall density $\rho$ [see Eq. (2)]. Hence, it follows from Eq. (6) that the density of particles with buoyant mass $m$ can be written as

$$\rho_m = \rho e^{\beta(\mu_m - \mu)}. \tag{7}$$

Integrating Eq. (7) over $m$ on both sides, and using Eq. (2) on the left-hand side, leads to

$$\rho = \rho \int \mathrm{d}m\, e^{\beta(\mu_m - \mu)}. \tag{8}$$

Since $\rho \neq 0$, we obtain

$$e^{\beta\mu} = \int \mathrm{d}m\, e^{\beta\mu_m}, \tag{9}$$

which constitutes an exact analytic expression for the chemical potential of the monodisperse bulk system

$$\mu = k_{\mathrm{B}}T \ln\left(\int \mathrm{d}m\, e^{\beta\mu_m}\right), \tag{10}$$

in terms of the chemical potentials of the individual species $\mu_m$ in the mass-polydisperse system. In a monodisperse system, there exists only a single species and Eq. (10) holds trivially.

### B. Particle model

To proceed, we need the bulk equation of state (EOS) of the monodisperse colloidal system, $\rho_{\mathrm{EOS}}(\mu)$. Given an interparticle interaction potential, several methods can be used to obtain the corresponding bulk EOS. These include, e.g., density functional theory,[40] liquid state integral equation theory,[41–43] computer simulations,[44–46] and empirical expressions.[47–49] Here, and with the only purpose of illustrating our theory, we use a model (fabricated) EOS that contains two phase transitions [see Fig. 1(a)]. Our model EOS satisfies both the ideal gas limit

$$\lim_{\mu\to-\infty}\rho_{\mathrm{EOS}}(\mu)\sim e^{\beta\mu} \tag{11}$$

and also the close packing limit characteristic of systems with hard core interactions

$$\lim_{\mu\to\infty}\eta_{\mathrm{EOS}}(\mu)/\eta_{\mathrm{cp}}=1, \tag{12}$$

where $\eta_{\mathrm{EOS}}$ is the packing fraction (percentage of volume occupied by the particles) according to the EOS and $\eta_{\mathrm{cp}}$ is the close packing fraction. Such EOS could represent, e.g., a lyotropic colloidal system with two first-order bulk phase transition, say isotropic–nematic and nematic–smectic.

Apart from the model EOS, we also illustrate and validate the theory by studying sedimentation of a suspension of hard-spheres. We use the analytical EOS proposed by Hall,[50] which describes the liquid ($L$) and solid crystalline ($S$) phases of a hard sphere system.

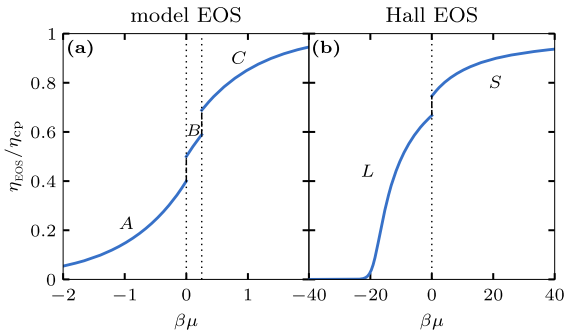


**FIG. 1.** Packing fraction $\eta_{\mathrm{EOS}}$ relative to close packing $\eta_{\mathrm{cp}}$ as a function of the scaled chemical potential $\beta\mu$ for (a) our model equation of state and (b) the Hall equation of state[50] for hard spheres. Our model EOS (a) contains three different bulk phases named *A*, *B*, and *C* that could correspond to, e.g., the isotropic, the nematic, and the smectic phases of a lyotropic liquid crystal. The Hall EOS (b) describes the liquid ($L$) and the solid crystalline ($S$) phases of a hard-sphere system. The vertical dotted lines indicate the chemical potentials of the different bulk phase transitions. Without loss of generality, we have translated the origin of chemical potential such that it coincides with the chemical potential of (a) the *A*–*B* and (b) the *L*–*S* transitions.

The Hall EOS was originally formulated using the compressibility factor as a function of the density. Following Ref. 51, we numerically integrate the analytical Hall EOS to obtain the chemical potential as a function of the density [see Fig. 1(b) for a graphical representation]. It is sufficient to fix $\rho_{\mathrm{EOS}}(\mu)$ up to an arbitrary additive constant in $\mu$. Hence, for convenience, we choose $\mu = 0$ as the chemical potential at the liquid–solid first order phase transition.

### C. Sedimentation

To incorporate gravity into our theory, we extend sedimentation path theory[32,52] as formulated for finite height samples[31,33] to include mass-polydispersity. As often done in colloidal sedimentation, we assume that all horizontal slices of a sample in sedimentation–diffusion–equilibrium can be described as a bulk equilibrium state and also that they are independent of each other. This local-equilibrium approximation is justified if the correlation lengths are small compared to the gravitational lengths $\xi_m = k_{\mathrm{B}}T/(m_b g)$, which is the case in many colloidal systems. Here, $g$ is the acceleration of gravity.

We work in units of the thermal energy $k_{\mathrm{B}}T$, the gravitational constant $g$, and the reference mass $m_0$ for ease of comparability between different systems. Using $m_0$, we define a reference gravitational length $\xi = k_{\mathrm{B}}T/(m_0 g)$, which acts as our fundamental length scale.

We treat the slices for each elevation $z$ as a bulk system with local chemical potentials for each species $\mu_m$ given by

$$\mu_m(z) = \mu_m^0 - m_b g z. \tag{13}$$

Here, $\mu_m^0$ is the chemical potential of the species with buoyant mass $m$ at elevation $z = 0$. The set of constant offsets $\mu_m^0$ in $\mu_m(z)$ is *a priori* unknown and must be determined via an iterative numerical procedure to match the prescribed mass-resolved density distribution $\rho_m$. Returning to the discussion about the thermal wavelengths, altering the value of $\Lambda_m$ would only introduce a constant term $\ln(\Lambda_m)$ in Eq. (6) that can be reabsorbed in Eq. (13) as a shift of the chemical potential $\mu_m$ via the offset $\mu_m^0$. The offsets $\mu_m^0$ depend therefore on the choice of $\Lambda_m$. However, the sedimentation profiles $\rho_m(z)$ remain unchanged, since $\mu_m^0$ are determined to match the prescribed density distribution.

Equation (13) is the sedimentation path[31–33,52] of the species with buoyant mass $m$. It hence describes how the chemical potential of each species varies linearly with $z$ in the range $0 \le z \le h$, with $h$ the sample height. The local chemical potential for each species either decreases ($m_b > 0$) or increases ($m_b < 0$) with the elevation $z$, depending on the sign of the buoyant mass.

The sedimentation path of each species $\mu_m(z)$ is just a straight line [see Fig. 2(a)] as in the case of monodisperse systems. Next, we combine all paths at each elevation $z$ to obtain an effective chemical potential $\mu_{\mathrm{eff}}(z)$. Inserting $\mu_m(z)$ in Eq. (13) into Eq. (10) yields the sedimentation path of a mass-polydisperse system

$$\mu_{\mathrm{eff}}(z) = k_{\mathrm{B}}T\,\ln\left(\int \mathrm{d}m\, e^{\beta(\mu_m^0 - m_b g z)}\right). \tag{14}$$

Equation (14), which has the form of a `LogSumExp` function, describes how the effective chemical potential of the mass-polydisperse system varies vertically along the sample in

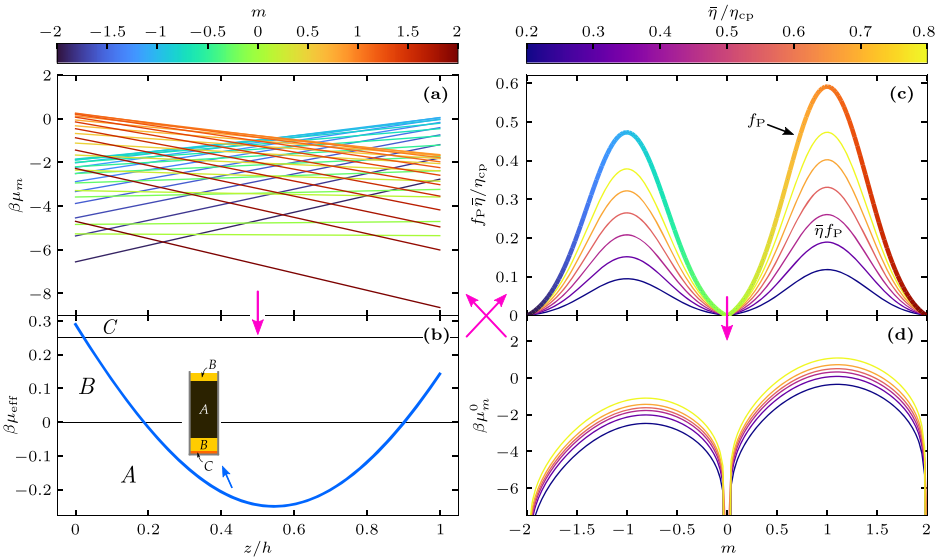


**FIG. 2.** (a) Local chemical potentials $\beta\mu_m(z)$ as a function of the elevation $z$ scaled with the sample height $h$. Each sedimentation path varies linearly with $z$ and it is colored according to the buoyant mass of the species $m$ (top-left color bar). (b) Effective chemical potential $\beta\mu_{\rm eff}(z)$ as a function of the scaled elevation $z/h$. The non-linear sedimentation path of the mass-polydisperse system (b) is the result of combining the sedimentation paths of each species (a) according to the `LogSumExp` structure in Eq. (14). The sedimentation paths are defined in the interval $0 \le z \le h$, and the sample height is $h = 2\xi$. (c) Imposed parent distribution $f_{\rm P}(m)$ and plots of the parent distribution scaled with several values of the average packing fraction $\bar\eta$ (see color bar). The imposed $f_{\rm P}(m)$ and the value of $\bar\eta$ in (c) fix the offsets $\beta\mu_m^0$ for all buoyant masses $m$, which are shown in panel (d). The pink arrows illustrate the iterative procedure to find the effective sedimentation path: for a fixed distribution $f_{\rm P}(m)$ and packing fraction $\bar\eta$ (c), we give an initial guess for the offsets $\mu_m^0$ (d), calculate the individual paths $\mu_m(z)$ (a), and combine them to get the effective path $\mu_{\rm eff}(z)$ (b). Using the effective path, we obtain the density profile and then the resulting distribution of particles and the average packing fraction. With this information, we readjust the offsets $\mu_m^0$ until the output distribution and packing fraction are the desired ones.

sedimentation–diffusion–equilibrium. We give an example of $\mu_{\rm eff}(z)$ in Fig. 2(b). The sedimentation path is obtained from the set of $\mu_m(z)$ in Fig. 2(a) via Eq. (14). The sedimentation path is no longer a straight line even though the individual paths for each species are lines. Since (i) the logarithm is a concave function, (ii) the scalars $\exp(\beta\mu_m^0)$ are positive, and (iii) the exponential is a convex function, it follows that $\mu_{\rm eff}(z)$, as given by Eq. (14), is a convex function of the elevation $z$. This is a strong constraint on the possible shapes of $\mu_{\rm eff}(z)$. It means that (i) $\mu_{\rm eff}(z)$ can have only one minimum and also that (ii) the local maxima of $\mu_{\rm eff}(z)$ in the interval $0 \le z \le h$ are either $z = 0$, $z = h$, or both of them. As we discuss below, the extrema of the path $\mu_{\rm eff}(z)$ are important because they determine the layers of different bulk phases that form in the sample.

Via the equation of state $\rho_{\rm EOS}(\mu)$ for the bulk density, we then obtain the density profile across all species

$$\rho(z) = \rho_{\rm EOS}(\mu_{\rm eff}(z)) \tag{15}$$

at elevation $z$ from Eq. (14).

The density of species with buoyant mass $m$ at elevation $z$ follows then by inserting Eqs. (13)–(15) into Eq. (7),

$$\rho_m(z) = \rho(z) e^{\beta(\mu_m^0 - m_b g z - \mu_{\rm eff}(z))}. \tag{16}$$

The average density of particles with buoyant mass $m$ in a sample with height $h$ is then given by

$$\bar\rho_m = \frac{1}{h}\int_0^h {\rm d}z\, \rho_m(z). \tag{17}$$

The value of $\bar\rho_m$ is also the density of particles with buoyant mass $m$ in the initial distribution, i.e., before the particles sedimented and equilibrated.

The average packing fraction is

$$\bar\eta = \frac{v_0}{h}\int_0^h {\rm d}z\, \rho(z), \tag{18}$$

where $v_0$ is the particle volume.

The parent distribution, which gives the overall probability of finding a particle with buoyant mass $m$ anywhere in the sample, can be obtained as

$$f_{\rm P}(m) = \frac{\bar\rho_m}{\int {\rm d}m\, \bar\rho_m} = \frac{A}{N}\int_0^h {\rm d}z\, \rho_m(z), \tag{19}$$

with $N = hA\int {\rm d}m\, \bar\rho_m = A\int {\rm d}m \int_0^h {\rm d}z\, \rho_m(z)$ the total number of particles, and $A$ being the area of a cross section of the sample. Both $\bar\eta$ and $f_{\rm P}(m)$ are directly comparable with experimental results, since $\bar\eta$ is the concentration of particles in the stock solution (before

sedimentation) and $f_P(m)$ describes the mass-polydispersity of the particles, normalized by the total concentration.

From the definitions (18) and (19), we can get back the average density of specie $m$ via

$$\bar{\rho}_m = \frac{\bar{\eta}}{v_0} f_P(m). \tag{20}$$

To obtain the sedimentation–diffusion–equilibrium of a mass-polydisperse colloidal system, we start prescribing the sample height $h$, the average packing fraction of the sample $\bar{\eta}$, and the parent distribution $f_P(m)$. An illustrative parent distribution that contains particles with both positive and negative buoyant masses is shown in Fig. 2(c). These initial conditions are sufficient to find the as yet undetermined offsets on the chemical potential for each species $\mu_m^0$ [see Eq. (13)]. We discretize $f_P(m)$ and then numerically determine $\mu_m^0$ via a least square algorithm that iteratively solves for the prescribed $\bar{\eta} f_P(m)$ in a sample of height $h$. With the offsets $\mu_m^0$, we calculate the corresponding $\mu_{\text{eff}}(z)$ via Eq. (14). Next, we obtain $\rho(z)$ and $\rho_m(z)$ via Eqs. (15) and (16), respectively. The profiles $\rho(z)$ and $\rho_m(z)$ determine both $\bar{\eta}$ and $f_P(m)$ via Eqs. (18) and (19), respectively. The least square algorithm finds then the offsets that minimize the difference to the prescribed (target) values of $\bar{\eta}$ and $f_P(m)$.

For example, we show in Fig. 2(d) the offsets $\mu_m^0$ corresponding to the distribution prescribed in Fig. 2(c). We discretize in $m$, and hence the number of input variables $\bar{\rho}_m$ and unknown variables $\mu_m^0$ is the same. The self-consistency problem of finding $\mu_m^0$ is therefore well defined. The set of sedimentation paths $\mu_m(z)$ in Fig. 2(a) are obtained with the offsets calculated in Fig. 2(d). The effective sedimentation path $\mu_{\text{eff}}(z)$ [see Fig. 2(b)] of the mass-polydisperse system follows then from the set of paths for each species $\mu_m(z)$.

The sedimentation path of the mass-polydisperse system determines the stacking sequence, i.e., the set of layers of bulk phases that are observed in the sample under gravity. Every time the path crosses the coexistence chemical potential of a bulk transition, an interface between the coexisting phases appears in the cuvette. By looking at the crossings between the sedimentation path and the bulk binodals, we determine the stacking sequence and the position of the interfaces between stacks. For example, the sequence corresponding to the path in Fig. 2(b) is *BABC* (from top to bottom of the sample).

**Extended Gibbs phase rule.** Given the convexity properties of the sedimentation path, recall our discussion following Eq. (14), we conclude that the maximum number of layers that can appear in a sedimented sample of a mass-polydisperse system is $2n_b - 1$, with $n_b$ the number of different stable phases in bulk. This corresponds to the stacking sequence of a mass-polydisperse suspension with positive and negative buoyant masses in which all phases occur repeatedly except the middle layer, which corresponds to the bulk phase stable at low chemical potential. In our model EOS, the stacking sequence with the maximum number of layers is *CBABC*, for which the sedimentation path is similar to the one in Fig. 2(b) but extended such that it reenters the *C* region at high elevations.

If the parent distribution contains only buoyant masses of the same sign, the maximum number of layers in a stacking sequence is simply $n_b$, the number of stable bulk phases.

### D. Stacking diagram

Different sedimentation paths can give rise to distinct stacking sequences. The set of all possible stacking sequences can be represented in a stacking diagram. In binary mixtures, the sedimentation paths of both species vary linearly with $z$. In mass polydisperse systems, we average the linear local chemical potentials $\mu_m(z)$ [Eq. (13)] of all species together, according to Eq. (14), and obtain a non-linear effective chemical potential $\mu_{\text{eff}}(z)$. Even though the sedimentation paths are no longer straight lines, the same ideas as in the case of binary mixtures[31,32] apply for the construction of the stacking diagram. In short, we must find all the sedimentation paths that constitute a boundary between two or more stacking sequences in the stacking diagram. Examples of such paths are shown in Fig. 3(a). The boundary paths are the sedimentation paths $\mu_{\text{eff}}(z)$ that either end [paths 1 and 4 in Fig. 3(a)], start (paths 2 and 5), or are tangent (paths 3 and 6) to a bulk binodal. These paths are a boundary between two or more stacking sequences since an infinitesimal change of the path, in general, alters the stacking sequence. Without gravity (i.e., in bulk), the mass-polydisperse system behaves like a monocomponent system, since the interparticle interaction potential is independent of the buoyant mass. Thus, in bulk, there is only a single relevant chemical potential. In the chemical potential vs height plane, the bulk transitions are simply horizontal lines independent of $z$ [see Fig. 3(a)]. Hence, given that the sedimentation path is convex, a path tangent to a bulk binodal is also a path for which the minimum coincides with the chemical potential of the bulk transition, e.g., paths 3 and 6 in Fig. 3(a). For other types of bulk phase coexistence, such as critical and triple points, the procedure to find the boundary paths is the same as the one just described for a bulk binodal.

Next, we find the total density profile $\rho(z)$ and the average packing fraction $\bar{\eta}$ corresponding to each of the boundary sedimentation paths via Eqs. (15) and (18), respectively. To obtain the full stacking diagram, we repeat the procedure for every sample height $h$ ranging from zero to the desired maximal sample height. This provide us with the stacking diagram in the (experimentally relevant) plane of average packing fraction $\bar{\eta}$ and sample height $h$ [see Fig. 3(b)]. Each point in the stacking diagram represents one sedimentation path and it hence represents one specific sample in sedimentation–diffusion–equilibrium.

For each bulk phase transition, there can be at most three boundary lines in the stacking diagram, so-called sedimentation binodals.[31–33] The sedimentation binodals corresponding to the paths that either start or end at the binodal are always present independently of the parent distribution and the sample height. On the other hand, the sedimentation binodal corresponding to paths tangent to the bulk transition appears if and only if the sedimentation path presents a minimum at intermediate values of $z$. It follows from Eq. (14) that a minimum in $\mu_{\text{eff}}(z)$ not located at the bottom ($z \neq 0$) or the top ($z \neq h$) of the sample can appear only if the parent distribution contains both positive and negative buoyant masses. Even in that case, there might be sample heights for which the path does not have a minimum at intermediate elevations.

In our illustrative example, there are two bulk phase transition ($A$–$B$ and $B$–$C$) [see Fig. 1(a)] and the parent distribution is made of particles with positive and negative buoyant masses [see Fig. 2(c)]. The stacking diagram contains six sedimentation binodals [see Fig. 3(b)]. For sample heights $h/\xi \lesssim 0.4$, only two types of sedimentation binodals can be observed. In this low height regime, we cannot find sedimentation paths tangent to the binodal since $\mu_{\text{eff}}(z)$ does not have a minimum at intermediate elevations $0 < z < h$.

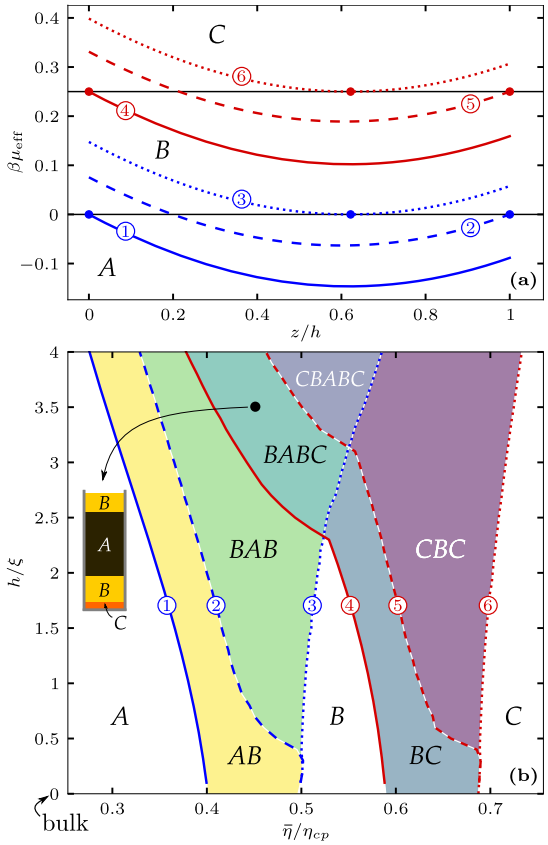


**FIG. 3.** (a) Sedimentation paths in the plane of effective chemical potential $\beta\mu_{\rm eff}$ as a function of the elevation $z/h$ for samples of height $h = 1.7\xi$ and a parent distribution like in Fig. 2(c). The coexistence chemical potentials for the $A$–$B$ ($\mu_{\rm coex} = 0$) and for the $B$–$C$ ($\beta\mu_{\rm coex} = 0.25$) bulk transitions are indicated by solid black horizontal lines. There are six sedimentation paths labeled from 1 to 6. The average packing fraction $\overline{\eta}$ of each sample is such that the corresponding path either ends at (solid paths 1 and 4), starts at (dashed paths 2 and 5), or is tangent to (dotted paths 3 and 6) a bulk binodal (horizontal lines). The points where the paths touch the coexistence bulk chemical potential are marked by solid circles. (b) Stacking diagram in the plane of average packing fraction $\overline{\eta}/\eta_{\rm cp}$ and sample height $h/\xi$ for the model EOS in Fig. 1(a) and parent distribution as in Fig. 2(c). The position of the six boundary sedimentation paths in (a) is marked in (b) using the corresponding labels 1–6. The sedimentation binodals of paths that end, start, and are tangent to the bulk binodals are indicated with solid, dashed, and dotted lines, respectively. The stacking sequences are labeled from the top of the sample to the bottom. Each point in the stacking diagram is a sample in sedimentation. The sketch shows the stacking sequence *BABC* and relative layer thicknesses of the sample with $\overline{\eta}/\eta_{\rm cp} = 0.45$ and $h/\xi = 3.5$ (indicated by a black circle).

Within our local equilibrium approximation, in the limit $h \to 0$, the sedimentation path reduces to a point and hence the stacking diagram reduces to the bulk phase diagram. In a real system, confinement and surface effects, such as wetting and layering, will become relevant in the limit of short sample heights.

**Mass-monodisperse system.** Our method to construct the stacking diagram for mass-polydisperse systems contains as a limiting case the monodisperse system. In a monodisperse system, all particles possess the same buoyant mass. Hence, Eq. (14) reduces to

$$\mu_{\rm eff}(z) = \mu_m(z) = \mu_m^0 - m_b g z. \tag{21}$$

Thus, as expected, the sedimentation path of a monodisperse system is the segment of a line, linear in $z$. In the stacking diagram, only the sedimentation binodals of paths that start, i.e., $\mu_{\rm eff}(h) = \mu_{\rm coex}$, or end, i.e., $\mu_{\rm eff}(0) = \mu_{\rm coex}$, at the bulk binodal (given by $\mu_{\rm coex}$) appear. The sedimentation path of a monodisperse system can never have a minimum at intermediate elevations.

## III. RESULTS

We next apply our theory to the arguably best studied colloidal system to date: hard spheres. We study sedimentation of a mass-polydisperse hard sphere system using the Hall equation of state,[50] represented in the plane of $\mu$ and $\eta$ in Fig. 1(b), to describe the bulk of the system.

### A. Species-resolved probability distributions in mass-polydisperse systems

The imposed parent distribution of the mass-polydisperse system, $f_{\rm P}(m)$, describes the probability of finding a particle with a certain buoyant mass $m$ anywhere in the system. Experimentally, this corresponds to the stock solution. After letting the dispersion settle under gravity to reach sedimentation–diffusion–equilibrium, a height-dependent density profile develops. The overall probability distribution integrated over the whole sample is still $f_{\rm P}(m)$ since particles are conserved. However, at each horizontal slice, the mass composition is generally different from $f_{\rm P}(m)$. One expects, e.g., heavier particles to concentrate next to the bottom of the sample as compared to lighter particles. Sedimentation path theory allows us to carry out a detailed study of the mass distribution along the sample.

We study first a mass-polydisperse dispersion of hard spheres with only positive buoyant mass. The parent distribution is a Gaussian centered around $m = 1$ and cut at $m = 0$ and $m = 2$, i.e., only buoyant masses in the range $0 \le m \le 2$ are allowed. The mean packing fraction is $\overline{\eta}/\eta_{\rm cp} = 0.6$. Under gravity, the sample develops the stacking sequence: top liquid and bottom solid ($LS$). We show the probability $f(m,z)$ of finding a particle with buoyant mass $m$ at elevation $z$ in Fig. 4(a). The probability distribution $f_m(z)$ for a fixed buoyant mass $m$ and resolved in $z$, as well as the probability distribution $f_z(m)$ for a fixed $z$ resolved in $m$ are shown in Figs. 4(b) and 4(c), respectively. The distributions $f_m(z)$ and $f_z(m)$ correspond to vertical and horizontal slices of the full distribution $f(m,z)$, respectively. The distributions $f_z(m)$ are shifted and skewed [Fig. 4(c)] as compared to the parent distribution $f_{\rm P}(m)$ (black dashed line) that is symmetric with respect to $m = 1$. As expected, heavier particles are more frequently found at the bottom of the sample. This becomes more apparent when we look at $f_m(z)$ [Fig. 4(b)]. There is a clear depletion of lighter particles from the bottom of the sample. Interestingly, the probability distribution along $z$ of particles with $m \lesssim 1.01$ is not monotonically increasing toward the bottom of the sample, but has a maximum up to $0.5h$ above the bottom. Lighter particles

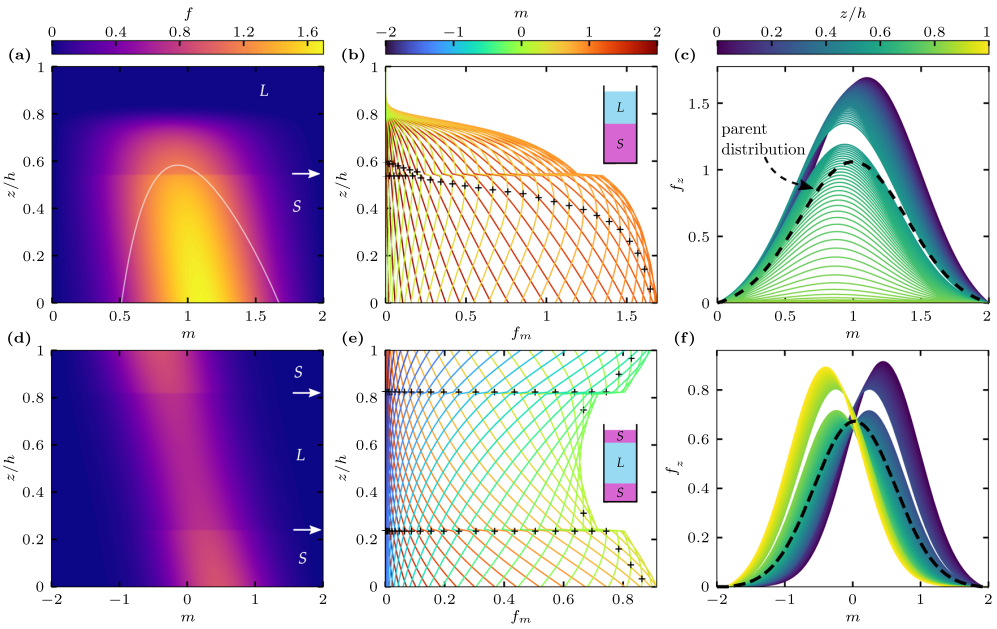


**FIG. 4.** (a) Probability of finding a particle with buoyant mass $m$ at elevation $z$ relative to the sample height $h$ in a hard sphere system modeled using the Hall EOS. The light contour lines in (a) indicate points $(m, z)$ at which the chemical potential $\mu_m(z)$ [see Eq. (13)] is equal to the bulk liquid–solid coexistence chemical potential. The white arrow indicates the position of the liquid ($L$)–solid crystalline ($S$) interface. (b) Vertical slices of panel (a) for fixed buoyant mass $m$ given by the colorbar. The inset is a sketch of the sample. (c) Horizontal slices of panel (a) for fixed elevation $z$ given by the colorbar. The imposed parent distribution $f_P(m)$ is a Gaussian with standard deviation 0.4 and centered around $m = 1$, i.e., the reference buoyant mass $m_0$ is the mean of the parent distribution (see black dashed line). The sample has a height $h = 80\xi$ with gravitational length $\xi$ and a packing fraction $\eta = 0.6\eta_{cp}$, relative to the close packing fraction $\eta_{cp}$. Panels (d)–(f) are the same as panels (a)–(c), but for a Gaussian with standard deviation 0.6 centered around 0.03 as the parent distribution $f_P(m)$ (black dashed line), slightly favoring particles with positive buoyant mass, sample height $h = 120\xi$, and packing fraction $\eta = 0.7\eta_{cp}$. The crosses in (b) and (e) indicate the position of the local maxima in the probability distribution $f_m(z)$ along elevation $z$ for fixed buoyant mass $m$.

are displaced by heavier particles from the bottom as a result of a balance between only two contributions: the gravitational energy and the entropy of mixing. The excess free energy does not play a role in determining the relative position of the particles according to their buoyant masses. Interchanging heavier for lighter particles and vice versa does not alter the overall density, and thus the excess free energy $F^{exc}[\rho]$, which is a functional of only the overall density $\rho$, is not affected.

We also show in Figs. 4(d)–4(f), the mass- and height-resolved probability distributions of a sample with a parent distribution containing both positive and negative buoyant masses. The parent distribution is a Gaussian centered around $m = 0.03$ and cut at $m = \pm 1.9$. The initial packing fraction is $\overline{\eta}/\eta_{cp} = 0.7$ and the stacking sequence is *SLS*. The liquid–solid interfaces occur at elevations $z/h = 0.25$ and 0.8 and are visible as discontinuities of the distribution functions. On the top (bottom) of the sample, particles with negative (positive) buoyant masses are more frequently found. This is visible in Fig. 4(f) as a shift toward negative or positive buoyant masses of the distributions belonging to the solid crystalline layers.

## B. Mass-polydispersity close to density matching

In density matching colloidal experiments, the mass density of the colloidal particles is very close to the mass density of the solvent. If the density match between particle and solvent is perfect, the buoyant mass of the colloids vanishes, and therefore gravity has no effect on the sample. This, in principle, would allow to carry out a direct comparison between bulk phenomena and sedimentation experiments. In practice, however, preparing experimentally a perfect density matching solution is challenging. Density matching is typically achieved by combining solvents with different mass densities in the correct proportions to match the mass density of the particles.[53–56] To sterically stabilize the colloidal particles, they are frequently coated with a polymer layer of a different density than that of the particle core.[57–61] Due to the polydisperse nature of most colloidal systems, the effective particle density (including both the core and the coating layer) can vary between the particles. As a result, not all the particles in the solution can have neutral buoyancy. The buoyant mass of the particles falls within a range roughly centered around neutral buoyancy. In general, there will be particles that have either slightly positive or slightly negative buoyant

masses. We will see here that small deviations from density matching can have a strong effect on sedimentation–diffusion–equilibrium experiments.

We model a system close to density matching by a parent Gaussian distribution $f_P(m)$ roughly centered around a buoyant mass $m = 0$, as shown in Fig. 5(a). We study four different cases, with the mean of the Gaussian $\bar{m}$ slightly shifted in the range of ±0.02, which is ~10% of their standard deviations. The distributions are cut at $m = \pm 0.95$ around their respective mean.

The stacking diagram for the case $\bar{m} = 0$ is shown in Fig. 5(b). Near density matching, the sedimentation paths are rather horizontal and sensitive to the precise form of the parent distribution. Hence, the small deviations between the (imposed) target and the (actual) numerical parent distributions that arise in the iterative procedure due to numerical inaccuracies can have a noticeable effect. This is the reason behind the scattered data points (symbols) in the sedimentation binodals of Fig. 5(b). With a symmetrical parent distribution around $m = 0$ (i.e., $\bar{m} = 0$) neither particles with positive nor with negative buoyant mass are favored. Thus, only symmetric stacking sequences (with respect to the midpoint of the sample $z = h/2$) occur, namely *L*, *S*, and *SLS*. Asymmetric sequences, such as *LS* or *SL*, do not appear.

The situation is different for $\bar{m} = -0.02$, where particles with negative buoyant mass that cream up are predominant [see Fig. 5(c)]. Consequently, we also observe the stacking sequence *SL*, with the denser, solid phase, on top of the sample.

In Figs. 5(d) and 5(e), we show the stacking diagram for the remaining cases $\bar{m} = 0.01$ and 0.02, respectively. For comparison, we show always the sedimentation binodals of the buoyant neutral suspension with $\bar{m} = 0$. The position of the sedimentation binodals for the cases $\bar{m} = -0.02$ and 0.02 are identical, but the associated stacking sequences are inverted. This was expected, since changing from $\bar{m} = -0.02$ to 0.02 is equivalent to inverting the direction of gravity and thus interchanging the meaning of top and bottom of the sample. This is also the reason why we observe the stacking sequence *LS* in Fig. 5(e) in the region occupied by *SL* in Fig. 5(c). The case $\bar{m} = 0.01$ shows the same characteristics as $\bar{m} = 0.02$, but with the position of the sedimentation binodals roughly rescaled in the $h/\xi$ axis by a factor of 1/2, which is the ratio between the mean of the corresponding parent distributions. Most notable, there is a qualitative difference between the case $\bar{m} = 0$ and any other parent distribution considered, namely the lack of asymmetric stacking sequences, such as *LS* and *SL*. Mass-polydispersity therefore plays an important role in colloidal suspensions close to density matching and even small deviation from density matching can have drastic effects on the stacking diagram.

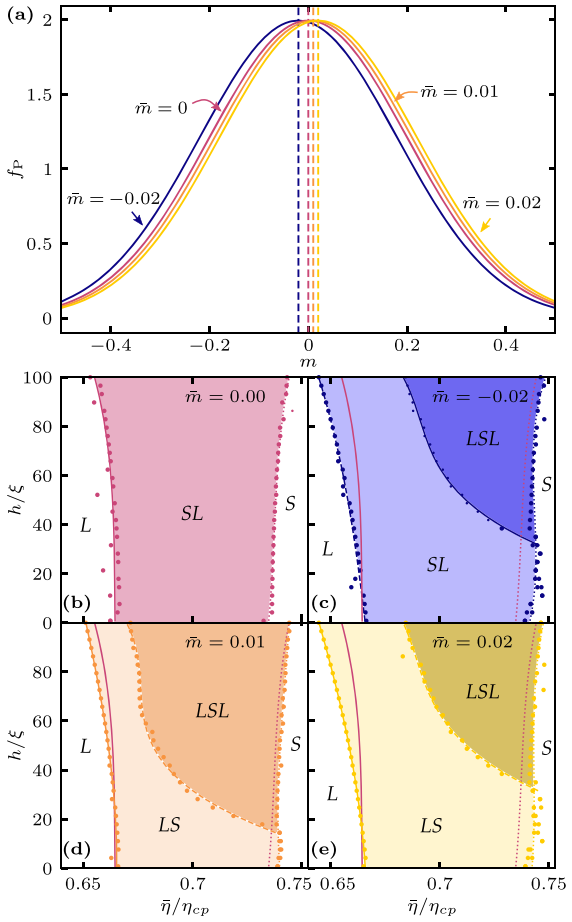


**FIG. 5.** (a) Four parent $f_P$ Gaussian distributions with slightly shifted mean $\bar{m}$ in the range $0 \pm 0.02$, as indicated. The standard deviation is 0.2 in all cases, and the distributions are cut at $m = \pm 0.95$ around their respective mean. The corresponding stacking diagrams for a mass-polydisperse system of hard spheres in the plane of average packing fraction $\bar{\eta}$ (relative to close packing $\eta_{cp}$) and sample height $h$ (relative to the gravitational length $\xi$) are shown in (b) for the parent distributions with $\bar{m} = 0$, in (c) for $\bar{m} = -0.02$, in (d) for $\bar{m} = 0.01$, and in (e) for $\bar{m} = 0.02$. The sedimentation binodals of paths that end, start, and are tangent to the bulk binodals are indicated with solid, dashed, and dotted lines, respectively. The symbols are the data points. The sedimentation binodals of the case $\bar{m} = 0$ are shown for reference in all the stacking stacking diagrams. Note that for the case $\bar{m} = 0$ the sedimentation binodals of paths that either start or end at the bulk transition coincide since the parent distribution is symmetrical around $m = 0$. The bulk system exhibits liquid ($L$) and solid crystalline ($S$) phases. The stacking sequences are labeled from the top to the bottom of the sample.

## C. Mass-polydispersity away from density matching

Not all types of parent distributions are as sensitive to mass-polydispersity as those representing a system near density matching. In many cases, the stacking diagram is robust against perturbations of the parent distribution. To show this, we construct here four classes of parent distributions and calculate the corresponding sedimentation paths. The sedimentation paths are quite similar within each class. We hence can conclude that the corresponding stacking diagrams are also alike. Recall that the stacking diagram is constructed from the set of special paths, $\mu_{\text{eff}}(z)$, that either start at, end at, or are tangent to the bulk binodal (see Fig. 3). Thus, if two systems share similar paths for a range of packing fractions and sample heights, the stacking diagrams will also be similar.

The four classes of parent distributions and the corresponding sedimentation paths are shown in Fig. 6. We construct several

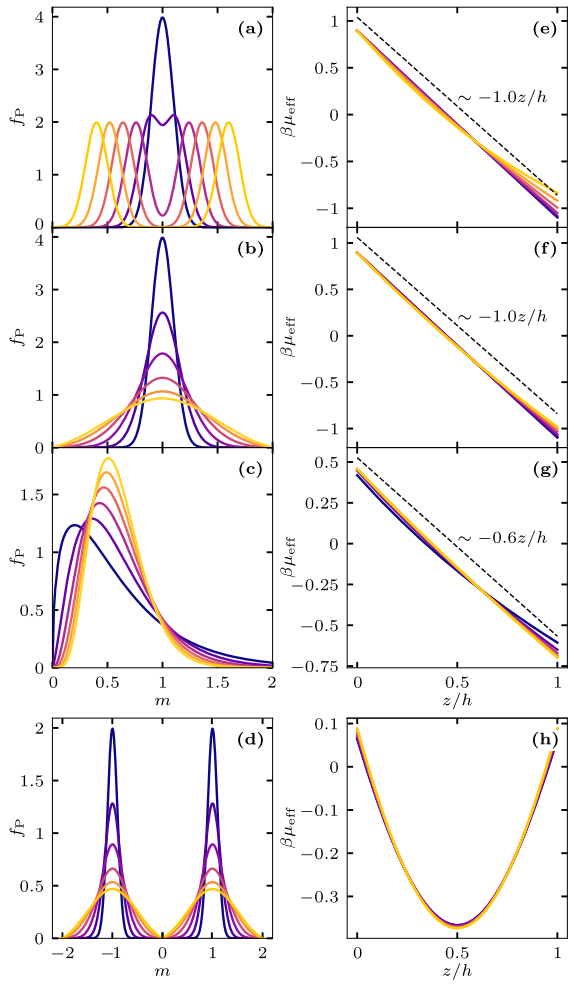


**FIG. 6.** Families of parent distributions $f_P(m)$ in the form of (a) the sum of two Gaussians that move apart symmetrically around the buoyant mass $m = 1$, (b) Gaussian with increasing standard deviation from 0.1 to 0.5, (c) $\chi^2$-distribution with the degree of freedom increasing from 3 to 13, and (d) sum of two Gaussians with mean values $m = -1$ and $m = 1$ and increasing standard deviation from 0.1 to 0.5. The distributions in (c) have mean 0.6 and standard deviation 1. The effective sedimentation paths $\beta\mu_{eff}$ as a function of the scaled elevation $z/h$ corresponding to the families of distributions in panels (a)–(d) are shown in panels (e)–(h), respectively. In all cases, we use the Hall EOS for hard spheres, the packing fraction is $\overline{\eta}/\eta_{cp} = 0.5$, and the sample height is $h/\xi = 80$. The dashed lines in panels (e)–(g) are the linear trends of the corresponding sedimentation paths (displaced vertically for a better visualization). The slopes (indicated next to each dashed line) coincide in all three cases with the mean mass of the corresponding family of distributions, which are 1 (a), 1 (b), and 0.6 (c).

distributions within each class by varying a control parameter. In Fig. 6(a), we increase the mass-polydispersity by interpolating between unimodal and bimodal Gaussian distributions. In Fig. 6(b), we increase the variance of a Gaussian distribution. In Fig. 6(c), we vary the skewness of the distribution while keeping the first and the second moment unaltered. In all cases, the distributions contain only positive masses and varying the control parameter has little effect on the sedimentation paths, even when we, e.g., drastically increase the degree of mass-polydispersity (second moment of the distribution). The corresponding sedimentation paths, shown in Fig. 6(e)–(g), deviate only slightly from a straight line with a slope given by the mean buoyant mass of the distribution. Hence, in sedimentation–diffusion–equilibrium, mass-polydisperse systems in which only positive or negative buoyant masses are present are similar to a reference monodisperse system. [Recall that $\mu(z) = \mu_0 - m_b gz$ for a monodisperse system.] The monodisperse reference system has the same particle mass as the mean of the mass distribution of the mass-polydisperse system.

We also consider a class of parent distributions with both positive and negative buoyant masses, where we increase the variance of a bimodal distribution [see Fig. 6(d)]. Due to the presence of buoyant masses with different sign, the suspension does not behave like a monodisperse system under gravity, and hence $\mu_{eff}(z)$ is not close to a straight line [see Fig. 6(h)]. Still the increase in the degree of mass-polydispersity does not affect the behavior of the system strongly since the paths do not deviate much from each other.

## IV. SUMMARY AND CONCLUSIONS

Sedimentation path theory[32,33] was initially developed to study sedimentation–diffusion–equilibrium of binary mixtures. The theory describes systems that are in equilibrium under the presence of a gravitational field and therefore cannot be used to describe non-equilibrium phenomena, such as drying,[62,63] or systems that get arrested due to, e.g., the formation of glasses[58] and non-equilibrium gels.[64] Depending, among other factors, on the buoyant mass of the colloids, the experimental equilibration times can vary from a few hours to several months.[28] We have extended here sedimentation path theory to deal with mass-polydisperse colloidal systems, i.e., the particles are identical except for the value of their buoyant masses. We derived an exact equation for the sedimentation path of the mass-polydisperse system [Eq. (14)] that combines all the sedimentation paths of the individual species. The resulting equation has the structure of the `LogSumExp` function, often used in machine learning algorithms for its smooth approximation to the maximum function.[65] Adding mass-polydispersity to a binary mixture is, in principle, a straightforward extension of the present work.

In bulk, mass-polydispersity has no effect on the phase behavior. Hence, our mass-polydisperse model allows us to highlight the interplay between polydispersity and gravity, eliminating by construction the complex effects that shape-polydispersity and size-polydispersity generates in bulk.[5,7–9,12,14,16,19,20,66] Beyond its fundamental interest, a mass-polydisperse system can be specifically realized experimentally by, e.g., synthesizing core–shell nanoparticles[67–70] with the same overall size but different relative size between the core and the shell. In addition, if the degree of size-polydispersity is small, mass-polydispersity is likely the dominant effect in sedimentation–diffusion–equilibrium. This is particularly relevant in colloidal suspensions near density matching[53–56] in which mass-polydispersity has a big effect on the stacking diagram under gravity: two mass distributions that are only slightly different

can give rise to topologically different stacking diagrams containing different stacking sequences.

Granular media is a related system in which the particles can be polydisperse.[71–74] It would be interesting to analyze the effects of mass-polydispersity in granular systems. For example, phase separation induced by mass-polydispersity might occur in vibrated monolayers[75,76] of granular systems.

Despite the relevance of the hard-sphere model in soft matter, there are only a few experiments on the sedimentation–diffusion–equilibrium of (quasi) hard-spheres. Moreover, colloids with a relatively large buoyant mass are often used[57,59] and the sample height is not used as a control parameter. A systematic experimental study of the stacking diagram of hard spheres would be valuable.

In bulk, it is sometimes possible to approximate the free energy of a polydisperse system using only a finite number of moments of the parent distribution.[77,78] In a similar way, using the first moment of the parent distribution, it is possible to obtain a reasonable approximation for the effective sedimentation path of the mass-polydisperse system and hence an approximated stacking diagram.

Polydispersity in the size of the particles affects the bulk behavior of the suspension and, therefore, also the sedimentation–diffusion–equilibrium. For example, van der Kooij *et al.* studied the sedimentation of polydisperse colloidal platelets.[26] Their particle distribution contained platelets of different sizes but only positive buoyant masses. By changing the overall packing fraction, they found a striking inversion of the stacking sequence from the expected top isotropic and bottom nematic, *IN*, to top nematic and bottom isotropic, *NI*. Due to the geometric properties of the sedimentation path of a mass-polydisperse system, such inversion of the sequence cannot occur in a mass-polydisperse system that contains particles with only positive (or only negative) buoyant masses. As correctly pointed out in Ref. 26, the inversion must therefore be a consequence of the interplay between gravity- and size-polydispersity. Sedimentation path theory could be applied on top of a bulk theory for size-polydisperse systems in order to describe such effects.

## ACKNOWLEDGMENTS

We acknowledge useful discussions with Peter Sollich and Stefan Egelhaaf. This work was supported by the German Research Foundation (DFG) via Project No. 436306241.

## AUTHOR DECLARATIONS

### Conflict of Interest

The authors have no conflicts to disclose.

### Author Contributions

**Tobias Eckert**: Conceptualization (equal); Investigation (lead); Methodology (lead); Software (lead); Writing – original draft (equal); Writing – review & editing (equal). **Matthias Schmidt**: Conceptualization (equal); Investigation (equal); Writing – original draft (equal); Writing – review & editing (equal). **Daniel de las Heras**: Conceptualization (equal); Investigation (equal); Writing – original draft (equal); Writing – review & editing (equal).

## DATA AVAILABILITY

The data that support the findings of this study are available within the article.

## APPENDIX: EULER–LAGRANGE EQUATION

Carrying out the functional derivative with respect to $\rho_m$ in Eq. (5) for the ideal free energy contribution to $\Omega$ yields

$$\frac{\delta F^{\mathrm{id}}[\rho_m]}{\delta \rho_{m'}} = k_{\mathrm{B}}T \ln(\rho_m). \tag{A1}$$

For the excess contribution, we find

$$\frac{\delta F^{\mathrm{exc}}[\rho]}{\delta \rho_{m'}} = \frac{\delta F^{\mathrm{exc}}[\rho]}{\delta \rho}, \tag{A2}$$

where we have used the functional chain-rule and also the definition of the overall density [Eq. (2)] to calculate the functional derivative

$$\frac{\delta \rho}{\delta \rho_m} = \frac{\delta}{\delta \rho_m} \int \mathrm{d}m' \rho_{m'} = \int \mathrm{d}m' \delta(m - m') = 1. \tag{A3}$$

Hence, introducing the excess chemical potential $\mu_{\mathrm{exc}} = \delta F^{\mathrm{exc}}[\rho]/\delta\rho$ in Eq. (A2), it follows

$$\frac{\delta F^{\mathrm{exc}}[\rho_m]}{\delta \rho_{m'}} = \mu_{\mathrm{exc}} = \mu - k_{\mathrm{B}}T \ln(\rho). \tag{A4}$$

Here, $\mu = \mu_{\mathrm{exc}} + k_{\mathrm{B}}T\ln(\rho)$ is the total chemical potential, including the ideal contribution $k_{\mathrm{B}}T\ln(\rho)$, of the corresponding monodisperse system with the same overall density $\rho$ as the mass-polydisperse system.

For the last contribution to $\Omega[\rho_m]$ in Eq. (4), we get

$$\frac{\delta}{\delta \rho_m} \int \mathrm{d}m' \rho_{m'} \mu_{m'} = \mu_m. \tag{A5}$$

Hence, adding Eqs. (A1), (A4), and (A5) according to the minimization principle [Eq. (5)] yields the Euler–Lagrange equation shown in Eq. (6).

## REFERENCES

[1] R. P. Murphy, K. Hong, and N. J. Wagner, "Synthetic control of the size, shape, and polydispersity of anisotropic silica colloids," J. Colloid Interface Sci. **501**, 45 (2017).
[2] J. Roller, J. D. Geiger, M. Voggenreiter, J.-M. Meijer, and A. Zumbusch, "Formation of nematic order in 3D systems of hard colloidal ellipsoids," Soft Matter **16**, 1021 (2020).
[3] M. Voggenreiter, J. Roller, J. Geiger, L. Ebner, A. Zumbusch, and J.-M. Meijer, "Preparation and tracking of oblate core-shell polymethyl-methacrylate ellipsoids," Langmuir **36**, 13087 (2020).
[4] J. Roller, A. Laganapan, J.-M. Meijer, M. Fuchs, and A. Zumbusch, "Observation of liquid glass in suspensions of ellipsoidal colloids," Proc. Natl. Acad. Sci. U. S. A. **118**, e2018072118 (2021).
[5] P. Sollich, "Predicting phase equilibria in polydisperse systems," J. Phys.: Condens. Matter **14**, R79 (2001).
[6] F. M. van der Kooij, K. Kassapidou, and H. N. W. Lekkerkerker, "Liquid crystal phase transitions in suspensions of polydisperse plate-like particles," Nature **406**, 868 (2000).

[7]Y. Martínez-Ratón and J. A. Cuesta, "Enhancement by polydispersity of the biaxial nematic phase in a mixture of hard rods and plates," Phys. Rev. Lett. **89**, 185701 (2002).
[8]M. Fasolo and P. Sollich, "Effects of colloid polydispersity on the phase behavior of colloid-polymer mixtures," J. Chem. Phys. **122**, 074904 (2005).
[9]C. Ferreiro-Córdova, C. P. Royall, and J. S. van Duijneveldt, "Anisotropic viscoelastic phase separation in polydisperse hard rods leads to nonsticky gelation," Proc. Natl. Acad. Sci. U. S. A. **117**, 3415 (2020).
[10]Y. Martínez-Ratón and E. Velasco, "Effect of combined roundness and polydispersity on the phase behavior of hard-rectangle fluids," Phys. Rev. E **106**, 034602 (2022).
[11] A. V. Petukhov, D. van der Beek, R. P. A. Dullens, I. P. Dolbnya, G. J. Vroege, and H. N. W. Lekkerkerker, "Observation of a hexatic columnar liquid crystal of polydisperse colloidal disks," Phys. Rev. Lett. **95**, 077801 (2005).
[12]D. Sun, H.-J. Sue, Z. Cheng, Y. Martínez-Ratón, and E. Velasco, "Stable smectic phase in suspensions of polydisperse colloidal platelets with identical thickness," Phys. Rev. E **80**, 041704 (2009).
[13]M. W. Matsen, "Polydispersity-induced macrophase separation in diblock copolymer melts," Phys. Rev. Lett. **99**, 148304 (2007).
[14]P. N. Pusey, "The effect of polydispersity on the crystallization of hard spherical colloids," J. Phys. **48**, 709 (1987).
[15]D. A. Kofke and P. G. Bolhuis, "Freezing of polydisperse hard spheres," Phys. Rev. E **59**, 618 (1999).
[16]S. Auer and D. Frenkel, "Suppression of crystal nucleation in polydisperse colloids due to increase of the surface free energy," Nature **413**, 711 (2001).
[17]M. Fasolo and P. Sollich, "Equilibrium phase behavior of polydisperse hard spheres," Phys. Rev. Lett. **91**, 068301 (2003).
[18]P. Sollich and N. B. Wilding, "Crystalline phases of polydisperse spheres," Phys. Rev. Lett. **104**, 118302 (2010).
[19]P. Sollich and N. B. Wilding, "Polydispersity induced solid–solid transitions in model colloids," Soft Matter **7**, 4472 (2011).
[20]M. A. Bates and D. Frenkel, "Influence of polydispersity on the phase behavior of colloidal liquid crystals: A Monte Carlo simulation study," J. Chem. Phys. **109**, 6193 (1998).
[21] P. Maßhoff, I. Elsner, M. A. Escobedo-Sánchez, J. P. Segovia-Gutiérrez, A. Pamvouxoglou, and S. U. Egelhaaf, "Shear-induced crystallisation in binary colloidal suspensions investigated using confocal microscopy," J. Phys.: Matter **3**, 035004 (2020).
[22]A. Fortini and R. P. Sear, "Stratification and size segregation of ternary and polydisperse colloidal suspensions during drying," Langmuir **33**, 4796 (2017).
[23]O. Cusola, S. Kivistö, S. Vierros, P. Batys, M. Ago, B. L. Tardy, L. G. Greca, M. B. Roncero, M. Sammalkorpi, and O. J. Rojas, "Particulate coatings via evaporation-induced self-assembly of polydisperse colloidal lignin on solid interfaces," Langmuir **34**, 5759 (2018).
[24]E. Zaccarelli, S. M. Liddle, and W. C. K. Poon, "On polydispersity and the hard sphere glass transition," Soft Matter **11**, 324 (2015).
[25]D. Heckendorf, K. J. Mutch, S. U. Egelhaaf, and M. Laurati, "Size-dependent localization in polydisperse colloidal glasses," Phys. Rev. Lett. **119**, 048003 (2017).
[26]F. M. van der Kooij, D. van der Beek, and H. N. W. Lekkerkerker, "Isotropic–nematic phase separation in suspensions of polydisperse colloidal platelets," J. Phys. Chem. B **105**, 1696 (2001).
[27]R. Piazza, S. Buzzaccaro, and E. Secchi, "The unbearable heaviness of colloids: Facts, surprises, and puzzles in sedimentation," J. Phys.: Condens. Matter **24**, 284109 (2012).
[28]D. de las Heras, N. Doshi, T. Cosgrove, J. Phipps, D. I. Gittins, J. S. van Duijneveldt, and M. Schmidt, "Floating nematic phase in colloidal platelet-sphere mixtures," Sci. Rep. **2**, 789 (2012).
[29]R. Piazza, "Settled and unsettled issues in particle settling," Rep. Prog. Phys. **77**, 056602 (2014).
[30]J. Á. Pariente, Á. Blanco, and C. López, "Colloidal photonic crystals formation studied by real-time light diffraction," Nanophotonics **11**, 3257 (2022).
[31] T. Eckert, M. Schmidt, and D. de las Heras, "Gravity-induced phase phenomena in plate-rod colloidal mixtures," Commun. Phys. **4**, 202 (2021).
[32]D. de las Heras and M. Schmidt, "The phase stacking diagram of colloidal mixtures under gravity," Soft Matter **9**, 8636 (2013).
[33]T. Geigenfeind and D. de las Heras, "The role of sample height in the stacking diagram of colloidal mixtures under gravity," J. Phys.: Condens. Matter **29**, 064006 (2016).
[34]T. Drwenski, P. Hooijer, and R. van Roij, "Sedimentation stacking diagrams of binary mixtures of thick and thin hard rods," Soft Matter **12**, 5684 (2016).
[35]D. de las Heras, L. L. Treffenstädt, and M. Schmidt, "Reentrant network formation in patchy colloidal mixtures under gravity," Phys. Rev. E **93**, 030601 (2016).
[36]G. Avvisati, T. Dasgupta, and M. Dijkstra, "Fabrication of colloidal laves phases via hard tetramers and hard spheres: Bulk phase diagram and sedimentation behavior," ACS Nano **11**, 7702 (2017).
[37]T. Dasgupta and M. Dijkstra, "Towards the colloidal laves phase from binary hard-sphere mixtures via sedimentation," Soft Matter **14**, 2465 (2018).
[38]R. Braz Teixeira, D. de las Heras, J. M. Tavares, and M. M. Telo da Gama, "Phase behavior of a binary mixture of patchy colloids: Effect of particle size and gravity," J. Chem. Phys. **155**, 044903 (2021).
[39]T. Eckert, M. Schmidt, and D. de las Heras, "Sedimentation of colloidal plate-sphere mixtures and inference of particle characteristics from stacking sequences," Phys. Rev. Res. **4**, 013189 (2022).
[40]R. Evans, "The nature of the liquid-vapour interface and other topics in the statistical mechanics of non-uniform, classical fluids," Adv. Phys. **28**, 143 (1979).
[41] Y. C. Chiew, "Percus-Yevick integral-equation theory for athermal hard-sphere chains," Mol. Phys. **70**, 129 (1990).
[42]K. S. Schweizer and J. G. Curro, "Equation of state of polymer melts: General formulation of a microscopic integral equation theory," J. Chem. Phys. **89**, 3342 (1988).
[43]F. Lado, "Equation of state of the hard-disk fluid from approximate integral equations," J. Chem. Phys. **49**, 3092 (1968).
[44]J. K. Johnson, J. A. Zollweg, and K. E. Gubbins, "The Lennard-Jones equation of state revisited," Mol. Phys. **78**, 591 (1993).
[45]I. Saika-Voivod, F. Sciortino, and P. H. Poole, "Computer simulations of liquid silica: Equation of state and liquid-liquid phase transition," Phys. Rev. E **63**, 011202 (2000).
[46]R. L. Rowley and M. M. Painter, "Diffusion and viscosity equations of state for a Lennard-Jones fluid obtained from molecular dynamics simulations," Int. J. Thermophys. **18**, 1109 (1997).
[47]R. Span and W. Wagner, "A new equation of state for carbon dioxide covering the fluid region from the triple-point temperature to 1100 K at pressures up to 800 MPa," J. Phys. Chem. Ref. Data **25**, 1509 (1996).
[48]G. Soave, "Equilibrium constants from a modified Redlich-Kwong equation of state," Chem. Eng. Sci. **27**, 1197 (1972).
[49]D.-Y. Peng and D. B. Robinson, "A new two-constant equation of state," Ind. Eng. Chem. Res. **15**, 59 (1976).
[50]K. R. Hall, "Another hard-sphere equation of state," J. Chem. Phys. **57**, 2252 (1972).
[51] A. Mulero, C. A. Faúndez, and F. Cuadros, "Chemical potential for simple fluids from equations of state," Mol. Phys. **97**, 453 (1999).
[52]D. de las Heras and M. Schmidt, "Sedimentation stacking diagram of binary colloidal mixtures and bulk phases in the plane of chemical potentials," J. Phys.: Condens. Matter **27**, 194115 (2015).
[53]T. E. Kodger, R. E. Guerra, and J. Sprakel, "Precise colloids with tunable interactions for confocal microscopy," Sci. Rep. **5**, 14635 (2015).
[54]H. Guo, T. Narayanan, M. Sztuchi, P. Schall, and G. H. Wegdam, "Reversible phase transition of colloids in a binary liquid solvent," Phys. Rev. Lett. **100**, 188303 (2008).
[55]C. P. Royall, W. C. K. Poon, and E. R. Weeks, "In search of colloidal hard spheres," Soft Matter **9**, 17 (2013).
[56]W. C. K. Poon, "The physics of a model colloid polymer mixture," J. Phys.: Condens. Matter **14**, R859 (2002).
[57]S. E. Paulin and B. J. Ackerson, "Observation of a phase transition in the sedimentation velocity of hard spheres," Phys. Rev. Lett. **64**, 2663 (1990).
[58]P. N. Pusey and W. van Megen, "Phase behaviour of concentrated suspensions of nearly hard colloidal spheres," Nature **320**, 340 (1986).

[59]B. J. Ackerson, S. E. Paulin, B. Johnson, W. van Megen, and S. Underwood, "Crystallization by settling in suspensions of hard spheres," Phys. Rev. E **59**, 6903 (1999).
[60]F. M. van der Kooij and H. N. W. Lekkerkerker, "Liquid-crystal phases formed in mixed suspensions of rod- and platelike colloids," Langmuir **16**, 10144 (2000).
[61]F. M. van der Kooij, E. S. Boek, and A. P. Philipse, "Rheology of dilute suspensions of hard platelike colloids," J. Colloid Interface Sci. **235**, 344 (2001).
[62]A. Fortini, I. Martín-Fabiani, J. L. De La Haye, P.-Y. Dugas, M. Lansalot, F. D'Agosto, E. Bourgeat-Lami, J. L. Keddie, and R. P. Sear, "Dynamic stratification in drying films of colloidal mixtures," Phys. Rev. Lett. **116**, 118301 (2016).
[63]M. Kundu and M. P. Howard, "Dynamic density functional theory for drying colloidal suspensions: Comparison of hard-sphere free-energy functionals," J. Chem. Phys. **157**, 184904 (2022).
[64]R. Harich, T. W. Blythe, M. Hermes, E. Zaccarelli, A. J. Sederman, L. F. Gladden, and W. C. K. Poon, "Gravitational collapse of depletion-induced colloidal gels," Soft Matter **12**, 4300 (2016).
[65]F. Nielsen and K. Sun, "Guaranteed bounds on information-theoretic measures of univariate mixtures using piecewise log-sum-exp inequalities," Entropy **18**, 442 (2016).
[66]S. M. Liddle, T. Narayanan, and W. C. K. Poon, "Polydispersity effects in colloid–polymer mixtures," J. Phys.: Condens. Matter **23**, 194116 (2011).
[67]N. Toshima, M. Kanemaru, Y. Shiraishi, and Y. Koga, "Spontaneous formation of core/shell bimetallic nanoparticles: A calorimetric study," J. Phys. Chem. B **109**, 16326 (2005).
[68]R. Ghosh Chaudhuri and S. Paria, "Core/shell nanoparticles: Classes, properties, synthesis mechanisms, characterization, and applications," Chem. Rev. **112**, 2373 (2012).
[69]S. Wei, Q. Wang, J. Zhu, L. Sun, H. Lin, and Z. Guo, "Multifunctional composite core–shell nanoparticles," Nanoscale **3**, 4474 (2011).
[70]A. Pajor-Świerzy, K. Szczepanowicz, A. Kamyshny, and S. Magdassi, "Metallic core-shell nanoparticles for conductive coatings and printing," Adv. Colloid Interface Sci. **299**, 102578 (2022).
[71]C. Voivret, F. Radjaï, J.-Y. Delenne, and M. S. El Youssoufi, "Space-filling properties of polydisperse granular media," Phys. Rev. E **76**, 021301 (2007).
[72]C. Voivret, F. Radjaï, J.-Y. Delenne, and M. S. El Youssoufi, "Multiscale force networks in highly polydisperse granular media," Phys. Rev. Lett. **102**, 178001 (2009).
[73]M. R. Shaebani, M. Madadi, S. Luding, and D. E. Wolf, "Influence of polydispersity on micromechanics of granular materials," Phys. Rev. E **85**, 011301 (2012).
[74]D.-H. Nguyen, E. Azéma, F. Radjai, and P. Sornay, "Effect of size polydispersity versus particle shape in dense granular media," Phys. Rev. E **90**, 012202 (2014).
[75]V. Narayan, N. Menon, and S. Ramaswamy, "Nonequilibrium steady states in a vibrated-rod monolayer: Tetratic, nematic, and smectic correlations," J. Stat. Mech.: Theory Exp. **2006**(01), P01005.
[76]M. González-Pinto, F. Borondo, Y. Martínez-Ratón, and E. Velasco, "Clustering in vibrated monolayers of granular rods," Soft Matter **13**, 2571 (2017).
[77]P. Sollich and M. E. Cates, "Projected free energies for polydisperse phase equilibria," Phys. Rev. Lett. **80**, 1365 (1998).
[78]P. Sollich, P. Warren, and M. Cates, "Moment free energies for polydisperse systems," Adv. Chem. Phys. **116**, 265 (2001).

Soft Matter

PAPER

View Article Online
View Journal



Cite this: DOI: 10.1039/d3sm00191a

# Effect of sample height and particle elongation in the sedimentation of colloidal rods

Tobias Eckert, Matthias Schmidt and Daniel de las Heras *

Received 14th February 2023,
Accepted 2nd March 2023

DOI: 10.1039/d3sm00191a

rsc.li/soft-matter-journal

We study theoretically the effect of a gravitational field on the equilibrium behaviour of a colloidal suspension of rods with different length-to-width aspect ratios. The bulk phases of the system are described with analytical equations of state. The gravitational field is then incorporated *via* sedimentation path theory, which assumes a local equilibrium condition at each altitude of the sample. The bulk phenomenology is significantly enriched by the presence of the gravitational field. In a suspension of elongated rods with five stable phases in bulk, the gravitational field stabilizes up to fifteen different stacking sequences. The sample height has a non-trivial effect on the stable stacking sequence. New layers of distinct bulk phases appear either at the top, at the bottom, or simultaneously at the top and the bottom when increasing the sample height at constant colloidal concentration. We also study sedimentation in a mass-polydisperse suspension in which all rods have the same shape but different buoyant masses.

## I. Introduction

Hard particles possess an interaction potential that is infinite if two particles overlap and zero otherwise. Hard spherocylinders, which are cylinders capped with hemispheres at both ends, are among the most popular hard particle models,[1] partly because computing whether two particles overlap or not is relatively simple, and also because their phase behaviour is rich. Hard models are suitable candidates to study the phase behaviour of colloidal systems since the interaction between colloidal particles is often short-ranged and primarily repulsive. As revealed by computer simulations[2–5] hard spherocylinders can form isotropic, nematic, smectic, and crystalline phases depending on their length-to-width aspect ratio and the overall packing fraction. The percolation,[6–9] random close packing,[10–12] and random sequential adsorption[13,14] of hard spherocylinders have been subject of intense investigation due to the versatility of the model to describe a wide range of systems ranging from lyotropic liquid crystals to granular particles. Theoretically, classical density functional theory[15] has been widely used to study the phase behaviour of hard spherocylinders *via* functionals based on smoothed density approximations,[16,17] weighted density approximations,[18,19] and fundamental measure theory.[20–22]

Beyond bulk phenomena, several works have focused on inhomogeneous systems of hard spherocylinders. Interfacial phenomena,[23–27] wetting,[28–30] capillary nematization[28,30–33] and smectization[34,35] in planar pores, as well as confinement-induced phenomena in different geometries[36–39] have been studied with density functional approximations and computer simulations.

The hard spherocylinder model has been also used as a reference system to build up more complex interparticle potentials. These include spherocylinders with dipolar,[40–44] Coulombic[45,46] and patchy[47–49] interactions, active spherocylinders,[50–53] as well as spherocylinders coated with soft layers.[54,55] Moreover, the hard spherocylinder model can be a reasonable approximation to the shape and the interaction of real colloidal particles such as natural clay rods,[56] fd virus,[57] rod-like boehmite particles,[58] polystyrene ellipsoids,[59] silica rods,[60–62] as well as PMMA rods[63,64] and ellipsoids.[65,66]

Sedimentation experiments, in which a colloidal suspension is equilibrated under the influence of a gravitational field, are one of the basic tools to investigate phase behaviour in colloidal science. Zhang and van Duijn-eveldt[56] investigated the isotropic-nematic transition in a polydisperse suspension of natural clay rods in sedimentation. Polydispersity induces a nematic-nematic phase separation with strong fractionation in the rod length. Kuijk *et al.*[61] performed sedimentation experiments on silica rods with different aspect ratios and constructed an approximated bulk phase diagram by estimating the packing fractions at different heights. Beyond isotropic, nematic, and smectic A phases, they found a smectic B phase that preempts the formation of a full crystalline state, likely due to polydispersity and the presence of charges.

The gravitational field can have a strong and far from trivial effect in sedimentation experiments, especially if the

*Theoretische Physik II, Physikalisches Institut, Universität Bayreuth, D-95440 Bayreuth, Germany. E-mail: delasheras.daniel@gmail.com, www.danieldelasheras.com*

gravitational length is smaller or comparable to the height of the vessel,[67] which is often the case in colloidal science. To correctly extract information about bulk phenomena from sedimentation experiments it is essential to understand the effect of the gravitational field on the suspension. Not much theoretical and simulation work has been devoted to understand the effects of gravity on a suspension of hard spherocylinders. Viveros-Méndez *et al.*[68] studied with Monte Carlo simulations the sedimentation of a neutral mixture of oppositely charged spherocylinders. Savenko and Dijkstra[69] studied sedimentation-diffusion-equilibrium in suspensions of hard spherocylinders with length-to-width aspect ratio of 5 using the macroscopic osmotic equilibrium conditions, and compared the results to Monte Carlo simulations. Depending on the average packing fraction and the height of the sample they found a rich variety of stacking sequences with up to four layers of different bulk phases (top isotropic followed by nematic, smectic and finally a bottom layer of a crystal phase).

Here, we do a systematic theoretical study of the effect of particle elongation and sample height in the sedimentation of suspensions of colloidal hard spherocylinders in equilibrium. We use the equations of state (EOS) proposed by Peters *et al.*[70] to describe the bulk of the suspensions, and sedimentation path theory[71,72] to incorporate the effect of gravity. The EOS by Peters *et al.*[70] are based on scaled particle theory[73] and extended cell theory,[74] and reproduce quantitatively the full phase behaviour of hard spherocylinders for all aspect ratios. We study sedimentation of monodisperse suspensions with four characteristic values of the aspect ratio that cover the whole range of bulk phase phenomena. We also investigate the evolution of the stacking sequences upon varying the height of the vessel at constant packing fraction. By increasing the sample height new layers can appear in the sample either at the top, the bottom, or simultaneously at the top and the bottom of the sample. Using a recent extension of sedimentation path theory to mass-polydisperse suspensions,[75] in which the particles differ only in their buoyant mass, we study the interplay between mass-polydispersity and gravity in suspensions near density matching. Under such conditions it is possible to find stacking sequences with up to seven layers and, in contrast to monodisperse systems, new layers can also appear in the middle of the sample.

## II. Theory

A full account of the theory for monodisperse and mass-polydisperse colloidal suspensions is given by Eckert *et al.*[75] Here, we give only a brief summary of the theory.

### A. Sedimentation path theory for monodisperse and mass-polydisperse systems

Sedimentation path theory is based on a local equilibrium approximation to describe sedimentation-diffusion-equilibrium in a colloidal suspension under a gravitational field. In monodisperse suspensions, the state of the sample at altitude $z$ (measured from the bottom of the sample) is approximated by a bulk state with an effective chemical potential given by

$$\mu_{\mathrm{eff}}(z) = \mu^0 - m_{\mathrm{b}} g z, \quad 0 \le z \le h. \tag{1}$$

Here $m_{\mathrm{b}}$ is the buoyant mass of the particles, $g$ is the acceleration of gravity, $h$ is the sample height and $\mu^0$ is a constant offset of the effective chemical potential that can be interpreted as the colloid chemical potential at position $z = 0$. The value of $\mu^0$ determines the total colloidal density of the sample. The local equilibrium approximation is accurate provided that all correlation lengths are small compared to the gravitational length $\xi = k_{\mathrm{B}}T/(m_{\mathrm{b}}g)$, with $k_{\mathrm{B}}$ being the Boltzmann's constant and $T$ being the absolute temperature.

In the plane of $z$ and $\mu_{\mathrm{eff}}$ the effective chemical potential is just the segment of a line, see Fig. 1(a), known as the sedimentation path.[71,72] The sedimentation path is directly related to the stacking sequence observed in sedimentation, *i.e.* the sequence of layers of different bulk phases. An interface appears in the

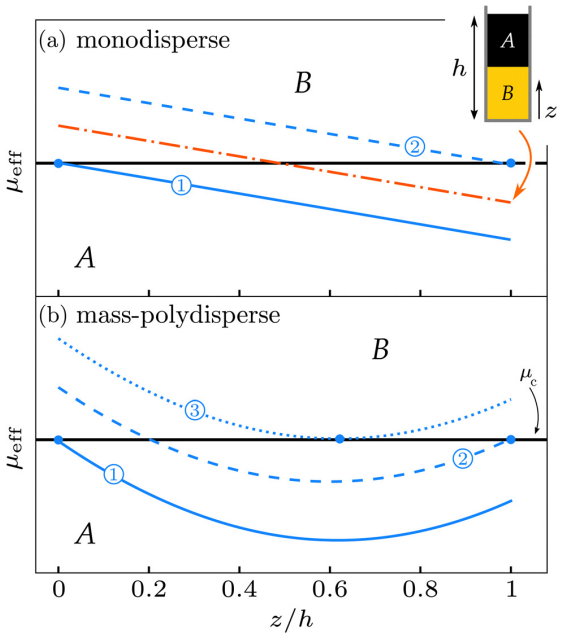


Fig. 1 Sedimentation path theory. Schematic plots of the effective chemical potential $\mu_{\mathrm{eff}}$ *vs.* the altitude $z$ scaled with the sample height $h$ in sedimentation samples of monodisperse (a) and mass-polydisperse (b) colloidal suspensions. The horizontal black line indicates the chemical potential $\mu_{\mathrm{c}}$ of a bulk transition between two phases labeled *A* and *B*. Several representative sedimentation paths are plotted. The paths are straight lines in monodisperse suspensions (a) and curves in mass-polydisperse suspensions (b). The sample corresponding to the orange dash-dotted path is sketched in the inset of (a). The blue paths form the sedimentation binodals between two different stacking sequences. An infinitesimal change of any of the blue paths can alter the stacking sequence. Represented are paths that end at the bulk coexistence, *i.e.* $\mu_{\mathrm{eff}}(z = 0) = \mu_{\mathrm{c}}$ (blue-solid paths marked with an encircled 1), paths that start at the binodal, *i.e.* $\mu_{\mathrm{eff}}(z = h) = \mu_{\mathrm{c}}$ (blue-dashed paths marked with an encircled 2), and a path that is tangent to the binodal (blue-dotted path marked with an encircled 3).

vessel when the sedimentation path crosses a bulk binodal. That is, an interface between two bulk phases $A$ and $B$ at position $z_0$ occurs if $\mu_{\text{eff}}(z_0) = \mu_c$ with $\mu_c$ the bulk chemical potential of the coexisting phases, see the orange sedimentation path in Fig. 1(a).

In a mass-polydisperse suspension there is a distribution of colloidal particles that differ only in their buoyant masses. Such system can be experimentally created with *e.g.* core–shell colloidal particles[65,76] of identical overall size and shape but with internal cores of different sizes. The interparticle interactions and hence the bulk phenomena (without gravity) are the same as in the corresponding monodisperse suspension. This greatly simplifies the theoretical treatment while it still highlights the interplay between polydispersity and gravity.

The effective chemical potential of the species of mass $m$ in a gravitational field is in generalization of eqn (1) approximated by

$$\mu_m(z) = \mu_m^0 - m_b g z, \quad 0 \le z \le h. \tag{2}$$

Here $m = m_b/m_0$ is a scaled buoyant mass with $m_b$ being the actual buoyant mass and $m_0$ being a reference buoyant mass such that $m$ is dimensionless. A sensible choice is to relate $m_0$ with either the average buoyant mass or with the standard deviation of the parent distribution, which is the initial distribution of buoyant masses in bulk. The constant $\mu_m^0$ sets the overall density of the species with mass $m$ in the suspension. Using eqn (2) for the chemical potential of species with mass $m$, one arrives at the following exact expression for the effective chemical potential of the suspension along the sedimentation path[75]

$$\mu_{\text{eff}}(z) = k_B T \ln\left(\int \mathrm{d}m e^{\beta(\mu_m^0 - m_b g z)}\right), \quad 0 \le z \le h, \tag{3}$$

where the integral is over the whole range of masses in the parent distribution. We therefore have successfully mapped a mass-polydisperse system under gravity onto an effective monodisperse system with local chemical potential $\mu_{\text{eff}}(z)$. The sedimentation path is no longer a straight line, although the LogSumExp structure of eqn (3) imposes severe restrictions to the possible shapes of the path. In particular, it follows from eqn (3) that $\mu_{\text{eff}}(z)$ is a concave function of the altitude $z$ and hence it can have at most one strict minimum. If only a single value of the buoyant mass is allowed in the parent distribution, then the integral in eqn (3) collapses to a single buoyant mass and the effective chemical potential reduces to the monodisperse case, eqn (1). That is, the mass-polydisperse system contains the monodisperse system as the limit in which the parent distribution is a delta distribution.

To translate between chemical potentials and densities, we need a bulk equation of state (EOS) in the form of density $\rho_{EOS}(\mu)$ as a function of the chemical potential $\mu$, which describes the bulk phase behavior of the system, *i.e.* in absence of gravity. Then, using the equation of state together with eqn (2) and (3) we obtain $\rho_m(z)$, the density profile of the species with mass $m$ and $\rho(z) = \int \mathrm{d}m \rho_m(z)$, the overall density profile across all species.

Usually, we set an initial (desired) parent distribution of particles and then find the offsets $\mu_m^0$ in eqn (3) that reproduce the parent distribution. That is, we find the offsets $\mu_m^0$ such that the overall density of species $m$ in sedimentation, which is $1/h\int_0^h \mathrm{d}z \rho_m(z)$, is equal to the density of particles with mass $m$ in the parent distribution. The offsets are found numerically *via* a simple iterative procedure.[75]

In our study of hard spherocylinders, we use the EOS proposed by Peters *et al.*,[70] which is depicted in Fig. 2 for four different values of the aspect ratio $L/D$, where $L$ is the length of the cylinder and $D$ the diameter of the spherocylinders. We represent the EOS in the plane of $\mu$ and $\eta$, with $\eta = \rho v_0$ the packing fraction and $v_0$ the particle volume.

### B. Construction of the stacking diagram

The analogue to the bulk phase diagram in presence of a gravitational field is the stacking diagram[72] that groups all possible stacking sequences of a given colloidal suspension in sedimentation-diffusion-equilibrium. To construct the stacking diagram one needs to find the sedimentation binodals that determine the boundaries between distinct stacking sequences.

In monodisperse and mass-polydisperse suspensions, the sedimentation binodals are formed by a set of three different types of sedimentation paths: (i) paths that end at a bulk binodal, *i.e.* $\mu_{\text{eff}}(z = 0) = \mu_c$ with $\mu_c$ the chemical potential at coexistence in a bulk transition, (ii) paths that start at a bulk binodal, *i.e.* $\mu_{\text{eff}}(h) = \mu_c$, and (iii) paths that are tangent to a bulk binodal. Examples of all types of paths are shown in Fig. 1(a) and (b) for monodisperse and mass-polydisperse suspensions, respectively. The third type of paths (tangent to a bulk binodal) is only present in mass-polydisperse suspensions since there the sedimentation path can be curved. These three types of sedimentation paths form the sedimentation binodals because an infinitesimal change of the path can alter the stacking sequence.

We construct the stacking diagrams in the (experimentally relevant) plane of average colloidal packing fraction of the sample and sample height. For a detailed account of the construction of stacking diagrams in monodisperse and mass-polydisperse systems see Eckert *et al.*[75]

## III. Results

We start in Section III.A summarizing the main results for the bulk of the system. The effect of the gravitational field is then presented in Section III.B (stacking diagrams), Section III.C (effect of sample height), and Section III.D (effect of mass-polydispersity).

### A. Bulk phase behaviour

Several theoretical and simulation techniques have been used to study the equation of state of hard spherocylinders. These include Monte Carlo simulations,[78,79] molecular dynamics simulations,[80] Brownian dynamics simulations,[51,81] scaled particle theory[73,82] and cell model theory.[74] We use here the EOS by

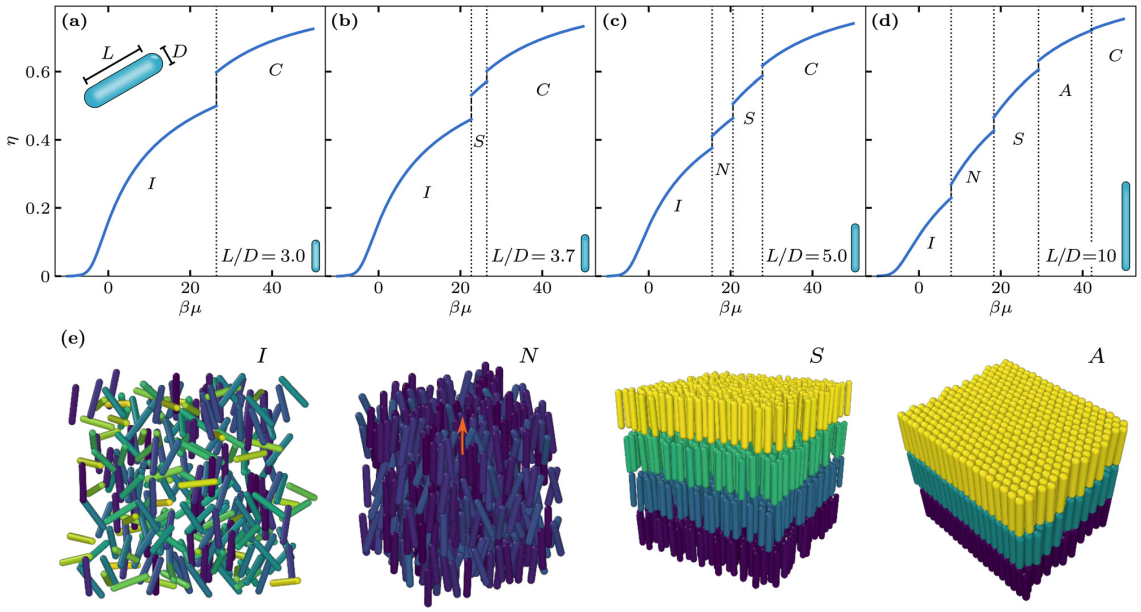


Fig. 2 Bulk phenomena. Bulk equation of state in the plane of chemical potential $\beta\mu$ and packing fraction $\eta$ for colloidal hard spherocylinders according to Peters *et al.*[70] for different length-to-width aspect ratios: (a) $L/D$ = 3.0, (b) $L/D$ = 3.7, (c) $L/D$ = 5.0, and (d) $L/D$ = 10.0. The vertical dotted lines indicate the position of the (first order) phase transitions. The occurring bulk phases are isotropic (I), nematic (N), smectic-A (S), AAA crystal (A), and ABC crystal (C). Panel (e) shows sketches of spherocylinders forming several bulk phases: isotropic state with no positional order and no orientational order, nematic state with no positional order and with orientational order along the director (orange arrow), smectic state with orientational order and positional order along one direction, and AAA crystal with orientational order and positional order along the three spatial directions. Particles in the isotropic and the nematic (the smectic and the crystal) states are colored according to their orientation (vertical coordinate). In the AAA crystal the particles in different layers are located on top of each other whereas in the ABC crystals their location is like in a FCC crystal. Sketches created with OVITO.[77]

Peters *et al.*[70] to model the bulk properties of the system. These closed-form equations of state are simple yet they provide an accurate description of the full phase behaviour of hard spherocylinders, depicted in Fig. 2. We show the bulk phase diagram for rods with four different aspect ratios selected to illustrate the entire phenomenology of hard spherocylinders.[5,70] Five different phases occur in bulk, namely isotropic (I), nematic (N), smectic-A (S), AAA crystal (A), and ABC crystal (C). See schematics in Fig. 2(e). For low aspect ratios, *e.g.* $L/D$ = 3.0 in Fig. 2(a), there is only a first order phase transition from isotropic fluid to ABC crystal. Increasing the aspect ratio to *e.g.* $L/D$ = 3.7 stabilizes also a smectic phase at intermediate densities, see Fig. 2(b). The nematic state appears at larger aspect ratios such as $L/D$ = 5 shown in Fig. 2(c). Finally, for rather elongated rods, *e.g.* $L/D$ = 10 in Fig. 2(d), an AAA crystal is stable between the smectic and the ABC crystal. In all cases the phase transitions are of first order (note the jumps in packing fractions at the transitions in Fig. 2).

### B. Stacking diagram of monodisperse spherocylinders

We next combine the bulk equations of state with sedimentation path theory to obtain the stacking diagrams of hard spherocylinders in a gravitational field. In Fig. 3 we present several stacking diagrams in the plane of average packing fraction $\bar{\eta}$ and sample height $h$ (scaled with the gravitational length $\xi$) for monodisperse colloidal suspensions of hard spherocylinders with different aspect ratios, as indicated. In all cases, we assume a positive buoyant mass of the spherocylinders. Each point in the stacking diagram represents a sedimentation path and therefore a sample under gravity (the sketched samples in Fig. 3 correspond to the points marked by a yellow star in the stacking diagrams). Depending on the aspect ratio, we find systems which form stacking sequences with up to five different layers.

Since all particles share the same buoyant mass, the effective local chemical potential $\mu_{\text{eff}}(z)$ is just linear in the vertical coordinate $z$ and there exist only two types of sedimentation binodals. Those are formed by the set of sedimentation paths that either start (dashed-lines in Fig. 3) or end (solid-lines in Fig. 3) at a bulk transition, see illustrative examples of sedimentation paths in the inset of Fig. 3(a).

In the stacking diagram the two types of sedimentation binodals have opposite slope in the plane of $\bar{\eta}$ and $h$. Furthermore, two sedimentation binodals of the same type never cross each other and two sedimentation binodals of different type cross each other at most once. This gives rise to the intertwined pattern of the two types of sedimentation binodals that can be seen in Fig. 2. When crossing a sedimentation binodal in the stacking diagram, one layer either appears or disappears from

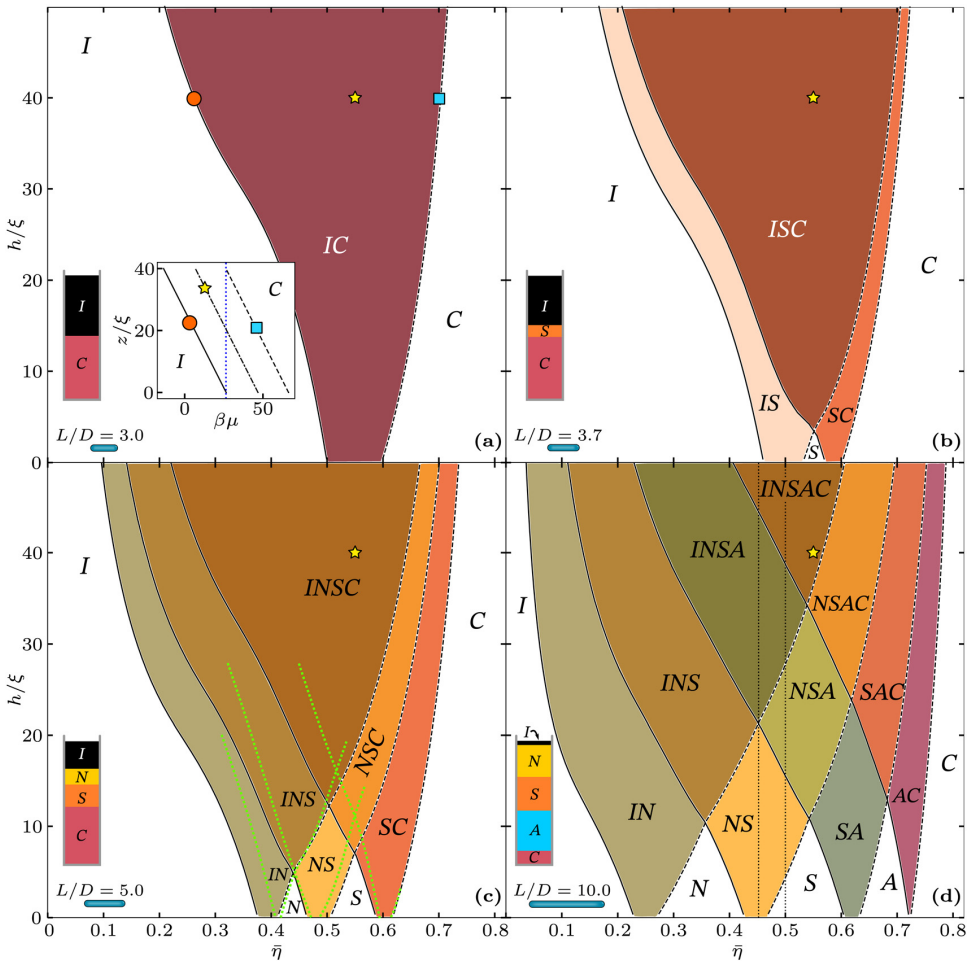


Fig. 3 Sedimentation of monodisperse rods. Stacking diagram in the plane of average packing fraction $\bar{\eta}$ and sample height $h/\xi$ for a monodisperse colloidal suspension of hard spherocylinders of different length-to-width aspect ratios: (a) $L/D$ = 3.0, (b) $L/D$ = 3.7, (c) $L/D$ = 5.0, and (d) $L/D$ = 10.0. Here $\xi$ is the gravitational length. The stacking sequences are labeled from top to bottom of the sample. The occurring layers are isotropic (I), nematic (N), smectic-A (S), AAA crystal (A), and ABC crystal (C). The solid- and dashed-black lines are sedimentation binodals formed by those sedimentation paths that either end or start at a bulk binodal, respectively. The dotted green lines in panel (c) are results from Savenko and Dijkstra.[69] The yellow stars indicate the position of the sample with ($\bar{\eta}$, $h/\xi$) = (0.55, 40) in all stacking diagrams. A sketch of the corresponding stacking sequences at this state point illustrating the relative thickness of each layer in the stacking sequence is provided within each panel. The inset in panel (a) depicts three sedimentation paths in the plane of chemical potential $\mu$ and altitude $z$. The vertical blue line indicates the value $\beta\mu_c$ = 26.4 of the I–C bulk transition. The path labeled with an orange circle ends at the binodal, *i.e.* $\mu(0) = \mu_c$, and the path labeled with a blue square starts at the binodal, *i.e.* $\mu(h) = \mu_c$. Both paths form part of the sedimentation binodals in the stacking diagram, as indicated by the orange circle and the blue square in panel (a). The path labeled with a star in the inset of panel (a) corresponds to the sketched sample in (a).

either the top or the bottom of the sample. Four different stacking sequences merge at the points where two sedimentation binodals cross each other. At those crossing points, the slope of the sedimentation binodals in the stacking diagram changes as a direct consequence of the density jump of the associated bulk phase transitions (recall that all bulk transition are of first order). The change in slope is particularly noticeable if the density jump in bulk is large, like *e.g.* for spherocylinders with $L/D$ = 3.7, *cf.* Fig. 2(b) and 3(b). Increasing the sample height also increases the length of the sedimentation path, making it possible to find sequences with more layers. The maximal number of layers in a monodisperse suspension is always the total number of different bulk phases. It is worth noting that due to the local equilibrium approximation, the limit $h \to 0$ of the stacking diagram corresponds to the bulk of the system (the sedimentation path becomes a single point in this limit).

For short spherocylinders, aspect ratio $L/D \lesssim 3.1$, the stable bulk phases are isotropic (I) and ABC crystal (C).[5] Under gravity, the possible stacking sequences are: pure I, pure C and IC, see Fig. 3(a). In bulk, *i.e.* in the limit $h \to 0$ in Fig. 3, the region of

packing fractions where isotropic and columnar phases coexist is $0.5 \leq \eta \leq 0.6$. Under gravity, the range of average packing fraction $\bar{\eta}$ in which we find the stacking sequence IC broadens significantly with increasing sample height. For example for $h/\xi = 50$ the IC sequence appears in a range of average packing fractions $0.21 < \bar{\eta} < 0.72$. This representative example illustrates the importance of including the effect of gravity when analysing and interpreting sedimentation experiments in colloidal science.

For $L/D = 3.7$ the stable bulk phases are isotropic (I), smectic-A (S), and ABC crystal (C). The stacking diagram contains six different stacking sequences, see Fig. 2(b). Besides the pure I, S and C stacks, we also find the sequences IS, SC and ISC. Again, the two-phase bulk coexistence regions broaden by increasing the sample height. However, there are now two regions of phase coexistence in bulk, namely I + S and S + C, which give rise to the stacking sequences IS and SC. The regions where IS and SC are stable in the stacking diagram overlap for $h/\xi > 3.3$, forming the additional stacking sequence ISC. Note that there is no isotropic–smectic–crystal triple point in bulk. The formation of the three layer sequence, ISC, is purely due to the gravitational field. Even though I, S, and C phases are stable in bulk, not all possible combinations of layers appear in the stacking diagram. For example, the occurrence of the sequence IC is not possible for this aspect ratio. Only two phases that coexist in bulk can appear consecutively in the stacking diagram.

A nematic (N) bulk state is stable for rods with $L/D = 5.0$, as depicted in Fig. 2(c). The corresponding stacking diagram, shown in Fig. 3(c), contains up to ten different stacking sequences. In a general monodisperse suspension with no triple points in bulk, the amount of distinct stacking sequences $n_s$ is given by the triangular number of the total number of stable bulk phases $n_b$, that is

$$n_s = \sum_{i=1}^{n_b} i = \frac{n_b(n_b+1)}{2}. \quad (4)$$

We also show in Fig. 3(c) results from Savenko and Dijkstra[69] (green dotted lines). They used an EOS from data obtained *via* computer simulations by McGrother *et al.*[4] (For a detailed comparison between the equation of state by McGrother *et al.* and the one used here see Peters *et al.*[70]) Savenko and Dijkstra[69] used a local equilibrium approximation together with the equilibrium macroscopic condition $dP(z)/dz = -mg\rho(z)$, with $P$ the osmotic pressure, to calculate the sedimentation of hard spherocylinders with $L/D = 5.0$. Their results agree semiquantitatively with our predictions. The approach by Savenko and Dijkstra[69] is equivalent to sedimentation path theory and therefore the small differences can be attributed to differences in the underlying bulk equation of state (note that both approaches differ slightly in the limit $h \to 0$). Although both approaches are equivalent, working with the chemical potential is in general more convenient since this quantity varies linearly with the altitude within the local equilibrium approximation. Therefore, the sedimentation path, the density profiles, and the sedimentation binodals can be easily computed. Moreover, the theory can be straightforwardly applied to binary mixtures[72,83,84] and mass-polydisperse systems.[75]

By increasing the aspect ratio, hard spherocylinders form an additional crystal AAA (A) phase,[5] see the bulk diagram for $L/D = 10$ in Fig. 2(d). This additional bulk phase increases the complexity of the stacking diagram, see Fig. 3(d), which now contains $n_s = 15$ different sequences, see eqn (4). Here, the stacking sequence INSAC is stable at large values of sample height h and it contains, in a single sample, all the different bulk phases that hard spherocylinders develop in bulk. The sample sketched in Fig. 3(d) corresponds to a height $h/\xi = 40$. We estimate that in an experimental system made of boehmite rods with polyisobutene coating suspended in toluene[85] and lengths $L$ between 1 μm and 200 nm, the corresponding sample heights would vary between approx. 0.2 cm and 20 cm, respectively.

In all cases, by increasing the sample height, the range of chemical potentials covered by the path becomes larger. Hence, the sequence with the largest number of layers (*e.g.* INSAC for $L/D = 10$) appears always and dominates the stacking diagram for sufficiently large values of the sample height.

We have assumed a positive value of the buoyant mass. For negative buoyant masses, the only change is a reversed order of the layers in the stacking sequences. For example, the sequence ISC (from top to bottom) in rods with positive buoyant mass, would be CSI if the rods had negative buoyant mass.

### C. Influence of the sample height on the stacking sequences

The effect of varying the sample height (at fixed average colloidal concentration) in sedimentation of colloidal binary mixtures can be counterintuitive with new layers appearing at the top, at the bottom, or in the middle of the sample.[67,83,84] We study here the evolution of the stacking sequence by increasing the sample height in monodisperse colloidal systems. We select two illustrative average packing fractions $\bar{\eta} = 0.452$ and 0.50 in a suspension of elongated hard spherocylinders with $L/D = 10.0$, see vertical dotted lines in Fig. 3(d). We then vary the sample height while keeping the packing fraction constant and track the stable layer at a given elevation $z$. The results are shown in Fig. 4.

For $\bar{\eta} = 0.50$ the system is a pure smectic-A phase in the bulk limit $h \to 0$, see Fig. 4(a). By increasing the sample height, a nematic layer develops at the top of the sample, followed by a crystal AAA layer at the bottom. Next an isotropic layer forms at the top, and finally a crystal ABC layer appears at the bottom of the sample. There is therefore an alternating pattern of layers growing either at the top or at the bottom of the sample by increasing sample height.

For $\eta = 0.452$, see Fig. 4(b), the bulk system phase separates into a nematic phase and a smectic-A phase. Due to the phase separation taking place in bulk, the sedimented samples never show a sequence with a single layer. Instead, short samples develop the sequence NS. By increasing the sample height two layers develop simultaneously: an isotropic layer is formed on top of the sample and an AAA-crystal forms at the bottom. The

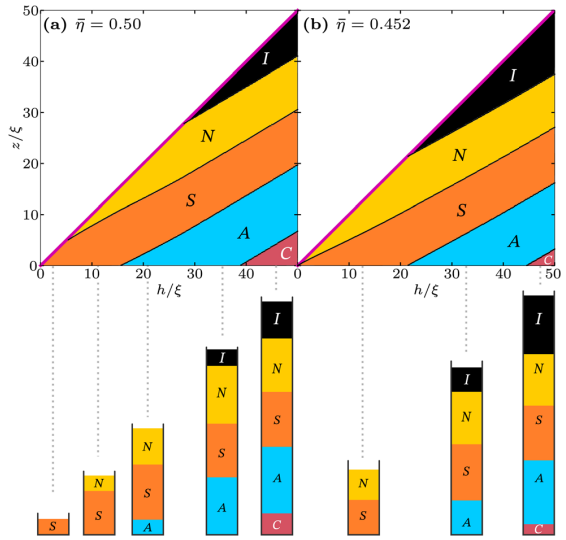


Fig. 4 Effect of sample height. Stable layer at elevation $z/\xi$ as a function of the sample height $h/\xi$ for colloidal hard spherocylinders with length-to-width aspect ratio $L/D$ = 10.0. The average packing fraction is fixed to (a) $\bar{\eta}$ = 0.50 and (b) $\bar{\eta}$ = 0.452, indicated by vertical dotted lines in the stacking diagram shown in Fig. 3(d). The layers are isotropic (I), nematic (N), smectic-A (S), AAA crystal (A), and ABC crystal (C). The thick violet lines indicate the air-sample interfaces at $z = h$. The sketches show all different stacking sequences at selected heights (indicated by vertical dotted lines).

simultaneous introduction of two layers at the top and at the bottom can also be observed in the stacking diagram, see Fig. 3(d). The dotted vertical line at $\bar{\eta}$ = 0.452 goes through the crossing point between two sedimentation binodals. Finally, for samples with $h/\xi > 44.3$ an ABC-crystal layer is formed at the bottom of the sample, see Fig. 4(b). No further changes in the stacking sequence occur for larger values of the sample height.

The evolution of the stacking sequence for two different packing fractions shown in Fig. 4 emphasizes the importance of the sample height as a crucial variable in colloidal sedimentation studies.[83] The stacking diagram results from the bulk diagram. However, knowing how the stacking sequences evolve by changing the sample height is not obvious from the bulk phase diagram, and complex phenomena such as the simultaneous growth of two layers can occur.

### D. Effects of mass-polydispersity close to density matching

We have studied the effects of mass-polydispersity (particles with identical shape but different buoyant masses) on sedimentation,[75] and identified that mass-polydispersity can play a crucial role in systems that are close to density matching, *i.e.* close to neutral buoyancy. If the average buoyant mass is close to neutral buoyancy, there will in general be particles in the suspension with positive and negative buoyant masses. Thus, there exist competing effects with some particles settling under gravity and other particles creaming up. Close to density matching the effective sedimentation paths are rather horizontal.[75] Hence, small changes in the distribution of buoyant masses can have a large effect on the stacking diagram, changing even its topology.

We illustrate here the effects of mass-polydispersity by considering a system of hard spherocylinders with aspect ratio $L/D$ = 5.0 and a parent distribution of buoyant masses close to density matching. The parent distribution gives the probability of finding a particle with buoyant mass m and it is therefore normalized such that $\int \mathrm{d}m f_{\mathrm{P}}(m) = 1$. We use a Gaussian with mean 0.02 and standard deviation of 0.2, see inset in Fig. 5(a). This distribution is close to density matching and it contains particles with positive as well as with negative buoyant masses. In Fig. 5(a) we show the corresponding stacking diagram in the plane of average packing fraction $\bar{\eta}$ and scaled sample height $h/\xi$. The stacking diagram contains 17 different stacking sequences and it is therefore significantly richer than its monodisperse counterpart (10 stacking sequences), *cf.* Fig. 3(c) and 5(a). The sedimentation path $\mu_{\mathrm{eff}}(z)$ for mass-polydisperse suspensions is curved and it can have a minimum at intermediate altitudes. Hence, for each bulk phase transition there is an extra sedimentation binodal formed by those paths for which the minimum of $\mu_{\mathrm{eff}}(z)$ at intermediate altitudes coincides with $\mu_{\mathrm{c}}$, the value of the chemical potential at bulk coexistence, *i.e.* $\mu_{\mathrm{eff}}(z) = \mu_{\mathrm{c}}$. Even though more stacking sequences develop in the mass-polydisperse system than in the monodisperse one, it is worth noting that there seem to exist sequences that only occur in the monodisperse case, *e.g.* INSC and NSC.

The sequence with the maximum possible number of layers CSNINSC starts to form in samples with $h/\xi > 395$. By increasing $h$ this sequence will eventually dominate the stacking diagram and occur for almost any average packing fraction. All the other stacking sequences that we observe are subsequences of CSNINSC. However, not all subsequences occur. For example, we observe the sequences NS and SNS, but not the sequence SN (top smectic and bottom nematic). This is due to the asymmetric parent distribution that in this example contains a larger proportion of particles with positive buoyant mass.

On the upper left part of the stacking diagram in Fig. 5(a), we observe a slim region with the sequence INS, followed by a reentrant INI stacking sequence. Note that the sequence INI already appeared for smaller sample heights and higher packing fractions. Sedimentation binodals of mass-polydisperse suspensions can cross each other multiple times. In contrast, we do not observe multiple crossings of the sedimentation binodals in the case of monodisperse particles, see Fig. 3. Another difference is that in mass-polydisperse systems, new layers can enter the stacking sequence in the middle of the sample and not only at the top or at the bottom. For example, by increasing the height at constant average packing fraction $\bar{\eta}$ = 0.52, the sequence changes from S to SNS, see Fig. 5(a). That is, a nematic layer nucleates in the middle of the sample.

Fractionation effects such as *e.g.* the accumulation of short rods in the isotropic phase occur in suspensions of hard spherocylinders with shape polydispersity.[86] In our mass-polydisperse suspension all particles have the same shape and hence such effects cannot occur by construction. However, we do observe mass fractionation induced by the gravitational field. As an

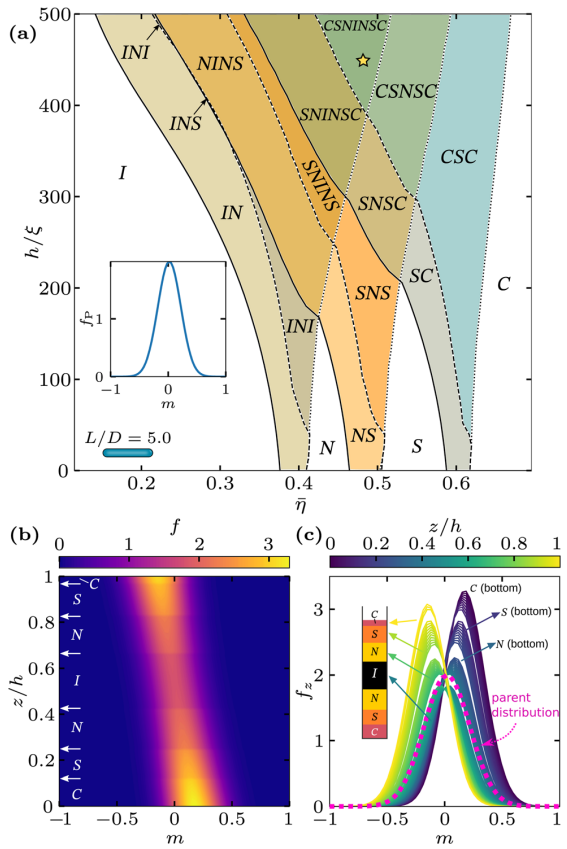


Fig. 5 Sedimentation of mass-polydisperse rods. (a) Stacking diagram in the plane of average packing fraction $\bar{\eta}$ and sample height $h/\xi$ of mass-polydisperse colloidal hard spherocylinders with aspect ratio $L/D$ = 5.0 close to density matching. The parent distribution $f_P$ of buoyant masses $m$, a Gaussian with mean 0.02 and standard deviation 0.2, is shown in the inset. Here $m = m_b/m_0$ with $m_0$ a reference buoyant mass which corresponds to 5 times the standard deviation of the parent distribution. The stacking sequences are labeled from the top to the bottom of the sample. The solid, dashed, and dotted lines are the sedimentation binodals formed by the sedimentation path that either end, start, or are tangent to a bulk binodal, respectively. (b) Probability $f(m,z)$ of finding a particle with buoyant mass m at an altitude $z$ in a sample with $h/\xi$ = 450 and $\bar{\eta}$ = 0.48, marked with a yellow star in panel (a). The stacking sequence is CSNINSC. The white arrows indicate the position of the interfaces. (c) Probability $f_z(m)$ of finding a particle with mass m at fixed elevation $z$ (see color bar). The initial parent distribution $f_P$ is represented with a dashed-pink line.

illustration, we show in Fig. 5(b) and (c) how the distribution of buoyant masses changes along the vertical coordinate in a given sample with stacking sequence CSNINSC. There is a strong mass fractionation with particles with positive (negative) buoyant mass concentrating in the bottom (top) of the sample.

## IV. Conclusions

We have calculated the stacking diagram of monodisperse suspensions of hard spherocylinders with different aspect ratios and studied the effect of varying the sample height. The stacking diagrams are significantly richer than their bulk counterparts. Increasing the sample height results in general in complex stacking sequences with several layers of different bulk phases. For sufficiently large values of the sample height a stacking sequence with layers from all possible bulk phases develops.

Multilayer stacking sequences are often found in sedimentation experiments. For example, van der Kooij and Lekkerkerker[87] found a sequence with five layers in plate-rod colloidal mixtures. This experimental observation has recently been linked to the occurrence of bulk quintuple (five-phase) coexistence in model plate-rod mixtures.[88] The striking bulk phase phenomenon identified by Opdam *et al.*[88] occurs in absence of a gravitational field.

From the viewpoint of sedimentation path theory, the occurrence of the experimentally observed[87] sedimentation stacks is a rather direct consequence of the influence of gravity. As we have shown,[84] systematically analysing sedimentation paths allows to theoretically predict the number as well as the correct ordering of the experimentally observed[87] stacking sequences. This quantitative treatment involves no need for higher (*e.g.* quintuple) multiphase bulk coexistence. While every two adjacent phases in a stacking sequence necessarily involve a corresponding two-phase bulk binodal, non-adjacent layers need not coexist in bulk, and in general they will not coexist in bulk. As an illustrative example, already in a one-component system of rods with aspect ratio $L/D$ = 10 the stacking sequence INSAC appears in samples of sufficient vertical height, see Fig. 4(d), even though only two-phase coexistences (I–N, N–S, S–A, and A–C) are stable in bulk, see Fig. 2(d). Nevertheless, it would be very interesting to study the influence of the presence of a bulk quintuple point on the resulting stacking sequences that occur under gravity.

We have also studied here the effect of mass-polydispersity in a suspension near density matching. The coupling between mass-polydispersity and the gravitational field increases the number of possible stacking sequences with respect to the monodisperse case. In a real colloidal suspension with low shape-polydispersity in *e.g.* the particle diameters, the effect of mass-polydispersity might dominate over that of size-polydispersity, especially near density matching. Nevertheless, size-polydispersity has a strong influence in the phase behaviour of hard spherocylinders[86,89–91] and will also have an effect in sedimentation. An extension of sedimentation path theory to incorporate also the effect of shape-polydispersity will be presented in future work.

It is apparent from the stacking diagrams that the sample height plays a role as relevant as the average packing fraction in the determination of the stacking sequence. Even though varying the sample height should be straightforward experimentally, we are not aware of experimental studies that have systematically considered the effect of the sample height on the phase behaviour of colloidal systems under sedimentation.

Surface and interfacial effects are not taken into account here due to the assumed local equilibrium condition. Wetting

and layering at the bottom of the sample[92–94] might be specially relevant for low height samples and high packing fractions. Due to the local equilibrium approximation, the theory predicts that new layers in the stacking sequence start to develop with an infinitesimally small thickness. The surface tension will in reality prevent layers to be stable until a critical thickness is reached, affecting therefore the position of the sedimentation binodals in the stacking diagram. A full minimization of a density functional theory for hard spherocylinders could be used to describe surface and interfacial effects.

## Conflicts of interest

There are no conflicts to declare.

## Acknowledgements

This work is funded by the Deutsche Forschungsgemeinschaft (DFG, German Research Foundation) under project number 436306241.

## References

1 L. Mederos, E. Velasco and Y. Martínez-Ratón, *J. Phys.: Condens. Matter*, 2014, **26**, 463101.
2 D. Frenkel, H. Lekkerkerker and A. Stroobants, *Nature*, 1988, **332**, 822.
3 J. A. C. Veerman and D. Frenkel, *Phys. Rev. A: At., Mol., Opt. Phys.*, 1990, **41**, 3237.
4 S. C. McGrother, D. C. Williamson and G. Jackson, *J. Chem. Phys.*, 1996, **104**, 6755.
5 P. Bolhuis and D. Frenkel, *J. Chem. Phys.*, 1997, **106**, 666–687.
6 I. Balberg, N. Binenbaum and N. Wagner, *Phys. Rev. Lett.*, 1984, **52**, 1465–1468.
7 A. L. R. Bug, S. A. Safran and I. Webman, *Phys. Rev. Lett.*, 1985, **54**, 1412–1415.
8 T. Schilling, M. A. Miller and P. van der Schoot, *Europhys. Lett.*, 2015, **111**, 56004.
9 W. Xu, X. Su and Y. Jiao, *Phys. Rev. E*, 2016, **94**, 032122.
10 C. Ferreiro-Córdova and J. S. van Duijneveldt, *J. Chem. Eng. Data*, 2014, **59**, 3055–3060.
11 L. Meng, Y. Jiao and S. Li, *Powder Technol.*, 2016, **292**, 176–185.
12 J. O. Freeman, S. Peterson, C. Cao, Y. Wang, S. V. Franklin and E. R. Weeks, *Granul. Matter.*, 2019, **21**, 84.
13 S. M. Ricci, J. Talbot, G. Tarjus and P. Viot, *J. Chem. Phys.*, 1994, **101**, 9164–9180.
14 M. Cieśla, P. Kubala and W. Nowak, *Phys. A: Stat. Mech. Appl.*, 2019, **527**, 121361.
15 R. Evans, *Adv. Phys.*, 1979, **28**, 143.
16 A. Poniewierski and R. Hołyst, *Phys. Rev. Lett.*, 1988, **61**, 2461–2464.
17 A. Poniewierski and T. J. Sluckin, *Phys. Rev. A: At., Mol., Opt. Phys.*, 1991, **43**, 6837–6842.
18 A. M. Somoza and P. Tarazona, *Phys. Rev. A: At., Mol., Opt. Phys.*, 1990, **41**, 965–970.
19 E. Velasco, L. Mederos and D. E. Sullivan, *Phys. Rev. A: At., Mol., Opt. Phys.*, 2000, **62**, 3708–3718.
20 H. Hansen-Goos and K. Mecke, *Phys. Rev. Lett.*, 2009, **102**, 018302.
21 A. Härtel and H. Löwen, *J. Phys.: Condens. Matter*, 2010, **22**, 104112.
22 R. Wittmann, M. Marechal and K. Mecke, *J. Phys.: Condens. Matter*, 2016, **28**, 244003.
23 R. Hołyst and A. Poniewierski, *Phys. Rev. A: At., Mol., Opt. Phys.*, 1988, **38**, 1527–1533.
24 W. E. McMullen, *Phys. Rev. A: At., Mol., Opt. Phys.*, 1988, **38**, 6384–6395.
25 B. G. Moore and W. E. McMullen, *Phys. Rev. A: At., Mol., Opt. Phys.*, 1990, **42**, 6042–6051.
26 E. Velasco, L. Mederos and D. E. Sullivan, *Phys. Rev. A: At., Mol., Opt. Phys.*, 2002, **66**, 021708.
27 R. Wittmann and K. Mecke, *J. Chem. Phys.*, 2014, **140**, 104703.
28 M. Dijkstra, R. van Roij and R. Evans, *Phys. Rev. A: At., Mol., Opt. Phys.*, 2001, **63**, 051703.
29 D. de las Heras, L. Mederos and E. Velasco, *Phys. Rev. A: At., Mol., Opt. Phys.*, 2003, **68**, 031709.
30 P. E. Brumby, H. H. Wensink, A. J. Haslam and G. Jackson, *Langmuir*, 2017, **33**, 11754–11770.
31 M. C. Lagomarsino, M. Dogterom and M. Dijkstra, *J. Chem. Phys.*, 2003, **119**, 3535–3540.
32 D. de las Heras, E. Velasco and L. Mederos, *J. Chem. Phys.*, 2004, **120**, 4949–4957.
33 E. Basurto, P. Gurin, S. Varga and G. Odriozola, *Phys. Rev. Res.*, 2020, **2**, 013356.
34 D. de las Heras, E. Velasco and L. Mederos, *Phys. Rev. Lett.*, 2005, **94**, 017801.
35 D. de las Heras, E. Velasco and L. Mederos, *Phys. Rev. A: At., Mol., Opt. Phys.*, 2006, **74**, 011709.
36 J. Dzubiella, M. Schmidt and H. Löwen, *Phys. Rev. A: At., Mol., Opt. Phys.*, 2000, **62**, 5081–5091.
37 Y. Trukhina and T. Schilling, *Phys. Rev. A: At., Mol., Opt. Phys.*, 2008, **77**, 011701.
38 P. X. Viveros-Méndez, A. Gil-Villegas and S. A. Espinoza, *J. Chem. Phys.*, 2017, **147**, 234902.
39 D. Rajendra, J. Mandal, Y. Hatwalne and P. K. Maiti, *Soft Matter*, 2023, **19**, 137–146.
40 J. J. Weis, D. Levesque and G. J. Zarragoicoechea, *Phys. Rev. Lett.*, 1992, **69**, 913–916.
41 D. Levesque, J. J. Weis and G. J. Zarragoicoechea, *Phys. Rev. A: At., Mol., Opt. Phys.*, 1993, **47**, 496–505.
42 D. C. Williamson and F. del Rio, *J. Chem. Phys.*, 1997, **107**, 9549–9558.
43 S. C. McGrother, A. Gil-Villegas and G. Jackson, *Mol. Phys.*, 1998, **95**, 657–673.
44 J. C. Shelley, G. N. Patey, D. Levesque and J. J. Weis, *Phys. Rev. A: At., Mol., Opt. Phys.*, 1999, **59**, 3065–3070.
45 C. Avendaño, A. Gil-Villegas and E. González-Tovar, *J. Chem. Phys.*, 2008, **128**, 044506.

46 G. Jiménez-Serratos, C. Avendaño, A. Gil-Villegas and E. González-Tovar, *Mol. Phys.*, 2011, **109**, 27–36.
47 R. Vácha and D. Frenkel, *Biophys. J.*, 2011, **101**, 1432–1439.
48 C. Zhang, X. Jian and W. Lu, *Soft Matter*, 2015, **11**, 1362–1368.
49 M. Jurásek and R. Vácha, *Soft Matter*, 2017, **13**, 7492–7497.
50 M. C. Bott, J. M. Brader, R. Wittmann, F. Winterhalter, M. Marechal and A. Sharma, *Phys. Rev. E*, 2018, **98**, 012601.
51 W. Yan, H. Zhang and M. J. Shelley, *J. Chem. Phys.*, 2019, **150**, 064109.
52 P. Stengele, A. Lüders and P. Nielaba, *Phys. Rev. E*, 2022, **106**, 014603.
53 V. D. Alaniz and H. Híjar, *Phys. A: Stat. Mech. Appl.*, 2023, **609**, 128298.
54 A. Cuetos, B. Martínez-Haya, L. F. Rull and S. Lago, *J. Chem. Phys.*, 2002, **117**, 2934–2946.
55 G. Campos-Villalobos, M. Dijkstra and A. Patti, *Phys. Rev. Lett.*, 2021, **126**, 158001.
56 Z. X. Zhang and J. S. van Duijneveldt, *J. Chem. Phys.*, 2006, **124**, 154910.
57 K. R. Purdy, S. Varga, A. Galindo, G. Jackson and S. Fraden, *Phys. Rev. Lett.*, 2005, **94**, 057801.
58 P. A. Buining and H. N. W. Lekkerkerker, *J. Phys. Chem.*, 1993, **97**, 11510–11516.
59 A. A. Shah, H. Kang, K. L. Kohlstedt, K. H. Ahn, S. C. Glotzer, C. W. Monroe and M. J. Solomon, *Small*, 2012, **8**, 1551–1562.
60 T. Ding, Z. Liu, K. Song and C.-H. Tung, *Colloids Surf., A*, 2009, **336**, 29–34.
61 A. Kuijk, D. V. Byelov, A. V. Petukhov, A. van Blaaderen and A. Imhof, *Faraday Discuss.*, 2012, **159**, 181.
62 J. L. Abbott, J. A. Spiers, Y. Gao, D. G. A. L. Aarts and R. P. A. Dullens, *J. Phys. D: Appl. Phys.*, 2018, **52**, 024002.
63 K. Keville, E. Franses and J. Caruthers, *J. Colloid Interface Sci.*, 1991, **144**, 103–126.
64 D. Mukhija and M. J. Solomon, *Soft Matter*, 2011, **7**, 540–545.
65 J. Roller, J. D. Geiger, M. Voggenreiter, J.-M. Meijer and A. Zumbusch, *Soft Matter*, 2020, **16**, 1021–1028.
66 J. Roller, A. Laganapan, J.-M. Meijer, M. Fuchs and A. Zumbusch, *Proc. Natl. Acad. Sci. U. S. A.*, 2021, **118**, e2018072118.
67 T. Eckert, M. Schmidt and D. de las Heras, *Phys. Rev. Research*, 2022, **4**, 013189.
68 P. X. Viveros-Méndez, A. Gil-Villegas and S. Aranda-Espinoza, *J. Chem. Phys.*, 2014, **141**, 044905.
69 S. V. Savenko and M. Dijkstra, *Phys. Rev. A: At., Mol., Opt. Phys.*, 2004, **70**, 051401.
70 V. F. D. Peters, M. Vis, H. H. Wensink and R. Tuinier, *Phys. Rev. E*, 2020, **101**, 062707.
71 D. de las Heras, N. Doshi, T. Cosgrove, J. Phipps, D. I. Gittins, J. S. V. Duijneveldt and M. Schmidt, *Sci. Rep.*, 2012, **2**, 789.
72 D. de las Heras and M. Schmidt, *Soft Matter*, 2013, **9**, 8636–8641.
73 M. A. Cotter, *J. Chem. Phys.*, 1977, **66**, 1098–1106.
74 H. Graf and H. Löwen, *Phys. Rev. A: At., Mol., Opt. Phys.*, 1999, **59**, 1932.
75 T. Eckert, M. Schmidt and D. de las Heras, *J. Chem. Phys.*, 2022, **157**, 234901.
76 Y. Lu, Y. Yin, Z. Li and Y. Xia, *Nano Lett.*, 2002, **2**, 785–788.
77 A. Stukowski, *Model. Simul. Mater. Sci. Eng.*, 2009, **18**, 015012.
78 G. Few and M. Rigby, *Chem. Phys. Lett.*, 1973, **20**, 433–435.
79 J. Vieillard-Baron, *Mol. Phys.*, 1974, **28**, 809–818.
80 D. W. Rebertus and K. M. Sando, *J. Chem. Phys.*, 1977, **67**, 2585.
81 H. Löwen, *Phys. Rev. A: At., Mol., Opt. Phys.*, 1994, **50**, 1232–1242.
82 G. Lasher, *J. Chem. Phys.*, 1970, **53**, 4141–4146.
83 T. Geigenfeind and D. de las Heras, *J. Phys.: Condens. Matter*, 2016, **29**, 064006.
84 T. Eckert, M. Schmidt and D. de las Heras, *Commun. Phys.*, 2021, **4**, 202.
85 F. M. van der Kooij and H. N. W. Lekkerkerker, *Langmuir*, 2000, **16**, 10144–10149.
86 A. Speranza and P. Sollich, *J. Chem. Phys.*, 2002, **117**, 5421.
87 F. M. van der Kooij and H. N. W. Lekkerkerker, *Phys. Rev. Lett.*, 2000, **84**, 781–784.
88 J. Opdam, V. F. D. Peters, H. H. Wensink and R. Tuinier, *J. Phys. Chem. Lett.*, 2022, **14**, 199–206.
89 M. A. Bates and D. Frenkel, *J. Chem. Phys.*, 1998, **109**, 6193–6199.
90 H. Meyer, P. van der Schoot and T. Schilling, *J. Chem. Phys.*, 2015, **143**, 044901.
91 C. A. De Filippo, S. Del Galdo, P. Corsi, C. De Michele and B. Capone, *Soft Matter*, 2023, **19**, 1732.
92 A. Mori, S. Ichiro Yanagiya, Y. Suzuki, T. Sawada and K. Ito, *Sci. Technol. Adv. Mater.*, 2006, **7**, 296–302.
93 M. Marechal and M. Dijkstra, *Phys. Rev. A: At., Mol., Opt. Phys.*, 2007, **75**, 061404.
94 K. Sandomirski, E. Allahyarov, H. Löwen and S. U. Egelhaaf, *Soft Matter*, 2011, **7**, 8050.